



MONASH University

***4-Acryloylmorpholine-Based Bottle Brush Polymers as Drug
Carrier Candidate: Synthesis and Evaluation of Their
Performance in Biological System***

Erny Sagita

Master of Pharmaceutical Sciences

A thesis submitted for the degree of *Doctor of Philosophy*
at Monash University in 2021

Drug Delivery, Disposition and Dynamics
Monash Institute of Pharmaceutical Sciences
Monash University (Parkville Campus)
381 Royal Parade, Parkville
Victoria 3052, Australia

Copyright Notice

© Erny Sagita (2021).

I certify that I have made all reasonable efforts to secure copyright permissions for third-party content included in this thesis and have not knowingly added copyright content to my work without the owner's permission.

Abstract

Studies of nanoparticles in the biological environment have unveiled the superiorities of non-spherical particles toward their spherical equivalent, such as longer plasma residence time, reduced macrophage uptake, increased tumour retention, deeper penetration in tumour and enhanced cell internalization. Molecular bottle-brush polymers (BBPs) are examples of polymer-based non-spherical materials, which have not been widely explored for biological application. While the potential application of BBPs in the nanomedicine field has been reported in some published articles, the majority of the studies were limited to *in vitro* evaluation. The synthesis of well-defined and low dispersity BBPs also remains a challenge. Hence, easy and straightforward synthesis and purification of BBPs need to be developed, to produce BBPs with remarkable characteristics for clinical application and to allow production on an industrial scale.

The general objective of this thesis is to develop a platform of bottle brush polymers using simple and easy method of synthesis and purification. 4-acryloylmorpholine (NAM) was used as the main component of side chains. Poly-NAM is a hydrophilic polymer that has not yet been extensively investigated for biological application elsewhere, but the hydrophilicity and hydrophobicity are similar to polyethyleneglycol (PEG), the most widely used polymer in biological application. Therefore, PNAM might demonstrate similar performance to PEG.

In Chapter 1, the background of knowledge related to nanomedicine and BBPs are discussed. This includes the potential application of BBPs in the biomedicine field as well as the polymerization technique to produce BBPs.

In Chapter 2, I have developed BBPs in a fast and easy manner, using a grafting-from approach Reversible Addition-Fragmentation Chain Transfer (RAFT) polymerization. With this method, I have successfully produced a library of NAM-based BBPs with well-

defined structure, remarkable dispersities ($\bar{M}_w/\bar{M}_n < 1.35$) and biologically applicable. The library includes BBPs with a variation of lengths and grafting densities.

In Chapter 3, I evaluated the performance of the NAM-based BBPs, which includes *in vitro* cell cytotoxicity, association and internalization and *in vivo* pharmacokinetics and biodistribution in healthy rats. All BBPs were non-toxic to several cell lines and were internalized by the cells. After intravenous injection in rats, all BBPs exhibited remarkably prolonged circulation (half-life >30 hours), compared to their associated linear polymers. Their deposition in major organs was relatively low (<15%), indicating the compounds were still circulating systemically after 24 h. The pharmacokinetics and biodistribution of the NAM-based BBPs were also similar to PEG-based BBP, revealing their potency to be used as alternative for PEG.

In Chapter 4, I studied the performance of the NAM-based BBPs in 4T1 syngeneic tumour models. This study demonstrated their high distribution to tumour tissues (9-14% ID per g tissue) after 24 hours post-injection. The very low clearance, together with a low level of unspecific organ accumulation and relatively high accumulation in tumour tissues, suggest that my BBPs could be excellent candidates for drug delivery applications.

Declaration

This thesis is an original work of my research and contains no material which has been accepted for the award of any other degree or diploma at any university or equivalent institution and that, to the best of my knowledge and belief, this thesis contains no material previously published or written by another person, except where due reference is made in the text of the thesis.

Signature:

Print Name: ERNY SAGITA

Date: 28 March 2021

Acknowledgements

In the name of Allah, The Most Gracious and The Most Merciful.

Firstly and foremost, I would like to express my deepest gratitude and appreciation to my principal supervisor, Dr. Joaquin Sanchis-Martinez for his trust in me when he accepted me as a PhD candidate at Monash University and then his endless support on both academic research and career development during my candidature. His motivation, patience, and guidance have helped me through my PhD research journey and thesis writing. I could not asked for a better teacher, mentor and friend, who always try to understand my condition. My sincerest gratitude also goes to my co-supervisor, Professor Sebastien Perrier, from University of Warwick, UK. He was the first person I contacted when I was looking for a PhD supervisor before he forwarded me to Dr. Joaquin Sanchis-Martinez. Although he homebased in UK and I only met physically once, his support, advice and encouragement via email and online meeting are valuable. I feel so fortunate, motivated and inspired to have both of them as my supervisors.

I would like to extend my gratitude to Professor Colin Pouton, Dr. Kristian Kempe, and Professor Thomas P. Davis as my PhD panel committee, who have given me some advice and insights regarding to my PhD project. In addition, I would like to thank Professor Ben Boyd for organizing the professional development hours program for D4 specialty.

I would like to thank people from Centre of Excellence in Convergent Bio-Nano Science and Technology (CBNS), especially to Professor Thomas P. Davis, Dr. John Quinn and Dr. Michael Whittaker, who have provided me with working space, laboratory facilities and knowledge so I can conduct my research in polymer chemistry smoothly and safely. Thanks to Dr. Francesca Ercole, who can always be a place to ask questions about polymerization and have given her time to review my thesis draft.

I would like to thank Professor Christopher Porter and teams for allowing me to work in his laboratory. Very special thanks to Dr. Orlagh Feeney, Dr. Tri Hung Nguyen and Dr.

Estelle Suys who have trained me doing animal surgery and helped me conducting animal studies.

I thank Karen Drakatos for her help and support with my enrolment. I thank technical staff of MIPS for their dedication and expertise. I would also like to thank everyone in the laboratory for the fabulous working environment. Very special thanks to people in Ximo's army: Cheng Sun, Carlos Arellano, Khoi Nguyen, Andrew Kerr, Sean Ellacott and Hyun Suk. You are amazing people and I have learned a lot of things from you all. Also, people who have been in laboratory with me to share some thoughts and jokes: Ayaat Mahmoud, Aadarash Zia, Nam Dao, James Grace, Adrian Sulistio, May Lai, Joanne Ly, Emily Pilkington, Zihnil Mazrad, Shanti Sibuea, Gracia, Nathania Leong, Enyuan Cao, Daniel Brundel, and many more. I wish I could mention all the names on this page.

I am largely indebted many things to parents and father-in-law, especially for trusting and supporting me to start a PhD journey overseas. My sister Dina and my brother Dyas who have been taking care of our parents while I am doing my PhD. Also to my brothers and sisters in law: Sis, Andi, Bayu, Yulia, Rini, Yusuf, Dhia who have been very pleasant people.

Finally to the best person in my life: my husband and friend, Tri Setiawan, who has spared his own career to accompany and support me doing my PhD, helping me take care of the kids. My precious first born, Almira Putri Setiawan, who has been a very cooperative and smart girl, and teaches me about life. My dearest Nawasena Putra Setiawan who had accompanied me working in the lab while he was still in my belly, and who often does funny things after he was born that can release my stress and anxiety. I am looking forward to our next adventure with three of you.

ERNY SAGITA

Table of Contents

Copyright Notice.....	ii
Abstract.....	iii
Declaration.....	v
Acknowledgements.....	vi
Table of Contents.....	viii
List of Tables.....	xi
List of Figures.....	xii
List of Schemes.....	xv
List of Equations.....	xvi
List of Appendices.....	xvii
List of Abbreviations.....	xviii
CHAPTER 1. GENERAL INTRODUCTION.....	1
1.1 POLYMERIC NANOMEDICINES.....	1
1.1.1 Polymer Therapeutics.....	4
1.1.2 Polymer Conjugates.....	6
1.2 SHAPE MATTERS.....	8
1.3 BOTTLE BRUSH POLYMERS IN NANOMEDICINE.....	12
1.4 METHOD OF SYNTHESIS OF BOTTLE BRUSH POLYMERS.....	18
1.5 LIVING RADICAL POLYMERIZATION: RAFT POLYMERIZATION.....	20
1.6 PNAM AS ALTERNATIVE FOR PEG.....	29
1.7 SCOPE OF THESIS.....	31
CHAPTER 2. SYNTHESIS AND CHARACTERIZATION OF 4- ACRYLOYLMORPHOLINE-BASED BOTTLE BRUSH POLYMERS.....	33
2.1 INTRODUCTION.....	33
2.2 EXPERIMENTAL METHOD.....	37
2.2.1 Materials.....	37
2.2.2 Characterization Equipment.....	38
2.2.3 Synthesis of 2-[(butylsulfanyl)carbonothiol]sulfanyl Propanoic Acid.....	39
2.2.4 Synthesis of Backbone.....	40
2.2.4.1 Synthesis of Poly-Hydroxyethyl Acrylamide (PHEAm _a).....	40
2.2.4.2 Synthesis of Poly-(Hydroxyethyl Acrylamide-co-4- Acryloylmorpholine) (P(HEAm-co-NAM) _{b%,a}).....	41
2.2.5 Synthesis of CTA-PHEAm _a and PCTA-P(HEAm-co-NAM) _{b%,a}	41
2.2.6 Synthesis of BBPs.....	42
2.2.6.1 Synthesis of Brush [PNAM _x] _a	42
2.2.6.2 Synthesis of Brush [PNAM _x] _{50%,c} and Brush [PNAM _x] _{25%,c}	42
2.2.6.3 Synthesis of Brush [PnBA _y] _a	43

2.2.6.4	Synthesis of Brush [PnBA _y - <i>b</i> -PNAM _x] _a	43
2.2.6.5	Synthesis of Brush [P(NAM _x -co-NHSA _y)] _a , Brush [P(NAM _x -co-NHSA _y)] _{50%,c} and Brush [P(NAM _x -co-NHSA _y)] _{25%,c}	44
2.2.7	End Group Modification	45
2.2.8	Dynamic Interchange	45
2.2.9	RAFT End Group Stability	46
2.3	RESULTS AND DISCUSSION	47
2.3.1	Synthesis of Backbone Precursors (PHEAm _a)	48
2.3.2	Synthesis of PCTA-PHEAm _a	53
2.3.3	Synthesis of Brush [PNAM _x] _a	57
2.3.4	Synthesis of Comb [PNAM _x] _{50%,a} and Comb [PNAM _x] _{25%,a}	62
2.3.5	Synthesis of Brush [PnBA _y - <i>b</i> -PNAM _x] _a	68
2.3.6	Synthesis of Brush [P(NHSA _z -co-NAM _x)] _a	75
2.3.7	Morphology of BBPs	77
2.3.8	Brush End Group Modification	80
2.3.9	Stability of Z-groups	92
2.3.10	Statistical Z-groups Interchange	95
2.4	CONCLUSION AND FUTURE DIRECTION	101
	CHAPTER 3. <i>IN VITRO</i> CELL STUDIES, PHARMACOKINETICS AND BIODISTRIBUTION OF POLY-4-ACRYLOYLMORPHOLINE-BASED BOTTLE BRUSH POLYMER	103
3.1	INTRODUCTION	103
3.2	EXPERIMENTAL METHOD	106
3.2.1	Materials	106
3.2.2	Synthesis Procedure	107
3.2.2.1	Synthesis of Lin-NAM	107
3.2.2.2	Fluorescence Labelling	107
3.2.2.3	Radiolabelling	108
3.2.3	<i>In vitro</i> Cell Studies	109
3.2.3.1	Cells	109
3.2.3.2	Growth Inhibition Assay	110
3.2.3.3	Confocal Microscopy	110
3.2.3.4	Flow Cytometry	111
3.2.4	Pharmacokinetics and biodistribution studies	112
3.2.4.1	Animals	112
3.2.4.2	Pharmacokinetics Studies	112
3.2.4.3	Biodistribution Studies	113
3.2.4.4	Urine	114
3.2.4.5	Calculation of Pharmacokinetic Parameters	115
3.3	RESULTS AND DISCUSSION	115

3.3.1	Biocompatibility Studies	115
3.3.2	Cell Association	119
3.3.3	Cell Internalization	124
3.3.4	<i>In vitro</i> Degradation Study	127
3.3.5	Pharmacokinetics and Biodistribution	129
3.4	CONCLUSION AND FUTURE DIRECTION	138
CHAPTER 4. BIODISTRIBUTION OF 4-ACRYLOYLMORPHOLINE-BASED BOTTLE BRUSH POLYMERS IN 4T1 TUMOUR MICE MODEL		139
4.1	INTRODUCTION	139
4.2	EXPERIMENTAL METHOD	141
4.2.1	Materials	141
4.2.2	Cells	141
4.2.3	Animals	141
4.2.4	Tumour Induction	141
4.2.5	Qualitative Biodistribution Studies	142
4.2.6	Calculation of Fluorescence Intensity	142
4.2.7	Quantitative Biodistribution Studies	143
4.3	RESULTS AND DISCUSSION	144
4.3.1	Tumour Induction	144
4.3.2	Qualitative Biodistribution Studies	148
4.3.3	Quantitative Biodistribution Studies	153
4.4	CONCLUSION AND FUTURE DIRECTION	157
CHAPTER 5. SUMMARY AND FUTURE PERSPECTIVE		158
REFERENCES		160
APPENDIX		171

List of Tables

Table 1.1 Examples of unimolecular bottle brush polymers and their biological application.....	17
Table 2.1 Characteristics for polymerization of HEAm to make backbone PHEAm _a	51
Table 2.2 M _n and Đ values of PolyCTAs as determined by DMac-GPC analysis with polystyrene standard.....	56
Table 2.3 Results from varying the ratio of CTA _{shuttle} :CTA _{backbone} for the synthesis of brush [PNAM ₅₀] ₁₅₀ . All reactions were done in DMF with [M] = 2 M, [I ₀] = 70°C, 1.5 h.....	59
Table 2.4 Results from varying the ratio of CTA _{shuttle} /CTA _{backbone} for the synthesis of brush [PNAM ₅₀] ₅₀₀	60
Table 2.5 M _n and Đ values of polymers as determined by DMac-GPC analysis with polystyrene standard.....	65
Table 2.6 M _n and Đ values of PCTA-P(HEAm-co-NAM) _{b%,a} as determined by DMac-GPC analysis with polystyrene standard	66
Table 2.7 Results from varying the ratio of CTA _{shuttle} /CTA _{backbone} for the synthesis brush [PNAM _x] _{b%,a}	68
Table 2.8 Summary of all reactions of brush [PnBA _y] _a	70
Table 2.9 Summary of reaction of brush [PnBA _y -b-PNAM _x] _a	74
Table 2.10 GPC characteristic of the produced NHSA-functionalized BBPs synthesized via CTA-shuttle R-group approach.....	77
Table 2.11 Summary of BBPs size obtained by analysis of AFM images using FIJI ImageJ	78
Table 2.12 Molecular weight of all BBPs before and after Z-group removal using ACVA, analyzed by DMac-GPC	86
Table 2.13 Summary of interchange reactions with different ratio and time	99
Table 3.1 Calculated pharmacokinetic parameters and urine recovery after intravenous administration of polymers to rats at normalized dose 5 mg/kg.....	132
Table 4.1 Tumour growth analysis of 4T1 cells in syngeneic female BALB/c mice	147

List of Figures

Figure 1.1 Schematic illustration of EPR effect	3
Figure 1.2 Three main class of nanomedicines	4
Figure 1.3 Cartoon of Ringsdorf's model.....	7
Figure 1.4 Illustration on how nanoparticles with elongated shape will be a helpful strategy to maximize the delivery of anticancer drugs.	11
Figure 1.5 Cartoon of polymer-based elongated nanoparticles.....	13
Figure 1.6 Use of bottle brush polymers for delivery of biomedical molecules	15
Figure 1.7 Three main strategies for producing molecular brush polymers.....	19
Figure 1.8 Comparison between condensation polymerization and addition polymerization	21
Figure 1.9 Stages of traditional free radical polymerization.....	22
Figure 1.10 Illustration of some types of living radical polymerization	23
Figure 1.11 Generic structure of RAFT agent	26
Figure 1.12 Proposed mechanism of RAFT polymerization	27
Figure 1.13 Schematic representation of chain generation in RAFT polymerization	28
Figure 1.14 Structure comparison between PEG and PNAM.....	30
Figure 2.1 Proposed mechanism of grafting from approach via Z-group RAFT polymerization	34
Figure 2.2 Proposed mechanisms of the grafting-from approach via R-group	35
Figure 2.3 Proposed mechanisms of the grafting-from approach via R-group RAFT polymerization with an addition of shuttle-CTAs	36
Figure 2.4 ^1H NMR peak to calculate monomer conversion by comparing DMF signal and monomer signal at the initial time and the final crude reaction.	48
Figure 2.5 Kinetic plots of the polymerization of PHEAm _a mediated by C4 at 70°C. The dashed lines serve as guide to the eye to highlight the linear region in the plot of $\ln([M]_0/[M]_n)$ versus time.	50
Figure 2.6 Overlay of GPC-DMAc chromatograms of PHEAm _a	52
Figure 2.7 Comparison of ^1H NMR spectra of representative backbone precursor and polyCTA from PHEAm ₁₀₀	55
Figure 2.8 Representative GPC chromatogram of PCTA-PHEAm _a (full line) which is shifted from its corresponding backbone (dash line) and overlay of GPC-chromatograms of all produced polyCTAs.	56
Figure 2.9 Effect of $\text{CTA}_{\text{shuttle}}/\text{CTA}_{\text{backbone}}$ on the dispersity of brush $[\text{PNAM}_{50}]_{150}$ and chromatogram of the crude products	58
Figure 2.10 Effect of $\text{CTA}_{\text{shuttle}}/\text{CTA}_{\text{backbone}}$ on the dispersity of brush $[\text{PNAM}_{50}]_{500}$ and chromatogram of the crude products	60
Figure 2.11 Evolution of GPC chromatogram from the synthesis and purification of brush $[\text{PNAM}_{50}]_{150}$ and overlay of GPC chromatogram of the purified brush $[\text{PNAM}_x]_a$	61
Figure 2.12 Evolution of ^1H NMR spectra from the synthesis of $[\text{PNAM}_{50}]_{150}$	62
Figure 2.13 Structure illustration of molecular brushes with different grafting densities	62
Figure 2.14 ^1H NMR peak used to calculate monomer conversion by comparing DMF signal and monomer signal at the initial time and at the stopped reaction time.	64
Figure 2.15 Reaction kinetics and molar mass evolution of $\text{P}(\text{HEAm-co-NAM})_{50\%,500}$	64
Figure 2.16 Overlay of GPC-chromatograms of all produced $\text{P}(\text{HEAm-co-NAM})_{b\%,a}$	65
Figure 2.17 Overlay of GPC-chromatograms of all produced PCTA- $\text{P}(\text{HEAm-co-NAM})_{b\%,a}$	67
Figure 2.18 Effect of $\text{CTA}_{\text{shuttle}}/\text{CTA}_{\text{backbone}}$ on the dispersity of brushes with grafting density <50% and (lower panel) GPC chromatogram of (a) brush $[\text{PNAM}_{50}]_{50\%,500}$ (b) brush $[\text{PNAM}_{50}]_{50\%,150}$ (c) brush $[\text{PNAM}_{50}]_{25\%,500}$	67
Figure 2.19 Illustration of BBPs with a hydrophobic core	69
Figure 2.20 Kinetics plots of the synthesis of brush $[\text{PnBA}_y]_{500}$ via “CTA-shuttled” R-group approach.....	71
Figure 2.21 Kinetics plots of the synthesis of brush $[\text{BA}_y]_{500}$ via “CTA-shuttled” R-group approach using $\text{CTA}_{\text{shuttle}}/\text{CTA}_{\text{backbone}}$ 3:1	72
Figure 2.22 Representative evolution of GPC chromatogram of brush $[\text{PnBA}_y]_a$ before and after precipitation in methanol and Overlay of GPC chromatograms of all produced brush $[\text{PnBA}_y]_a$	73

Figure 2.23 Overlay of GPC chromatograms of all produced brush $[PnBA_y-b-PNAM_x]_a$	75
Figure 2.24 Representative comparison between BBPs with and without NHSA overlay of GPC chromatogram of all produced NHSA-functionalized BBPs.....	77
Figure 2.25 AFM images of BBPs on mica, air-dried from chloroform: A. brush $[PNAM_{50}]_{150}$, B. brush $[PNAM_{50}]_{50\%,150}$, C. brush $[PNAM_{50}]_{25\%,150}$, D. brush $[PNAM_{50}]_{500}$, and E. brush $[PNAM_{50}]_{50\%,500}$	79
Figure 2.26 Representative 1H NMR spectra of BBPs (a) before end group removal and (b) after end group removal performed in $CDCl_3$	84
Figure 2.27 UV-Vis spectrum of brush $[PNAM_{50}]_{150}$ before and after radical induced end group removal.....	84
Figure 2.28 Brush (a) $[P(NHSA_3-co-NAM_{50})]_{150}$ and (b) $[P(NHSA_3-co-NAM_{50})]_{500}$ solution in PBS pH 7.4, before and after Z-group removal.....	85
Figure 2.29 (a) Representative comparison of GPC chromatogram of BBPs before and after end group removal using radical-induced substitution method and (b) overlay of GPC chromatogram of all BBPs after end group removal.....	86
Figure 2.30 Proposed illustration of Z-group interchange in RAFT polymerization.....	87
Figure 2.31 Illustration of Z-group interchange in BBPs.....	88
Figure 2.32 Proposed mechanism of Z-group interchange.....	88
Figure 2.33 The chemical structure and distinguishable 1H NMR spectra of C4 and BM.....	89
Figure 2.34 1H NMR spectra of brush (a) $[PNAM_{50}]_{150}$ and (b) $[PNAM_{50}]_{500}$, before and after Z-group interchange.....	91
Figure 2.35 UV-Vis spectrum of brush $[PNAM_{50}]_{150}$ before and after Z-group interchange showing identical λ_{max}	91
Figure 2.36 UV-Vis spectra of BBPs in (a) PBS pH 7.4, (b) PBS pH 7.4 + 1 eq. of ethanolamine to Z-groups and (c) PBS pH 7.4 + 20 eq. of ethanolamine to Z-groups.....	93
Figure 2.37 GPC chromatogram of (a) dry BBPs, (b) after incubation in PBS pH 7.4 (control), (c) after incubation in PBS pH 7.4 + 1 eq. of ethanolamine to Z-groups and (d) after incubation in PBS pH 7.4 + 20 eq. of ethanolamine to Z-groups.....	94
Figure 2.38 Proposed principle of Z-groups statistical interchange.....	96
Figure 2.39 1H NMR spectra of brush $[NAM_5]_{150}$ (a) before interchange (b) after interchange with BM/PABTC 1:1, (c) after interchange with BM/PABTC 5:1 and (d) after interchange with BM/PABTC 10:1. The crossed-out signals are solvent impurities.....	97
Figure 2.40 1H NMR spectra of original polyCTA, showing no peak at δ (ppm) 2.68 and an intense peak at δ (ppm) 0.89.....	98
Figure 2.41 Proportion of BM in brush polymer vs time. Samples were isolated from crude reaction prior to analysis.....	99
Figure 2.42 Proposed mechanism of dynamic interchange.....	100
Figure 2.43 Library of NAM-based BBPs that I have produced.....	102
Figure 3.1 Morphology of cell lines used for viability studies in 80% confluence.....	117
Figure 3.2 Toxicity profile of the compounds in 3T3 and MDA-MB-231-HM cells determined by MTT assay after incubation for 72 h at 37°C.....	118
Figure 3.3 Cellular fluorescence intensity associated with AlexaFluor™488 as determined by flow cytometry after incubation of the compounds for 3 h at 4°C, 3 h at 37°C and 24 h at 37°C in 3T3 and MDA-MB-23-HM cells.....	120
Figure 3.4 Atomic Force Microscopy (AFM) images of (a) SB-NAM, (b) SC50-NAM and (c) SC25-NAM.....	122
Figure 3.5 Cellular fluorescence intensity associated with Cy5.5 as determined by flow cytometry after incubation of the compounds for 3 h at 4°C, 3 h at 37°C and 24 h at 37°C in 3T3 and MDA-MB-23-HM cells.....	123
Figure 3.6 Confocal images of MDA-MB-231-HM cells treated with Alexa-488-labelled polymers (green) for 24 h at 37°C at a concentration of 0.3 mg/mL. L.....	125
Figure 3.7 Confocal images of MDA-MB-231-HM cells treated with Cy5.5-labelled polymers (red) for 24 h at 37°C at a concentration of 0.3 mg/mL.....	126
Figure 3.8 Brush illustration and its hydrolyzable groups.....	127
Figure 3.9 GPC chromatograms of SB-NAM and SC25-NAM, after incubation at 37°C in PBS pH 7.4, 6.5 and 5.5 for 28 days.....	128
Figure 3.10 SEC Chromatogram of pure $[^{14}C]$ -labelled polymers obtained by liquid scintillation counting of collected fractions (1 mL per fraction).....	130

Figure 3.11 (a) Plasma concentration versus time profiles (normalized dose to 5 mg/kg), (b) percent of dose recovery in urine, (c) biodistribution (% injected dose per organ) and (d) biodistribution (% injected dose per g tissue), 24 h after intravenous administration of Lin-NAM, SB-PEG, SB-NAM and LB-NAM at 2.5-10 mg/kg.....	132
Figure 3.12 (a) Plasma concentration versus time profiles (normalized dose to 5 mg/kg), (b) percent of dose recovery in urine, (c) biodistribution (% injected dose per organ) and (d) biodistribution (% injected dose per g tissue), 24 h after intravenous administration of SB-NAM, SC50-NAM and SC25-NAM at 2.5-10 mg/kg.	136
Figure 4.1 (a) Schematic illustration of 4T1 cells inoculation to mouse and (b) tumour bearing female BALB/c mice.....	146
Figure 4.2 Profile of 4T1 tumour growth (a) from all female BALB/c mice, (b) grouped by similar tumour growth rate.....	147
Figure 4.3 IVIS images of BBPs accumulation in tumours 4T1 tumour-bearing mice, treated with Cy5.5-labelled polymers.....	149
Figure 4.4 IVIS images obtained from an individual scan of ex-vivo organs of each mouse on a well-plate 24 hours after administration of Cy5.5-labelled polymers.....	150
Figure 4.5 IVIS images obtained from a simultaneous scan of ex-vivo organs on a black mat 24 hours after administration of Cy5.5-labelled polymers.....	151
Figure 4.6 Biodistribution of Cy5.5-labelled BBPs after sacrificed at 24 h: (A) fluorescence per organ and (B) normalized fluorescence by area. Fluorescence values were obtained from IVIS images analysis using Fiji ImageJ.....	152
Figure 4.7 Biodistribution of ¹⁴ C-labelled BBPs after sacrifice at 24 h.....	155

List of Schemes

Scheme 1.1 General equilibrium in NMP using (a) bicomponent and (b) monocomponent initiating system	24
Scheme 1.2 General equilibrium condition in ATRP	25
Scheme 2.1 Schematic illustration of the synthesis of BBPs via the CTA-shuttled R-group Grafting-from approach: (A) synthesis of backbone, (B) synthesis of polyCTA and (C) grafting of monomers from the backbone.	47
Scheme 2.2 General synthesis of backbone PHEAm _a	48
Scheme 2.3 Representative reaction scheme of polyCTA backbone formation.....	53
Scheme 2.4 Tautomerisation of EDC (adapted from Williams and Ibrahim ¹⁴⁶).....	53
Scheme 2.5 General reaction of brush [PNAM _x] _a	57
Scheme 2.6 General synthesis of P(HEAm-co-NAM) _{b%,a}	63
Scheme 2.7 General synthesis of PCTA-P(HEAm-co-NAM) _{b%,a}	66
Scheme 2.8 General reaction scheme for grafting of nBA from PolyCTAs.	69
Scheme 2.9 General reaction of brush [PnBA _y -b-PNAM _x] _a	74
Scheme 2.10 General synthesis of brush [P(NHSA _z -co-NAM _x)] _a	76
Scheme 2.11 The most commonly used techniques for removal of thiocarbonylthio groups from polymer chains.....	81
Scheme 2.12 Mechanism of reaction of Z-groups replacement by azoinitiator with LPO assistance	82
Scheme 2.13 Representative RAFT end group removal in BBPs using radical-induced addition-fragmentation-coupling process	83
Scheme 2.14 General reaction scheme of Z-group interchange in BBPs	90
Scheme 2.15 Proposed possible aminolysis reaction of BBPs	92
Scheme 2.16 PCTA-PHEAm _a interchange reaction scheme	97
Scheme 3.1 Comparison of the studied polymers.....	104
Scheme 3.2 Chemical structure of Lin-NAM and SB-PEG.....	105

List of Equations

Equation 2.1 Calculation of monomer conversion by comparison of the integral value of monomer signal relative to DMF	49
Equation 2.2 Calculation of BM proportion in the final brush.....	98
Equation 3.1 Determination of viable cells from MTT cytotoxicity assay	110
Equation 3.2 Tissue processing efficiency	114
Equation 3.3 Correction of [¹⁴ C] content	114
Equation 4.1 Calculation of tumour volume based on measurement using vernier calliper.....	142
Equation 4.2 Calculation of corrected total fluorescence	142

List of Appendices

Table A.1 Calculation of BM proportion compared to PABTC in polyCTA after interchange	177
Table A.2 Calculation of fluorescence correction factors for Alexa-488-labelled polymers.....	182
Table A.3 Calculation of fluorescence correction factors for Cy5.5-labelled polymers	183
Table A.4 Biodistribution of NAM-based BBPs in 4T1 tumour-bearing mice (%ID per g tissue)...	191
Figure A.1 ¹ H NMR spectrum of C4	171
Figure A.2 Representative ¹ H NMR spectrum of PHEAm ₅₀₀	171
Figure A.3 Representative ¹ H NMR spectrum of isolated PCTA-PHEAm ₁₅₀	172
Figure A.4 Representative ¹ H NMR spectrum of isolated brush [PNAM ₅₀] ₅₀₀	172
Figure A.5 Representative ¹ H NMR spectrum of P(HEAm-co-NAM) _{50%,500}	173
Figure A.6 Representative ¹ H NMR spectra of isolated PCTA-P(HEAm-co-NAM) _{50%,500}	173
Figure A.7 Representative ¹ H NMR spectra of isolated brush [PNAM ₅₀] _{50%,500}	174
Figure A.8 Representative ¹ H NMR spectrum of isolated brush [PnBA ₁₂ -b-PNAM ₃₉] ₅₀₀ perfor	174
Figure A.9 Representative ¹ H NMR spectra of isolated brush [PnBA ₁₂ -b-PNAM ₃₉] ₅₀₀	175
Figure A.10 Representative ¹ H NMR spectra of isolated brush [P(NHSA ₃ -co-NAM ₅₀)] ₁₅₀	175
Figure A.11 Interchange analysis of BM/PABTC 1:1	176
Figure A.12 Interchange analysis of BM/PABTC 5:1	176
Figure A.13 Interchange analysis of BM/PABTC 10:1	177
Figure A.14 The AFM image of brush [PNAM ₅₀] ₁₅₀	178
Figure A.15 The AFM image of brush [PNAM ₅₀] _{50%,150}	178
Figure A.16 The AFM image of brush [PNAM ₅₀] _{25%,150}	179
Figure A.17 The AFM image of brush [PNAM ₅₀] ₅₀₀	180
Figure A.18 The AFM image of brush [PNAM ₅₀] _{50%,500}	180
Figure A.19 Toxicity profile of the compounds in HEK-293 and 4T1 cells determined by MTT assay after incubation for 72 h at 37°C	181
Figure A.20 Calibration curve of Alexa-488-labelled polymers	182
Figure A.21 Calibration curve of Cy5.5-labelled polymers	183
Figure A.22 Confocal images of MDA-MB-231 breast cancer cells treated with AlexaFluor™ 488- labelled polymers (green) for 24 h at 37°C at a concentration of 0.3 mg/mL	184
Figure A.23 Confocal images of 3T3 cells treated with AlexaFluor™ 488-labelled polymers (green) for 24 h at 37°C at a concentration of 0.3 mg/mL	185
Figure A.24 Confocal images of MDA-MB-231-HM cells treated with Cy5.5-labelled polymer for 24 h at 37°C at a concentration of 0.3 mg/mL	186
Figure A.25 Confocal images of 3T3 cells treated with Cy5.5-labelled polymer for 24 h at 37°C at a concentration of 0.3 mg/mL	187
Figure A.26 Raw Image of mice from IVIS system 24 hours after injection of Cy5.5-labelled polymers	188
Figure A.27 Raw images of organs from individual scan from IVIS system 24 hours after injection of Cy5.5-labelled polymers	189
Figure A.28 Raw image of organs from simultaneous scan from IVIS system 24 hours after injection of Cy5.5-labelled polymers	190
Figure A.29 Biodistribution of ¹⁴ C-labelled BBPs after sacrifice at 24 h, expressed by %ID per organ.	191

List of Abbreviations

ABC	Accelerated Blood Clearance
ACVA	4,4'-Azobis(4-cyanovaleric acid), radical initiator
AIBN	2,2'-Azobis(2-methylpropionitrile), radical initiator
ATRP	Atom transfer radical polymerization
nBA	n-Butyl Acrylate, monomer
BBP	Bottle-brush polymers
BD	Biodistribution
BM	3-((((1-carboxyethyl)thio)carbonothioyl)thio) propanoic acid, RAFT agent (CTA)
C4	2-[(Butylsulfanyl)carbonothiol]sulfanyl propanoic acid, RAFT agent/CTA
CRP	Controlled Radical polymerization
CTA	Chain Transfer Agent
DMAc	Dimethylacetamide
DMF	Dimethyl Formamide
DP	Degree of polymerization
EPR	Enhanced Permeability and Retention
GPC	Gel Permeation Chromatography
ID	Injected Doses
LB-NAM	Long Brush (DP backbone 500)
LC50-NAM	Long Comb 50% Grafting Density (DP backbone 500)
Lin-NAM	Linear PNAM
LPO	Lauroyl Peroxide
LRP	Living Radical polymerization
HEAm	Hydroxyethyl Acrylamide, monomer
NAM	4-Acryloylmorpholine, monomer

NHSA	Acrylic acid N-hydroxysuccinimide ester
NMP	nitroxide mediated polymerization
¹ H NMR	Proton Nuclear Magnetic Resonance
PEG	Polyethylene Glycol
PEGMA	Poly(ethylene glycol) methacrylate
PHEAm	Poly Hydroxyethyl Acrylamide
PK	Pharmacokinetics
PNAM	Poly-4-Acryloylmorpholine
PolyCTA	Poly chain-transfer agent, macro-CTA
RAFT	Reversible addition-fragmentation chain transfer
RES	Reticuloendothelial System
ROI	Region of interests
SB-NAM	Short Brush with PNAM arms
SC25-NAM	Short Comb 25% Grafting Density (DP backbone 150)
SC50-NAM	Short Comb 50% Grafting Density (DP backbone 150)
SEC	Size exclusion Chromatography

CHAPTER 1. GENERAL INTRODUCTION

1.1 POLYMERIC NANOMEDICINES

In the last decades, countless publications have been devoted to the term “nanomedicines”. Since the existence of nanomedicines, optimism has risen that the use of nano-sized objects will significantly improve the diagnosis and treatment of disease. In 2004, the European Science Foundation defined the field of nanomedicines as *“the science and technology of diagnosing, treating and preventing disease and traumatic injury, of relieving pain, and of preserving and improving human health, using molecular tools and molecular knowledge of the human body”*.¹ This field involves five main subdisciplines: (1) analytical tools, (2) nanoimaging, (3) nanomaterials and nanodevices, (4) novel therapeutics and drug delivery systems, and (5) clinical, regulatory and toxicological issues. While the broader term “nanotechnology” involves particles with a size between 1 to 100 nm, nanoparticles for medical applications cannot strictly adhere to this threshold.² They are defined in a broader range of size, between 1 and 1000 nm, which can adequately cover all type of nanomaterials².

Drug delivery systems that employ nanomaterials as drug carriers have attracted tremendous interest, due to their remarkable performance in overcoming some problems in drug use. They offered troubleshoots that relate to physicochemistry problems such as poor aqueous solubility and biological execution such as blood circulation (pharmacokinetics) and toxicity.³⁻⁶ Loading a poorly soluble drug to a water-soluble nanocarrier can improve its solubility. The blood circulation of a short half-life drug can be extended due to the nano-scale size, which can avoid renal filtration. An example for this is Doxil®, a commercial liposome-formulated doxorubicine, which outperformed the free doxorubicine in terms of pharmacokinetics (longer half-life and slower clearance), tumor accumulation and side effect minimization⁷.

One of the objectives in developing nanomedicine is to improve cancer therapy by what is called “targeted therapy”. This is because the treatment of cancer using cytotoxic drugs generates many unwanted side effects. The therapeutic index of cytotoxic drugs is razor-thin, meaning the difference between the dose required for antitumour effect and that causes intolerable toxicity is very small⁸. As such, targeted therapy is required to maximize the antitumour activity while minimizing the toxicity to other healthy tissues.

In the 1980s, Hiroshi Maeda reported a new concept of macromolecular therapeutics for cancer chemotherapy, which then became the foundation of passive targeting to cancer tissues. They first found that their drug delivery system SMANCS, a copolymer of styrene and maleic acid (SMA) conjugated to antitumour protein neocarzinostatin (NCS), showed a more pronounced antitumour activity with reduced toxicity, compared to the free NCS⁹. He then discovered that the increased antitumour activity and decreased toxicity were due to more effective accumulation of SMANCS in the tumour than normal tissues.¹⁰ The reason accounted for this phenomenon is because the solid tumour tissues exhibited leaky vasculature and poor development of the lymphatics. This pathological anatomy allows large particles, including proteins, polymers, liposomes and micelles, with certain sizes to enter and be retained in tumour tissues due to poor lymphatic drainage. This concept of tumour tissue physiology has been termed and well-known as enhanced permeability and retention (EPR) effect (Figure 1.1). The fundamental principle of EPR effect has been exploited as the rationale for designing nanoparticles as a drug delivery carrier. It is postulated that nanoparticles with the right characteristics, mainly size, will be able to evade renal clearance, circulate long, and accumulate in tumour tissues due to EPR effect. Then when the nanoparticles are carrying cytotoxic drugs, the drugs could eradicate the cancerous cells with minimal toxicity to other tissues. Thus, the side effects of chemotherapy can be mitigated.

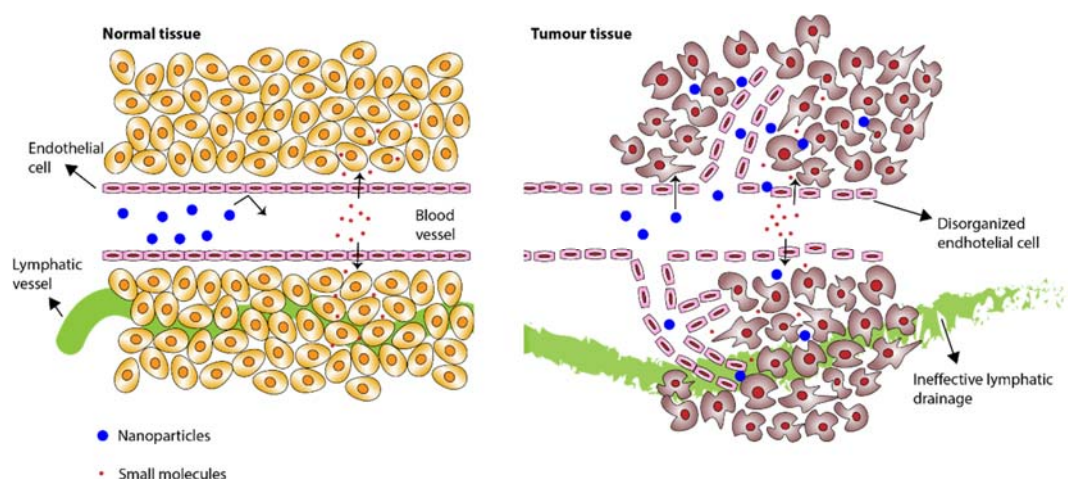


Figure 1.1 Schematic illustration of EPR effect

Among many nanomaterials used as therapeutic carriers, the most extensively investigated clusters are inorganic nanoparticles (metal-based), liposomes (lipid-based) and polymeric nanoparticles (polymer-based) (Figure 1.2). Inorganic nanoparticles have been comprehensively developed as diagnostic agents, due to their physical and/or optical attributes such as wavelength-dependent scattering and absorption (gold¹¹ and silver¹² nanoparticles), superparamagnetic properties (iron oxide nanoparticles¹³) and size- and composition-dependent fluorescence emission spectra (quantum dots¹⁴). However, some controversial issues, such as toxicity and instability in solution, have restricted their clinical application.

Lipid-based drug delivery system such as liposomes have been extensively explored and considered as safer. Their biocompatibility is not debated since they are composed of self-assembly lipid bilayer conformation, which resemble the structure of cell membrane. They have the capability to solubilize both hydrophilic and hydrophobic drugs, where the hydrophilic ones are entrapped inside the aqueous core and the hydrophobic materials will locate themselves inside the phospholipid bilayer. Due to this capability, they have been applied for treatment of various diseases such as cancers¹⁵ and fungal infections^{16,17}. However, although some liposomal formulations have been approved and are available in

the market, their pharmaceutical development and regulatory concerns remain a challenge. The challenges include scalability of the manufacturing process, stability issues, denaturation of the encapsulated protein drugs due to manufacturing process (excessive heat or organic solvents), residual organic solvents in the formulation and relatively high cost of phospholipids.¹⁸

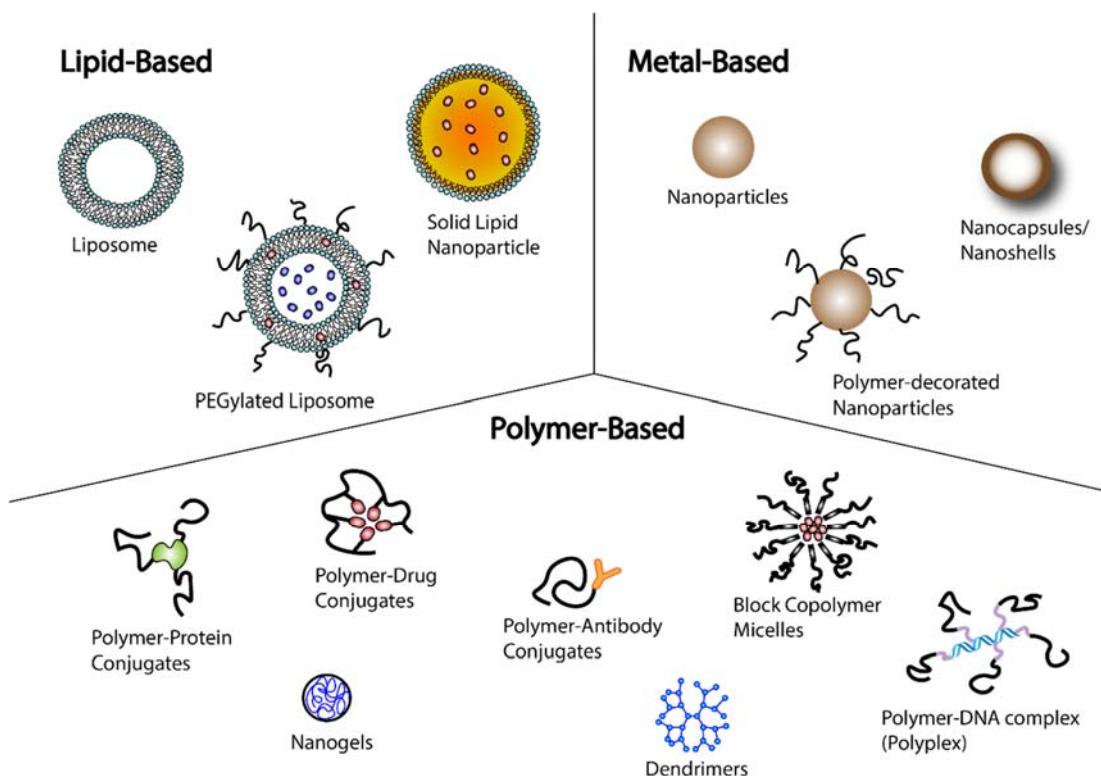


Figure 1.2 Three main class of nanomedicines

1.1.1 Polymer Therapeutics

To overcome some limitations of metallic and lipid-based nanoparticles, researchers have attempted to combine those type of nanoparticles and polymer chemistry. For example, the surface modification of metallic and lipid-based nanoparticles with hydrophilic polymers such as poly(ethylene glycol) (PEG) can enhance their stability in solution by preventing undesirable aggregation.¹⁹ Decorating the nanoparticles with polyethylene glycol

(PEGylation) has successfully reduced the interaction with phagocytic cells.²⁰ PEG forms a non-charged hydrophilic layer around particles that preserve particles adsorption by opsonins.²¹ Since the first report of their use to enhance protein delivery in around 1970 by Davis group,²²⁻²⁴ PEG has become the most popular as well as FDA-approved hydrophilic polymers for drug or protein delivery system. It has been used in many nanoparticle formulations, either alone or in combination with other nanoparticulate structure such as liposome and dendrimers.²⁵ Nowadays, there are numerous commercial PEG-containing products available in the market. This includes PEG as an adjuvant in liposome system such as PEGylated-liposome Doxil® and Marqibo®,²⁶ as well as PEG-conjugates such as PEGASYS® (PEGylated interferon alfa-2a, for treatment of hepatitis C and hepatitis B) and PEG-INTRON® (PEGylated interferon alfa-2b, for treatment of hepatitis C and melanoma).²⁷

Over the past decade, polymeric nanomedicines have emerged as a promising platform for drug delivery carrier, due to their flexibility in synthesis and modification. From nature-origin to synthetics, there is a wide range of biocompatible and/or biodegradable polymers which have been investigated for their potential use as polymer therapeutics, including the aforementioned PEG, poly(ethyleneimine), dextran, chitosan, polyoxazoline, polyacryloylmorpholine, and many more. They can be engineered as linear chains as well as branched structures, and they can be functionally designed as unimolecular as well as self-assembly system such as polymeric micelles. Beside the flexibility in synthesis, polymeric nanomedicine also provides flexibility in how the drugs can be incorporated into the system. Typically, the pharmacologically active ingredients can be either physically entrapped in the polymeric nanoparticles or covalently-bound to the individual polymer chain. The latter belongs to an umbrella term “polymer therapeutics”, which was first coined by Prof. Ruth Duncan nearly 20 years ago.²⁸ Since then, the field has become an interesting topic of research and the number of publications in the field has grown exponentially. The focus of the research in this field is divided into four main topics.²⁹ 1) design of prospective

polymeric conjugates, which can be used for cancer and other diseases, 2) physico-chemical characterization method, 3) design and synthesis of well-defined polymeric carrier with various architecture, and 4) use of polymer for combination therapy.

The term “polymer therapeutics” is used to cover some systems, which include polymeric drugs, polymer-drug conjugates, polymer-protein conjugates, polymeric micelles with a covalently-bound drug, and polymer-DNA complex (polyplex).²⁸ It is important to remark that the pharmacologically active ingredients are covalently linked to the polymeric carrier, which consequently changes the characteristics of the active ingredient itself, such as solubility and pharmacokinetics. This new system is regarded as a new chemical entity (NCE), and thus, has to undergo a complete set of preclinical/clinical phase before it can enter the market. To date, 25 products have been licensed for clinical use as polymeric drugs, sequestrants, conjugates, and imaging agent.³⁰ Two of those licensed products, Neulasta® (PEGylated recombinant human granulocyte colony-stimulating factor, for stimulation of white blood cells production in infection) and Copaxone® (immunomodulator polymeric drugs for the treatment of multiple sclerosis), were even featured in the top-10 selling pharmaceuticals list.³¹ Following that, there are about 20 polymer-protein/aptamer conjugates and 22 polymer-drug conjugates under clinical trials.³² In the last 10 years, there are a substantial amount of publications (around 92,000) dedicated to “polymer therapeutics” in the PubMed database, indicating that the topic still remains a great interest.

1.1.2 Polymer Conjugates

So, what polymers can do to improve the therapy of an already-established pharmacologically active ingredient? First, the size of the conjugates is bigger than the glomerular filtration cut-off size (6 nm³³ or 50 kDa³⁴) and thus, will not cross the glomerulus for renal excretion. In the case of PEG as the polymeric carrier, the conjugates are also able to avoid clearance by macrophages due to the shielding property of PEG. By avoiding the

renal excretion and macrophages clearance, the conjugates can demonstrate prolonged circulation half-life compared to the free drugs or proteins.

In 1975, Helmut Ringsdorf visualized an ideal polymer conjugates system, named Ringsdorf's model, which until now becomes the foundation of the development of polymer conjugates, especially polymer-drug conjugates.³⁵ The Ringsdorf's model consists of a linear polymer chain with water-soluble groups, covalently-bound drugs and targeting moieties (Figure 1.3). The water-soluble groups must be kept available to make the whole system soluble. It is noteworthy that even though the drugs are attached to the backbone covalently, they have to be linked to the backbone via a site-specific cleavable linkage. The linkage is useful to ensure that the drugs will be liberated once they reach the target site, and perform their original pharmacological action. Decoration with targeting moiety is necessary to drive the system to the specific site of action, and therefore minimize their toxicity to other tissues.

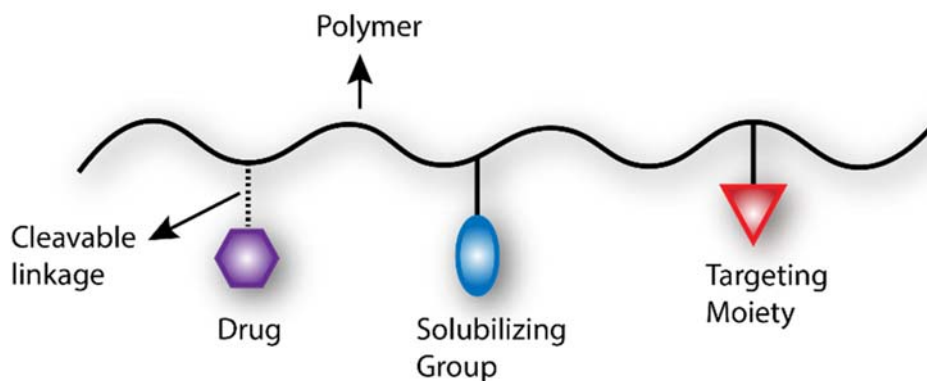


Figure 1.3 Cartoon of Ringsdorf's model

Reflecting on the Ringsdorf's model, the choice of polymer design and architecture must be considered carefully. In the past days, using polymers for pharmaceutical application might be challenging. Due to their heterogeneous nature (high dispersity) and limited characterization method, it was difficult to produce a well-defined polymer species, which then influence their biological activity. However, those issues can now be minimized

with a rapid advance in polymer chemistry as well as characterization method, allowing the synthesis of polymers with narrow dispersity and defined characteristics. Nowadays, the quest for synthetic polymers as potential drug delivery carrier is not only limited to linear chain but also a more complex architecture such as branched polymers, dendronized polymers, star polymers, and grafted polymers.

1.2 SHAPE MATTERS

Designing a polymer as a drug carrier is strenuous, especially if the intention is to deliver their cargo to the targeted sites. To achieve maximum targeting efficacy, they should be able to withstand entire biological hurdles during their journey. As soon as they are injected into the blood, they will circulate along with the blood flow wherein, as foreign objects, they will be subjected to clearance, either by kidney filtration and/or reticuloendothelial system (RES) organs. Evading clearance by the kidney is relatively not difficult. As long as the size of nanoparticles is more than 6 nm or 50 kDa, the glomerular filtration-size threshold,^{33,34} they will be able to avoid renal excretion. However, as the size increases, the propensity to be recognized and then cleared by RES also increases, and this has become the main reason some nanoparticles cannot circulate long. Then if the nanoparticles are finally able to mitigate RES clearance, they still need to undergo a complex series of impediments, such as interactions with plasma protein (corona formation and opsonisation), migration to the vessel wall, interaction with the target tissues and/or cells and then release the payload via endosomotropic route for maximum therapeutic effect.³⁶

Size has been acknowledged as one of the critical factors that determine blood circulation half-life of nanoparticles, with particles ranging from nanometer size to approximately 15 μm tend to accumulate primarily in the liver and spleen.³⁷ Nevertheless, another factor that should also be taken into consideration is particle geometry. Despite the fact that most nanoparticles are spherical, it has been recognised that non-spherical shape

showed augmented biological performance compared to spherical³⁶. In fact, tailoring both size and shape has been proven to dictate the potencies of particle carriers in the biological system.

The influence of particle shape in phagocytosis have been intensively demonstrated in several studies done by Mitragotri group. They demonstrated that the macrophage membrane ruffles might contribute in how particles can attach and orient themselves to the macrophages.^{38,39} Champion and Mitragotri first studied the influence of particle shape in phagocytosis using styrene particles.⁴⁰ They reported that the uptake of the particles by rat alveolar macrophages is dependent on their shape and surface curvature. The particles with flat side, such as elliptical disk (major axis 3-14 μm , aspect ratio 2-4, thickness 400-1,000 nm), resulted in simple spreading of the macrophages on the surface of the particles without performing internalization. In a separate study, they found that worm-like particle with aspect ratio >20 exhibits minor phagocytosis compared to the spherical particles of equal volume.⁴¹ Sharma *et al.*, showed that prolate ellipsoid particles (low curvature, more flat side) are internalized by macrophages in a lower extent, compared to the spheres and oblate ellipsoid particles (higher curvature, more curve side).⁴² Although the majority of the studies are on macrophages in culture media, they generally demonstrated that particles with an elongated dimension would undergo lower uptake by macrophages. Since the main mechanism of clearance in the liver is uptake by Kupffer cells,⁴³ the macrophages that reside in that organ, these *in vitro* results theoretically will relate to the *in vivo* biodistribution to this organ.

The mechanism of clearance in the spleen is slightly different from that in the liver. In the spleen, the primary mechanism of particle clearance is filtration.⁴³ Generally, non-deformable particles larger than 200 nm cannot pass through the splenic pores and will be caught in the spleen for uptake by resident macrophages.^{44,45} Engineering non-spherical particles with minor and major axis could manipulate splenic filtration. This approach creates the possibility to use particles with larger volume but with one of the axis smaller

than the pore size of the spleen. This minor axis would align with the splenic pores and then help the particles to pass through. Geng *et al.*, reported that filamentous polymer micelle known as filomicelles, with diameters <60 nm and lengths up to 18 μm , can elude the splenic filters.⁴⁶ They demonstrated that the filomicelles have the ability to weave and then pass through the splenic pores via their small diameters. However, in the case of avoiding splenic filtration, shape alone is not enough. It is suggested that the rigidity of the structure of the nanoparticles also plays an important role. For example, Park *et al.* showed that the spleen:liver ratio of iron oxide nanoworms (theoretically more rigid than the filomicelles) is higher than the nanospheres counterpart.⁴⁷ ¹⁹⁸Au-Doped pegylated nanorod also showed higher spleen accumulation compared to the nanospheres equivalent.⁴⁸ This is presumably due to the reduced probability of the rigid particles to navigate and align their minor axis with the splenic filter. From all these results, we can conclude that an interplay between shape, size and rigidity affects the overall complex process of nanoparticles' clearance by the body.

Despite the varied results regarding nanoparticles distribution in liver and spleen, some studies agree that nanoparticles with elongated structure, by optimising other parameters such as size and rigidity, provide a beneficial strategy for minimising their uptake by RES organs, and thus prolong their blood circulation time. This is also proven by aforementioned filomicelles by Geng *et al.*, which can be retained in the blood circulation ten times longer than their spherical counterparts, even with length size up to micrometer scale⁴⁶. In another study, Geng *et al.* also showed that delivering anticancer drug paclitaxel using filomicelles resulted in more effective tumour shrinkage and more tumour-specific cytotoxicity.⁴⁹ Nanochains composed of iron-oxide nanospheres and liposomes (aspect ratio of approximately 4, 36 \times 10 nm) exhibited lower liver uptake and longer blood residence time than the liposomes alone.⁵⁰ The longer blood residence time is also followed by the higher tumour distribution of the nanochains.

In addition of uptake by macrophages and prolonged blood circulation, some *in vitro* studies demonstrated that particles shape could influence their uptake by cancerous cells. For example, rod-shaped mesoporous silica nanoparticles were internalized by A375 human melanoma cells to a greater extent than the sphere-shaped particles.⁵¹ Meng *et al.*, also reported that mesoporous silica nanoparticles with higher aspect ratio (up to 2.1-2.5) showed higher uptake by HeLa cells than spheres.⁵²

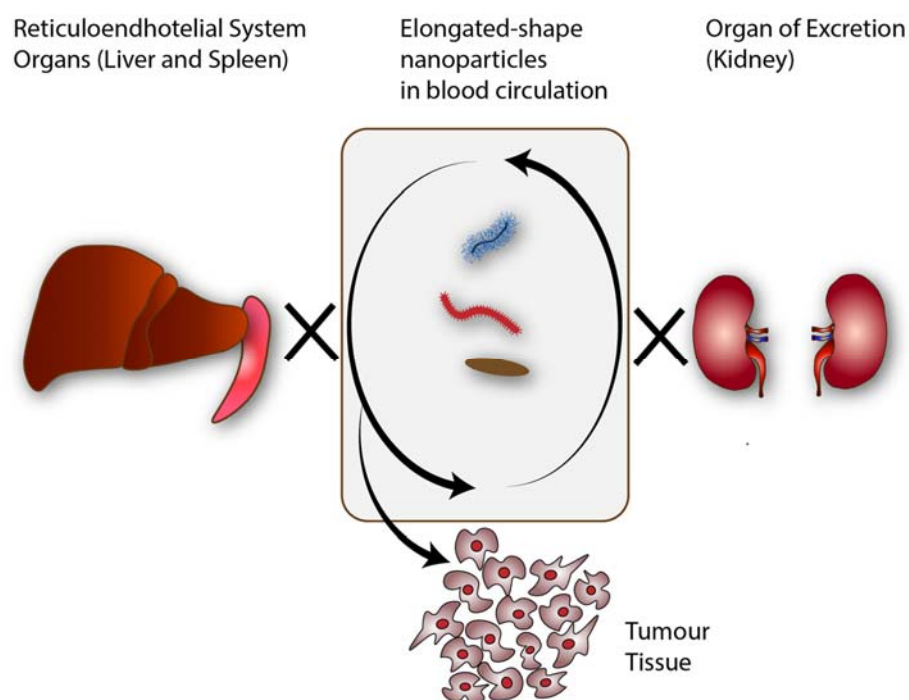


Figure 1.4 Illustration on how nanoparticles with elongated shape will be a helpful strategy to maximize the delivery of anticancer drugs.

It is interesting to know that the uptake of nanoparticle shape in cancerous cells revealed the opposite trend in phagocytic cells. Using the elongated-shape particles can reduce the clearance of the nanoparticles by RES organs, resulting in longer circulation time. Since the extravasation of nanoparticles to tumour tissues often proportionally correlate with their circulation time⁵³, longer circulation time might result in higher accumulation in tumour tissue. Then providing that the elongated shape will be internalized

by cells in a greater extent than the round shape, I postulate that the use of elongated particles will be a helpful strategy to maximise the delivery of anticancer drugs (Figure 1.4).

1.3 BOTTLE BRUSH POLYMERS IN NANOMEDICINE

Synthetic polymers have become one of the highly explored nanocarriers due to their flexibility in synthesis and tailoring to various architecture, especially to create a non-spherical structure. Polymeric filomicelles^{46,49,54,55}, supramolecular self-assembly nanotubes⁵⁶⁻⁵⁸ and bottle-brushes⁵⁹⁻⁶² (Figure 1.5) are examples of elongated polymer which have shown promising *in vivo* behaviour, such as improved plasma retention, reduced liver uptake, increased cytotoxicity and/or increased tumour regression when used to deliver anticancer drugs. Therefore, non-spherical nanoparticles made of polymers is an interesting field, yet they have not been extensively studied compared to the spherical structure.

The formation of polymeric filomicelles and nanotubes requires self-assembly processes, which is sensitive to environmental change, such as dilution, change in salt concentration and pH. Note that the nanotubes mentioned here are those made of cyclic peptide, decorated with polymers. Bottle brush polymer (BBP), on the other hand, are different from their relatives. They are built as covalently-linked construction and thus retain their elongated shape in various environments. BBPs generally consist of a polymer backbone, grafted with highly dense polymer side chains that force the backbone to stretch and form a cylindrical shape. Other references mentioned BBPs as densely grafted copolymers^{63,64}, molecular (polymer) brushes⁶⁵⁻⁶⁸, (molecular) bottlebrush⁶⁹⁻⁷², cylindrical polymer brushes (CPBs)^{62,73}, or nanorods⁵⁹. However, based on IUPAC nomenclature recommendation for non-linear copolymer molecules, bottle-brush polymers fall under “comb” group.⁷⁴ In some cases, the name “comb” can be replaced by “graft”, e.g. polystyrene-*comb*-poly(ethyleneoxide) or polystyrene-*graft*-poly(ethyleneoxide).⁷⁵

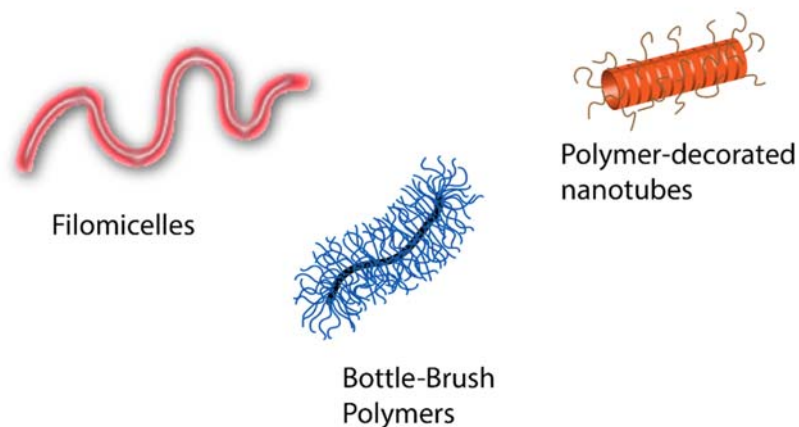


Figure 1.5 Cartoon of polymer-based elongated nanoparticles

Polymeric brushes grafted to a surface have been used in various applications ranging from nonbiofouling surface, cell adhesive, protein binding and immobilization, chromatography supports, antibacterial coating and low friction surface (the topic has been comprehensively reviewed by Barbey *et al.*⁷⁶). However, only over the past six years BBPs in solution have been studied to investigate their promising application in drug delivery.

Depending on the chemical structure, BBPs in solution can present as intermolecular assembled system or unimolecular structure. Micelles comprised of brush polymers showed remarkable characteristics, such as aqueous stability^{77,78}, high drug loading capacity^{77,78}, and more controlled drug release in comparison with micelles made of linear polymer⁷⁷. However, those reported assembled brush polymers are spherical, based on the microscopic images, and therefore do not represent elongated structure. For this reason, I am focusing my attention on unimolecular brush polymers construction since they will exhibit an elongated structure when prepared with appropriate design.

Unimolecular short BBPs, composed of polyethylene glycol (PEG) as side chain, have been used to conjugate anticancer drugs. Yu *et al.* used brush polymers made of polylactide (PLA) as backbone and PEG as side chains as a carrier for anticancer drugs paclitaxel⁷⁹ and doxorubicin⁸⁰. Similar types of anticancer drug-BBP conjugates were also developed by Zou *et al.*⁸¹, and Johnson *et al.*^{82,83}. However, their studies only limited to *in*

vitro drug release with pH-sensitive release profile, cytotoxicity toward cell lines and qualitative study in cell uptake.

Beside anticancer drugs, BBPs have also been used to deliver fluorescence imaging agent. Sowers *et al.*⁸⁴ developed a redox responsive BBP for MRI and fluorescence imaging, bringing both reduction-resistant spirocyclohexyl nitroxide (Chex) and Cy5.5. Both compounds are covalently tethered to PEG macromonomers after which undergoing the grafting-through process. They showed that their system displayed *in vivo* MRI contrast enhancement, possibly due to the high nitroxide density.

Not only for delivering small molecule drugs, polymer brush has also been investigated as a carrier for larger molecules such as peptide, protein, antibody and nucleic acid. Blum *et al.*⁸⁵ created a cell-penetrating peptide polymer with the brush structure. The brush structure contained block copolymer of oligoethyleneglycol (OEG) and a sequence of peptide, decorated with arginine as cell penetrator sequence. They demonstrated that their peptide polymers were able to penetrate cells, maintain their sequence specific cytotoxic function, and be resistant to proteolysis. Qi *et al.*⁸⁶ conjugated exendin-4 (exendin), a therapeutic peptide that is clinically used to treat type 2 diabetes mellitus, to poly[oligo(ethylene glycol) methyl ether methacrylate] (POEGMA) brush polymers. The conjugates showed the ability to extend the glucose-lowering effect of exendin for up to 120 h, compared to the native exendin. Moreover, the conjugates also demonstrated less antigenicity compared to two FDA-approved drugs, Adagen (a PEGylated adenosine deaminase for treating severe combined immunodeficiency disease (SCID)) and Krystexxa (a PEGylated uricase for treating chronic refractory gout). Wang *et al.*⁸⁷ incorporated ovalbumin (OVA) to poly(L-lysine)-poly(p-phenyleneethynylene) (PLL-PPE) polymer brushes for a dendritic cell (DC)-based vaccines. The OVA-polymer brush complexes were highly water-soluble with excellent antigen-loading capacity. Compared with free OVA, the OVA-polymer brush complexes exhibited better actions such as higher cellular uptake, induction of DC maturation and cytokines release, robust immune response and high

antitumour activity against B16F10 tumour model. The delivery of small interfering RNAs (siRNAs) using poly(ethylene glycol) bottle brush polymer resulted in ~25-fold increase in blood elimination half-life and a ~19-fold increase in the area under the curve compared with siRNA alone.⁸⁸ Lu *et al.*⁸⁹ has reported that the stability of oligonucleotides against nuclease increases when they are incorporated into polymer brush. The system consists of nucleic acid strands covalently linked to the backbone of a brush polymer having PEG side chains. Their findings suggested that the brush polymer has the capability to shield DNA from proteins and bypass serum opsonisation due to the densely arranged side chains of the brush. They also showed that the brush structure could outperform the linear counterpart by limiting the nuclease accessibility for the DNA. Following the study, Jia *et al.*⁹⁰ also performed the effect of DNA anchoring location and length of backbone to the shielding ability from nucleases *in vitro*. The nucleic acid must be anchored at the centre part of the sequence in order to gain full protection from nuclease. The application of BBPs in biomedical field is summarized in Figure 1.6.

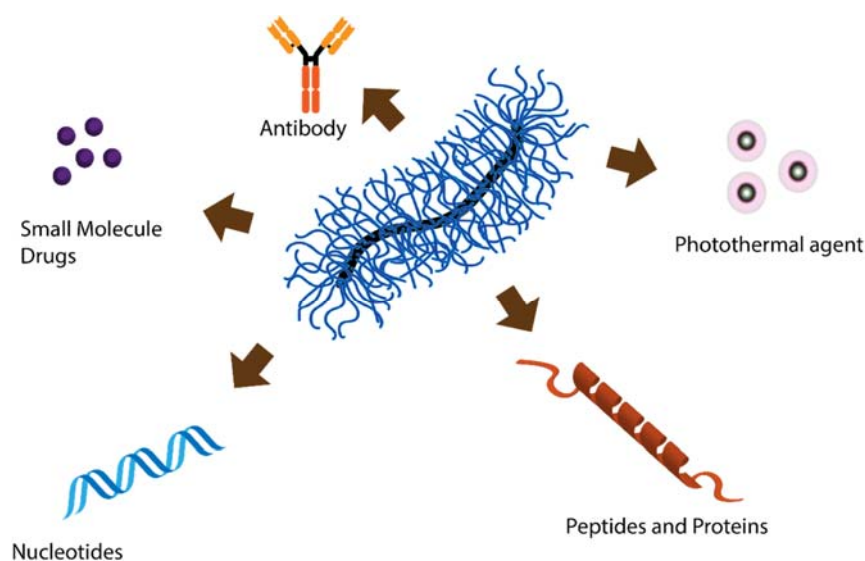


Figure 1.6 Use of bottle brush polymers for delivery of biomedical molecules

While the potential application of BBPs in nanomedicine field has been reported in many published articles, the majority of the studies were limited to *in vitro* evaluation. Besides, the most highlighted feature of the BBPs was the high loading capacity and shielding ability. In addition, all studied BBPs displayed near to round shape rather than cylindrical, and thus lacking knowledge on the *in vitro* and/or *in vivo* behaviour of BBPs as anisotropic materials. The studies of biomedical application of BBPs are summarized in Table 1.1.

As far as I know, Müllner *et al.*⁶² is the first who reported the *in vivo* clearance, distribution and half-life of PEG-based BBPs (without cargo) by evaluating the impact of various length (55 nm, 200 nm and 1050 nm) and rigidity (with polycaprolactone (PCL) and without PCL)⁶². From the *in vitro* cell association study using RAW264.7 macrophages, the longest brushes (1050 nm) showed the highest uptake regardless the addition of PCL core. The high macrophage uptake of the longest brush was also reflected by its higher clearance (half-life around 20 h) and higher accumulation in the liver and spleen (around 20%), compared to the shorter brushes. Nevertheless, the information about their uptake in non-phagocytic cells was not available. Then Zhang *et al.* also compared PEG-based BBPs with various shorter lengths (~34, 60 and 119 nm)⁹¹. They reported that longer BBPs demonstrated higher cellular uptake in SH-SY5Y (bone marrow neuroblastoma) and HUVEC cells than the shorter ones. However, the *in vivo* studies revealed that the longer BBPs showed shorter blood circulation time, with half-life around 4.9 and 6.5 hours for the longest and shortest BBPs, respectively. Particles larger than 1000 nm are more favourable to experience phagocytosis by phagocytic cells, such as macrophages, neutrophils, or dendritic cells^{92,93}, while for non-phagocytic cells, the size of 50-200 nm exhibits the most optimum cell internalization⁹³. Therefore, based on the previously reported results and this knowledge, I suggest that the optimum length of brushes would be between 30 to 200 nm.

Table 1.1 Examples of unimolecular bottle brush polymers and their biological application

Side chains	Method of synthesis	polymerization of side chain	MW (kDa) ^a	\bar{D}	Length (nm)	Diameter (nm)	Cargo	Biologically Relevant Studies	Ref
PEG	Graft to	n.d.	68	1.16	10-30 ^b	n.d.	Paclitaxel	<i>In vitro</i>	79
PEG	Graft through	ROMP	125-595	1.06-1.16	n.d.	60-90 ^b	Paclitaxel	<i>In vitro</i>	81
PEG	Graft to	n.d.	55.4	1.33	n.d.	26 ^c	Doxorubicin	<i>In vitro</i>	80
PEG	Graft to	n.d.	34-1960	1.04-1.27	n.d.	6-50 ^c	Doxorubicin	<i>In vitro</i>	83
PEG	Graft through	ROMP	33-500	1.04-1.70	n.d.	6.2-15 ^c	Camptotechin & Doxorubicin	<i>In vitro</i>	82
PAA-PEG	Graft to	ATRP and RAFT	250-399	1.49-1.47	20-177 ^e	18	IR780 iodide	<i>In vitro, In vivo</i>	94
PMMA	Graft from	ATRP	n.d.	n.d.	n.d.	228-1500 ^c	Porphyrazine	<i>In vitro</i>	95
PEG	Graft through	ROMP	n.d.	1.03-1.30	n.d.	24-42 ^c	Nitroxide comp. and Cy5.5	<i>In vivo</i>	84
PEG	Graft to	n.d.	9.9-14.5	1.6-2.3	n.d.	n.d.	AAF	<i>In vitro</i>	96
PEG	Graft to	ROMP	12-93	1.01-1.17	n.d.	<60	KLA peptide	<i>In vitro</i>	85
POEG	Graft through	ATRP	25-155	1.03-1.16	n.d.	4-16 ^c	Exendin-4	<i>In vivo</i>	86
PLL	Graft from	ROMP	17-38	1.48-1.73	n.d.	220 ^c	Ovalbumine	<i>In vitro, in vivo</i>	87
POX	Graft through	cationic ROMP	600-3200	~2	n.d.	64-76 ^c	antiDEC205	<i>In vitro</i>	97
PEG	Graft through	ROMP	48-204	1.10-1.40	16-27 ^b	16-27	DNA	<i>In vitro</i>	90
PEG	Graft through	ROMP	178-285	1.10-1.15	n.d.	34-48 ^c	DNA	<i>In vitro</i>	89
PEG	Graft through	ROMP	76-310	1.10-1.18	n.d.	25-34 ^b	DNA	<i>In vitro, In vivo</i>	98
PEG	Graft through	ROMP	330	1.20	n.d.	64 ^c	RNAi	<i>In vitro, In vivo</i>	88
PSC	Graft from	NCA	5800- 12200	1.72 and 1.74	310-1012 ^d	20-25 ^d	siRNA	<i>In vitro</i>	99
PEGMA	Graft from	ATRP or ROMP	5000-412000	n.d.	35-1200 ^{c,e}	70 ^c	-	<i>In vitro, In vivo</i>	61,62
PEG	Graft to	n.d.	30.9-106.8	1.09-1.13	34-119 ^e	18	-	<i>In vitro, In vivo</i>	91

^aGPC, ^bTEM, ^cDLS, ^dKuhn Statistical Segment Length, ^eAFM

PEG = Polyethylene Glycol, POX = Polyoxazoline, PSC = Polysarcosine, PEGMA = Polyethyleneglycol methacrylate, POEG = Poly(olygoethyleneglycol), PLL = Poly-L-Lysine, PMMA = Polymethacrylic Acid, PAA = Polyacrylic Acid, NCA = N-carboxyanhydrides, AAF = 5-(Aminoacetamido)fluorescein

In conclusion, molecular brush polymer is an interesting material that has potential use in biomedical field, from therapeutic to diagnostic. However, most of the reported studies employed close-to-round shape brush polymers and were limited to *in vitro* studies. Despite the studies investigating the influence of length and rigidity of the brushes on their biological performance, there are still many other parameters that need to be explored. These include grafting density, the linkage between side chain and backbone (for biodegradability), end group of side chains, the composition of side chains, et cetera.

1.4 METHOD OF SYNTHESIS OF BOTTLE BRUSH POLYMERS

While brush polymers have shown some promising performance as a drug delivery carrier, the synthesis and characterization of such complicated structure remain a challenge. Generally, three approaches can be used to synthesize the molecular brush polymer: 1) grafting-through, 2) grafting-to, and 3) grafting-from approach¹⁰⁰⁻¹⁰² (Figure 1.7). When designing a brush polymer, some structural parameters can be taken into consideration, such as chemical composition, grafting density and degree of polymerization of the backbone as well as side chains. However, none of those three approaches has the capability to control all parameters at a time. For example, while one approach can produce brushes with very high grafting density, it might not be able to create very long brushes. Moreover, from the synthesis point of view, not all polymerization techniques can be employed within each approach.

The grafting-through approach (Figure 1.7a) is a one-step reaction where the “grafting” of side chains is conducted “through” the polymerization of the backbone. This strategy guarantees 100% of grafting density because each repeating unit (macromonomers) of the polymerized backbone has a side chain. The well-defined side chain length can also be obtained since the macromonomers are prepared and characterized prior to the grafting-through process. However, depending on the macromonomer length and type, producing BBPs with long backbone while maintaining low dispersity is a major challenge, due to increasing steric barriers from the bulky macromonomers while the backbone is extending¹⁰⁰. This steric constraint will also result in slow polymerization, low conversion and unfavour

termination reaction. As a result of the low conversion, separating the resulting brushes with the unreacted macromonomers will be problematic and takes time. Moreover, high dispersity will make characterization more difficult.

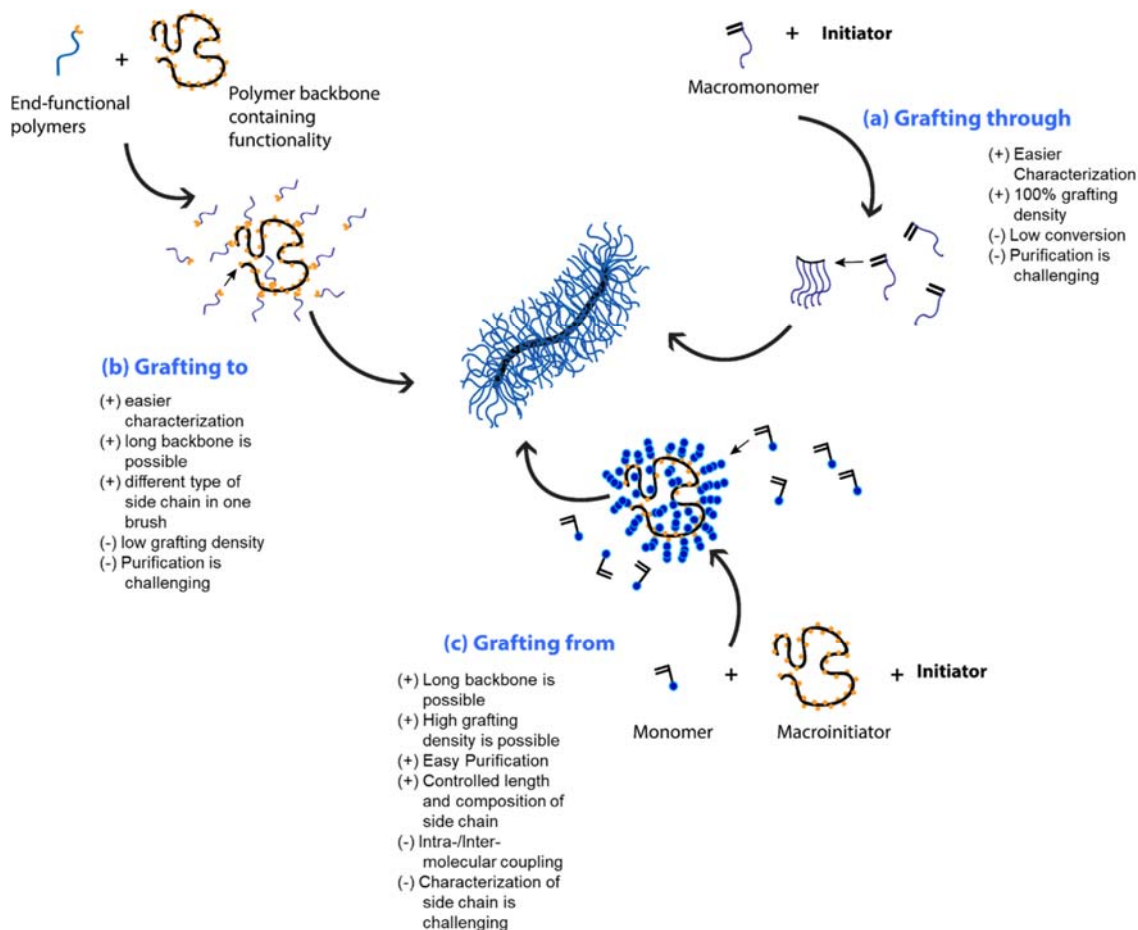


Figure 1.7 Three main strategies for producing molecular brush polymers: (a) grafting through, (b) grafting onto, and (c) grafting from.

In the grafting-to or grafting-onto approach (Figure 1.7b), the backbone and the side chains are synthesized separately. This approach requires a backbone that contains a functional group on each repeating unit. The side chains are then “grafted to” the functional group in the backbone by creating a covalent bond using click chemistry¹⁰³, nucleophilic substitution¹⁰⁴, or any other synthetic method. Since both the backbone and side chains are

prepared independently, any appropriate polymerization technique will be feasible and characterization of each component will be more accurate. In addition, it is very possible to create brushes with different types of side chains along the backbone. With this approach, brushes with long backbone can be achieved, but grafting density is limited. The limitation in grafting density is because increasing the density of side chains will stop the incorporation of new chains due to steric repulsion between bulky side chains.¹⁰⁰ Also, similar to the grafting-through method, the purification to remove the excess side chains will be challenging.

The grafting-from approach involves the grafting of side chains gradually “from” the polyinitiator or macroinitiator backbone (Figure 1.7c). Theoretically, the grafting density can be determined by the number of initiation sites available in the backbone.¹⁰⁰ The gradual elongation of side chains allows all initiation sites to grow with minimal steric issues. Depending on the method of polymerization, this approach allows the production of brushes with a long backbone and high density of side chains. Nevertheless, the high grafting density will depend on the nature of the monomer unit and the initiation efficiency. Compared to the grafting through and grafting to, the control of side chain length is limited. In addition, there is a probability of intramolecular crosslinking or termination among the propagating side chain.

Considering the benefits and drawbacks of each approaches, I suggest that the grafting-from approach is the most suitable method to create bottle brush polymers with cylindrical structure and high density of side chains. Additionally, with grafting-from approach, the composition of side chains can be easily tailored for biological application. The issue of intramolecular crosslinking can actually be minimized by a suitable polymerization technique.

1.5 LIVING RADICAL POLYMERIZATION: RAFT POLYMERIZATION

Generally, based on the kinetics scheme, there are two types of polymerization: step-growth polymerization and chain-growth polymerization (Figure 1.8).¹⁰⁵ In step-growth polymerization, short chains of polymers are formed and then combine to become longer polymer. One most common type of step-growth polymerization is condensation polymerization. Condensation polymerization involves reaction of monomer molecule which

has reactive groups at both ends, producing small molecules (such as water or methanol) as by-products. In this type of polymerization, the reaction between the reactants and polymer products is reversible. Therefore, to drive the reaction equilibrium to the right, removal of the by-products during the polymerization reaction is necessary.¹⁰⁶

Condensation polymerization (e.g. polyester)



Addition polymerization (e.g. vinyl monomers)

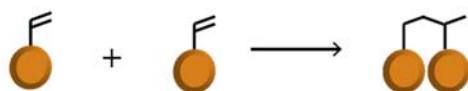


Figure 1.8 Comparison between condensation polymerization and addition polymerization

Chain-growth polymerization is a polymerization in which one monomer is added to the chain at a time. One most remarkable type of chain polymerization is free radical polymerization. Free radical polymerization involves conversion of vinyl monomers ($\text{R}-\text{C}=\text{C}$) into the polymers by the opening of the double bond. Unlike condensation polymerization, most of the free radical polymerization is irreversible and does not release any small molecule by-products. Hence, they can often be conducted in a more facile condition. Compared to ionic polymerization (another type of chain polymerization), free radical polymerization is more friendly for industrial process due to its tolerability to functionality and impurities.¹⁰⁷ In addition to that, free radical polymerization offers flexibility to accommodate a wide variety of monomers and solvents, as well as to create polymers with complex architecture.

Free radical polymerization includes three main stages (Figure 1.9): **initiation** (start of the polymerization by the thermal decomposition of an unstable initiator molecule to produce two free radicals), **propagation** (a monomer adds to the chain and then creates an active

radical site for the next addition) and **termination** (end of polymerization due to recombination of two radicals). In conventional free radical polymerization, random chain termination is unavoidable due to the high reactivity of radicals, resulting in not as expected chain length and high molecular weight distribution. It was almost impossible to prepare well-defined polymers with controlled molecular weight, dispersity, composition, chain architecture, and site-specific functionality.¹⁰⁸

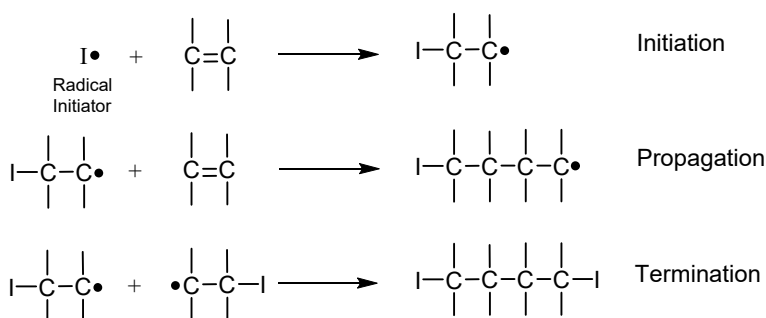


Figure 1.9 Stages of traditional free radical polymerization

In the past 80 years, polymer chemistry has progressively evolved to overcome the drawbacks related to early chain termination in free radical polymerization. Since Flory threw the theory of living radical polymerization (LRP) in the 1940s¹⁰⁹, this polymerization method continued to expand. Grubbs and Grubbs¹⁰⁹ defined “living” as, in an ongoing polymerization, all polymer chains grow at the same rate without irreversible transfer or termination (Figure 1.10). They also mentioned that it is more “close-to-living” because some degree of transfer or termination still occurs. Other names of living radical polymerization are controlled radical polymerization (CRP) and reversible deactivation radical polymerization (RDRP).¹¹⁰ To date, a number of LRP methods have been developed with the three most prominent techniques are nitroxide mediated polymerization (NMP), atom transfer radical polymerization (ATRP), and reversible addition-fragmentation chain transfer (RAFT) polymerization.

The “livingness” in LRP depends on an equilibrium between active (polymer chain that has radical and thus can insert a new monomer) and dormant (polymer chain that does not

have radical and therefore not actively propagates) chains. This can be achieved by one of two mechanisms: (1) reversible termination of active chain ends as in NMP and ATRP or (2) degenerative exchange between dormant and active chain as in RAFT. In order to achieve equilibrium between active and dormant chains, each mechanism requires a “control agent” which can temporarily deactivate the active radicals in the propagating polymer chains. This agent will go back and forth from the polymer, reversibly activating-deactivating the radicals in the growing chain. One of the main features of LRP is that the produced polymers can be further extended by sequential polymerization, as long as the control agent is still tethered in a polymer chain.

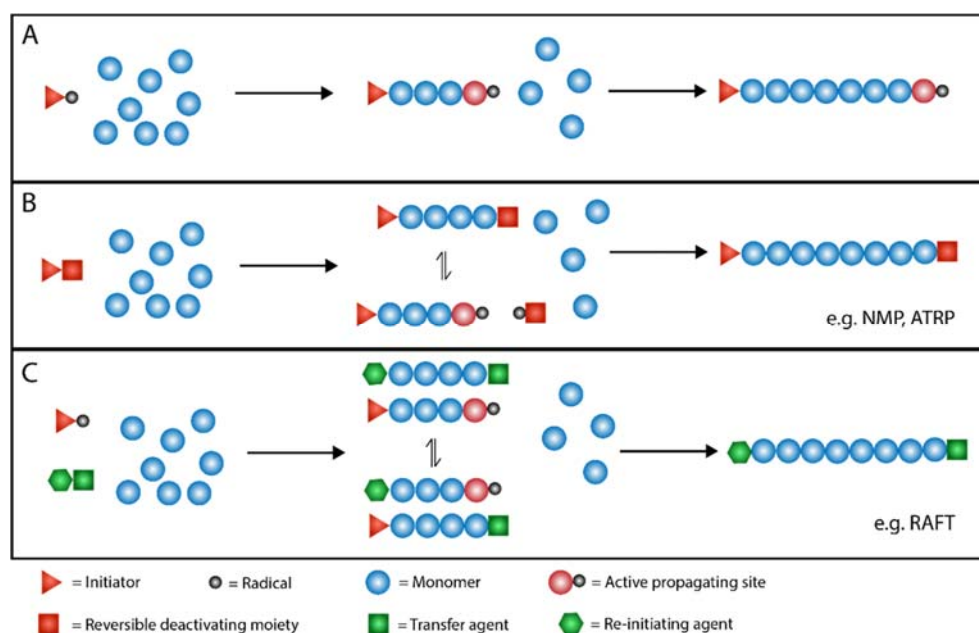
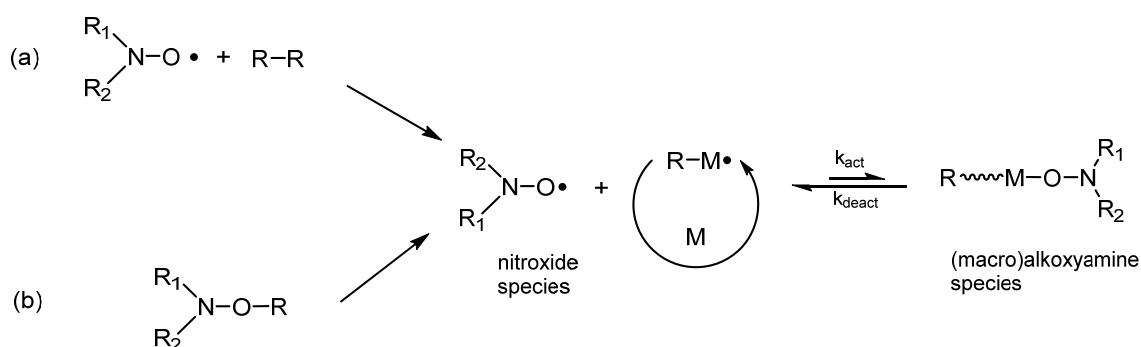


Figure 1.10 Illustration of some types of living radical polymerization. (A) Living polymerization without termination or transfer, where the active propagating site remains, although all monomers have been consumed. (B) Living polymerization with reversible radical deactivation, in which the majority of produced chains are capped with reversible deactivating moiety. (C) Living polymerization with a degenerative transfer of radical, in which the majority of produced chains are capped with the transfer agent. (Adapted from Grubbs¹⁰⁹)

Nitroxide mediated polymerization (NMP) was the first established LRP technology¹¹¹ (Scheme 1.1). It uses nitroxide compound as a control agent, which will reversibly terminate the propagating chains, yielding alkoxyamine-polymer chain as the major species. The

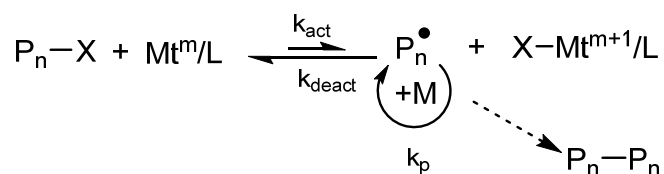
alkoxyamine-polymer chain is a dormant chain, which can generate back the polymer radicals and the nitroxide when the temperature increase.¹¹¹ Although NMP offers some key advantages such as simplicity, monomer compatibility and polymer purity, it also endures three main challenges: (1) slow polymerization kinetics which results in long polymerization time, (2) lack of ability to control the polymerization of methacrylates, and (3) difficulty on the synthesis of nitroxide and alkoxyamine as control agents.¹¹² In addition, NMP requires relatively a high temperature for the process.



Scheme 1.1 General equilibrium in NMP using (a) bicomponent and (b) monocomponent initiating system (adapted from Nicolas et al.¹¹¹)

Atom transfer radical polymerization (ATRP) is a reversible-deactivation radical polymerization mediated by redox-active transition metal complexes.¹¹³ The traditional ATRP reaction employs the interplay between initiators (normally alkyl-halides compound), catalysts (e.g. transition metals), and ligands (commonly amine-based ligands) to control the polymerization process (Scheme 1.2). The alkyl-halides generate radicals by bringing the transition metals into oxidation state.¹¹⁴ The monomers are then inserted to the alkyl radicals while the halides create a complex with the oxidized metal. The halides atom can return to the radical polymer chain and make it dormant. This dormant species is then reactivated by the transition metal to incorporate more monomers. The transition metals (copper is the most commonly used) and ligands form a complex that dictates the polymerization rate since they determine the equilibrium constant between the active and dormant species.¹¹⁵ In case of

metals used as catalyst, the ligand's main function is to solubilize the transition metal salts in the polymerization solvent, as well as dictate the reduction potential. Although ATRP has become one of powerful and robust polymerization techniques, it suffers from two main drawbacks: (1) the reaction is very sensitive to oxygen as it depends on the reduction-oxidation reaction of the transition metals and (2) trace amounts of metal ions present in the polymer products raise a problematic consideration for use in biological application.^{113,116} The metal-free ATRP has recently been developed using photocatalysts such as organic dyes. However, this method is still in early stage and faces some challenges such as poor initiation efficiency, high dispersity of the produced polymers, and discolouration of the produced materials during storage.¹¹⁶



Mt^m = transition metal in lower oxidation state
 Mt^{m+1} = transition metal in higher oxidation state
 P_n = polymer chain
 X = alkyl halide (Br or Cl)
 L = ligand
 Mt^m/L = activator
 Mt^{m+1}/L = deactivator

Scheme 1.2 General equilibrium condition in ATRP (adapted from Matyjaszewski¹¹³)

Reversible addition-fragmentation chain transfer (RAFT) polymerization is another type of LRP. A control agent in RAFT polymerization is called chain transfer agent (CTA) or RAFT agent, a thiocarbonylthio compound consisting of R- and Z-groups (Figure 1.11). The detachable R group reinitiates the growth of polymer chains, while the Z-group activates the thiocarbonyl bond to temporarily deactivate the propagating radicals.^{117,118} For an easy description in this thesis, Z-group means the Z-group together with the thiocarbonyl. Unlike the control agents in NMP and ATRP, a RAFT agent cannot generate radicals (Figure 1.10). Therefore, a RAFT polymerization needs a radical initiator (the most used is thermal initiator)

to provide the radicals and initiate the polymerization. The detailed mechanism of RAFT polymerization is illustrated in Figure 1.12.

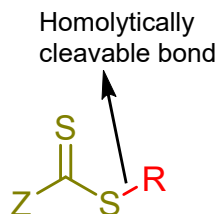


Figure 1.11 Generic structure of RAFT agent

First (step I and II), the radical source (I) decomposes and initiate the propagation of the monomers (M). Following this step, the radical species are transferred to the CTA from which the CTA enter an equilibrium between active and dormant species (step III and V). The R-group of CTA then reinitiate the propagation process by giving its radicals to other monomers (step IV), while the Z-groups temporarily stabilize the propagating chains and make them dormant. Generally, the overall process involves the incorporation of monomers between the R- and Z-group of CTA. These R- and Z-group will form α and ω end-group of the majority of the resulting polymeric chains. The rapid transfer of the radical chains to CTA ascertains that the concentration of radical chains is lower than stabilized radical intermediates during the polymerization process, thus minimizing termination reactions. Some degree of termination reactions still occur via combination or disproportionation mechanism (step VI).

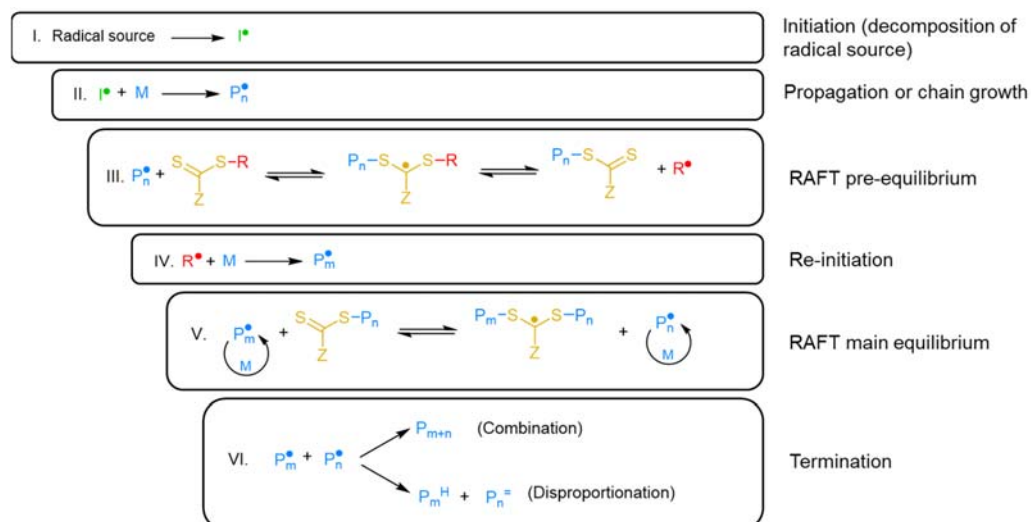


Figure 1.12 Proposed mechanism of RAFT polymerization (adapted from Boyer et al.¹¹⁹, and Perrier¹¹⁸)

The use of radical source such as free radical initiator in RAFT polymerization will tune the rate of propagation and number fraction of living chains.¹¹⁸ By controlling the amount of radicals at initial reaction, we can predict the amount of dead chain that would be produced. This is illustrated in Figure 1.13. For example, when two radicals initiate a reaction containing twelve monomers and six RAFT agents, there will be eight chains produced at the end of polymerization. The chains comprise of two dead chain (chains without thiocarbonythio end-group at the ω -end) and six living chains (chains with thiocarbonythio end-group at the ω -end). The livingness of the system can be calculated as $6/(6+2) \times 100 = 75\%$. Generally, the ratio between the produced dead chains and living chains will be the same as the ratio of the number of initiator and RAFT agent introduced at the beginning of the reaction. In regards to the origin of initiation (α -end), there will be two types of chain: initiator-derived and R group-derived chains.

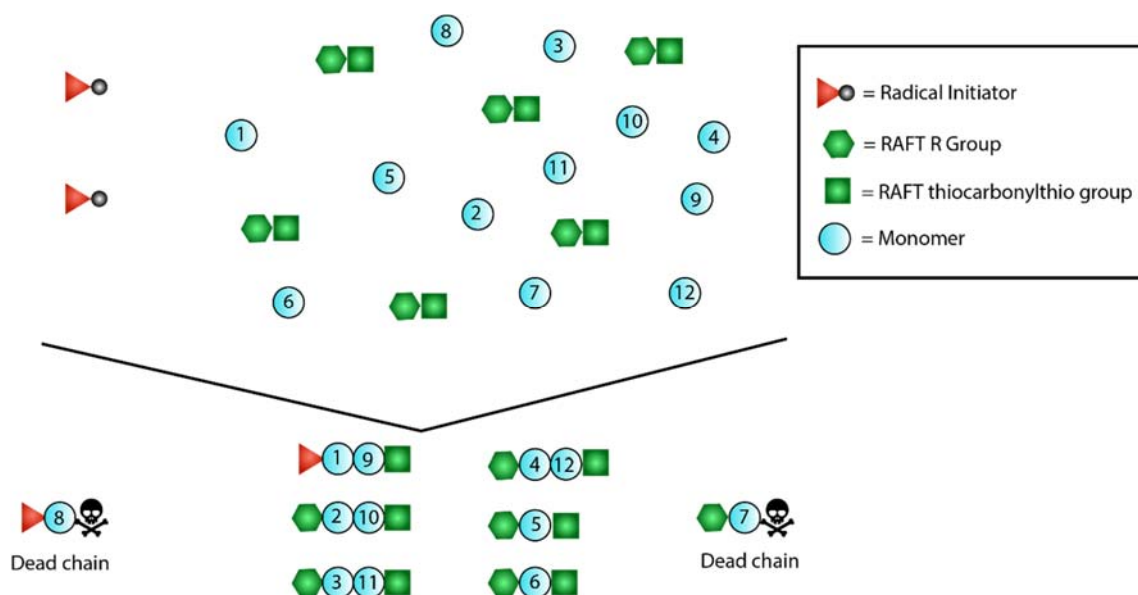


Figure 1.13 Schematic representation of chain generation in RAFT polymerization (adapted from Perrier¹¹⁸)

While it can be concluded that lowering the number of initiator can increase the livingness of the polymerization system, it is not necessarily lowering the polymerization rate. In fact there are other factors that can influence the rate of propagation such as monomer concentration and monomer propagation rate coefficient. The parameters that can affect the polymerization rate are summarized in the following equation:¹¹⁸

$$R_p(t) = k_p[M] \sqrt{\frac{fk_d[I]_0 e^{-k_d t}}{k_t}}$$

where R_p is the polymerization rate, k_p is the propagation rate coefficient, $[M]$ is the monomer concentration, f is the initiator efficiency, k_d is the decomposition rate coefficient of the initiator, $[I]_0$ is the initial initiator concentration, and k_t is the termination rate coefficient.

Since first reported in 1998, RAFT polymerization has become a widely recognised polymerization technique and has been proven for its versatility to synthesise complex polymeric architectures.¹¹⁸ This technique offers compatibility with a wide range of monomers in varying solvents, control of molecular weight and molecular weight distribution, livingness that leads to a high degree of conversion and tolerance of a wide variety of reaction conditions (e.g. trace amount of oxygen and impurities) and functionalities.¹¹⁷ It has been reported in

many research articles the use of RAFT polymerization to create complex polymeric architecture with a well-defined structure such as complex multiblock copolymers¹²⁰, star polymers¹²¹ and hyperbranched polymers¹²². In case of synthesis of brush polymers via grafting-from approach, RAFT is much less popular than ATRP. The reason for this is because the bi-radical brush-brush coupling is likely to occur¹²³. However, Zheng et al.¹²⁴ argued that if the coupling reaction was the primary reason, then any polymerization technique, including ATRP, should have the same issue. Since it rarely occurs to the grafting-from using ATRP, they hypothesized that the coupling issue might be caused by ineffective transfer of radicals from individual growing BBPs to another. While the copper halides as the catalysts in ATRP is small enough to be able to diffuse into and out of the growing BBPs, the RAFT agents are quite bulky to perform this. To prove their hypothesis, they performed a new method of grafting-from approach using RAFT polymerization called “CTA-shuttle R-group grafting from approach” which will be discussed in more detail in Chapter 2. This method has demonstrated better control on the grafting-from polymerization, resulting in brushes with relatively narrow distribution.^{124,125} This will be the technique I use for the synthesis of the BBPs.

1.6 PNAM AS ALTERNATIVE FOR PEG

So far, most of the BBPs intended for biological use are comprised of PEG as a side chains component, primarily synthesized via grafting through of PEG macromonomers. One issue in regard to using PEG macromonomers is that the polymerization of ethylene glycol to produce PEG is difficult. It is commercially available with a certain length (e.g. 500, 2000, 5000, 10,000 Da), yet the length is limited and non-customizable. However, despite the limitation in the synthesis and availability, PEG has still been a golden standard in polymeric nanomedicine.

Interestingly, some evidence showed the immunogenicity of PEG, where anti-PEG antibodies (including IgG and IgM) were found in patients treated with PEGylated drugs.¹²⁶⁻¹²⁸ IgG and IgM production against PEG results in accelerated blood clearance (ABC) phenomenon, which means the second dose of PEGylated nanoparticles showed faster blood

clearance than the first one. Interestingly, anti-PEG antibody has also been found in the patient without treatment with PEGylated drugs.¹²⁹ This pre-existing anti-PEG antibody is possibly caused by chronic exposure to consumer products that contain free PEG, such as cosmetics, conventional medicines, industrial food, etc. The existence of anti-PEG antibodies could lead to severe effects. The naturally circulating anti-PEG antibody could induce an allergic reaction caused by treatment with PEGylated drugs. The ABC phenomenon could also lower clinical efficacy and increase the risk and severity of infusion reactions.¹³⁰

Due to the chemistry and immunology issues of PEG, other polymers are being investigated as an alternative. For example, Bauer *et al.*¹³¹ have proposed poly(2-ethyl-2-oxazoline) (PEtOx) due to its comparable *in vitro* toxicity and hemocompatibility to PEG. Polysarcosine (PSar) has been used to deliver interferon (IFN) and the PSar-IFN conjugates showed stability against protease and prolonged *in vivo* circulation.¹³²

Poly 4-acryloylmorpholine (PNAM) is one of the non-charged hydrophilic polymers that have potential *in vivo* application. It exhibits good solubility in both aqueous and organic solvents¹³³, which is beneficial for the polymerization process as well as biological application. Linear polyNAM was proven to be able to extend the half-life of therapeutic protein, uricase, and was comparable to PEG.¹³⁴ More importantly, it is easier to tailor compared to PEG. In addition, PNAM has never been used in consumer products and thus, the pre-existing antibody for PNAM might not be present. Indeed, PNAM-coated poly(lactic acid) (PLA) nanoparticles¹³⁵ and PNAM-stealth liposomes¹³⁶ (the only two reported biological application of PNAM), showed prolonged plasma residence without encountering ABC phenomenon.



Figure 1.14 Structure comparison between PEG and PNAM

By looking at the chemical structure of PNAM and PEG, the lipophilic/lipophobic balance in NAM is similar to PEG, with a sequence of one oxygen and two $-CH_2$ (Figure 1.14). Therefore I postulated that PNAM would demonstrate similar characteristics to PEG, particularly regarding its biological performance. From the polymer synthesis point of view, polymerization of NAM is relatively easier and the length of the NAM chain can be easily achieved as predetermined. Additionally, the monomer NAM exhibits a fast and efficient polymerization rate using reversible addition-fragmentation chain transfer (RAFT) technique, even under low radical initiator concentration^{125,137}, thus, suitable for creating brush polymers structure via grafting from approach using RAFT polymerization. However, similar to PEG, PNAM does not have functional groups for molecule attachment, and thus, requires addition of other functional monomers.

1.7 SCOPE OF THESIS

The overall aim of this project is to develop a platform of cylindrical shape NAM-based bottle brush polymers using a simple and easy method of synthesis and purification. The produced NAM-based bottle brush polymers can ultimately be used as polymeric carriers for anticancer drugs due to their ability to accumulate in tumour tissues. To achieve this goal, the resulting BBPs need to meet several requirements as follows:

1. The backbone and the arms have to be very easily synthesized with a simple reaction.
2. They have to exhibit narrow molecular weight distribution to ensure homogenous characteristics of the BBPs.
3. The purification method should be relatively easy to be applied in large-scale production
4. They have to be water-soluble for the easiness in the formulation.
5. They should have some reactive sites to allow the conjugation of passenger molecules, since I intend to load the drugs via covalent conjugation

My main hypothesis is that NAM-based BBPs can be synthesised in a well-controlled manner resulting in narrow molecular weight distribution BBPs. The produced BBPs will exhibit

long blood circulation time and are capable of distributing to tumour tissues with minimum deposition to healthy organs.

To test my hypothesis, I proposed the following specific aims:

1. to establish a new method of synthesis of NAM-based BBP by Reversible Addition-Fragmentation Chain Transfer (RAFT) polymerization
2. to create and characterize a library of NAM-based BBP with control of length, side-chain structure, grafting density and end group functionalities.
3. to investigate their *in vitro* cell toxicity, association and internalization
4. to study the effect of the grafted structure of NAM-based polymers, length and grafting density on their pharmacokinetics and biodistribution of the carrier in healthy animals
5. to establish a syngeneic breast cancer model in mice.
6. to investigate the pharmacokinetics and biodistribution of the carrier in tumour animal models.

CHAPTER 2. SYNTHESIS AND CHARACTERIZATION OF 4- ACRYLOYLMORPHOLINE-BASED BOTTLE BRUSH POLYMERS

2.1 INTRODUCTION

Unimolecular bottle-brush polymers (BBPs) are a type of polymer with complex architecture, generally consisting of a polymer backbone, grafted with highly dense polymer side chains that force the backbone to stretch and form a cylindrical shape. Unlike linear polymers that form random coils in solution, BBPs can maintain their cylindrical structure within the size of colloids (0.001 to 1 μm), setting them in a position between linear polymers and nanoparticles.¹⁰² Due to their characteristics, BBPs can be applied as drug delivery carriers. For example, the high density of side chains offers a great amount of sites for covalent attachment of molecules, such as drugs. In addition, their anisotropic structure provides different physical interactions with biological species compared to spherical particles, making BBPs a more interesting carrier for investigation.

For use as drug delivery carrier, a polymeric carrier must be well-defined and exhibit low dispersity of individual molecular masses of chains to ensure the homogeneity and accuracy of the dose. Having said that, synthetic strategies to make BBPs with the required criteria is challenging. In particular, due to the steric hindrance introduced in producing BBPs with densely grafted side chains. Three main strategies for preparing molecular brushes have been established: “grafting through” (the polymerization of backbone in which each unit already brings side chain), “grafting onto” (the attachment of previously prepared side chains to a backbone), and “grafting from” (the polymerization of side chains from a macroinitiator backbone). Each of these strategies has their own advantages and disadvantages, which dictate the final grafting density and backbone length. As such, the grafting-from approach, enables the preparation of long-backbone molecular brushes with a high grafting density¹⁰⁰, thus becomes the most preferred method.

Various polymerization techniques have been employed to grow the side chains from the backbone, with the controlled free-radical polymerization (CRP) technique being the most frequently applied for synthesizing BBPs. The most common CRP technique used in grafting-from approach is atom transfer radical polymerization (ATRP). However, the conventional ATRP technique is very sensitive to oxygen, requiring demanding procedures such as freeze-thaw evacuate in order to remove oxygen to an acceptable level. In contrast, reversible addition–fragmentation chain transfer (RAFT) polymerization is less popular to prepare grafted polymers like BBPs. In particular, it has never been used to prepare BBPs for biological application. The reason for this is due to the high prevalence of side reactions such as coupling and formation of single arms, leading to broad molecular weight distribution.¹³⁸ However, RAFT polymerization offers advantages over ATRP. For example, it is more tolerant to oxygen, and therefore the removal of oxygen prior to the reaction by simple degassing technique with inert gas is sufficient.

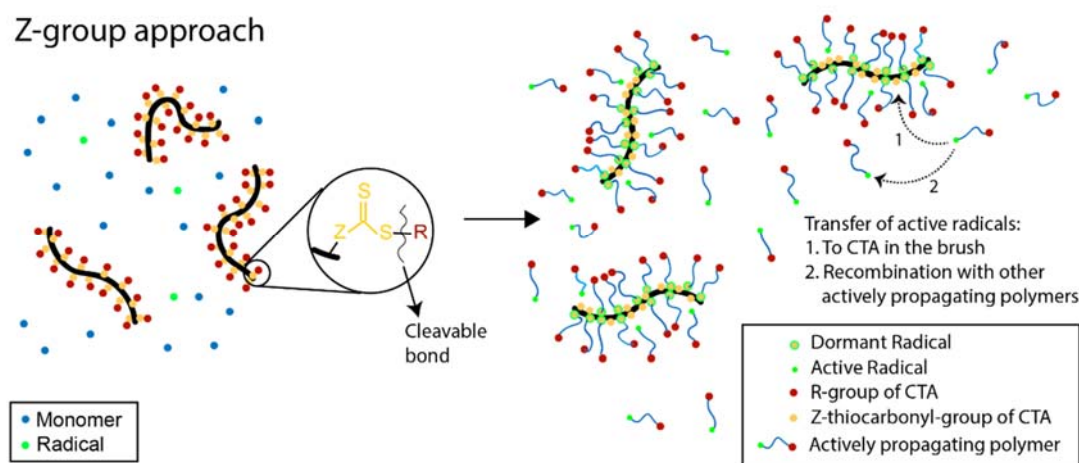


Figure 2.1 Proposed mechanism of grafting from approach via Z-group RAFT polymerization. The cleavable bond of RAFT agent indicates where the monomer will be incorporated. (adapted from Zheng et al.¹²⁴)

When using RAFT polymerization to grow the side chains from the backbone, there are two options to attach RAFT chain transfer agent (CTA) on a backbone, since a CTA comprises two divisible parts: the stabilising group (Z-group) and the re-initiating group (R-group). The Z-

group approach involves the attachment of CTAs to the backbone via their Z-groups (Figure 2.1). Later in the process of grafting polymerization, the side chains will propagate outside the backbone and then temporarily be stabilised by Z-groups in the backbone. This way the Z-group approach will present like the grafting-onto approach and might suffer from low grafting density due to steric hindrance.

On the other hand, the R-group approach represents the real grafting-from approach since the R-groups are tethered to the backbone and therefore the monomers will grow from the backbone (Figure 2.2). Using the R-group “grafting from” approach can ensure higher grafting density compared to the Z-group approach. However, as the side chains are growing in the backbone, there might be a chance of intramolecular coupling reactions among the growing side chains. Another problem is the intermolecular transfer of the active propagating radicals is hindered, resulting in unequal growth of side chains amongst the BBPs. This can cause a broad molecular weight distribution (MWD) of the produced BBPs.

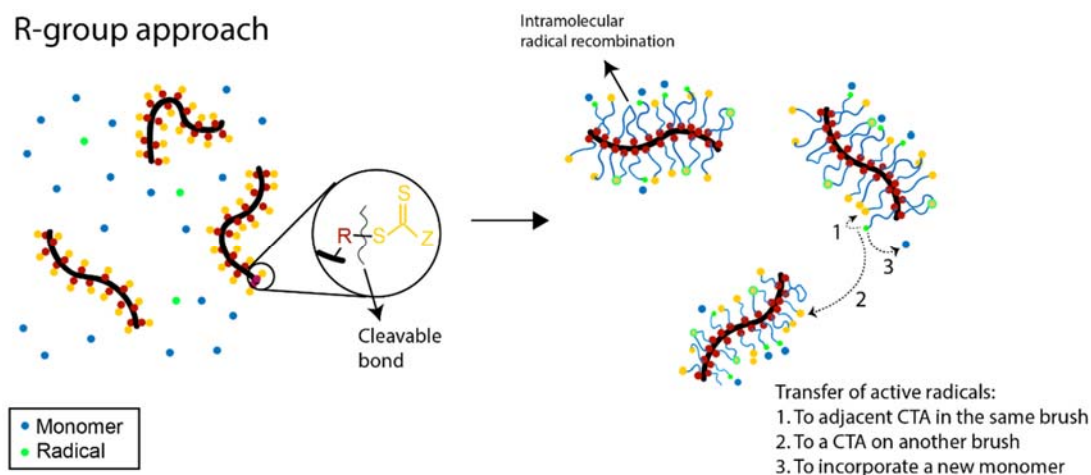


Figure 2.2 Proposed mechanisms of the grafting-from approach via R-group RAFT polymerization. The cleavable bond of RAFT agent indicates where the monomer will be incorporated. (Adapted from Zheng *et al.*¹²⁴)

To resolve this problem, Zheng *et al.*¹²⁴ reported “CTA-shuttled” R-group RAFT approach (Figure 2.3), which encompasses the addition of low molecular weight chain transfer agent (LMW-CTA) to the polymerization reaction. These LMW-CTAs and their derived linear

polymers help transfer the radicals from one BBP to another BBP and thus all BBP will have equal radicals available to grow their side chains. With this approach, they successfully synthesized BBPs with a backbone DP of up to 120 and with a narrow polydispersity index. This successful approach was followed by Wang *et al.* to synthesize longer BBPs (up to DP 1200) using the same backbone precursor¹³⁹. The only drawback of this method is that linear polymers derived from the LMW-CTAs are also produced simultaneously and, thus, require stringent purification.

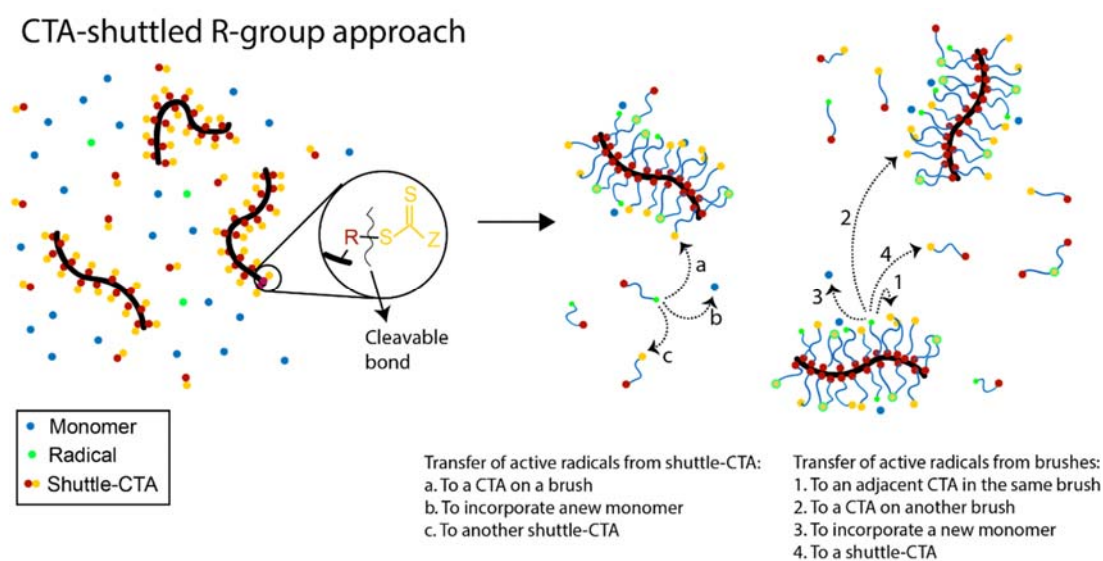


Figure 2.3 Proposed mechanisms of the grafting-from approach via R-group RAFT polymerization with an addition of shuttle-CTAs. The cleavable bond of RAFT agent indicates where the monomer will be incorporated. (Adapted from Zheng *et al.*¹²⁴)

In this chapter, I develop a synthesis method of BBPs with poly-4-acryloylmorpholine (PNAM) as the main component of side chains, using the similar CTA-shuttled R-group grafting-from approach. I want to understand the process and then use it to create a platform of NAM-based BBPs with diverse architectures, which later will be used in drug delivery. To provide ease in identifying all polymers in this chapter, I have provided a box filled with the general nomenclature of the produced polymers.

POLYMER NOMENCLATURE

PHEAm _a	= backbone consists of 'a' units of n-Hydroxyethyl Acrylamide (HEAm)
P(HEAm-co-PNAM) _{b%,a}	= backbone consists of random copolymer of HEAm and NAM, with 'b%' units of n-Hydroxyethyl Acrylamide (HEAm) with the total DP 'a'
PCTA-PHEAm _a	= macroinitiators made from backbone PHEAm _a
PCTA-P(HEAm-co-PNAM) _{b%,a}	= macroinitiators made from backbone P(HEAm-co-PNAM) _{b%,a}
Brush [PNAM _x] _a	= brush polymer consists of backbone PHEAm _a grafted with 'x' units of NAM
Brush [PnBA _y] _a	= brush polymer consists of backbone PHEAm _a grafted with 'y' units of n-Butyl Acrylate (nBA)
Brush [PnBA _y -b-PNAM _x] _a	= brush polymer consists of backbone PHEAm _a and grafted with block copolymer of 'y' units of nBA and 'x' unit of NAM
Brush [PNAM _x] _{b%,a}	= brush polymer consists of backbone P(HEAm-co-NAM) with 'b%' of HEAm from the total DP of 'a', grafted with 'x' units of NAM
Brush [P(NAM _x -co-NHSA _y)] _a	= brush polymer consists of backbone PHEAm _a grafted with random copolymer of 'x' unit of NAM and 'y' units of NHSA
Brush [P(NAM _x -co-NHSA _y)] _{b%,a}	= brush polymer consists of backbone P(HEAm-co-NAM) with 'b%' of HEAm from the total DP of 'a', grafted with random copolymer of 'x' unit of NAM and 'y' units of NHSA
Brush X-ACVA	= brush polymers which end groups have been replaced by ACVA
Brush X-BM	= brush polymers which end groups have been replaced by BM1429

2.2 EXPERIMENTAL METHOD

2.2.1 Materials

Hydroxyethylacrylamide (HEAm), 4-acryloylmorpholine (NAM), *n*-butyl acrylate (nBA), azobisisobutyronitrile (AIBN), butanethiol, carbon disulfide, 2-bromopropanoic acid, 4-dimethylaminopyridine (DMAP), lauroyl peroxide, sodium hydroxide (NaOH) and ethanolamine were purchased from Sigma-Aldrich. 2-[(butylsulfanyl)carbonothiol]sulfanyl propanoate (C4)

was synthesized in our lab using previously reported method¹⁴⁰. Methyl 2-[(butylsulfanyl)carbonothiol]sulfanyl propanoate (methylated-C4) was provided by my collaborator in University of Warwick. 4,4'-azobis(4-cyanovaleric acid) (ACVA) was purchased from Alfa-Aesar. N-(3-dimethylaminopropyl)-N'-ethylcarbodiimide hydrochloride (EDC.HCl) was purchased from Chem-Impex International. 3-((((1-carboxyethyl)thio)carbonothioyl)thio)propanoic acid (BM1429 or BM) was purchased from Boron Molecular. Acrylic acid N-hydroxysuccinimide ester (NHSA) was purchased from MetaGene Pty Ltd (Santa Cruz biotechnology).

Solvents used were dioxane (Sigma-Aldrich), acetone (Sigma-Aldrich), chloroform (Sigma-Aldrich), methanol (Sigma-Aldrich), N,N-dimethylacetamide (DMAc) (Sigma-Aldrich), N,N-dimethylformamide (DMF) (Sigma-Aldrich), petroleum benzene b.p. 60-80°C (Sigma-Aldrich), diethyl ether (Sigma-Aldrich). All solvents were analytical grade.

2.2.2 Characterization Equipment

Gel Permeation Chromatography (GPC)

GPC analyses of polymer samples were performed using mobile phase *N,N*-dimethylacetamide (DMAc) with 0.03% w/v LiBr and 0.05% 2,6-dibutyl-4-methylphenol (BHT) using a Shimadzu modular system comprising a DGU-12A degasser, a SIL-20AD automatic injector, and a 5.0 µm bead-size guard column (50 × 7.8 mm) followed by four 300 × 7.8 mm linear Phenogel columns (bead size: a 10.0 µm; pore sizes maximum: 5000 Å) and a RID-10A differential refractive-index detector. The temperature of the column was maintained at 40°C using a CTO-10A oven, and the flow rate was kept at 1 mL/min using an LC-10AT pump. A molecular weight calibration curve was produced using commercial narrow molecular weight distribution polystyrene standards with molecular weights ranging from 500 to 2×10⁶ g/mol. Polymer solutions were prepared in the eluent and filtered through 0.45 µm PTFE filters prior

to injection. Molar mass (M_n) and dispersity (\mathcal{D}) of samples were obtained from Shimadzu LabSolutions software.

Nuclear Magnetic Resonance Spectroscopy (^1H NMR)

^1H Nuclear magnetic resonance (^1H NMR) (400 MHz) spectra were obtained from Bruker Ultra Shield 400 MHz spectrometer at 25°C running Bruker Topspin Software. Samples from the spectra were dissolved in deuterated solvent (d_6 -DMSO or CDCl_3). Chemical shifts are reported as parts per million. The spectra were processed via MestRaNova software version 6.0.2-5475 (2009).

Atomic Force Microscopy (AFM)

AFM images of the brush polymer were prepared by Dr. Andrew Kerr, University of Warwick. AFM images were acquired in AC mode on a Cypher S system (Asylum Research). The probes used were the AC160TS from Olympus probes with a nominal resonant frequency of 300 kHz and a spring constant of approximately 40 Nm^{-1} on a Multimode AFM (Asylum Research).

Spectrophotometer UV-Vis

UV-VIS spectra were recorded on a Shimadzu UV3600 spectrophotometer in quartz cuvettes with a 10 mm path length.

Zeta potential

Zeta potential was measured using a Malvern Zetasizer Nano ZS. All measurements were performed at 25°C using filtered polymer solutions of 1 mg/mL in Milli-Q water.

2.2.3 Synthesis of 2-[(butylsulfanyl)carbonothiol]sulfanyl Propanoic Acid

2-[(butylsulfanyl)carbonothiol]sulfanyl propanoic acid (C4) was synthesized using the previously reported method.¹⁴⁰ A 50% w/w NaOH solution (8 g, containing 4 g, 100 mmol NaOH) was added to a stirred mixture of butanethiol (9.019 g, 100 mmol) and water (4 mL). Acetone

(5 mL) was then added and stirred for 0.5 h, resulting in a clear, colourless solution. The mixture was then cooled to near-room temperature. Carbon disulphide (6.7 mL, 8.54 g, 112.5 mmol) was added and then stirred for a further 0.5 h, resulting in a clear orange solution. The solution was then cooled in an ice bath. 2-Bromopropanoic acid (15.68 g, 102.5 mmol) was then added slowly so that the temperature did not exceed 30°, followed by the addition of 50% w/w NaOH (8.2 g, 102.5 mmol). The ice bath was then removed when the exotherm stopped and water (15 mL) was added. The reaction was stirred at room temperature for 24 h then diluted with water (25 mL). The solution was then stirred and cooled in an ice bath, and afterwards, 10 M HCl (15 mL) was added slowly (temperature was kept <10°C) to form a yellow oil. The stirring of the mixture was continued at ice temperature until the oil solidified. The solid was collected by vacuum filtration, washed with cold water, and dried under vacuum to a state of semi-dryness. The lumps were crushed with a spatula and then the granules were resuspended in fresh cold water, stirred for 15 min, and then re-filtered. The residue was washed with cold water and air-dried to obtain a powdery yellow solid. The yellow solid was recrystallised from petroleum benzine 60-80°C (180 mL) with gentle stirring to give bright yellow microcrystals (39 g, 80%). ¹H NMR (400MHz, d6-DMSO): δ 4.67 (1H, q, J=7.32 Hz), 3.38 (2H, t, J=7.36 Hz), 1.63 (2H, quin, J=7.56 Hz), 1.50 (3H, d, J=7.32 Hz), 1.36 (2H, sxt, J=7.48 Hz), 0.89 (3H, t, J=7.36 Hz). Full ¹H NMR spectra is shown in Figure A.1.

2.2.4 Synthesis of Backbone

2.2.4.1 Synthesis of Poly-Hydroxyethyl Acrylamide (PHEAm_a)

For backbone DP of 500, HEAm (2.3 g, 19.8 mmol), methylated-C4 (10 mg, 0.04 mmol), ACVA (1.39 mg, 0.0049 mmol) and DMF (145 mg, 1.98 mmol) were dissolved in dioxane and water (7.6 mL, 1:1) in a vial with a stirrer bar, sealed with a rubber septum and degassed with nitrogen for 30 minutes. The mixture resulted in monomer concentration of 2 M. The vial was placed in an oil bath heated to 70°C for 5 hours. Samples were taken using a nitrogen-purged syringe with a needle at predetermined time points to study the kinetics of polymerization. The

reaction mixture was precipitated in cold acetone in a falcon tube and centrifuged. The solid was re-dissolved in methanol and precipitated again in acetone. The final solid was dissolved in water and then freeze-dried (yield 75-85%). ^1H NMR (400MHz, $\text{d}_6\text{-DMSO}$): δ 7.96-7.27 (1H, m), 5.21-4.68 (2H, m), 3.95-2.67 (4H, m), 2.21-1.67 (2H, m).

For backbone with other DP, similar reaction condition was applied by maintaining the concentration of ACVA and changing the concentration of HEAm and methylated-C4.

2.2.4.2 Synthesis of Poly-(Hydroxyethyl Acrylamide-co-4-Acryloylmorpholine) ($\text{P(HEAm-co-NAM)}_{b\%,a}$)

HEAm (921 mg, 8 mmol), NAM (1129 mg, 8 mmol), methylated-C4 (24.2 mg, 0.096 mmol), ACVA (0.97 mg, 3.47×10^{-3} mmol) and DMF (236 mg, 3.2 mmol) were dissolved in a mixture of dioxane-water (1:1, 8.3 mL) in a vial with a stirrer bar, sealed with a rubber septum and degassed with nitrogen for 30 minutes. The vial was placed in an oil bath heated to 70°C for 2.5 hours. Samples were taken using a nitrogen-purged syringe with a needle at predetermined time points to study the kinetics of polymerization. The reaction mixture was precipitated in cold acetone in a falcon tube and centrifuged, re-dissolved in methanol and precipitated again in acetone. The solid was dissolved in water and then freeze-dried (yield 75-85%). A similar procedure was done for copolymer with HEAm:NAM = 1:3, using single solvent dioxane. ^1H NMR (400MHz, $\text{d}_6\text{-DMSO}$): δ 8.11-7.27 (1H, m), 5.12-4.43 (2H, m), 4.01-2.80 (12H, m), 2.65-0.93 (4H, m).

2.2.5 Synthesis of PolyCTA (PCTA-PHEAm_a and $\text{PCTA-P(HEAm-co-NAM)}_{b\%,a}$)

PHEAm_a or $\text{P(HEAm-co-NAM)}_{b\%,a}$ (300 mg, 0.0054 mmol with respect to alcohol groups) and C4 (431 mg, 1.8 mmol) were dissolved in 7 ml DMF in a dry 50 ml round bottom flask under nitrogen, cooled with an ice bath followed by the addition of DMAP (42 mg, 0.35 mmol) and EDC.HCl (683 mg, 3.56 mmol). The reaction mixture was stirred for 30 minutes, after which the ice bath was removed and stirred at room temperature for a further 24 h. The reaction mixture was precipitated twice in cold methanol-water (80:20). Solid was re-dissolved

in chloroform prior to the second precipitation. The precipitate was collected by centrifugation and dried with airflow.

PCTA-PHEAm_a: ¹H NMR (400MHz, CDCl₃): δ 7.61-6.71 (1H, m), 4.94-4.71 (1H, m), 4.48-4.04 (2H, m), 3.79-3.14 (2H, m), 2.50-1.23 (2H, m), 1.67 (2H, m), 1.60 (3H, m), 1.43 (2H, m), 0.93 (3H, m).

PCTA-P(HEAm-co-NAM)_{b,a%}: ¹H NMR (400MHz, CDCl₃): δ 7.61-6.71 (1H, m), 4.94-4.71 (1H, m), 4.48-4.04 (2H, m), 3.91-3.14 (12H, m), 2.50-1.23 (4H, m), 1.67 (2H, m), 1.60 (3H, m), 1.43 (2H, m), 0.93 (3H, m).

2.2.6 Synthesis of BBPs

2.2.6.1 Synthesis of Brush [PNAM_x]_a

For a typical reaction using C4_{backbone}/C4_{shuttle} 1:1, PCTA-PHEAm_a (a = 150 or 500, 32 mg, 0.086 mmol with respect of C4), C4 (20.5 mg, 0.086 mmol), NAM (1.3 g, 9.15 mmol), ACVA (6 mg, 0.021 mmol) and DMF (347 mg, 4.57 mmol) were dissolved in DMAc (3 mL) in a vial with a stirrer bar, sealed with a rubber septum and degassed with nitrogen for 30 minutes. The ratios of NAM:PCTA-PHEAm_a (equivalent to C4 unit):C4:ACVA were 110:1:1:0.25 and [NAM] was 2 M. The vial was placed in an oil bath heated to 70°C for 90 minutes, reaching 95-98% conversion. The reaction mixture was precipitated in cold acetone in a falcon tube and centrifuged. The solid was re-dispersed in chloroform and precipitated again in cold acetone until the GPC chromatogram only showed one peak. The precipitate was collected by centrifugation and dried with airflow, arouse yield ~80-85%. Similar reactions were done by varying the ratio between C4_{backbone}/C4_{shuttle}. ¹H NMR (400MHz, CDCl₃): δ 5.26-3.08 (12H, m), 2.87-2.28 (2H, m), 2.28-1.07 (11H, m), 0.94 (3H, m).

2.2.6.2 Synthesis of Brush [PNAM_x]_{50%,c} and Brush [PNAM_x]_{25%,c}

For a typical reaction using C4_{backbone}/C4_{shuttle} 1:1, PCTA-P(HEAm_a-co-NAM_b) (a/b = 1:1 or 1:3 with a+b = 150, 100 mg, 0.20 mmol with respect to C4), C4 (47 mg, 0.20 mmol), NAM

(2.97 g, 21.03 mmol), ACVA (14 mg, 0.05 mmol) and DMF (30 mg, 0.38 mmol) were dissolved in DMAc in a vial with a stirrer bar, sealed with a rubber septum and degassed with nitrogen for 30 minutes. The ratios of NAM: PCTA-P(HEAm_a-co-NAM_b) (equivalent to C4 unit):C4:ACVA were 110:1:1:0.25 and [NAM] was 2M. The vial was placed in an oil bath heated to 70°C for 90 minutes, reaching 95-98% conversion. The reaction mixture was precipitated in cold acetone in a falcon tube and centrifuged. The solid was re-dispersed in chloroform and precipitated again in cold acetone until the GPC chromatogram only showed one peak. The precipitate was collected by centrifugation and dried with airflow, arouse yield ~60-85%. Similar reactions were done by varying the ratio between C4_{backbone}/C4_{shuttle}. ¹H NMR (400MHz, CDCl₃): δ 5.26-3.08 (12H, m), 2.87-2.28 (2H, m), 2.28-1.07 (11H, m), 0.94 (3H, m).

2.2.6.3 Synthesis of Brush [PnBA_y]_a

For a typical reaction using C4_{backbone}/C4_{shuttle} 1:1, PCTA-PHEAm_a (160 mg), 0.43 mmol with respect of C4, C4 (101 mg, 0.43 mmol), nBA (2.4 g, 18.71 mmol), ACVA (30 mg, 0.10630 mmol) and DMF (273 mg, 3.74 mmol) were dissolved in DMAc in a vial with a stirrer bar, sealed with a rubber septum and degassed with nitrogen for 30 minutes. The ratios of nBA:PCTA-PHEAm_a (equivalent to C4 unit):C4:ACVA were 34:1:1:0.5 and [nBA] was 2.6 M. The vial was placed in an oil bath heated to 70°C for 30 minutes. The reaction mixture was precipitated in cold methanol in a falcon tube and centrifuged. The solid was re-dissolved in chloroform and precipitated again in cold methanol until the GPC chromatogram only showed one peak. The precipitated was collected by centrifugation and dried with airflow. Similar reactions were done by varying the ratio between C4_{backbone}/C4_{shuttle}. Yield = 80-85%. ¹H NMR (400MHz, CDCl₃): δ 4.83 (1H, m), 4.05(2H, m), 3.35 (2H, m), 2.65-1.81 (2H, m), 1.60 (2H, m), 1.38 (2H, m), 0.94 (3H, m).

2.2.6.4 Synthesis of Brush [PnBA_y-b-PNAM_x]_a

Brush [PnBA_y]_a (300 mg, 0.15 mmol with respect to C4), C4 (35 mg, 0.15 mmol), NAM (1.8 g, 13.06 mmol), ACVA (10 mg, 0.0372 mmol) and DMF (119 mg, 1.63 mmol) were

dissolved in DMAc (13.8 mL) in a vial with a stirrer bar, sealed with a rubber septum and degassed with nitrogen for 45 minutes. The ratios of NAM: Brush $[PnBA_y]_a$ (equivalent to C4 unit):C4:ACVA were 160:3:1:0.5 and $[NAM]$ was 2 M. The vial was placed in an oil bath heated to 70°C for 30 minutes, reaching 90% conversion. The reaction mixture was precipitated in cold acetone in a falcon tube and centrifuged. The solid was re-dissolved in methanol and precipitated again in cold acetone. The precipitated was collected by centrifugation and dried with airflow. Yield = ~75%. 1H NMR (400MHz, $CDCl_3$): δ 4.83 (1H, m), 4.05(2H, m), 3.35 (2H, m), 2.65-1.81 (2H, m), 1.60 (2H, m), 1.38 (2H, m), 0.94 (3H, m).

2.2.6.5 Synthesis of Brush $[P(NAM_x-co-NHSA_y)]_a$, Brush $[P(NAM_x-co-NHSA_y)]_{50\%,c}$ and Brush $[P(NAM_x-co-NHSA_y)]_{25\%,c}$

PCTA-PHEAm₁₅₀ (99.5 mg, 0.28 mmol with respect to CTA unit), C4 (67 mg, 0.28 mmol), NAM (4348 mg, 30.8 mmol), ACVA (39.24 mg, 0.14 mmol) and DMF (450 mg, 6.16 mmol) were dissolved in DMAc (7.5 mL) in a vial with a stirrer bar, sealed with a rubber septum and degassed with nitrogen for 20-30 minutes. The vial was placed in an oil bath heated to 70°C for 90 minutes. The reaction mixture was precipitated in cold acetone in a falcon tube and centrifuged. The solid was re-dispersed in chloroform and precipitated again in cold acetone. The precipitate was collected by centrifugation and dried with airflow. Yield = 60-65%. 1H NMR (400MHz, $CDCl_3$): δ 5.18 (1H, m), 4.02 (2H, m), 3.62 (8H, m), 3.30 (2H, m), 2.81-1.97 (3H, m), 1.97-1.01 (6H, m), 1.59 (2H, m), 1.37 (2H, m), 0.93 (3H, m).

In similar procedure, brush $[P(NAM_{50-co-NHSA_2})]_{500}$, $[(PNAM_{50-co-NHSA_2})]_{50\%,150}$, $[P(NAM_{50-co-NHSA_2})]_{25\%,150}$, and $[(PNAM_{50-co-NHSA_2})]_{50\%,500}$ were also prepared.

2.2.7 End Group Modification

2.2.7.1 Removal of RAFT Z-groups with Radical Initiator (Brush X-ACVA)

Brush polymers (4.0×10^{-2} mmol CTA), ACVA (311 mg, 1.1 mmol), lauroyl peroxide (44.2 mg, 0.11 mmol) were dissolved in anhydrous dioxane (15 ml), degassed with nitrogen for 20 minutes and heated in an oil bath at 80°C for six hours. The reaction mixture was precipitated three times into cold diethyl ether, then re-dissolved in water and dialyzed for three days using a 10k MWCO membrane. The aqueous solution was freeze-dried to yield a colourless powder.

2.2.7.2 Interchange of Z-groups in Brush with Z-groups from another RAFT agent (Brush X-BM)

Brush [PNAM₅₀]₁₅₀ (227 mg, 0.03 mmol respect to CTA unit), BM1429 (76 mg, 0.3 mmol), ACVA (0.84 mg, 0.003 mmol) were dissolved in DMAc (2 mL) in a vial with a stirrer bar, sealed with a rubber septum and degassed with nitrogen for 15 minutes. The vial was placed in an oil bath heated to 70°C for 3 hours. Samples were isolated by precipitation in diethyl ether twice, dried with airflow and measured in ¹H NMR. Interchange in brush [PNAM₅₀]₅₀₀ was prepared in a similar condition.

2.2.8 Dynamic Interchange

2.2.8.1 Z-group interchange in PolyCTA

For CTA_{Interchange}/CTA_{Backbone} 1:1, PCTA-PHEAm₅₀₀ (26 mg, 0.07 mmol respect to CTA unit), BM1429 (18 mg, 0.07 mmol), AIBN (1.44 mg, 0.00875 mmol) were dissolved in DMF (700 µL) in a vial with a stirrer bar, sealed with a rubber septum and degassed with nitrogen for 15 minutes. The vial was placed in an oil bath heated to 70°C. Samples were withdrawn at 1, 2 and 3 hours using a nitrogen-purged syringe with a needle. Samples were isolated by precipitation in chloroform, dried with airflow and measured in ¹H NMR using DMSO. In a

similar procedure, two sets of reactions were prepared with CTA_{Interchange}/CTA_{Backbone} 5:1 and 10:1.

2.2.8.2 Z-group interchange in Brush [PNAM₅]₁₅₀

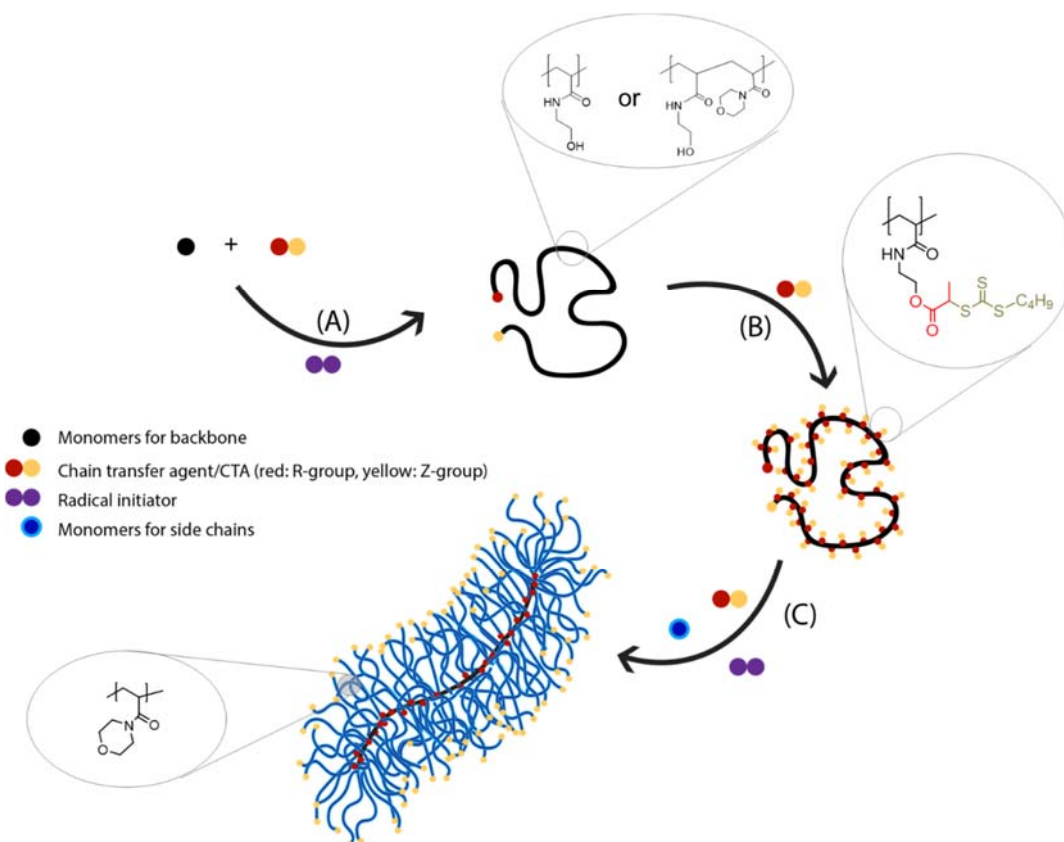
For CTA_{Interchange}/CTA_{Backbone} 1:1, brush [PNAM₅]₁₅₀ (51 mg, 0.055 mmol respect to CTA unit), BM1429 (14 mg, 0.055 mmol), ACVA (1.54 mg, 0.0055 mmol) were dissolved in DMAc (118 μ L) in a vial with a stirrer bar, sealed with a rubber septum and degassed with nitrogen for 15 minutes. The vial was placed in an oil bath heated to 70°C for 3 hours. Samples were isolated by precipitation in acetone twice, dried with airflow and measured in ¹H NMR.

In a similar procedure, two sets of reactions were prepared with CTA_{Interchange}/CTA_{Backbone} 5:1 and 10:1, by maintaining the molarity of BM1429.

2.2.9 RAFT End Group Stability

18 mg [PNAM₅₀]₁₅₀-BM were dissolved in 10 mL of PBS pH 7.4. 1 eq. of ethanolamine (relative to the Z-groups) was added and the solution was mixed quickly, after which 1 mL of initial sample was taken. The mixture was then incubated in water bath 37°C. 1 mL of sample was taken at each predetermined time point. The samples were then stored in the freezer until analysis time. All samples were then analyzed using UV-Vis spectrophotometer. In a similar procedure, two sets of reactions were prepared with 20 eq. of ethanolamine and without ethanolamine as control.

2.3 RESULTS AND DISCUSSION

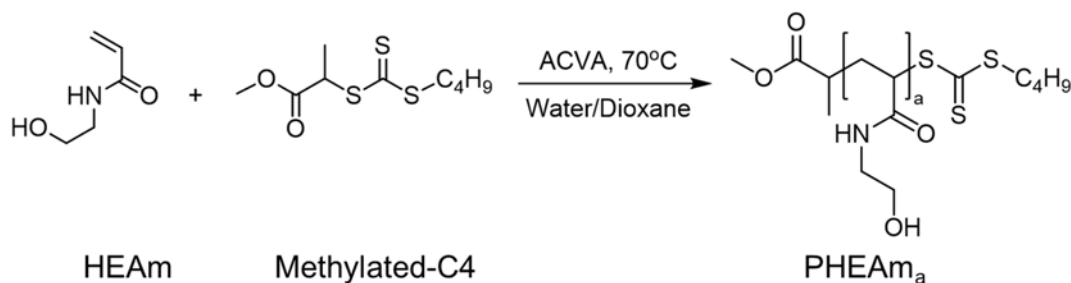


Scheme 2.1 Schematic illustration of the synthesis of BBPs via the CTA-shuttled R-group Grafting-from approach: (A) synthesis of backbone, (B) synthesis of polyCTA and (C) grafting of monomers from the backbone.

My main objective is to create a versatile synthesis platform of bottle-brush polymers that is adjustable to meet some substantial biomedical application requirements. For this reason, I have developed a method of synthesis of BBPs using RAFT polymerization due to its simplicity, flexibility, versatility and ease to purify the final product. The method involves three main steps (Scheme 2.1), which include the synthesis of backbone via RAFT polymerization (step A), the synthesis of polyCTA by esterification of backbone and RAFT agents (step B), and then the grafting of side chains from the backbone (step C) via CTA-shuttle R-group RAFT grafting-from approach adapted from the method of Zhang *et al.*¹²⁴ With

this method, I can create a library of well-defined NAM-based BBPs with narrow molecular weight distributions and different features such as size and side chain structure.

2.3.1 Synthesis of Backbone Precursors (PHEAm_a)



Scheme 2.2 General synthesis of backbone PHEAm_a

The first step of the synthesis is to create the polymeric backbone via RAFT polymerization. PHEAm_a (Scheme 2.2) was used as backbone precursor due to its functional hydroxyl groups which were later utilized to conjugate CTAs. For the backbone, I aimed to synthesize six different lengths: DP50 (PHEAm₅₀), DP100 (PHEAm₁₀₀), DP150 (PHEAm₁₅₀), DP500 (PHEAm₅₀₀), DP1000 (PHEAm₁₀₀₀), and DP2000 (PHEAm₂₀₀₀).

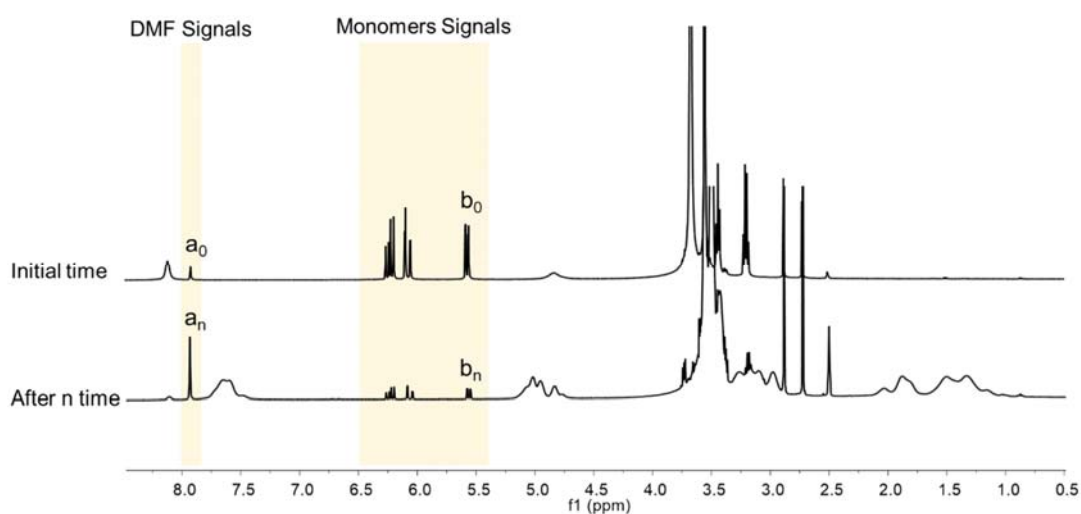


Figure 2.4 ¹H NMR peak to calculate monomer conversion by comparing DMF signal and monomer signal at the initial time and the final crude reaction. Samples were dissolved in d6-DMSO.

$$\text{Conversion (\%)} = \frac{\int \left(\frac{b_0}{a_0}\right) - \int \left(\frac{b_n}{a_n}\right)}{\int \left(\frac{b_0}{a_0}\right)}$$

Equation 2.1 Calculation of monomer conversion by comparison of the integral value of monomer signal relative to DMF

An ester form of C4 (methylated-C4) was used as CTA agent to remove any potential interaction of carboxylic groups on the backbone tips. A mixture of water and dioxane was used in the reaction to facilitate the solubilisation of the produced hydrophilic PHEAm and the hydrophobic methylated-C4. Without water, the resulting PHEAm, which is insoluble in dioxane, can precipitate due to its highly hydrophilic nature. The conversion was calculated by ^1H NMR by comparing the ratio between the integral value of the dimethylformamide (DMF) internal standard signal and monomer signal at time zero and the final polymerization time (Equation 2.1 and Figure 2.4). DMF was added to the reaction as an internal standard since it is inert and will not interfere with the polymerization reaction. It also has a higher boiling point (153°C) than the temperature used to run the polymerization (70°C) and consequently, it does not evaporate during the polymerization process. In addition, its peaks in ^1H NMR do not overlay with the peaks from the monomers and the produced polymers.

The kinetic studies were performed on the reactions of PHEAm₁₀₀, PHEAm₅₀₀, PHEAm₁₀₀₀ and PHEAm₂₀₀₀. The induction period (characterized by a very low conversion, $<5\%^{141}$) for all reactions did not follow a trend (Figure 2.5A). For example, an induction period is visible in PHEAm₁₀₀ and PHEAm₁₀₀₀, which is around 30 minutes and 60 minutes, respectively. However, for PHEAm₅₀₀ and PHEAm₂₀₀₀, an induction period might be less than 15 minutes, and therefore cannot be plotted in the graph. Controlling the induction period is difficult since it is related to the RAFT pre-equilibrium period and the consumption of traces of oxygen or other species that can react with the radicals. A shorter induction time can also be caused by higher initial concentration of radicals in the reaction of PHEAm₅₀₀ and PHEAm₂₀₀₀ compared to the other two, relative to the initial concentration of monomers.

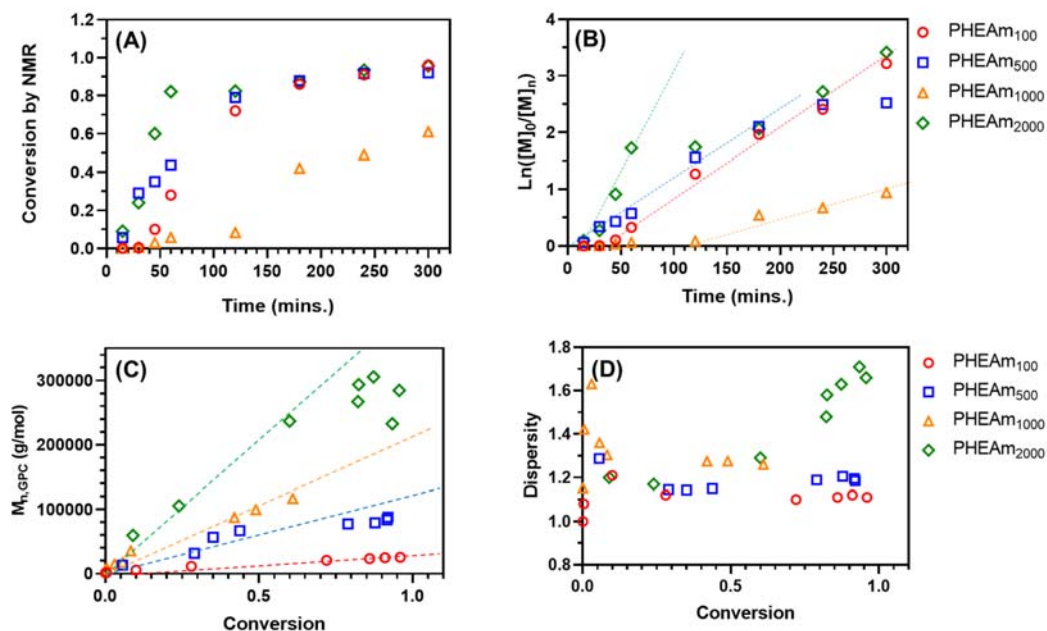


Figure 2.5 Kinetic plots of the polymerization of PHEAm_a mediated by C4 at 70°C. The dashed lines serve as guide to the eye to highlight the linear region in the plot of $\ln([M]_0/[M]_n)$ versus time.

After the induction period, a linear correlation between the $\ln([M]_0/[M]_t)$ and time was observed (Figure 2.5B). Also, the number-average molecular weights ($M_{n,SEC}$) increased linearly with the conversion (Figure 2.5C). This linearity is a typical pseudo-first-order reaction in RAFT controlled polymerization, which showed negligible number of initiator-derived chains compared to the number of CTA-derived chains.^{142,143} Also, in PHEAm₅₀₀, the linearity was observed only up to 3 h, where the conversion is around 88%. This could mean less monomer is present, and therefore, undesired termination reactions could have occurred.¹⁴⁴

Table 2.1 Characteristics for polymerization of HEAm to make backbone PHEAm_a at 70°C, [HEAm] = 2 M

Code	Target DP ^a	DP reaction ^b	CTA:I ^c	[I ₀] ^d (mM)	Monomer conversion ^e	DP achieved ^f	M _n theo (kDa) ^g	M _n GPC (kDa) ^h	Đ ⁱ
PHEAm ₅₀	50	50	50:1	1.0	76%	38	4.6	12.0	1.10
PHEAm ₁₀₀	100	100	20:1	1.0	96%	96	11.3	25.5	1.11
PHEAm ₁₅₀	150	156	20:1	0.9	96%	150	17.5	32.8	1.10
PHEAm ₅₀₀	500	500	8:1	0.5	92%	460	53.2	87.6	1.18
PHEAm ₁₀₀₀	1000	1000	5:1	0.4	61%	610	70.4	117.0	1.26
PHEAm ₂₀₀₀	2000	2000	1:1	1.0	96%	1920	221.3	284.4	1.66

^a Degree of polymerization (DP) means expected number of monomer per chain.

^b The molar ratio between monomer and CTA

^c The molar ratio between CTA and initiator

^d Initial concentration of radical initiators added at the beginning of reaction (before dissociation)

^e The conversion of the monomers obtained from ¹H NMR analysis

^f The actual DP achieved, obtained by multiplying conversion with DP reaction

^g Theoretical molecular weight calculated from DP achieved

^h Molecular weight obtained from DMAc-GPC

ⁱ Dispersity of polymers, obtained from DMAc-GPC, which represents M_w/M_n

The concentration of monomer in the reaction can influence the rate of propagation¹⁴⁵. In this reaction, the concentrations were kept the same for all lengths of backbone polymer (2 mol/L), which is enough to provide high conversion while maintaining low dispersity¹⁴⁵. Theoretically, since all reactions were carried out with the same monomer concentration, the rates of propagation should be similar. However, beside the monomer concentration, the initiator concentration also influence the rate of propagation¹¹⁸. I observed high conversion (>90%) in the reaction of PHEAm₁₀₀, PHEAm₅₀₀, and PHEAm₂₀₀₀ within 5 h, except in PHEAm₁₀₀₀ which only showed 61% conversion. I suggested the lower conversion in PHEAm₁₀₀₀ is due to lower concentration of initiator added. However, even with low conversion and low initiator concentration, the dispersity of PHEAm₁₀₀₀ is already higher than the shorter ones.

To determine the molecular weight of the produced PHEAm_a, I analyzed the pure polymers using DMAc-GPC. This way, I obtained PHEAm_a with a molecular weight ranging from 12 to 280 kDa. The molecular weight observed in DMAc-GPC chromatogram did not match the calculation from the signal integration in ¹H NMR (Table 2.1). This discrepancy could

arise from the different characteristics (e.g., hydrophilicity and polarity) of PHEAm_a and polystyrene, GPC calibration standards. Due to their –OH pendant groups, PHEAm_a is more hydrophilic and can swell more than polystyrene with similar size, and therefore can be retained to a different degree in the column pores. For this reason, the stoichiometry for the next reaction step was calculated based on the theoretical value from ¹H NMR. The representative ¹H NMR spectra of the backbone PHEAm_a with peak assignment is shown in Figure A.2.

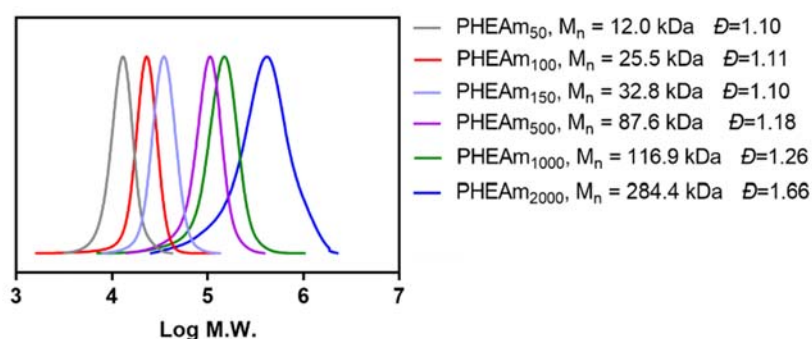


Figure 2.6 Overlay of GPC-DMAc chromatograms of PHEAm_a synthesised at 70°C in dioxane/water, [HEAm]= 2M, t= 5 hours.

Only PHEAm with DP up to DP500 exhibited relatively low dispersity (<1.20) (Figure 2.6). This is because in RAFT polymerization, an amount of initiator is required to ensure the availability of active radicals to commence the RAFT process. Increasing the amount of initiator as a way to increase the DP also leads to an increase in dead chains, which increases the overall dispersity of the polymers. With this shortfall of RAFT polymerization, I might not be able to produce a well-defined long BBP with a filamentous structure. However, a study by Müllner *et al.*,⁶² also showed that very long (up to micrometer size) PEGMA-based BBPs did not show better biological performance in terms of their pharmacokinetics, biodistribution and tumour uptake^{62,73}, compared to the shorter ones. Thus, I postulated that aiming for backbone longer than DP2000 might not be necessary.

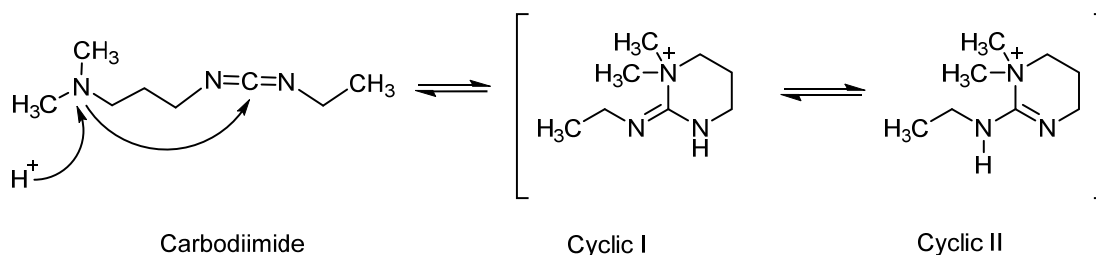
2.3.2 Synthesis of PCTA-PHEAm_a

Subsequently, from the previously produced backbones, I only used pHEAm₁₅₀, PHEAm₅₀₀, PHEAm₁₀₀₀ and PHEAm₂₀₀₀ to synthesise the polyCTA. In this step, CTAs were attached to the alcohol pendant groups of PHEAm_a via esterification. The reactive hydroxyl groups of PHEAm_a support conjugation via ester bond with the carboxylic R-group of C4, a RAFT chain transfer agent (CTA) (Scheme 2.3). This step aims to generate a macroinitiator backbone with CTA pendant groups in every unit of the backbone, from which the side chains will grow.



Scheme 2.3 Representative reaction scheme of polyCTA backbone formation

N-(3-Dimethylaminopropyl)-N-ethylcarbodiimide (EDC), a water-soluble carbodiimide, was chosen as a coupling agent. EDC is one type of zero-linker coupling agents that has been widely used to mediate the formation of amide bond between carboxylates and amines. However, since I aim for an ester bond, instead of an amide bond, 4-dimethylaminopyridine (DMAP) is required as a catalyst for driving the reaction.



Scheme 2.4 Tautomerisation of EDC (adapted from Williams and Ibrahim¹⁴⁶)

I have observed that using the tertiary base form of EDC resulted in very low conjugation efficiency. Instead, using the salt form of EDC (EDC.HCl) led to significantly higher conjugation efficiency (around 70-85%). This is probably because the cyclic form of EDC is the species that can efficiently activate the carboxylic acid (Scheme 2.4).^{146,147} A proton is required to transform the carbodiimide to the cyclic species. When using aprotic solvents like DMF, as in this conjugation reactions, protons from the solvent are not available to promote the cyclic formation of basic EDC.¹⁴⁶ On the other hand, EDC.HCl readily exists in the cyclic form when in solution and therefore works better in the conjugation reaction where an organic solvent is used.

The successful formation of an ester bond between PHEAm_a and C4 was monitored by ¹H NMR and GPC. ¹H NMR spectra of the corresponding backbone precursors and polyCTAs are shown in Figure 2.7. The successful attachment of CTA molecules to the backbone is verified by the shift of protons from δ (ppm) 2.8 to 4.0-4.5 (red dot), and the appearance of a peak at δ (ppm) 4.7-4.9, which corresponds to the protons from C4 (green dot). Secondly, the signal of PHEAm_a hydroxyl group at 4.8-5.4 ppm decreases, or even disappears at full conversion (blue dot). The produced compounds were then isolated by precipitation in a cold mixture of methanol-water 80:20, followed by vacuum drying to remove excess solvent. The representative ¹H NMR spectra with full proton annotation of isolated compounds are shown in Figure A.3 (Appendix). The amount of conjugated CTAs was calculated by comparing the ratio of protons in backbone and the total proton at δ (ppm) 1.1-1.3.

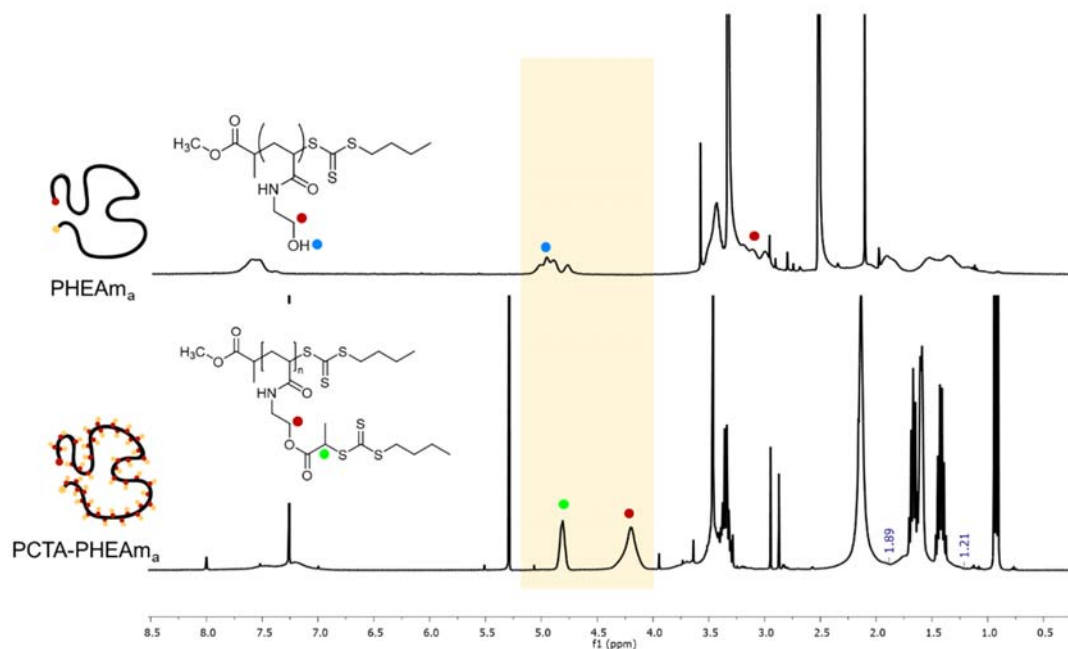


Figure 2.7 Comparison of ^1H NMR spectra of representative backbone precursor and polyCTA from PHEAm_{100} showing a new peaks at δ (ppm) 4.0-4.5 and 4.7-4.9.

GPC traces of polyCTA DP 150, 500 and 1000 are unimodal with relatively narrow dispersities ($\mathcal{D} \leq 1.50$, Figure 2.8). PCTA- PHEAm_{2000} showed high dispersity ($\mathcal{D} = 2.13$). To note, the straight line shown on the chromatogram of PCTA- PHEAm_{2000} is due to an issue in the calibration system and might affect the dispersity value obtained from the software. It is interesting that as the length of the backbone chain increases, the conjugation efficiency decreases from 85% for PCTA- PHEAm_{150} to 51% for PCTA- PHEAm_{2000} (Table 2.2). This is probably because the OH-groups in the longer backbone are more hindered and therefore less accessible for the coupling agents as well as C4. However, despite the relatively high conjugation efficiency (50-85%), the chromatograms only slightly shifted to higher molecular weight (Figure 2.8a). In fact, the molecular weights obtained from the GPC are closer to the theoretical values. This is probably due to the change in hydrophobicity of the polymer chains which is more similar to the polystyrene as GPC calibration standard. In addition to the GPC chromatogram shift, the new compound is more soluble in chloroform than in polar solvents

like DMSO or methanol because the backbone hydrophobicity increases. The summary of all polyCTAs is shown in Table 2.2.

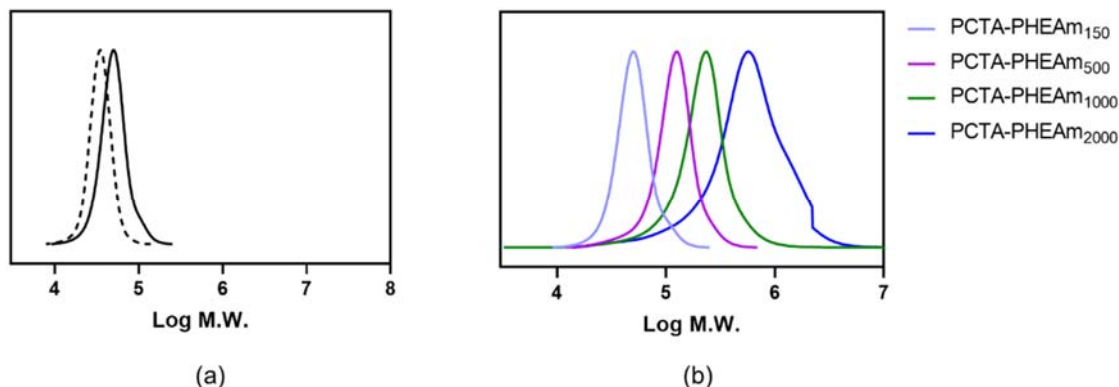


Figure 2.8 (a) Representative GPC chromatogram of PCTA-PHEAm_a (full line) which is shifted from its corresponding backbone (dash line) and (b) overlay of GPC-chromatograms of all produced polyCTAs.

In conclusion, I have been able to create polyCTAs using a simple conjugation and purification method. The conjugation efficiencies were relatively high which provided a remarkable amount of CTA from which the side chains can grow. However, narrow dispersity can only be maintained at backbone with DP up to 500.

Table 2.2 M_n and \bar{D} values of PolyCTAs as determined by DMAc-GPC analysis with polystyrene standard

Description	$M_{n,theory}^a$ (kDa)	$M_{n,GPC}^b$ (kDa)	Dispersity (\bar{D}) ^c	%CTAs in backbone ^d
PCTA-PHEAm ₁₅₀	44.3	46.2	1.16	85
PCTA-PHEAm ₅₀₀	138.7	103.8	1.25	70
PCTA-PHEAm ₁₀₀₀	163.4	172.0	1.42	64
PCTA-PHEAm ₂₀₀₀	454.6	355.3	2.13	51

^a Theoretical molecular weight calculated by addition of M_n theoretical of corresponding backbone PHEAm and percentage of conjugated C4

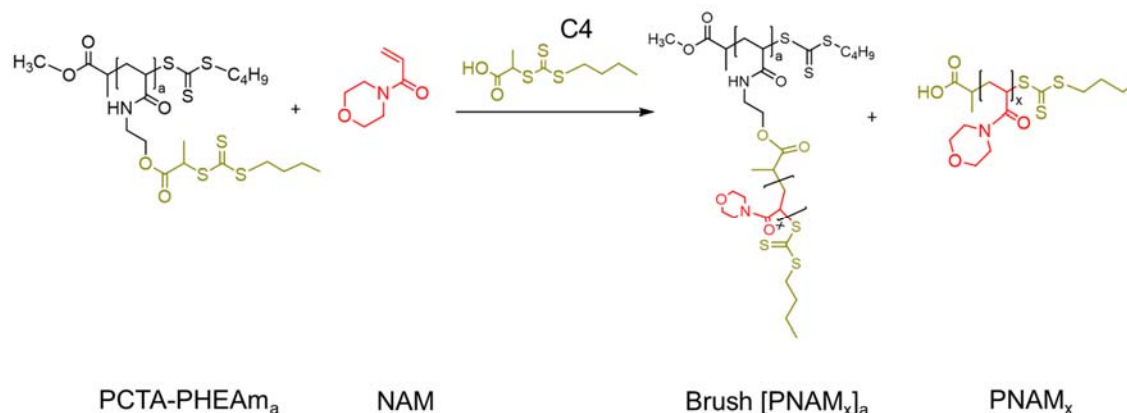
^b Molecular weight obtained from DMAc-GPC

^c Dispersity of polymers, obtained from DMAc-GPC, which represents M_w/M_n

^d Fraction of C4 units relative to HEAm unit in backbone PHEAm_a

2.3.3 Synthesis of Brush $[PNAM_x]_a$

Considering the dispersities of the previously produced polyCTAs, I then proceed to the grafting-from of side chains step with the backbone DP150 and DP500 only. The side chains were designed to achieve a DP of 50, which automatically becomes the radius of the brushes. With the ratio of backbone and twice side chains length (DP of $\sim 150 \times 100$ and $\sim 500 \times 100$), the produced brush polymers were expected to exhibit a cylindrical structure. For the grafting-from process, I adapted the aforementioned “CTA shuttled R-group approach”, which involves the addition of low molecular weight (LMW) CTA. This additional LMW CTA was added to act as shuttle for the active radicals and ensure all the chains grow continually and homogeneously. In the reaction, these LMW CTAs will also polymerize to form linear polymers with DP equivalent to the DP of side chains (Scheme 2.5). In this section, two factors were studied: 1) the optimum ratio of $CTA_{shuttle}/CTA_{backbone}$ and 2) isolation of the brushes.



Scheme 2.5 General reaction of brush $[PNAM_x]_a$

2.3.3.1 Optimization of $CTA_{shuttle}/CTA_{backbone}$

Brush $[PNAM_{50}]_{150}$

I first performed the grafting-from of 4-acryloylmorpholine (NAM) using C4 as LMW CTAs (Scheme 2.5). When Zheng *et al.*¹²⁴ firstly proposed the CTA-shuttle R-group technique,

they used 1 equivalent of LMW-CTAs to $\text{CTA}_{\text{backbone}}$, which is enough to create relatively narrow dispersity (1.07-1.30) BBPs with backbone DP of 30 and 120. Then Wang *et al.* synthesized longer BBPs (DP 1200) using the same equivalent of LMW-CTAs, resulting in BBPs with DP > 1.30. These results raised the question of whether changing the ratio between $\text{CTA}_{\text{shuttle}}$ and $\text{CTA}_{\text{backbone}}$ can improve the grafting process and the dispersity of the produced BBPs. Therefore, I examined the effect of the ratio of $\text{CTA}_{\text{shuttle}}/\text{CTA}_{\text{backbone}}$ in the grafting of side chains intending to obtain an optimal BBP.

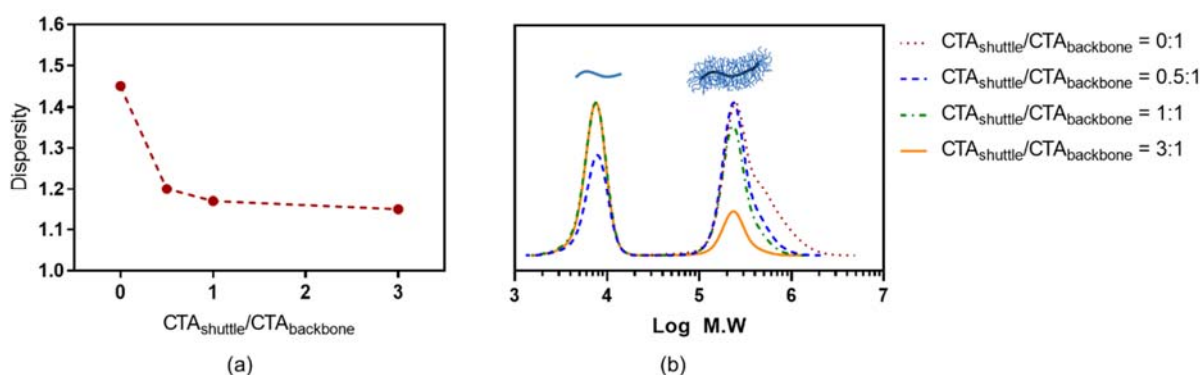


Figure 2.9 (a) Effect of $\text{CTA}_{\text{shuttle}}/\text{CTA}_{\text{backbone}}$ on the dispersity of brush $[\text{PNAM}_{50}]_{150}$ and (b) chromatogram of the crude products

First, I performed an experiment by varying the ratio of $\text{CTA}_{\text{shuttle}}/\text{CTA}_{\text{backbone}}$ to graft NAM from PCTA-PHEAm₁₅₀. This study proved that without the shuttle-CTA, the resulting BBPs showed extremely high dispersity with visible high-molecular weight shoulder in the GPC chromatogram (Figure 2.9b). An addition of 0.5 equivalents of shuttle-CTA is sufficient to lower the dispersity. Increasing the ratio of $\text{CTA}_{\text{shuttle}}$ to $\text{CTA}_{\text{backbone}}$ up to 3 equivalents resulted in even better dispersity. A more detail result is shown in Table 2.3.

Since the conversion of all reactions are similar, the theoretical molecular weight of the produced brushes should be similar. However, the densely packed structure of BBPs possess smaller hydrodynamic volume than linear ones with the same molecular weight. This caused the molecular weight obtained from gel permeation chromatography is much smaller than the

theoretical value (obtained by ^1H NMR). From this, it is interesting to notice that increasing amount of sacrificial CTAs resulted in decrease molecular weight obtained from GPC, despite the similar conversion. This suggest that the additional CTA can support a more controlled polymerization, preventing intra- or inter- molecular brush coupling by releasing the entrapped active radicals from BBPs, as mentioned earlier in the introduction.

Table 2.3 Results from varying the ratio of $\text{CTA}_{\text{shuttle}}:\text{CTA}_{\text{backbone}}$ for the synthesis of brush $[\text{PNAM}_{50}]_{150}$. All reactions were done in DMF with $[M] = 2\text{ M}$, $[I_0] = 70^\circ\text{C}$, 1.5 h.

Reaction	$\text{CTA}_{\text{shuttle}}^a/\text{CTA}_{\text{backbone}}^b$	Conv. ^c (%)	$M_{n,\text{theo}}^d$ (kDa)	M_n , GPC (kDa) ^e		Dispersity ^f (\bar{D})		Fraction ^g (%)	
				Brush	Linear	Brush	Linear	Brush	Linear
1	0:1	95.56	1,013	276.9	-	1.45	-	100	-
2	0.5:1	98.25	1,034	244.0	6.9	1.20	1.11	63	37
3	1:1	96.60	1,034	230.7	6.7	1.17	1.11	48	52
4	3:1	98.25	1,014	223.5	6.8	1.15	1.10	23	77

^a Free C4 added to the reaction

^b C4 in the backbone

^c Percentage of monomers which are converted into polymers

^d Molecular weight obtained from ^1H NMR based on conversion

^e Molecular weight obtained from DMAc-GPC

^f Dispersity of polymers, obtained from DMAc-GPC, which represents M_w/M_n

^g Ratio between the area under curve of brush peak and linear polymer peak in GPC chromatogram

Brush $[\text{PNAM}_{50}]_{500}$

After successfully producing brush $[\text{PNAM}_{50}]_{150}$, I aimed for brushes with a backbone DP of 500. For this longer BBP, I kept the length of the side chains equal to the $[\text{PNAM}_{50}]_{150}$. This gives us BBPs with similar diameters, and therefore, the aspect ratio is only dictated by the length of the backbone. Starting with PCTA-PHEAm₅₀₀ ($\bar{D} = 1.25$), I also tried to study the effect of $\text{CTA}_{\text{shuttle}}/\text{CTA}_{\text{backbone}}$ ratio. I hypothesized that the trend would be similar to that for $[\text{PNAM}_{50}]_{150}$ where 0.5 to 1 equivalent of shuttle-CTA would be enough to maintain the low dispersity of the produced BBPs. However, I found that with a longer backbone, the effect of increasing the $\text{CTA}_{\text{shuttle}}/\text{CTA}_{\text{backbone}}$ ratio is more apparent (Figure 2.10). Without the shuttle-CTA, the dispersity of the produced BBPs showed significantly high molecular weight distribution ($\bar{D} = 2.33$), with multimodality in GPC chromatogram (Figure 2.10b). The addition of shuttle-CTA by only 0.5 equivalent could significantly decrease the molecular weight

distribution to $\bar{D} = 1.60$ with monomodal GPC trace. Nevertheless, unlike brush $[\text{PNAM}_{50}]_{150}$, a minimum of three equivalent of shuttle-CTA is required to maintain the dispersity of brush $[\text{PNAM}_{50}]_{500}$ as low as the original polyCTAs. A more detail result is shown in Table 2.4.

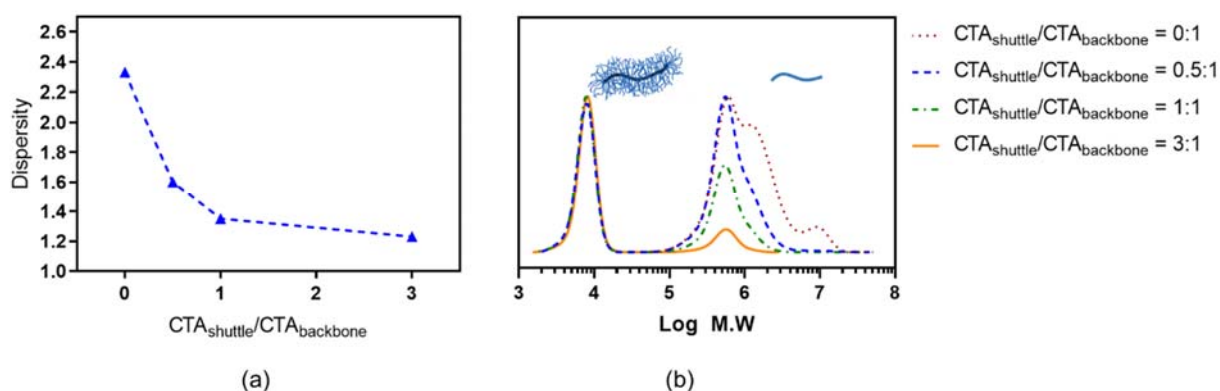


Figure 2.10 (a) Effect of $\text{CTA}_{\text{shuttle}}/\text{CTA}_{\text{backbone}}$ on the dispersity of brush $[\text{PNAM}_{50}]_{500}$ and (b) chromatogram of the crude products

Table 2.4 Results from varying the ratio of $\text{CTA}_{\text{shuttle}}/\text{CTA}_{\text{backbone}}$ for the synthesis of brush $[\text{PNAM}_{50}]_{500}$. All reactions were done in DMF with $[M] = 2 \text{ M}$, 70°C , 1.5h .

Reaction	$\text{CTA}_{\text{shuttle}}^{\text{a}}/\text{CTA}_{\text{backbone}}^{\text{b}}$	Conv. ^c (%)	$M_{\text{n,theo}}^{\text{d}}$ (kDa)	$M_{\text{n, GPC}}$ (kDa) ^e		Dispersity ^f (\bar{D})		Fraction ^g (%)	
				Brush	Linear	Brush	Linear	Brush	Linear
1	0:1	99.83	2,818	694.5	-	2.33	-	100	-
2	0.5:1	98.66	2,764	528.2	7.1	1.60	1.11	64	36
3	1:1	99.22	2,818	488.6	7.0	1.35	1.11	45	55
4	3:1	98.94	2,764	485.1	7.3	1.23	1.11	16	84

^a Free C4 added to the reaction

^b C4 in the backbone

^c Percentage of monomers which are converted into polymers

^d Molecular weight obtained from ^1H NMR based on conversion

^e Molecular weight obtained from DMAC-GPC

^f Dispersity of polymers, obtained from DMAC-GPC, which represents $M_{\text{w}}/M_{\text{n}}$

^g Ratio between the area under curve of brush peak and linear polymer peak in GPC chromatogram

2.3.3.2 Isolation of the BBPs from linear polymers

The shuttle-CTAs added to the reaction will also grow chains in the form of linear polymers. As shown in Table 2.3 and Table 2.4, the fractions of the produced linear polymers are proportional to the fractions of the shuttle-CTAs added to the reaction. For example, when

using a ratio of $\text{CTA}_{\text{shuttle}}/\text{CTA}_{\text{backbone}}$ 1:1 (shuttle-CTAs is 50% of total CTAs), the fraction of linear polymers from the crude reaction is around 50%, and when using a ratio of $\text{CTA}_{\text{shuttle}}/\text{CTA}_{\text{backbone}}$ 3:1 (shuttle CTAs is 75% of total CTAs) the fraction of linear polymers is also 75%. At a glance, removing these side products, especially for those from higher shuttle-CTAs fraction, might be difficult and time-consuming. However, to my surprise, the produced brush $[\text{PNAM}_x]_a$ could be easily isolated from crude reaction only by repeat precipitation in acetone. This purification method gave a relatively high yield (80-85%). The purity of the BBPs from the linear polymers can be observed in the chromatogram, where the peak of linear polymers disappeared after two precipitations, even for the reaction which used $\text{CTA}_{\text{shuttle}}/\text{CTA}_{\text{backbone}}$ 3:1 (Figure 2.11a).

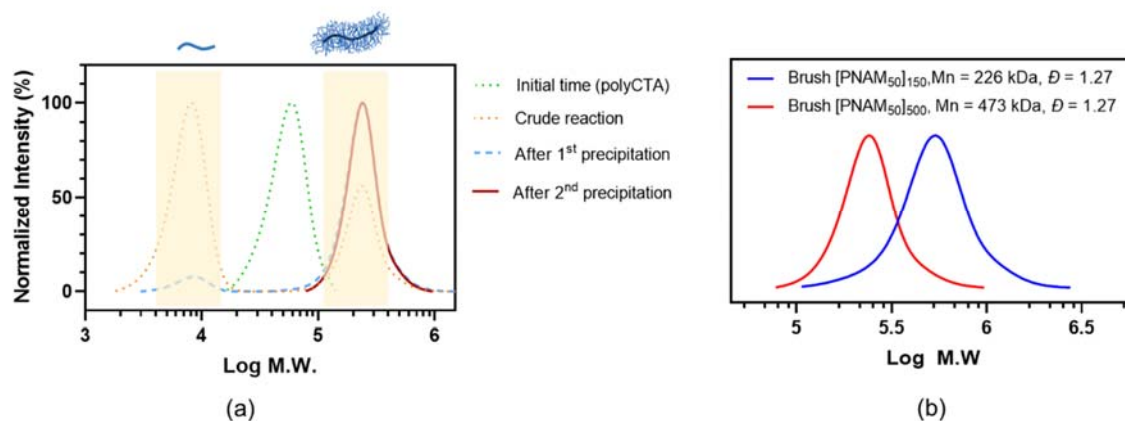


Figure 2.11 (a) Evolution of GPC chromatogram from the synthesis and purification of brush $[\text{PNAM}_{50}]_{150}$ and (b) overlay of GPC chromatogram of the purified brush $[\text{PNAM}_x]_a$

After the purification, brush $[\text{PNAM}_{50}]_{150}$ and brush $[\text{PNAM}_{50}]_{500}$ were characterized by DMAc-GPC and ^1H NMR. The purified BBPs still showed monomodality and narrow dispersity as shown in Figure 2.11b. The stacked representative ^1H NMR spectra of the purified brush $[\text{PNAM}_x]_a$ and its corresponding polyCTAs showed significant reduction of C4 signal (e.g. δ (ppm) 4.81, 4.19 and 0.91) due to the dominance of the NAM signal at δ 3.5-4.0 ppm (Figure

2.12). The representative ^1H NMR spectra of purified BBP and its peak assignments can be seen in Appendix, Figure A.4.

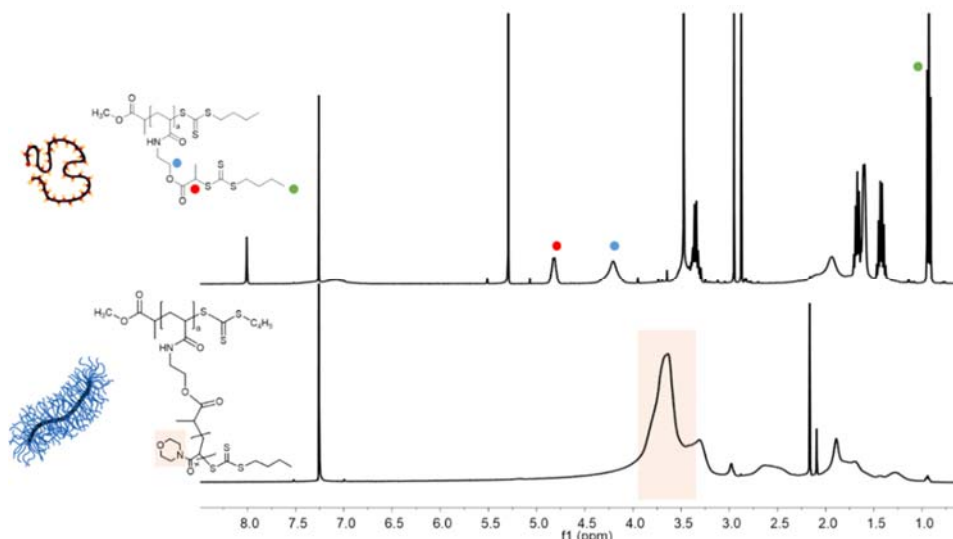


Figure 2.12 Evolution of ^1H NMR spectra from the synthesis of $[\text{PNAM}_{50}]_{150}$

2.3.4 Synthesis of Comb $[\text{PNAM}_x]_{50\%,a}$ and Comb $[\text{PNAM}_x]_{25\%,a}$

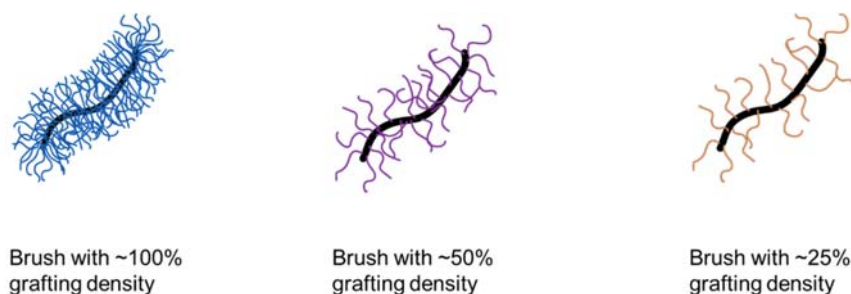
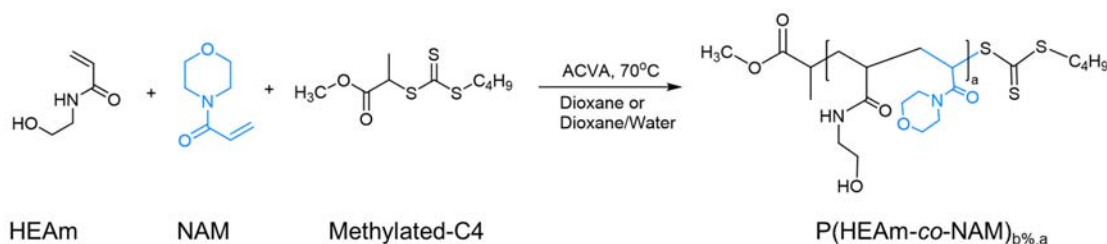


Figure 2.13 Structure illustration of molecular brushes with different grafting densities

After successfully establishing a method of synthesis for brush $[\text{PNAM}_x]_a$ with $>65\%$ grafting density, I then aimed for producing comb $[\text{PNAM}_x]_a$. I named the compounds “comb” since they possess less grafting density (50% and 25%) than the brushes (Figure 2.13). I postulated that the brushes with side chains of less than 50% of the backbone would have a more flexible structure due to less steric repulsion between the side chains. For this type of

BBPs, I created new backbone precursors, composed of random copolymers of HEAm and NAM 1:1, and 1:3 to provide 50% and 25%, respectively, functional groups (Scheme 2.6). Since only HEAm has the reactive hydroxyl groups, this approach will ensure the expected grafting density by targeting 100% conjugation of CTAs to all units of HEAm.



Scheme 2.6 General synthesis of $\text{P(HEAm-co-NAM)}_{b\%,a}$

2.3.4.1 Synthesis of backbone $\text{P(HEAm-co-NAM)}_{b\%,a}$

First, I studied the kinetics of RAFT polymerization of $\text{P(HEAm-co-NAM)}_{b\%,a}$, targeting a total DP (HEAm + NAM units) of 500 and ratio of HEAm/NAM 1:1 (HEAm 50%). The conversions of both HEAm and NAM were determined by following the integration in ^1H NMR signal of crude reaction at δ (ppm) 5.70 and 5.50, which corresponds to the signal of NAM and HEAm, respectively, compared to the signal of DMF, the internal standard (Figure 2.14). The polymerization was stopped at a conversion of $\sim 94\%$, which was achieved in 2.5 h. Both monomers showed pseudo-first-order kinetics with HEAm demonstrating a slightly lower polymerization rate than NAM (Figure 2.15). In a polymerization of two monomers with different reactivity, one of the monomers will be consumed faster than the other, causing a segment in the chain that is dominated by that monomer.¹⁴⁸ It is then followed by an attenuation of the monomer. Due to the depletion of the first monomer, the second monomer was then inserted to a greater extent, resulting in a segment rich in this monomer. This is called a gradient copolymer, which I assumed slightly happen to the $\text{P(HEAm}_x\text{-co-NAM}_y\text{)}_{x\%,a}$.

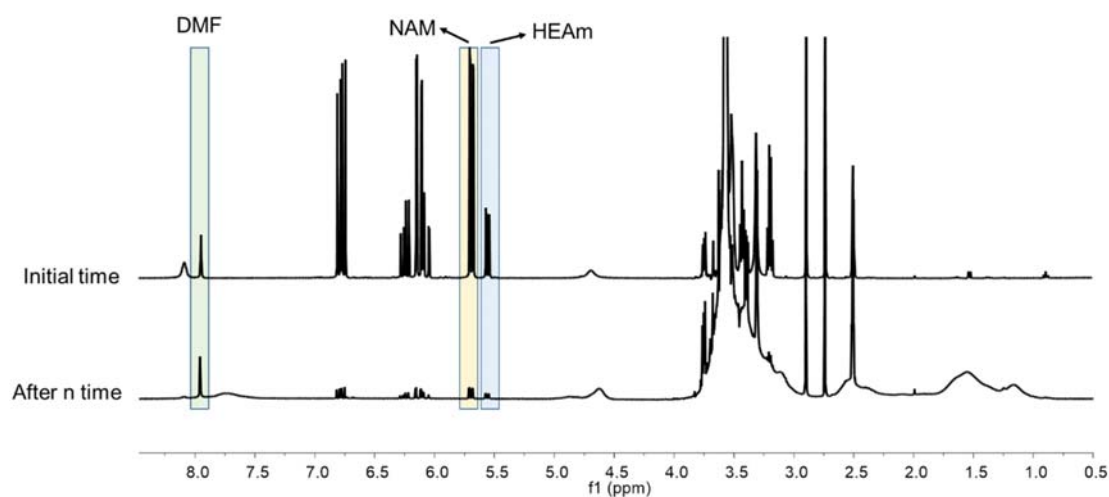


Figure 2.14 ^1H NMR peak used to calculate monomer conversion by comparing DMF signal and monomer signal at the initial time and at the stopped reaction time. Samples were dissolved in d_6 -DMSO. Images were obtained from the reaction with $[\text{NAM}]/[\text{HEAm}]$ 3:1.

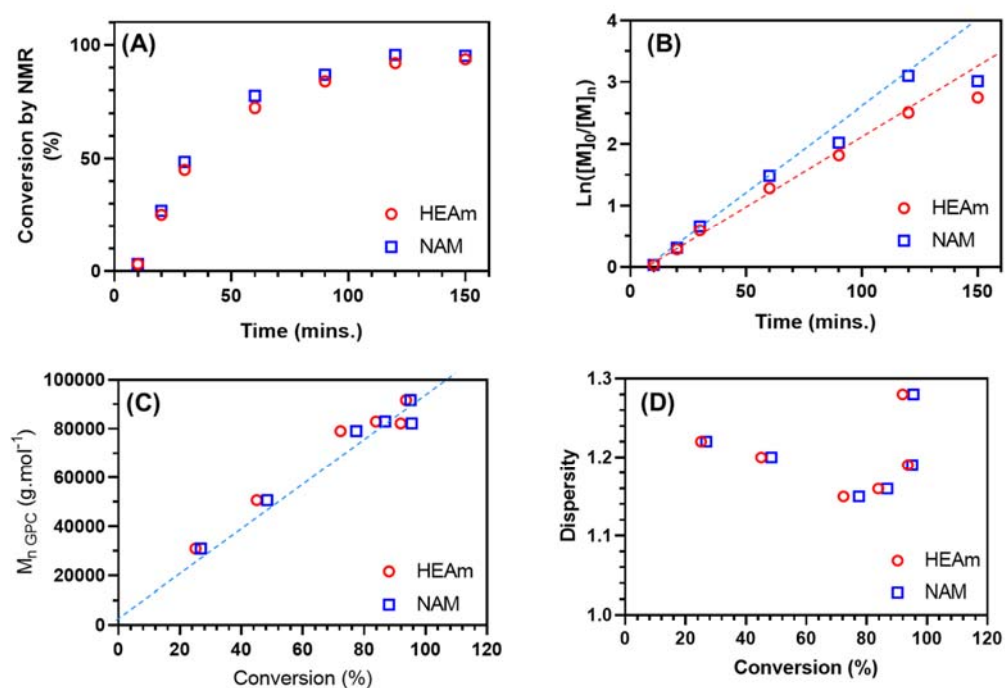


Figure 2.15 Reaction kinetics and molar mass evolution of $P(\text{HEAm-co-NAM})_{50\%,500}$ at 70°C in dioxane/water 1:1, $\text{CTA:I} = 8:1$, $[\text{HEAm} + \text{NAM}] = 2\text{M}$.

Based on the kinetics study, I then reproduced the backbone DP500 with 50% of HEAm and then produced backbone DP150 with 50% and 25% HEAm. Interestingly, while a mixture of dioxane-water is required in the polymerization of HEAm:NAM 1:1 to avoid precipitation of the polymer, single solvent dioxane is enough for the reaction of HEAm:NAM 1:3. This is because the hydrophilic –OH groups of HEAm is now less significant than NAM units.

All backbones were purified by precipitation in cold acetone. The GPC analysis of the pure compounds demonstrated narrow dispersities (<1.20), as shown in Table 2.5 and Figure 2.16. The representative ^1H NMR spectra of the pure polymer showed similarity with PHEAm_a with an additional significant peak at δ (ppm) 2.80-4.00, which corresponds to the morpholine ring of NAM (Appendix, Figure A.5).

Table 2.5 M_n and \bar{D} values of polymers as determined by DMAc-GPC analysis with polystyrene standard

Description	Approx. DP total of backbone	$M_{n,\text{theory}}$ (kDa) ^a	$M_{n,\text{GPC}}$ (kDa) ^b	Dispersity (\bar{D}) ^c
P(HEAm-co-NAM) _{50%,500}	500	67.2	91.7	1.19
P(HEAm-co-NAM) _{50%,150}	150	21.7	45.3	1.12
P(HEAm-co-NAM) _{25%,150}	150	22.7	36.0	1.15

^a Molecular weight obtained by calculation of conversion by ^1H NMR

^b Molecular weight obtained from DMAc-GPC

^c Dispersity of polymers, obtained from DMAc-GPC, which represents M_w/M_n

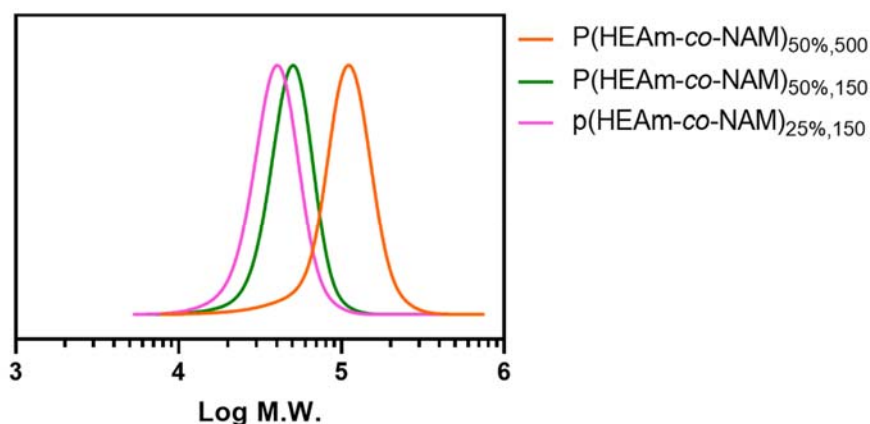
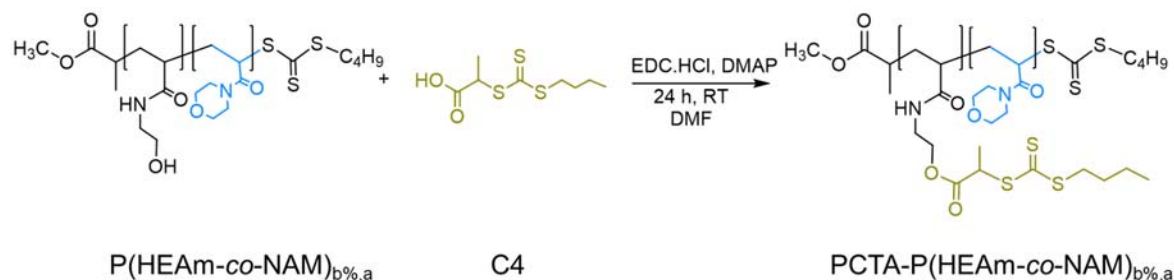


Figure 2.16 Overlay of GPC-chromatograms of all produced P(HEAm-co-NAM)_{b%,a}

2.3.4.2 Synthesis of PCTA-P(HEAm-co-NAM)_{b%,a}



Scheme 2.7 General synthesis of PCTA-P(HEAm-co-NAM)_{b%,a}

Subsequently, using the same approach as in PCTA-PHEAm_a, I created PCTA-P(HEAm-co-NAM)_{b%,a} (Scheme 2.7). GPC analysis revealed that all produced polyCTAs showed narrow dispersity (Table 2.6 and Figure 2.17, $\bar{D} < 1.20$). While I targeted a functionalisation degree of 50% and 25%, analysis by ^1H NMR spectra of the purified compounds confirmed slightly lower functionalisation degree of 42%, 41% and 17% for PCTA-P(HEAm-co-NAM)_{50%,500}, PCTA-P(HEAm-co-NAM)_{50%,150} and PCTA-P(HEAm-co-NAM)_{25%,150}, respectively. This low functionalisation degree ensures that the brushes produced from these backbone precursors will have less side-chain density. The representative ^1H NMR with the peak assignments can be seen in Figure A.6.

Table 2.6 M_n and \bar{D} values of PCTA-P(HEAm-co-NAM)_{b%,a} as determined by DMAc-GPC analysis with polystyrene standard

Description	$M_{n,\text{theo}}$ (kDa) ^a	$M_{n,\text{GPC}}$ (kDa) ^b	Dispersity (\bar{D}) ^c	%CTAs in backbone ^d
PCTA-P(HEAm-co-NAM) _{50%,500}	126.4	123.1	1.17	42
PCTA-P(HEAm-co-NAM) _{50%,150}	41.1	51.3	1.16	41
PCTA-P(HEAm-co-NAM) _{25%,150}	30.8	38.6	1.14	17

^a Molecular weight obtained by calculation of conversion by ^1H NMR

^b Molecular weight obtained from DMAc-GPC

^c Dispersity of polymers, obtained from DMAc-GPC, which represents M_w/M_n

^d Fraction of C4 units per chain of backbone

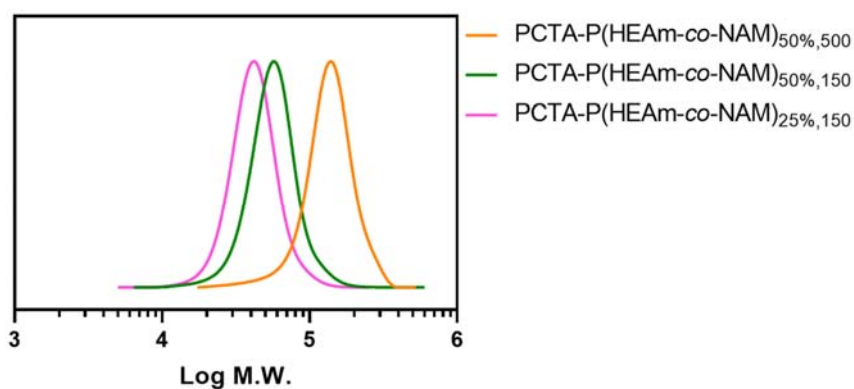


Figure 2.17 Overlay of GPC-chromatograms of all produced $\text{PCTA-P(HEAm-co-NAM)}_{b\%,a}$

2.3.4.3 Synthesis of Brush $[\text{PNAM}_{50}]_{b\%,a}$

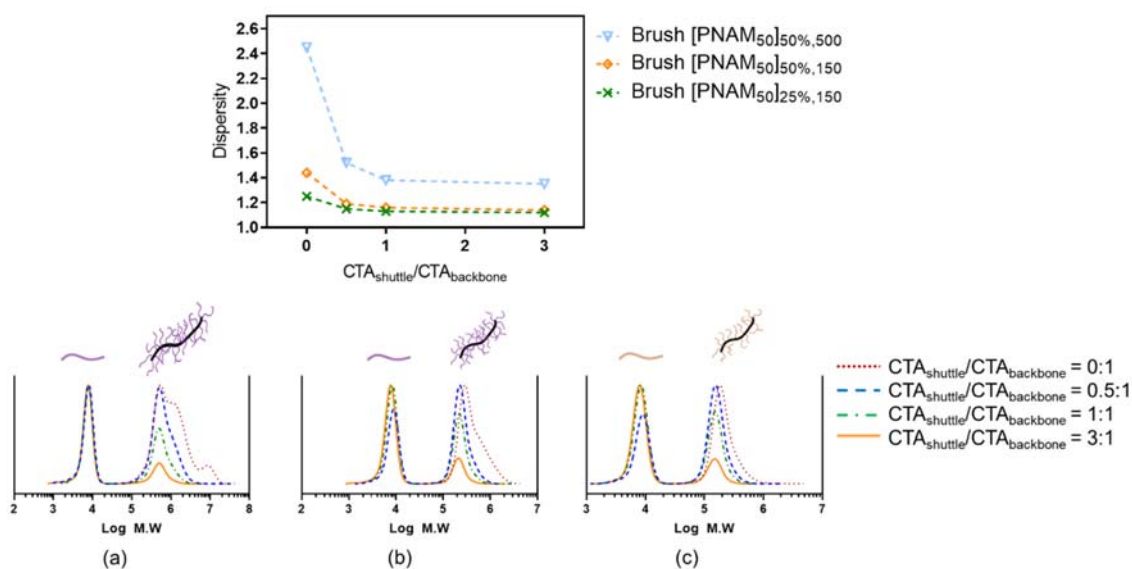


Figure 2.18 (Upper panel) Effect of $\text{CTA}_{\text{shuttle}}/\text{CTA}_{\text{backbone}}$ on the dispersity of brushes with grafting density <50% and (lower panel) GPC chromatogram of (a) brush $[\text{PNAM}_{50}]_{50\%,500}$ (b) brush $[\text{PNAM}_{50}]_{50\%,150}$ (c) brush $[\text{PNAM}_{50}]_{25\%,500}$

Following the production of $\text{PCTA-P(HEAm-co-NAM)}_{b\%,a}$, I synthesized the brushes with grafting density <50%. Using the same CTA-shuttle R-group approach, I also optimized the effect of the ratio of $\text{CTA}_{\text{shuttle}}/\text{CTA}_{\text{backbone}}$ on the grafting from process. First, I hypothesized

that the shuttle-CTA required for brushes with <50% grafting density would be less since the distance between the grafted side chains were greater, and thus, the steric hindrance is minimal. However, the results indicated a similar trend with the previous brush [PNAM₅₀]₁₅₀ and brush [PNAM₅₀]₅₀₀. Brush [PNAM₅₀]_{50%,150} and brush [PNAM₅₀]_{25%,150} required a minimum of 0.5 equivalents of shuttle-CTA, resulting in brushes with \bar{D} <1.20, the same as brush [PNAM₅₀]₁₅₀ (Figure 2.18). On the other hand, brush [PNAM₅₀]_{50%,500} requires a minimum of 3 equivalents of shuttle-CTA, as in brush [PNAM₅₀]_{50%,500}, in order to maintain low dispersity. A more detailed result is shown in Table 2.7, and the full ¹H NMR spectra with peak assignment is shown in Figure A.7 (Appendix).

Table 2.7 Results from varying the ratio of CTA_{shuttle}/CTA_{backbone} for the synthesis brush [PNAM_x]_{b%,a}. All reactions were done in DMF with [M] = 2 M, 70°C, 1.5h.

Reaction	Brush	CTA _{backbone} ^a : CTA _{shuttle} ^b	Conv. ^c (%)	M _{n,theo} ^d (kDa)	M _{n,GPC} ^e (kDa)		Dispersity ^f (\bar{D})		Fraction ^g (%)	
					Brush	Linear	Brush	Linear	Brush	Linear
1	[PNAM ₅₀] _{50%,500}	1:0	98.03	1,545	653.2	-	2.45	-	100	-
2		1:0.5	97.27	1,516	501.7	6.5	1.52	1.19	62	38
3		1:1	98.57	1,545	462.8	6.9	1.38	1.11	46	54
4		1:3	97.86	1,516	412.4	6.4	1.35	1.17	23	77
5	[PNAM ₅₀] _{50%,150}	1:0	98.32	515	189.0	-	1.25	-	100	-
6		1:0.5	98.10	515	151.7	7.7	1.15	1.14	59	41
7		1:1	97.62	515	144.7	7.5	1.13	1.12	43	57
8		1:3	97.17	506	138.9	7.2	1.12	1.10	20	80
9	[PNAM ₅₀] _{25%,150}	1:0	98.35	230	342.4	-	1.44	-	100	-
10		1:0.5	98.35	230	228.4	7.8	1.19	1.12	60	40
11		1:1	98.97	230	214.7	7.4	1.16	1.13	43	57
12		1:3	97.70	226	197.9	6.7	1.14	1.14	21	79

^a Free C4 added to the reaction

^b C4 in the backbone

^c Percentage of monomers which are converted into polymers

^d Molecular weight obtained from ¹H NMR based on conversion

^e Molecular weight obtained from DMAc-GPC

^f Dispersity of polymers, obtained from DMAc-GPC, which represents M_w/M_n

^g Ratio between the area under curve of brush peak and linear polymer peak in GPC chromatogram

2.3.5 Synthesis of Brush [PnBA_y-b-PNAM_x]_a

Having been able to produce low dispersity BBPs with side chains made of homopolymer NAM, I then intended to create BBPs with diblock side chains, which consists of *n*-butyl acrylate (nBA) as the first block (hydrophobic core layers) and NAM as the second

block (hydrophilic outer layer) (Figure 2.19). The hydrophobic core was introduced to increase the backbone's rigidity and to provide compartments that can be used to entrap hydrophobic drugs. The hydrophilic layers are required to ensure their water solubility since my BBPs are intended for use as a drug carrier.

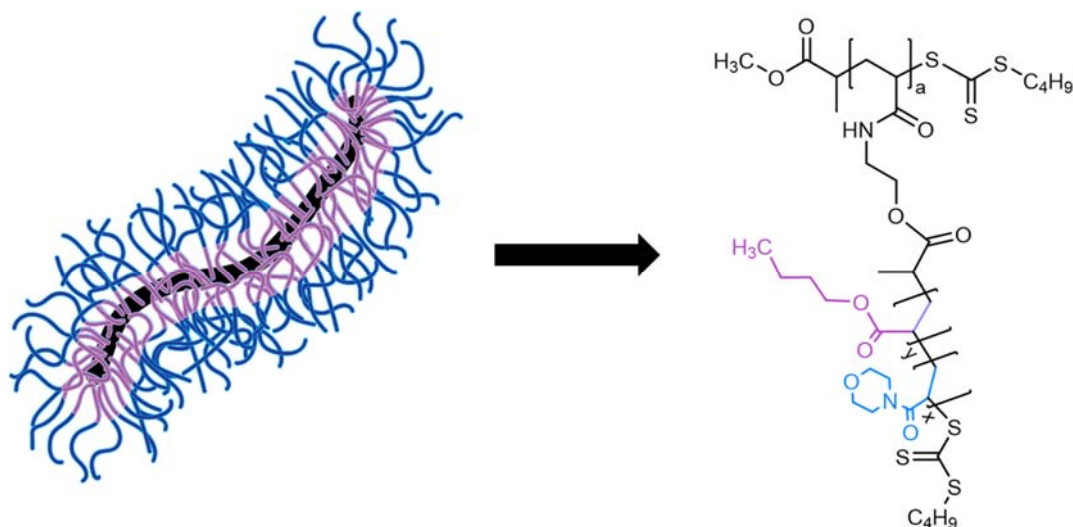
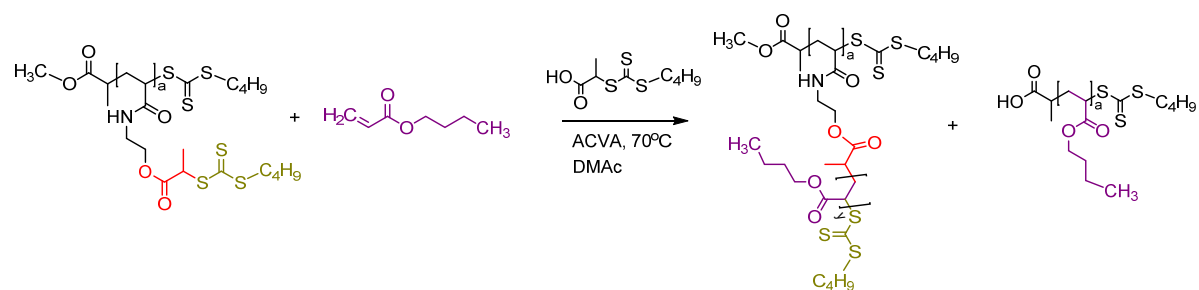


Figure 2.19 Illustration of BBPs with a hydrophobic core

2.3.5.1 Synthesis of Brush [PnBA_y]_a



Scheme 2.8 General reaction scheme for grafting of nBA from PolyCTAs.

To produce brushes with nBA core, I employed PCTA-PHEAm₁₅₀ and PCTA-PHEAm₅₀₀ as backbone precursors. The general reaction scheme of the synthesis is shown in Scheme 2.8. First, I tried the grafting of nBA from PCTA-PHEAm₅₀₀ and studied the polymerization

kinetics using ratio of $CTA_{\text{shuttle}}/CTA_{\text{backbone}}$ 1:1 (Table 2.8, BA1). For the kinetics study, I targeted DP50 of nBA chains for 100% conversion to investigate the polymerization profile. The polymerization was found to show a short induction period (less than 10 minutes), and achieved around 84% conversion after 90 minutes. Interestingly, the polymerization followed pseudo-first-order kinetics until 66% conversion, which was achieved within 45 minutes (Figure 2.20C). After that conversion, the evolution of the molecular weight showed significant broadening with dispersity >2.0 , which is also represented by multimodality in GPC chromatogram (Figure 2.20A and B).

Table 2.8 Summary of all reactions of brush [PnBA_y]_a. All reactions were done in DMAc with [M] = 2.6 M, 70°C

Reaction code	Brush Name	Initial DP	$CTA_{\text{shuttle}}/CTA_{\text{backbone}}$	Time	Conversion	DP achieved	$M_{n, 1H\ NMR}$ (kDa)	M_n GPC (kDa)	\bar{D}
BA1	[PnBA ₄₂] ₅₀₀	50	1:1	90 min	84%	42	2,183	624	>2.0
BA2	[PnBA ₃₈] ₅₀₀	50	1.5:1	90 min	76%	38	1,988	427	1.88
BA3	[PnBA ₁₄] ₅₀₀	20	3:1	45 min	80%	14	823	271	1.37
BA4	[PnBA ₁₂] ₅₀₀	20	3:1	30 min	60%	12	725	220	1.33
BA5	[PnBA ₁₄] _{150-A}	20	1:1	30 min	69%	14	306	98	1.25
BA6	[PnBA ₁₄] _{150-B}	30	3:1	30 min	46%	14	306	105	1.11

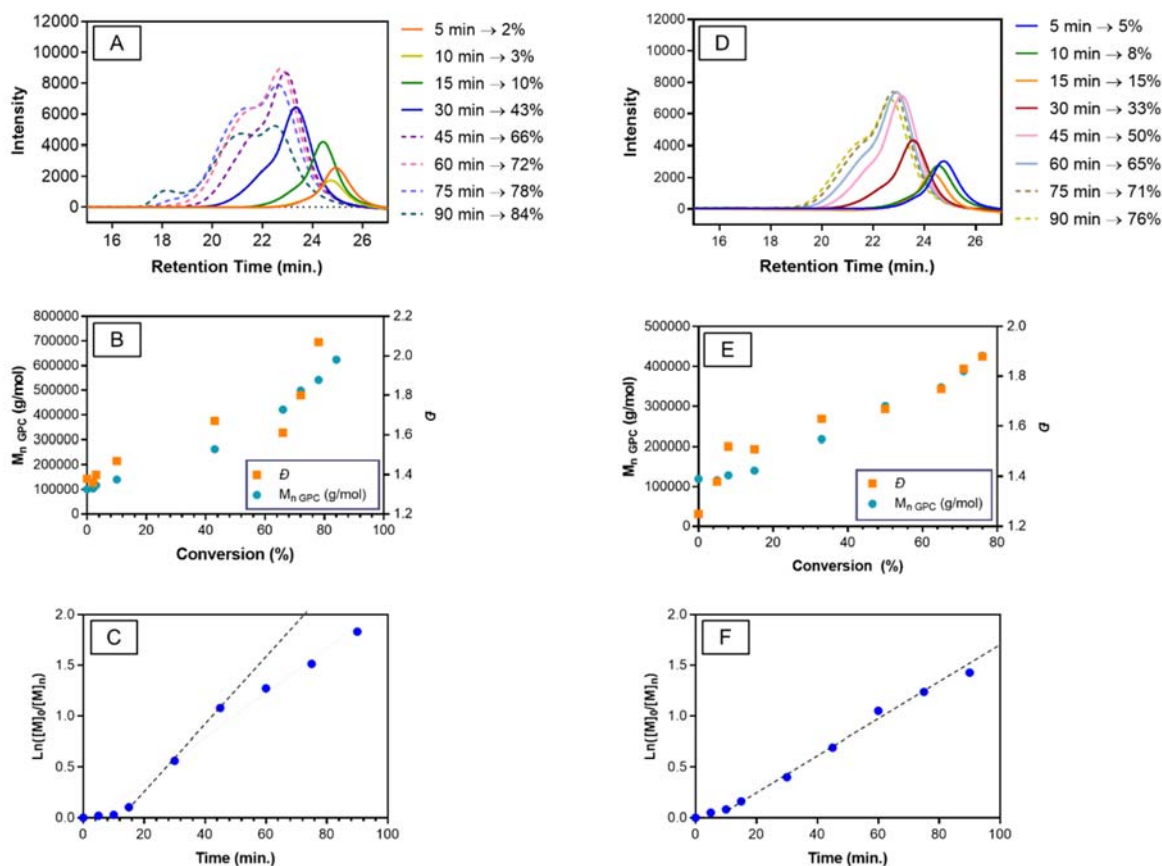


Figure 2.20 Kinetics plots of the synthesis of brush $[PnBA_y]_{500}$ via "CTA-shuttled" R-group approach. Evolution of GPC chromatogram with time for the reaction with CTA_{shuttle}/CTA_{backbone} 1:1 (A) and 1.5:1 (D). Development of M_n GPC and \bar{D} with conversion for reaction with CTA_{shuttle}/CTA_{backbone} 1:1 (B) and 1.5:1 (E). Pseudo first order plot for reaction with CTA_{shuttle}/CTA_{backbone} 1:1 (C) and 1.5:1 (F).

When I increased the CTA_{shuttle}/CTA_{backbone} to 1.5:1 (Table 2.8, BA2), the pseudo-first-order kinetics are more visible until 90 minutes reaction, achieving ~76% conversion (Figure 2.20F). However, despite the broad molecular weight distribution ($\bar{D} < 2.0$), the GPC chromatogram still showed monomodality (Figure 2.20D). I then increased the ratio of CTA_{shuttle}/CTA_{backbone} to 3:1 and studied the kinetics (Table 2.8, BA3). With this condition, the pseudo first-order kinetics is even more pronounced, and the reaction could reach 80% conversion while maintaining the dispersities < 1.40 and monomodality in GPC chromatogram (Figure 2.21). These results indicated that increasing the ratio of CTA_{shuttle}/CTA_{backbone} could improve the control of radical polymerization of nBA grafting.

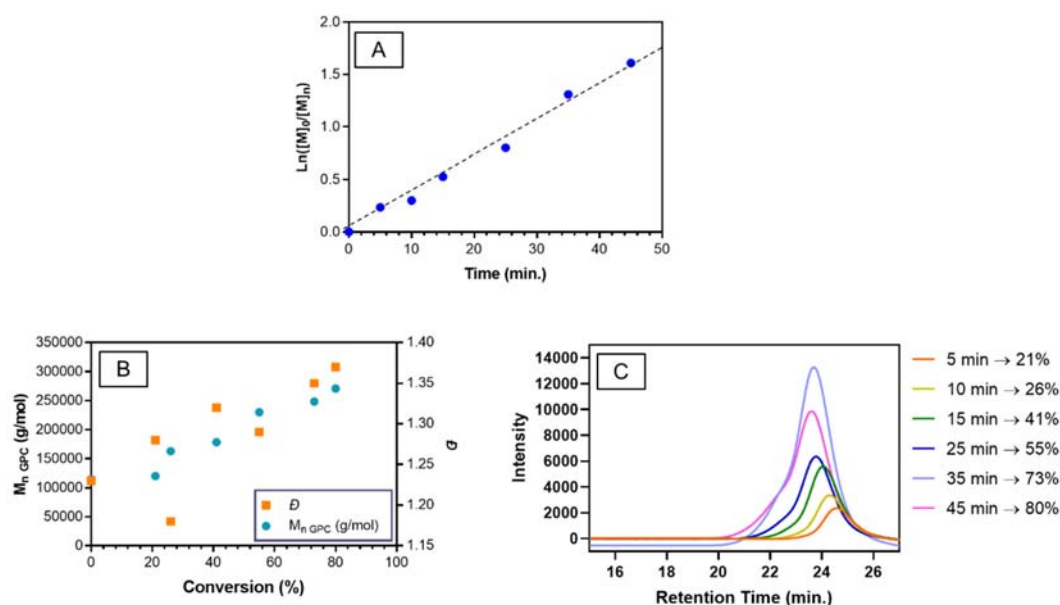


Figure 2.21 Kinetics plots of the synthesis of brush $[BA_y]_{500}$ via “CTA-shuttled” R-group approach using $CTA_{shuttle}/CTA_{backbone}$ 3:1. (A) Pseudo-first-order plot. (B) Development of $M_{n, GPC}$ and \bar{D} with the conversion. (C) Evolution of GPC chromatogram with time.

By adapting the reaction condition from the kinetics studies, I then produced brush $[PnBA_y]_{150}$ and brush $[PnBA_y]_{500}$ as precursors for brush $[PnBA_y-b-PNAM_x]_a$. The arms of the brush were designed to have 10-15 units of n-butyl acrylate as the first block and 35-40 units of NAM as the second block to make the total DP of side chains around 50, similar to brush $[PNAM_x]_a$. In order to obtain brushes with low \bar{D} value, in addition to using $CTA_{shuttle}/CTA_{backbone}$ 3:1, I also increased the initial DP to target lower conversion (Table 2.8, BA4). The reaction was stopped at 30 minutes, achieving 60% conversion. As a result, I could produce brush $[BA_{13}]_{500}$, having $\bar{D} = 1.33$.

For brush $[PnBA_y]_{150}$, I first performed a reaction with $CTA_{shuttle}/CTA_{backbone}$ 1:1 (Table 2.8, BA5), which I expected to be enough to yield brushes with $\bar{D} < 1.20$, since it started with a shorter backbone precursor as in brush $[PNAM_{50}]_{150}$. However, the resulting brush $[PnBA_y]_{150}$ showed broader dispersity ($\bar{D} = 1.25$) than brush $[PNAM_{50}]_{150}$ ($\bar{D} = 1.17$) even at 69% conversion. Therefore, I modified the reaction again by increasing the initial DP to target lower

conversion and the ratio of $CTA_{\text{shuttle}}/CTA_{\text{backbone}}$ to 3:1. This condition resulted in low conversion (46%), with significantly lower dispersity ($\mathcal{D} = 1.10$).

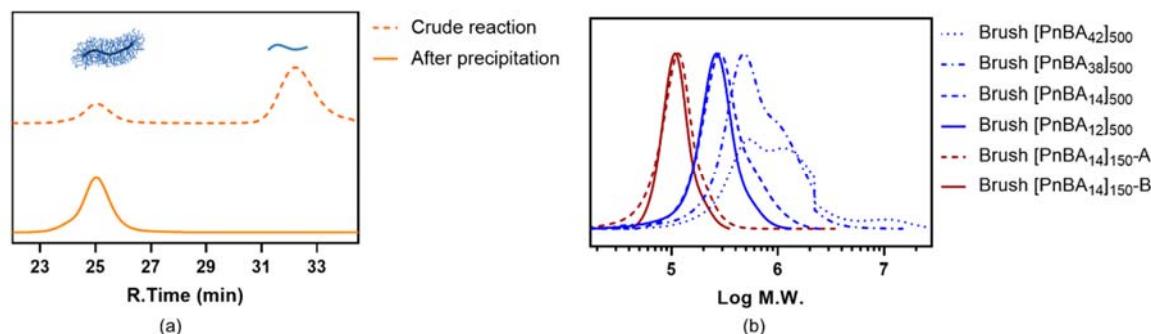
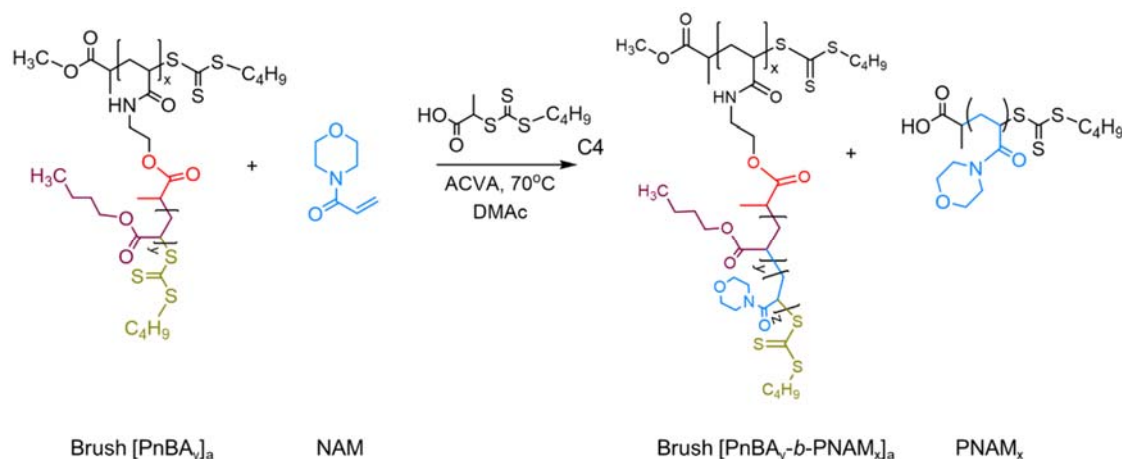


Figure 2.22 (a) Representative evolution of GPC chromatogram of brush [PnBA_y]_a before and after precipitation in methanol and (b) Overlay of GPC chromatograms of all produced brush [PnBA_y]_a.

In conclusion, the polymerization of nBA in grafting-from technique via RAFT polymerization showed different behaviour to NAM. The conversion must be kept low (under 60%) to maintain low dispersity. Maintaining the low dispersity of brush [PnBA_y]_a is essential as it will undergo further chain extension. Since the conversion is low, the purification of this compound is important to avoid any leftover nBA monomers that might interfere with the subsequent block polymerization. Therefore, I isolated the polymers from the crude reaction by precipitation in cold methanol. This method is able to remove the unreacted nBA monomers as well as the shuttle-CTA-derived linear poly-nBA. This was confirmed by the GPC chromatogram, which only showed one peak after precipitation (Figure 2.22a). The GPC chromatogram of all brush [PnBA_y]_a from all experiments are shown in Figure 2.22b, and the representative ¹H NMR spectra of the purified brush is shown in Figure A.8.

2.3.5.2 Synthesis of Brush [PnBA_y-*b*-PNAM_x]_a



Scheme 2.9 General reaction of brush [PnBA_y-*b*-PNAM_x]_a

I subsequently extended the nBA side chains from brush [PnBA₁₄]₁₅₀ with hydrophilic NAM. Since the shuttle-CTA (C4) was already eliminated from the previous reaction, fresh shuttle-CTA was added using a ratio of CTA_{shuttle}/CTA_{backbone} 3:1 (Scheme 2.9). Based on the analysis of ¹H NMR result, 90% of NAM monomers were incorporated to the brushes in 30 minutes, producing brush [PnBA₁₄-*b*-PNAM₃₅]₁₅₀ with narrow molecular weight distribution (\mathcal{D} = 1.11). Similar reaction conditions were employed to graft NAM from brush [PnBA₁₂]₅₀₀, producing brush [PnBA₁₂-*b*-PNAM₄₁]₅₀₀ with surprisingly low dispersity (\mathcal{D} = 1.19). The resulting brush [PnBA_y-*b*-PNAM_x]_a polymers were purified by precipitation in acetone, as in brush [PNAM_x]_a, resulting in brushes with monomodal GPC chromatograms (Figure 2.23). The representative ¹H NMR spectra of [PnBA_y-*b*-PNAM_x]_a is shown in Figure A.9 (Appendix).

Table 2.9 Summary of reaction of brush [PnBA_y-*b*-PNAM_x]_a. All reactions were done in DMAc with [M] = 2 M, 70°C, 30 minutes

Reaction code	Backbone	Initial DP	CTA _{shuttle} /CTA _{backbone}	Conversion	DP achieve	M _n GPC (kDa)	\mathcal{D}
BA-NAM-150	[PnBA ₁₄] ₁₅₀	40	3:1	90%	36	221	1.10
BA-NAM-500	[PnBA ₁₂] ₅₀₀	45	3:1	90%	41	488	1.19

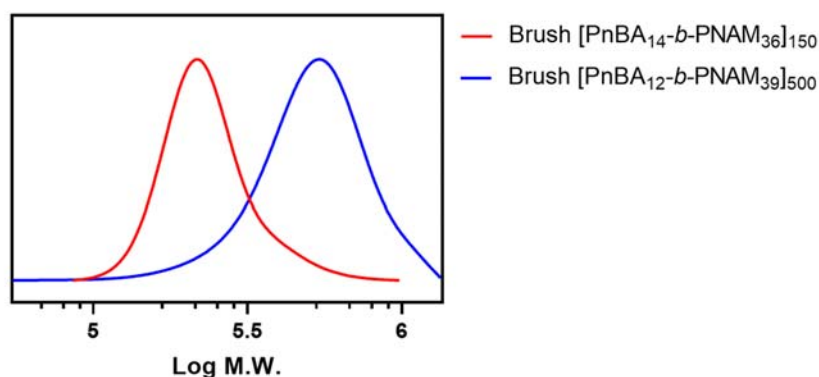


Figure 2.23 Overlay of GPC chromatograms of all produced brush $[PnBA_y-b-PNAM_x]_a$.

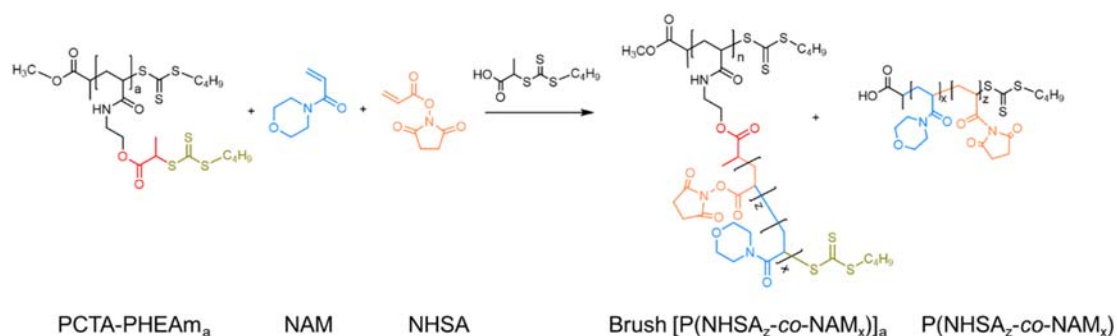
2.3.6 Synthesis of Brush $[P(NHSA_z-co-NAM_x)]_a$

In addition to having a narrow molecular weight distribution, sometimes it is necessary that the brushes have some functional groups for biological application. These functional groups will facilitate covalent attachment of passenger molecules such as drugs, targeting moieties and labelling molecules, especially when molecule entrapment is unfavourable. Since my previously produced brush $[PNAM_x]_a$ and brush $[PnBA_y-b-PNAM_x]_a$ do not possess any functional groups, I aimed to incorporate the groups into the brush structure.

Incorporation of glycidyl methacrylate into the polymer structure has been reported in some studies.^{62,149,150} The epoxy groups were proven to be versatile for post-functionalisation. However, these epoxy groups require further treatment to become more reactive before they can be used for molecule attachment, for example reaction with propargylamine or 5-hexynoic acid¹⁴⁹. Another approach is by incorporation of 7-oxanorbornenyl bromide (ONBr).⁸⁸ However, the bromide required azide substitution prior to molecules conjugation.

Herein, I incorporated acrylic acid *N*-hydroxysuccinimide ester (NHSA) into the brush structure to provide functionalities. The *N*-hydroxysuccinimide (NHS), together with 1-ethyl-3-(3-dimethylaminopropyl)carbodiimide hydrochloride (EDC), is recognised as the most common bioconjugation technique in use. Their effectiveness to conjugate proteins to polymeric nanoparticles has been extensively reported.¹⁵¹⁻¹⁵³ The conjugation reaction typically involved

the coupling reaction between EDC and carboxylic groups, followed by the coupling with NHS to produce NHS ester intermediate, which is more effective at reacting with amine molecules compared to EDC alone.¹⁵⁴ This two-step reaction can be waived using the commercially available and ready-to-use NHS ester, such as NHS-acrylic acid.



Scheme 2.10 General synthesis of brush [P(NHSA_z-co-NAM_x)]_a

The general synthesis of brush [P(NHSA_z-co-NAM_x)]_a is similar to the previous brushes, where shuttle-CTAs were added (Scheme 2.10). Backbone PHEAm₁₅₀, PHEAm₅₀₀, PHEAm_{50%,150}, PHEAm_{25%,150} and PHEAm_{50%,500} were used to create this type of BBPs. The NHSA monomers were copolymerized with NAM. I only targeted approximately 2-3 units of NHSA per side chain, which is enough to provide functionality. The amount of NHSA incorporated into the brush structure was confirmed by calculating the monomer conversion in ¹H NMR spectra. All produced brushes showed satisfactory characteristic with narrow molecular weight distribution, $\mathcal{D} < 1.25$ (Figure 2.24 and Table 2.10). The full ¹H NMR spectra are shown in Figure A.10 (Appendix).

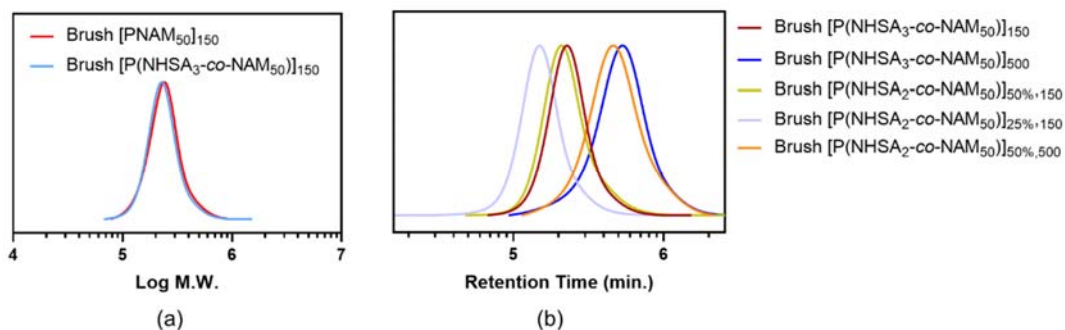


Figure 2.24 (a) Representative comparison between BBPs with and without NHSA (b) overlay of GPC chromatogram of all produced NHSA-functionalized BBPs

Table 2.10 GPC characteristic of the produced NHSA-functionalized BBPs synthesized via CTA-shuttle R-group approach at 70°C, $[M] = 2 \text{ M}$, $\text{CTA}_{\text{backbone}}/\text{CTA}_{\text{shuttle}} 3:1$, $\text{CTA}_{\text{total}}/I 8:1$, $t=90 \text{ minutes}$.

Brush	$M_{n,\text{Theo}}$ (kDa)	$M_{n,\text{GPC}}$ (kDa)	\bar{D}
$[\text{P}(\text{NHSA}_3\text{-co-NAM}_{50})]_{150}$	1,053	221	1.12
$[\text{P}(\text{NHSA}_3\text{-co-NAM}_{50})]_{500}$	2,570	465	1.22
$[\text{P}(\text{NHSA}_2\text{-co-NAM}_{50})]_{25\%,150}$	232	145	1.14
$[\text{P}(\text{NHSA}_2\text{-co-NAM}_{50})]_{50\%,150}$	519	210	1.15
$[\text{P}(\text{NHSA}_3\text{-co-NAM}_{50})]_{50\%,500}$	1,643	434	1.21

2.3.7 Morphology of BBPs

Atomic force microscopy (AFM) was used to establish the morphology and size of the produced BBPs. Images were extracted using Gwyddion software.¹⁵⁵ Table 2.11 summarizes the approximate size of the major axis (length) and minor axis (diameter) of the BBPs. The average length and diameter, as well as size distribution data, were generated using Fiji ImageJ¹⁵⁶ by manually selecting the region of interests (ROI). The manual selection method was chosen, instead of applying the threshold, in order to differentiate between brush particles that are partially stacked over the others.

Table 2.11 Summary of BBPs size obtained by analysis of AFM images using FIJI ImageJ

Brush	Major axis length (nm)	Minor axis length (nm)	Aspect ratio
[PNAM ₅₀] ₁₅₀	41±7	13±2	3±1
[PNAM ₅₀] _{50%,150}	33±4	15±2	2±0.3
[PNAM ₅₀] _{25%,150}	30±7	13±3	2±1
[PNAM ₅₀] ₅₀₀	131±32	24±6	6±2
[PNAM ₅₀] _{50%,500}	108±24	33±7	3±1

As shown in Figure 2.25A and Table 2.11, brush [PNAM₅₀]₁₅₀ demonstrated a rod-like structure with a dimension of 41×13 nm, resulting in an aspect ratio (the ratio between length and diameter of the brushes) of ~3. This aspect ratio value is twice higher than is expected from the ratio of $DP_{\text{backbone}}/(2 \times DP_{\text{side chain}})$ (150/100, aspect ratio 1.5). This is probably due to repulsion among the side chains, causing the backbone to stretch and establish longer size than theoretical value. Brush [PNAM₅₀]₅₀₀, brush with longer backbone, showed worm-like structure with dimension of 131×24 nm and aspect ratio of ~6 (Table 2.11 and Figure 2.25D). Unlike brush [PNAM₅₀]₁₅₀, the aspect ratio value of brush [PNAM₅₀]₅₀₀ is similar to the theoretical value based on ratio of $DP_{\text{backbone}}/(2 \times DP_{\text{side chain}})$ (500/100, aspect ratio 5). This is probably caused by slightly less grafting density of brush [PNAM₅₀]₅₀₀ compared to [PNAM₅₀]₁₅₀ (85% vs 70%, respectively), which resulted in less steric repulsion between side chains, and thus, less backbone stretching. Interestingly, despite the similar DP of side chains, the diameter of brush [PNAM₅₀]₁₅₀ is almost twice shorter than [PNAM₅₀]₅₀₀ based on measurement of AFM images. I suggested that this is also due to different grafting density (different inter-side chain steric repulsion) between both brushes, causing distinct flattening of the particles when they were deposited on mica.

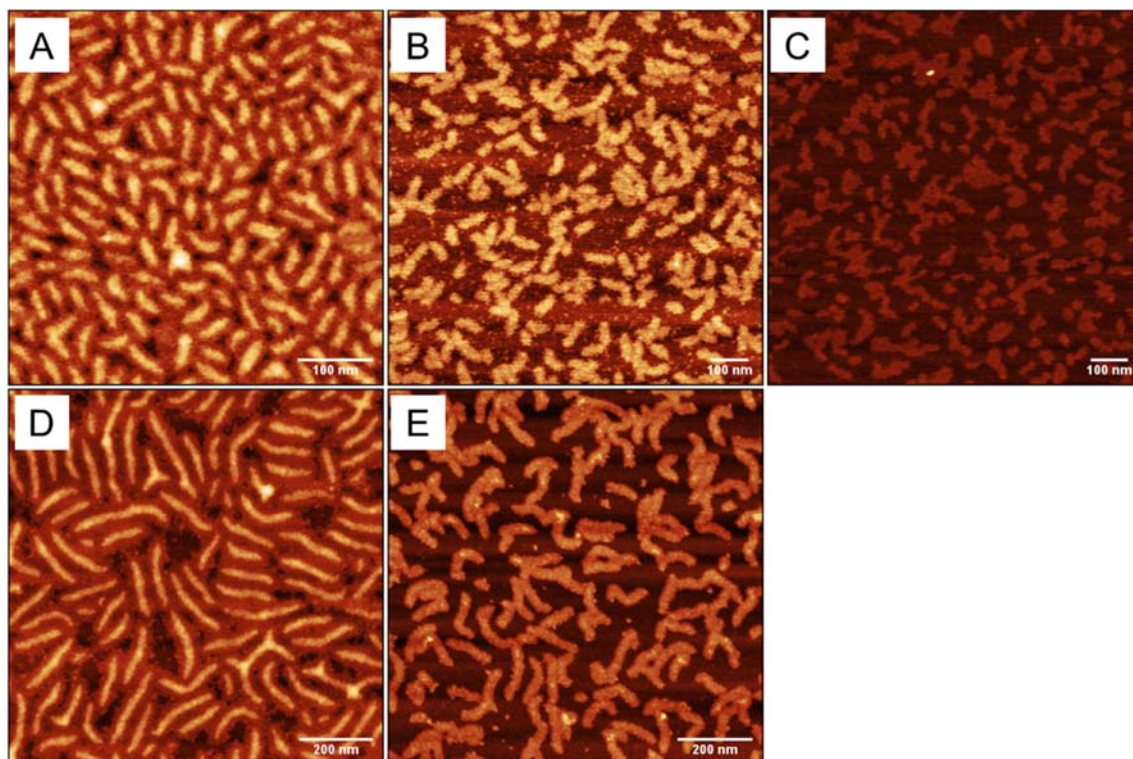


Figure 2.25 AFM images of BBPs on mica, air-dried from chloroform: A. brush [PNAM₅₀]₁₅₀, B. brush [PNAM₅₀]_{50%,150}, C. brush [PNAM₅₀]_{25%,150}, D. brush [PNAM₅₀]₅₀₀, and E. brush [PNAM₅₀]_{50%,500}.

The dimension of [PNAM₅₀]_{50%,150}, [PNAM₅₀]_{25%,150} and [PNAM₅₀]_{50%,500} are 33×15 nm, 30×13 nm, and 108×33 nm, respectively. However, analysing the size of brushes with a grafting density 50% or less is challenging due to the more curved structures and the tendency to agglomerate, making it harder to determine the boundaries and ROI of each particle. Therefore, the obtained dimension of [PNAM₅₀]_{50%,150}, [PNAM₅₀]_{25%,150} and [PNAM₅₀]_{50%,500} might not be accurate. For example, in brush [PNAM₅₀]_{50%,150} (Figure 2.25B), the structures look more curved than [PNAM₅₀]₁₅₀ despite the similar cylindrical architecture. This particularly more obvious in [PNAM₅₀]_{25%,150} with a less-defined structure (Figure 2.25C). The discrepancy of appearance on mica is also shown by [PNAM₅₀]₅₀₀ and [PNAM₅₀]_{50%,500} (Figure 2.25D and E, respectively), where [PNAM₅₀]₅₀₀ demonstrated a stiffer structure than [PNAM₅₀]_{50%,500}. The detail on ROI selection, height analysis and particle size distribution graph of each compound is shown in Figure A.14 - Figure A.18 (Appendix).

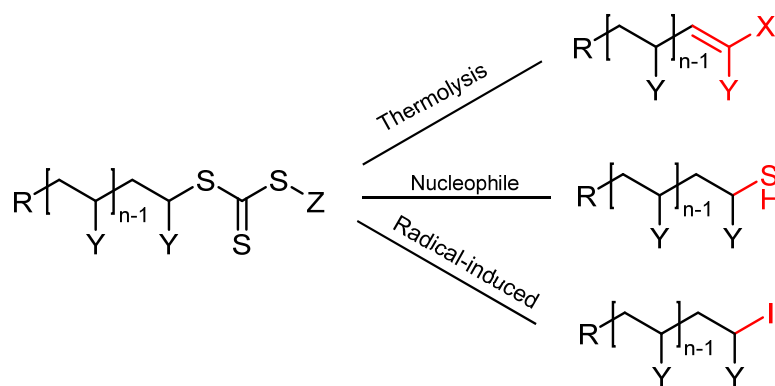
In conclusion of particle size analysis by AFM, all brushes demonstrated an elongated structure, with grafting density affected their appearance on mica. It is clearly visible that decreasing grafting density resulted in a more flexible structure. This visualisation by AFM might also reflect their conformation in solution, although the size might be slightly different. To obtain the exact size of the brushes, performing other technique might be required, for example, using small-angle X-ray scattering (SAXS).

2.3.8 Brush End Group Modification

2.3.8.1 Radical-Induced Substitution (Brush X-ACVA)

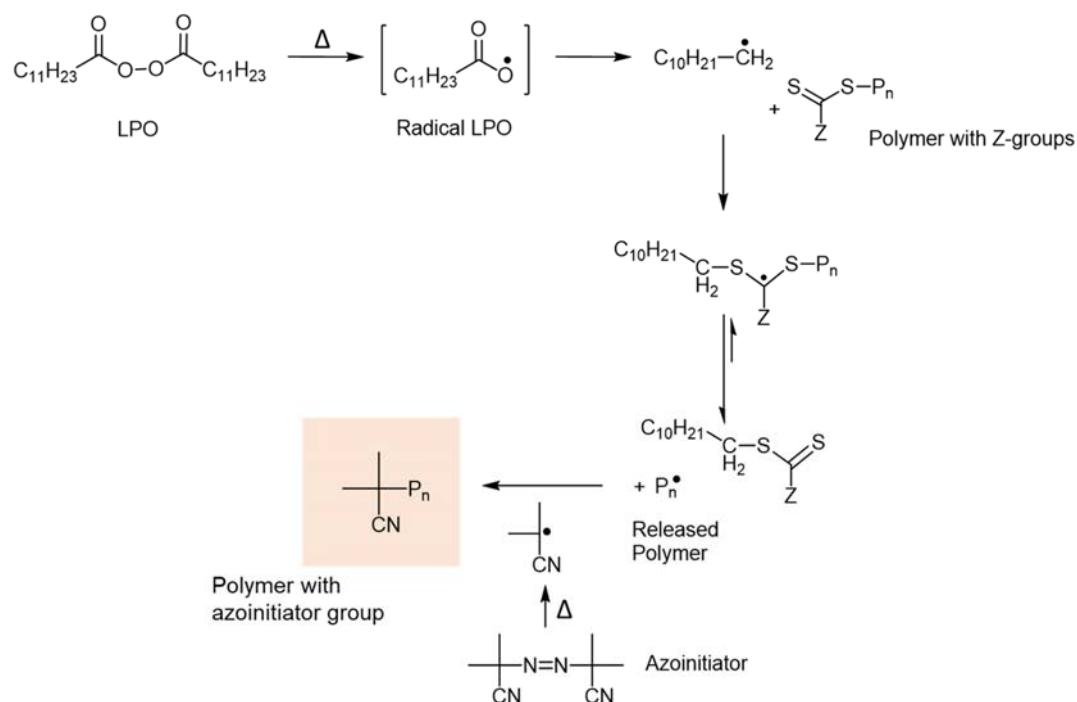
Despite having successfully produced a library of NHSA-functionalized NAM-based BBPs with narrow molecular weight distribution, I found an issue in their solubility in water. Although the BBPs consist of hydrophilic NAM as a component of side chain, they were surprisingly not water-soluble. This insolubility issue makes them not suitable for any systemic medical application.

In RAFT polymerization, the process involves the insertion of monomers between R- and Z-groups of RAFT agents.¹¹⁸ Therefore, the majority of the produced polymer chains will contain R- and Z-groups at each chain's end. In the process of grafting-from using RAFT polymerization R-group approach, the R-group of CTAs will be at the end of side chains, which tether to the backbone, while the Z-group of CTAs will be at the end of side chains, which orient to the surface (see the yellow dots in BBP illustration in Scheme 2.1). My CTAs, C4, possess a hydrophobic butyl group on the Z-part, which I postulated caused the poor water solubility of the BBPs. Therefore, I aimed to replace the Z-groups from the BBPs in order to make the BBPs more hydrophilic.



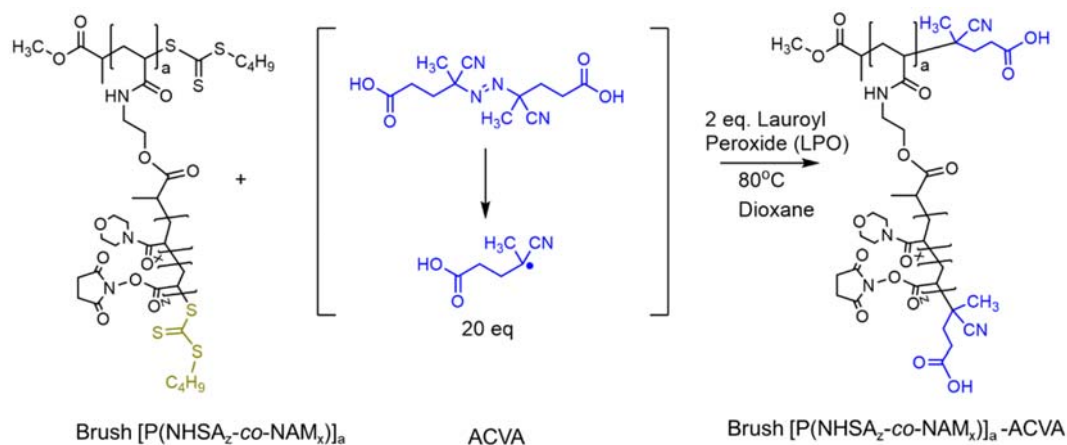
Scheme 2.11 The most commonly used techniques for removal of thiocarbonylthio groups from polymer chains (adapted from Willcock and O'Reilly¹⁵⁷)

Several techniques have been established to remove the retained Z-groups from the produced polymers with the most commonly used are thermal elimination, reaction with a nucleophile (aminolysis), and radical-induced substitution (Scheme 2.11).^{118,157} The thermal elimination (thermolysis) method offers the advantage of not involving reactants, and therefore minimising the complexity of the purification process. However, this method involves high temperature from 120-200°C and can degrade some functionalities in the polymer. The aminolysis method offers milder reaction conditions and generates reactive thiol end groups. These thiol end groups might be useful in many reactions, such as conjugation with drugs. However, they can create an intermolecular disulphide formation. Besides, the -SH group is less soluble in water and other polar solvents than their corresponding alcohols. The latter method, radical-induced substitution, involves a reaction of RAFT-derived polymers with an excess radical initiators¹⁵⁸, such as azoinitiator, under a temperature that is slightly higher than the decomposition temperature of the initiators. The molecules of the initiators will substitute the Z-groups in the polymers irreversibly and thus, ensure the removal of the thiocarbonylthio groups.



Scheme 2.12 Mechanism of reaction of Z-groups replacement by azoinitiator with LPO assistance (adapted from Chen et al.¹⁵⁹)

I chose the radical-induced substitution method to remove the Z-groups from the brushes due to simple preparation and reaction. I used 4,4'-azobis(4-cyanovaleric acid) (ACVA), an azoinitiator that generates radicals containing carboxylic groups. By introducing these carboxylic groups to the tip of the polymers, I hypothesized that the solubility of the BBPs in water would be improved. The addition of lauroyl peroxide (LPO) was proven to be able to obliterate the Z-group completely with minimal formation of bimodal molecular weight distributions¹⁵⁹. The role of LPO is as a "catcher" for the released thiocarbonylthio groups while the ACVA and polymers recombine (Scheme 2.12). The general reaction of RAFT Z-group replacement by ACVA is shown in Scheme 2.13.



Scheme 2.13 Representative RAFT end group removal in BBPs using radical-induced addition-fragmentation-coupling process

The modified BBPs were isolated by precipitation in diethyl ether. The successful RAFT Z-group removal was confirmed by the disappearance of C4 peak at δ (ppm) 0.89 (Figure 2.26), which means the Z-groups have been replaced by ACVA molecules. In addition, the peak from ACVA appears at δ (ppm) 1.88, which represents the proton from methyl groups. The physical appearance of the BBPs also changed from the typical yellow colour of trithiocarbonyl to white. UV-Vis spectrum analysis of the brushes before and after the end group removal showed the disappearance of trithiocarbonyl peak at λ_{max} 310 nm, even at significantly higher concentration (Figure 2.27). Following the successful Z-group removal, the NAM-based BBPs became water-soluble and thus more suitable for use in biological application (Figure 2.28).

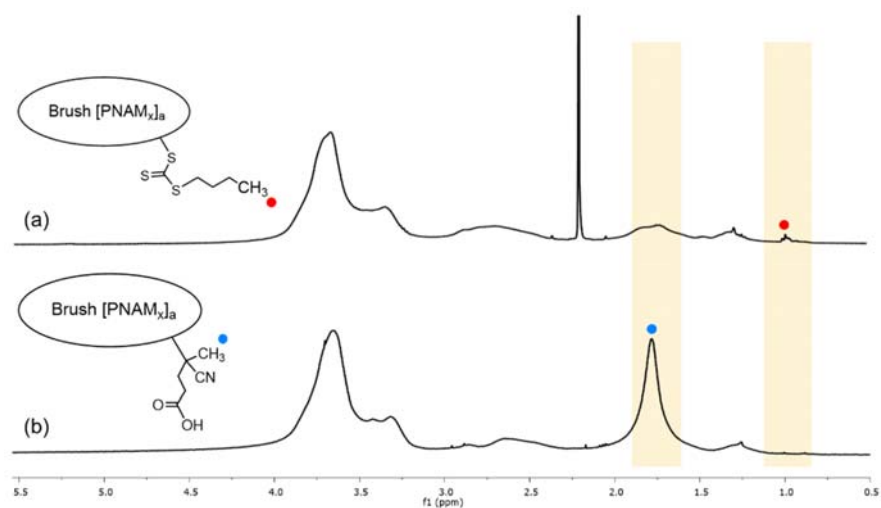


Figure 2.26 Representative ^1H NMR spectra of BBPs (a) before end group removal and (b) after end group removal performed in CDCl_3 . Images were obtained from Brush $\text{P}(\text{NHSA}_3\text{-co-NAM}_{50})_{500}$

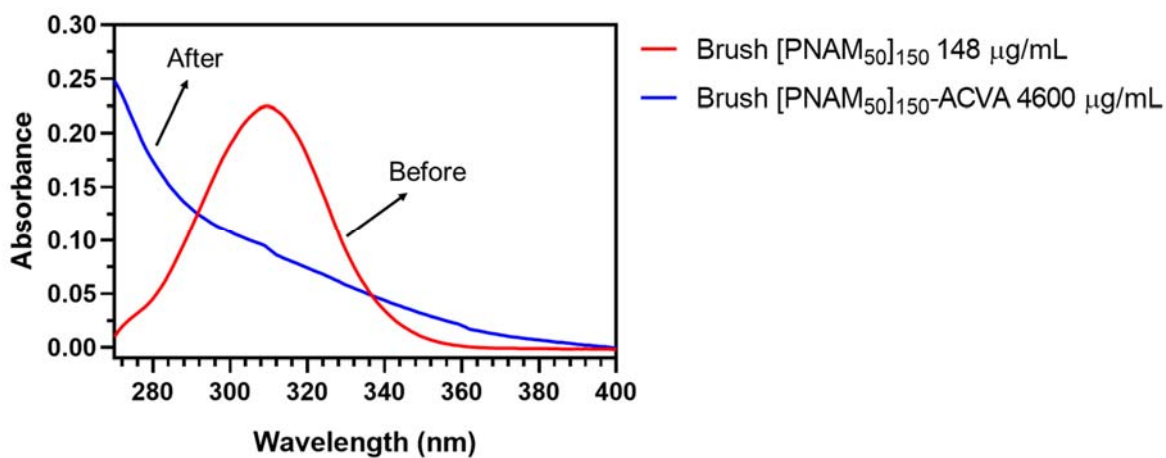


Figure 2.27 UV-Vis spectrum of brush $[\text{PNAM}_{50}]_{150}$ before and after radical induced end group removal

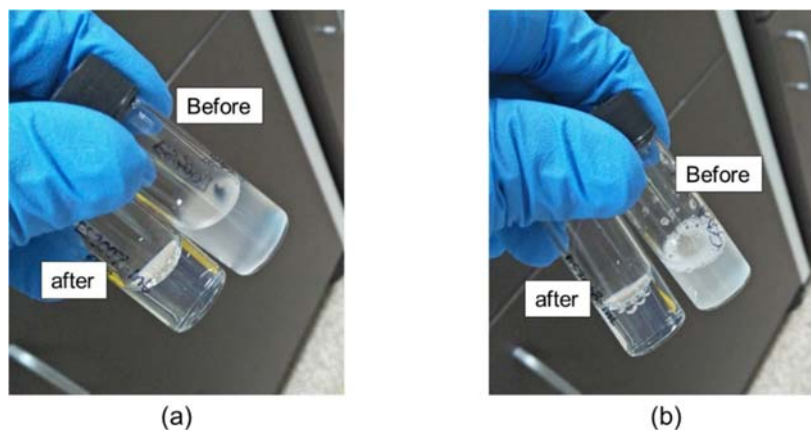


Figure 2.28 Brush (a) $[P(NHSA_3-co-NAM_{50})]_{150}$ and (b) $[P(NHSA_3-co-NAM_{50})]_{500}$ solution in PBS pH 7.4, before and after Z-group removal

The molecular weight of the brushes after ACVA substitution were only slightly higher from the original brushes (Figure 2.29a). This is because the molecular weight of the butyl carbonotrithioate of C4 (Z-groups) and the 4-cyanopentanoic acid of ACVA is only slightly different (166.32 vs 127.14 Da, respectively). I also noticed that the GPC chromatogram of brushes with ACVA showed additional high molecular weight component (shoulder at higher molecular weight) which caused higher dispersity (Table 2.12). This is probably because during the reaction, there were some intermolecular coupling reaction between brushes. Despite the higher dispersities, the overall GPC chromatograms of all BBPs still exhibited monomodal traces (Figure 2.29b).

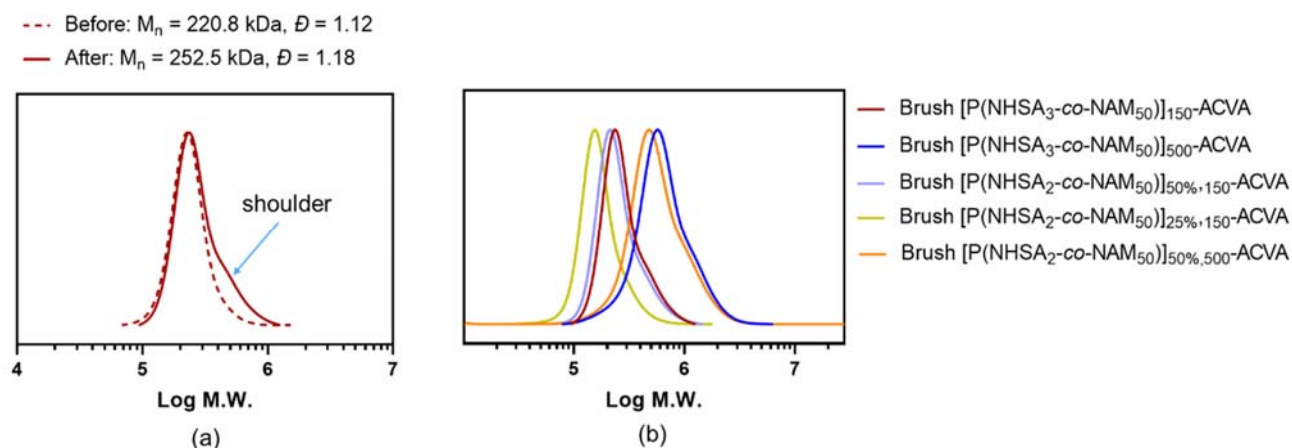


Figure 2.29 (a) Representative comparison of GPC chromatogram of BBPs before and after end group removal using radical-induced substitution method and (b) overlay of GPC chromatogram of all BBPs after end group removal.

Table 2.12 Molecular weight of all BBPs before and after Z-group removal using ACVA, analyzed by DMac-GPC

Brush	Before		After	
	$M_{n,GPC}$ (kDa)	\bar{D}	$M_{n,GPC}$ (kDa)	\bar{D}
[P(NHSA ₃ -co-NAM ₅₀)] ₁₅₀	221.8	1.12	252.5	1.18
[P(NHSA ₃ -co-NAM ₅₀)] ₅₀₀	465.8	1.22	536.9	1.35
[P(NHSA ₂ -co-NAM ₅₀)] _{25%,150}	144.8	1.14	156.2	1.18
[P(NHSA ₂ -co-NAM ₅₀)] _{50%,150}	210.8	1.15	227.6	1.20
[P(NHSA ₃ -co-NAM ₅₀)] _{50%,500}	433.7	1.21	467.6	1.38

2.3.8.2 RAFT Z-Groups Interchange

The drawback of employing the radical-induced substitution to modify the end groups of the BBPs is that the chains become dead, meaning that they will not be able to undergo further extension. This means incorporating other monomers after the modification is not possible. For this reason, I seek another way to modify the end groups while maintaining the livingness of the chains.

In the RAFT polymerization, the Z-groups of RAFT agent will simultaneously attach to and detach from the propagating chains. I then hypothesized that if two RAFT agents were

used in the reaction, the growing chains would contain a mixture of Z-group from both RAFT agents (Figure 2.30). While the polymerization is going on, both Z-groups will randomly move from one chain to another. With this hypothesis, I attempted to exchange the Z-groups in my brushes with the Z-groups of other RAFT agents. I call this approach as “Z-group interchange”.

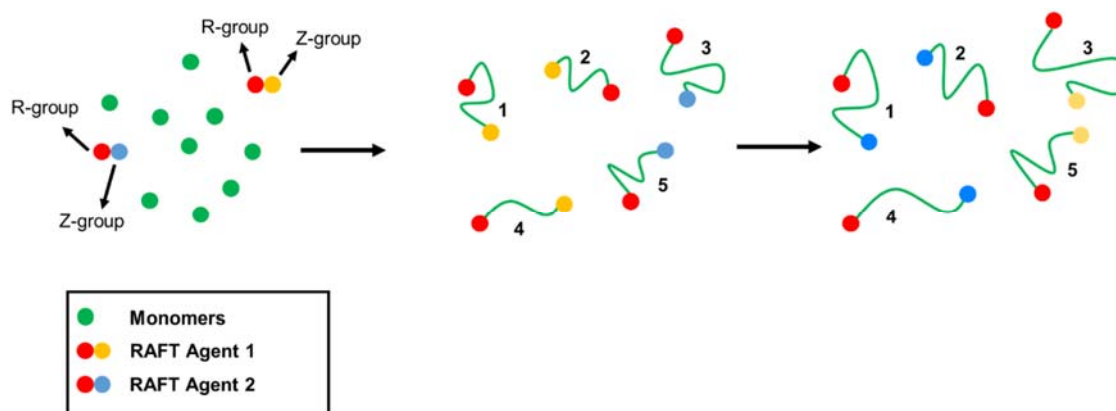


Figure 2.30 Proposed illustration of Z-group interchange in RAFT polymerization

The proposed mechanism of Z-group interchange in BBPs is as follows: when we conduct a reaction consists of the BBPs with their original Z-groups from C4, radical initiator and an excess amount of second RAFT agent, most of the original Z-groups in the brushes will be replaced by the Z-groups from the second RAFT agent (Figure 2.31 and Figure 2.32). With this approach, I can change the end groups of the brushes without losing their livingness.

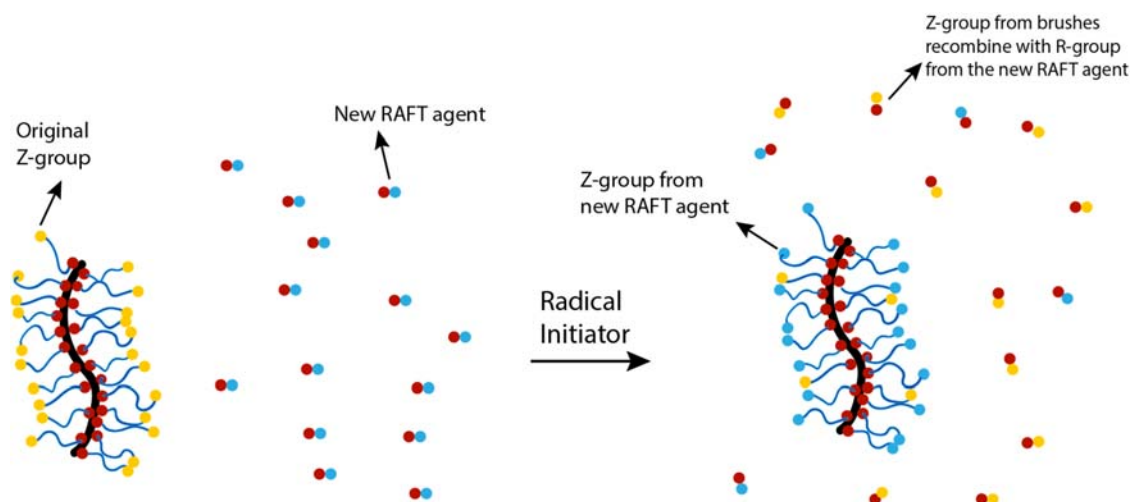


Figure 2.31 Illustration of Z-group interchange in BBPs

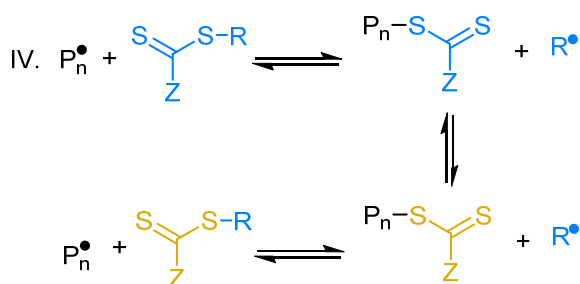
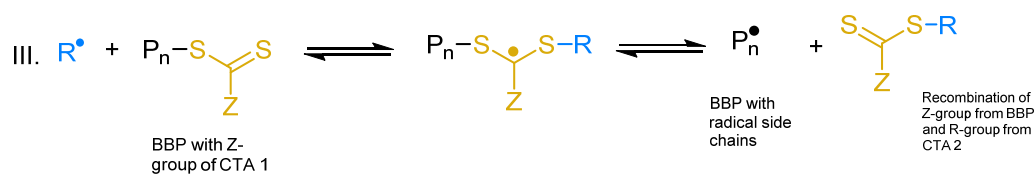
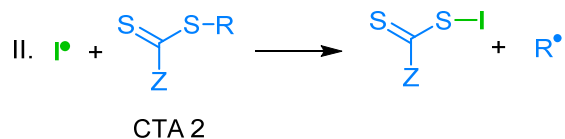


Figure 2.32 Proposed mechanism of Z-group interchange

Aiming to improve the water-solubility of my brushes while maintaining the livingness of the side chains, I then tested my hypothesis using 3-((((1-carboxyethyl)thio)

carbonothioyl)thio) propanoic acid (BM) as the new RAFT agent. The chemical structure of BM is similar to C4. The R-group of both RAFT agent is the same, which is carboxyethyl; however their Z-group is slightly different. While the Z-group of C4 contains butyl, the Z-group of BM contains propanoic acid. Therefore, it should be able to improve the aqueous solubility of the brushes when they are introduced on the tips of the brushes. In addition, the difference in both structures can be observed in ^1H NMR, which is essential to verify the successful Z-group interchange (Figure 2.33).

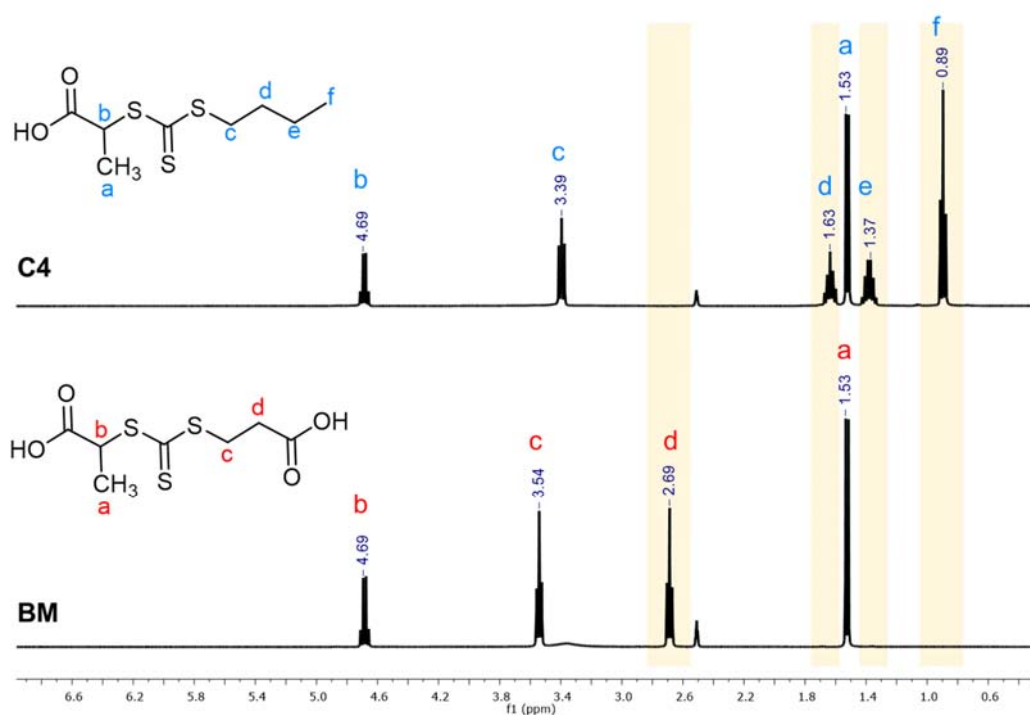
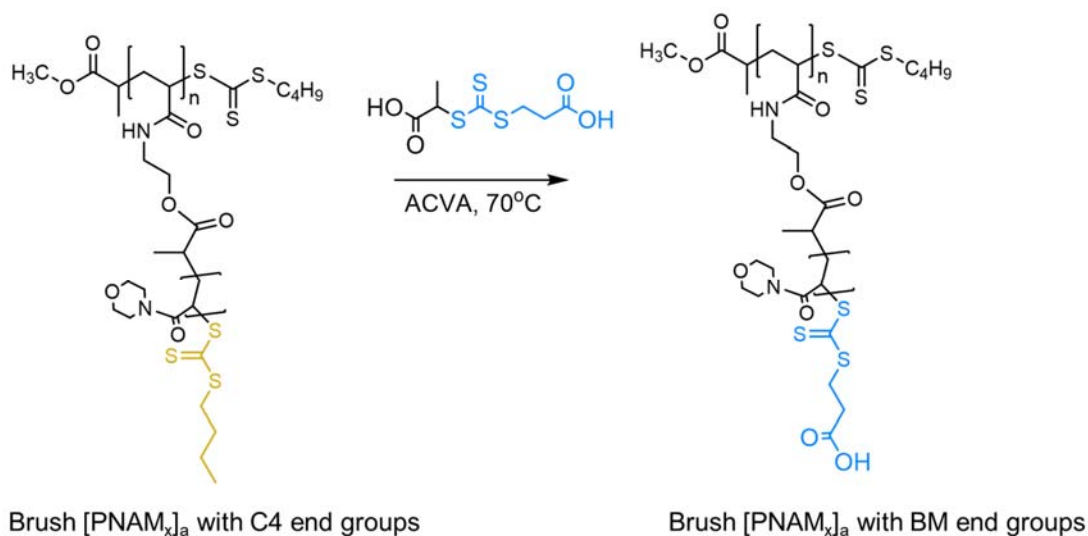


Figure 2.33 The chemical structure and distinguishable ^1H NMR spectra of C4 and BM



Scheme 2.14 General reaction scheme of Z-group interchange in BBPs

I conducted the Z-group interchange reaction in brush [PNAM₅₀]₁₅₀ and brush [PNAM₅₀]₅₀₀ (Scheme 2.14). The reaction involved 10 times molar excess of BM with respect to C4 units. The brush polymers were isolated from the crude reaction by precipitation in acetone prior to ¹H NMR analysis. Theoretically, if the Z-group interchange succeeded, I should be able to observe the appearance of peak at δ (ppm) 2.68, which corresponds to the proton adjacent to the carboxylic group from the Z-group of BM. I should also be able to notice that the peak at δ (ppm) 1.63, 1.37 and 0.89 from C4 disappear or reduce. However, due to the domination of the peak from backbone and side chain, the most noticeable change is only the disappearance of peak at δ (ppm) 0.89 (Figure 2.34).

It is possible that the molecules of ACVA used to induce the reaction will also be incorporated to the brush. If this happens, the intensity of UV-Vis absorbance of the brushes before and after interchange would change too. However, since the ACVA used was 100 times molar less than BM, I suggest the influence of incorporated ACVA could be neglected. On the other hand, the maximum wavelength (λ_{\max}) shown by the brushes before and after interchange must remain the same since C4 and BM are trithiocarbonyl compounds with the same typical λ_{\max} 310 nm. This is confirmed by the UV-Vis spectra depicted in Figure 2.35.

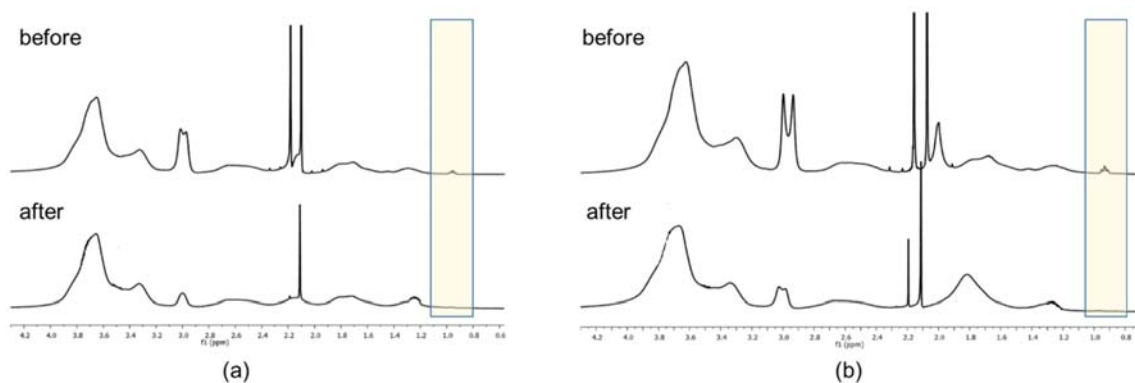


Figure 2.34 ^1H NMR spectra of brush (a) $[\text{PNAM}_{50}]_{150}$ and (b) $[\text{PNAM}_{50}]_{500}$, before and after Z-group interchange

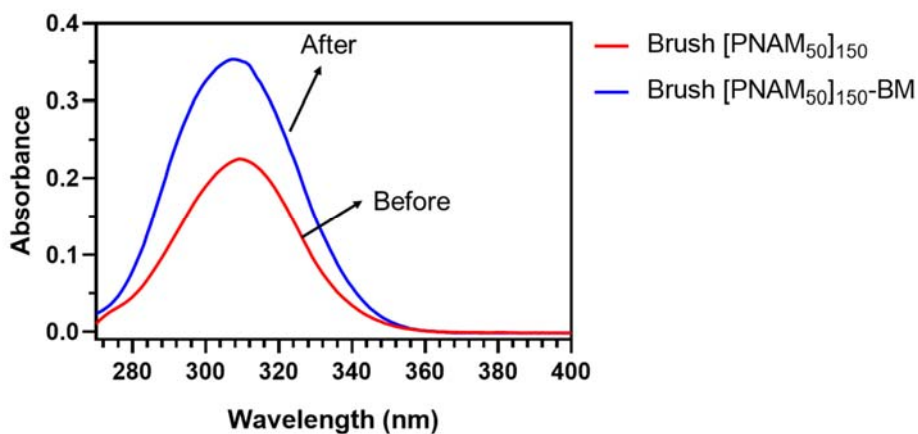
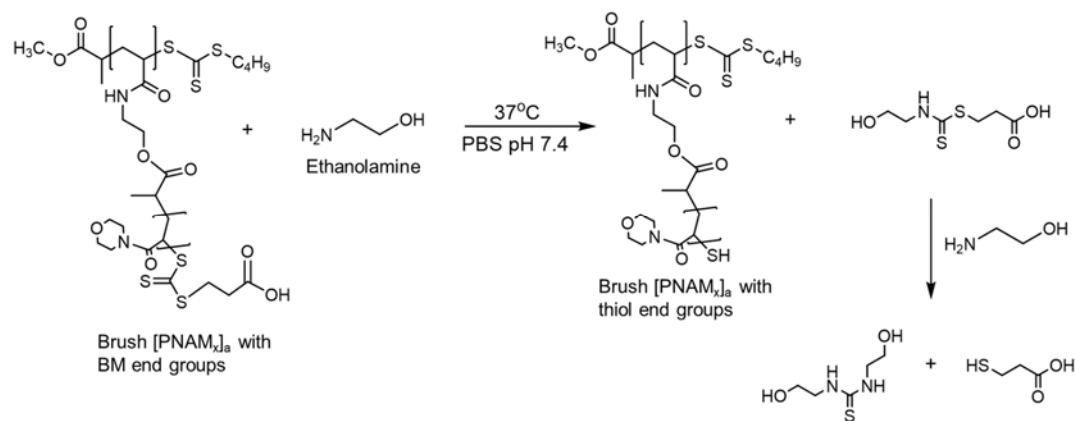


Figure 2.35 UV-Vis spectrum of brush $[\text{PNAM}_{50}]_{150}$ before and after Z-group interchange showing identical λ_{max} . Note that the concentrations of both compounds were different and therefore the absorbance are different too.

Since the interchanged brushes are supposed to have more charges because of the carboxylic groups, I then observed the zeta potential change. The zeta potential of brush $[\text{PNAM}_{50}]_{150}$ changed from -0.606 mV to -4.88 mV, while the zeta potential of brush $[\text{PNAM}_{50}]_{500}$ changed from -4.63 mV to -7.51 mV. I also observed a significant change in the aqueous solubility, as in the ACVA-modified brushes (brush X-ACVA). All these results might be considered as preliminary proof of my hypothesis on the proposed Z-groups interchange.

2.3.9 Stability of Z-groups

I have observed that the original Z-group of brushes can be exchanged with Z-groups from the new RAFT agent. In my case, the butyl groups of C4 were replaced by carboxylic groups of BM, and thus, the brushes become more soluble in water. The carboxylic groups on the tips of the brushes can also function as reactive groups for the attachment of small molecules. However, it has been known that the thiocarbonylthio groups are susceptible to aminolysis. They can be converted to a thiol (-SH) by primary or secondary amine.¹⁵⁷ For biological application, the thiol formation during blood circulation might cause unwanted behaviour since the thiol groups are very reactive. The most important thing to note: if the thiocarbonylthio groups in the polymers carry passenger molecules, such as drugs, then their detachment from the polymers is unfavourable as this will decline the function of the carrier and lead to unwanted drug release before they reach the pharmacological target. Therefore, I then conducted a study to investigate the stability of thiocarbonylthio groups in brush [PNAM₅₀]₅₀₀-BM. I dissolved the BBPs in PBS pH 7.4 and then incubated them at 37°C. The proposed possible aminolysis reaction is depicted in Scheme 2.15.



Scheme 2.15 Proposed possible aminolysis reaction of BBPs

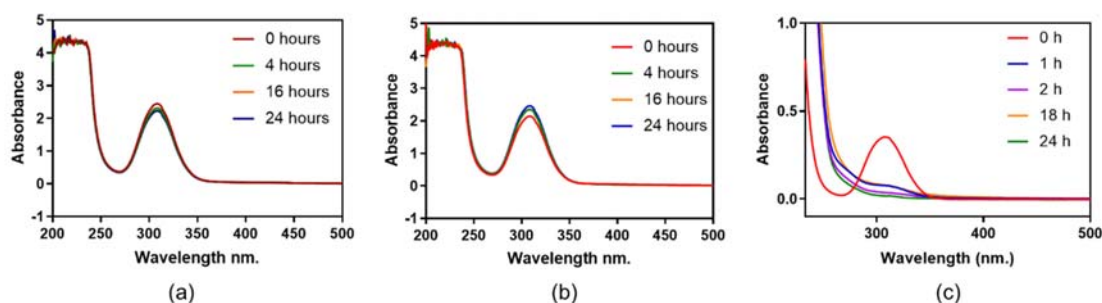


Figure 2.36 UV-Vis spectra of BBPs in (a) PBS pH 7.4, (b) PBS pH 7.4 + 1 eq. of ethanolamine to Z-groups and (c) PBS pH 7.4 + 20 eq. of ethanolamine to Z-groups

I analyzed the BBPs using UV-Vis at λ 310 nm, the typical wavelength of trithiocarbonyl RAFT agents, to observe whether the Z-groups remain. The control experiment (without ethanolamine treatment, Figure 2.36a) showed relatively unchanged UV-Vis spectra. In an environment where primary amine exists as much as 1 equivalent to the Z-groups in BBPs (Figure 2.36b), the Z-groups also remain in BBPs. Only when I increase the ethanolamine concentration 20 times (Figure 2.36c), I found that the UV spectra of the Z-groups disappear, indicating the degradation of the Z-groups.

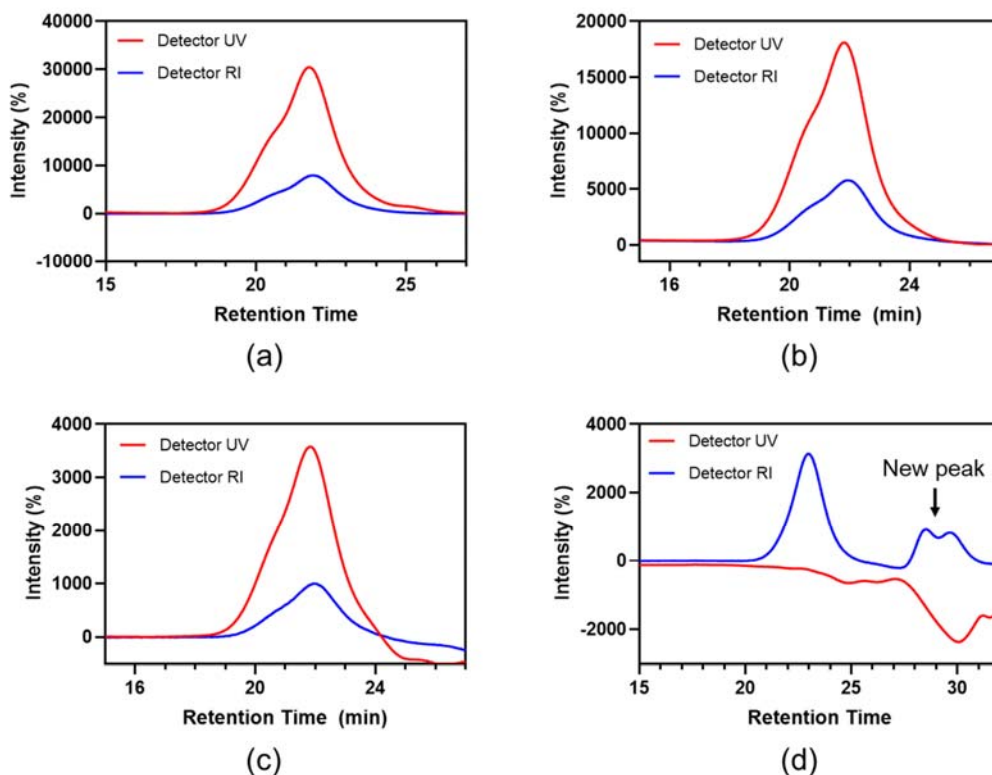


Figure 2.37 GPC chromatogram of (a) dry BBPs, (b) after incubation in PBS pH 7.4 (control), (c) after incubation in PBS pH 7.4 + 1 eq. of ethanolamine to Z-groups and (d) after incubation in PBS pH 7.4 + 20 eq. of ethanolamine to Z-groups.

The stability of the Z-groups was also confirmed by analysing the aliquot from 24 hours sample in GPC, using a refractive index (RI) detector and an ultraviolet (UV) detector at λ 310 nm (Figure 2.37). BBPs from control experiment and BBPs treated with 1 equivalent of ethanolamine showed overlaid UV-detected and RI-detected chromatogram, as in the original BBPs. These results indicated that the Z-groups remain in the brushes. For the BBPs treated with 20 equivalents of ethanolamine, the GPC chromatogram obtained from RI detector was still in place, while the chromatogram obtained from UV detector disappear (Figure 2.37d). Interestingly, there is a new peak appear at a longer retention time (lower molecular weight). This could be because some side chains, which are tethered to the backbone via an ester bond, were dislodged from the brushes due to the high concentration of ethanolamine. The

bimodal chromatogram of this new peak might be caused by the intermolecular disulphide bond formation between the detached side chains.

Based on the results from the stability study, I conclude that the Z-groups on the tips of the brushes are relatively stable. They only degraded after treatment with an excess of ethanolamine, which is unlikely to happen in the biological compartment. For example, the most prominent amine compounds in the body is neurotransmitters which include histamine, catecholamine and serotonin. Their level in blood are as low as ≤ 10 nmol/mL¹⁶⁰, 0.4-4.12 pmol/mL¹⁶¹ and 0.5-0.7 nmol/mL¹⁶², for histamine, catecholamine and serotonin, respectively. Therefore, I suggest that the Z-groups can remain in the brushes for biological application and can be utilised as a site of small molecule attachment such as drugs and targeting moieties.

2.3.10 Statistical Z-groups Interchange

2.3.10.1 Interchange in Brush [PNAM₅]₁₅₀

Based on the results from previous Z-groups interchange in the brushes, I then contemplated whether the interchange can occur statistically. What I mean with “statistically” is that the approximate proportion of Z-groups from C4 and Z-groups from BM in the final BBPs will be determined by the ratio of both compounds included in the reaction. For example, if I conducted the reaction with a ratio of BM/C4 1:1, then the end groups of the produced brush would contain Z-groups from BM and Z-groups from C4 with a ratio of 1:1 (Figure 2.38).

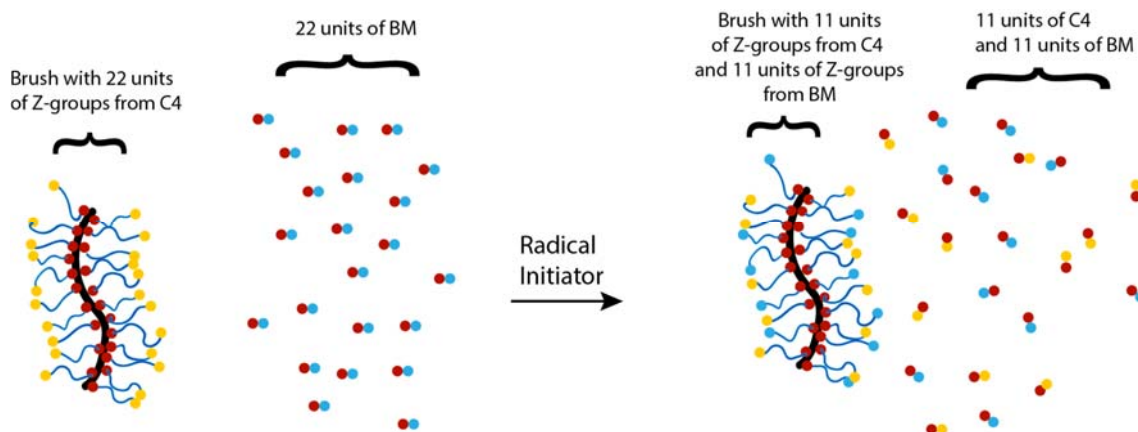


Figure 2.38 Proposed principle of Z-groups statistical interchange

To test my hypothesis, I investigated the Z-groups interchange by creating a model of BBP with short backbone (DP of 150) and short PNAM side chains (DP of 5) to minimize the domination of side chains peak in ^1H NMR spectra. I set up several reactions with a ratio of BM/C4 1:1, 5:1 and 10:1. Since the ^1H NMR spectra are distinguishable as depicted in Figure 2.33, I aimed to calculate the proportion of BM/C4 in the purified brushes by comparing the integration of the peak at δ (ppm) 2.68, which corresponds to one proton of BM and peak at δ (ppm) 0.89, which corresponds to three protons of C4. However, although the arms are short, the analysis on ^1H NMR is still challenging due to strong signals of the NAM arms at δ (ppm) 3.65, compared to both BM and C4. The peak at 2.68 was slightly evident in the brush $[\text{PNAM}_5]_{150}$ at BM/C4 10:1 (Figure 2.39). Although the interchange yield cannot be well calculated, I can observe the interchange by the decrease of the C4 signal at δ (ppm) 0.89 compared to NAM signal at 3.0-5.0.

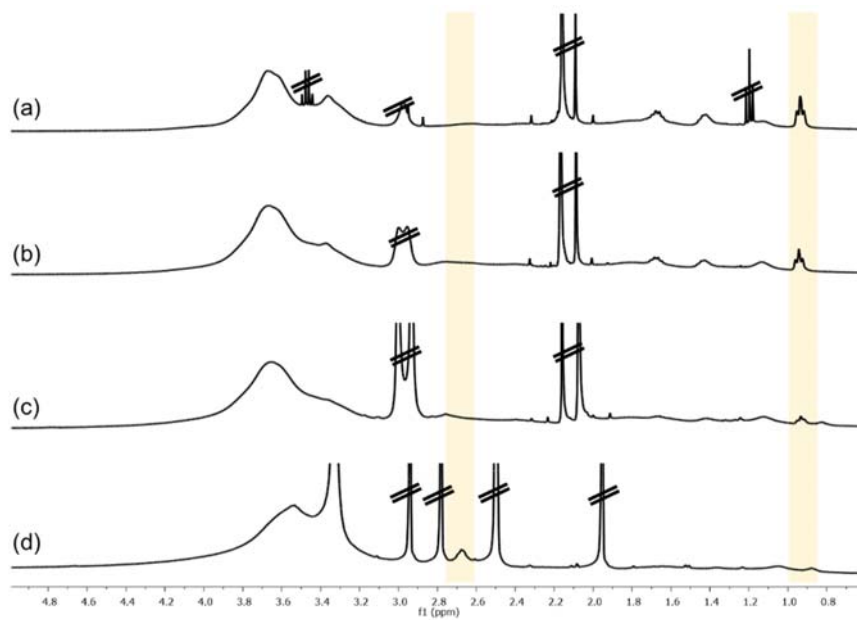
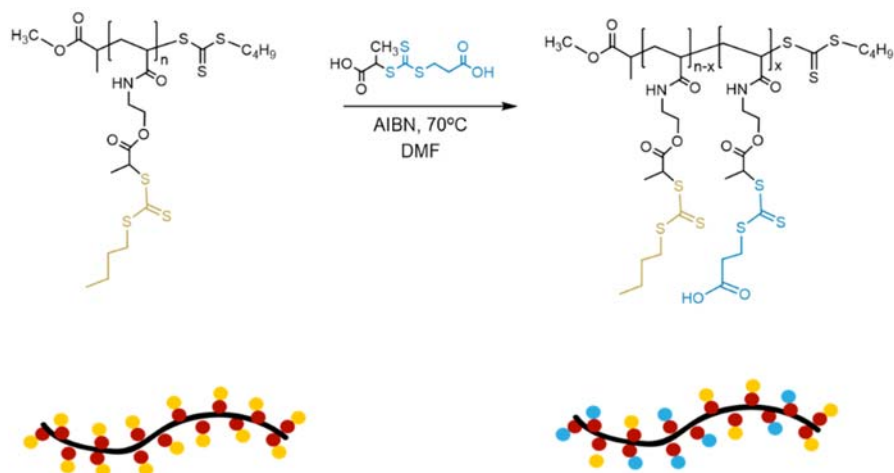


Figure 2.39 ^1H NMR spectra of brush $[\text{NAM}_5]_{150}$ (a) before interchange (b) after interchange with BM/PABTC 1:1, (c) after interchange with BM/PABTC 5:1 and (d) after interchange with BM/PABTC 10:1. The crossed-out signals are solvent impurities.

2.3.10.2 Interchange in PCTA-PHEAm_a



Scheme 2.16 PCTA-PHEAm_a interchange reaction scheme

Still aiming to investigate the statistical Z-groups interchange, I then experimented using polyCTAs only (Scheme 2.16). I expected to be able to calculate the proportion of BM/C4 in polyCCTA better than in brush $[PNAM_x]_a$, due to the absence of side chains, but the principle should be able to extrapolate to the brushes. As shown in Figure 2.40, the original polyCCTA does not show any peak at δ (ppm) 2.68 ppm. I conducted the experiments using different ratio of BM/C4 as in the brushes, 1:1, 5:1 and 10:1. In addition, I also withdrew an aliquot every hour for three hours, to study the rate of the interchange process. The samples were analyzed after isolation of polymers from the crude sample, and the percentage of Z-groups from BM incorporated into the brushes was calculated using Equation 2.2.

$$\%Z \text{ groups from BM} = \frac{\int \delta \text{ 2.68}}{\int \delta \text{ 2.68} + \int \delta \text{ 0.89}} \times 100\%$$

Equation 2.2 Calculation of BM proportion in the final brush

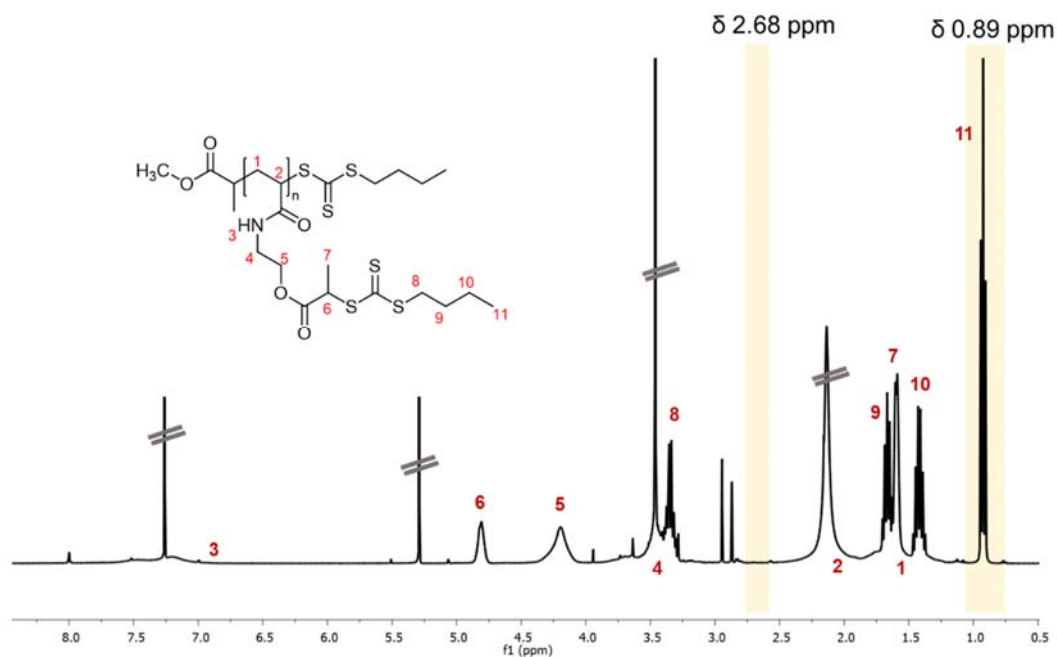


Figure 2.40 ^1H NMR spectra of original polyCCTA, showing no peak at δ (ppm) 2.68 and an intense peak at δ (ppm) 0.89

The summary of all calculations is shown in Table 2.13. In 1 hour, the proportion of BM in the polyCTAs were 36, 53 and 58% for BM/C4 ratio 1:1, 5:1 and 10:1, respectively. After 2 hours, these values increased to 44%, 69% and 82%, respectively. After 3 hours, the reactions became steady, and the final proportion for the three ratios was similar to the theoretical values, with BM fractions 52, 76, and 88% for BM/C4 ratio 1:1, 5:1 and 10:1, respectively. The detail of ^1H NMR peak integration as well as the calculation can be seen in Appendix (Figure A.11 - Figure A.13 and Table A.1).

Table 2.13 Summary of interchange reactions with different ratio and time

BM/C4 Reaction	BM/C4 in PCTA-PHEAm _a (%)			Theoretical BM/C4 in PCTA-PHEAm _a (%)
	1 hour	2 hours	3 hours	
1:1	36:64	44:56	52:48	50:50
5:1	53:47	69:31	76:24	83:17
10:1	58:42	82:18	88:12	91:9

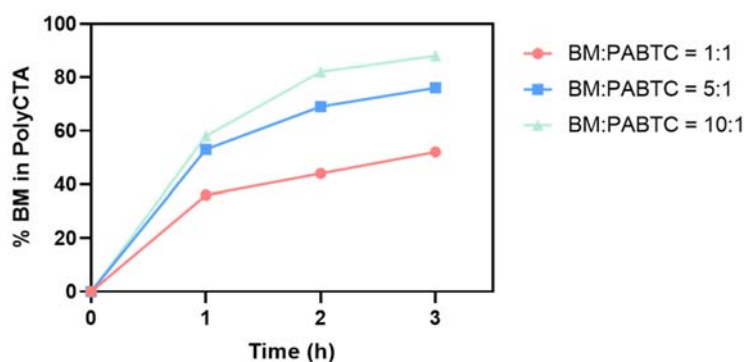


Figure 2.41 Proportion of BM in brush polymer vs time. Samples were isolated from crude reaction prior to analysis.

These results can be considered as preliminary hypothesis proof about statistical interchange. Although this is still a preliminary study, it offers possibility to build a new platform of how I can utilize the Z-groups of RAFT agents to easily functionalize the tips of the BBP. Since I also know that the Z-groups are relatively stable, this finding can be used to develop a

new method of drug attachment to the BBPs that I call as “dynamic conjugation”. This proposed method involves the conjugation of drugs or other molecules of interest to BM. Since the Z-groups of BM will be incorporated into the brush statistically, the amount of conjugated drugs will follow the amount of incorporated BM. The advantage of this method is that I can modify the drug payload in a fast manner only by changing the ratio of BM/C4 in the reaction, which can be achieved in approximately 3 hours. Moreover, if I conjugate BM with two or more different drugs, e.g. Drug 1 and Drug 2, I can attach both drugs to the BBPs at the same time, and thus reduce the conjugation and purification steps. A library of drug combination with different ratio of Drug 1 and Drug 2 can be created in a fast manner for further study in cells. The proposed mechanism is illustrated in the following image:

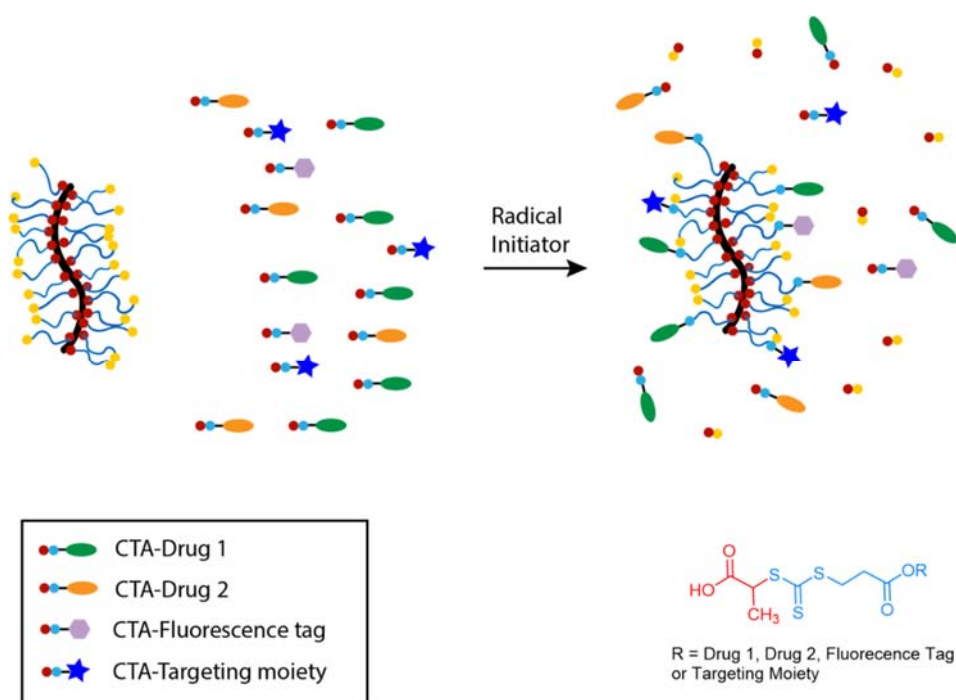


Figure 2.42 Proposed mechanism of dynamic interchange

2.4 CONCLUSION AND FUTURE DIRECTION

I have successfully synthesized NAM-based BBPs using CTA-shuttle grafting from R-group RAFT polymerization with a simple purification technique by precipitation in acetone (for brushes which contain side chain PNAM) or methanol (for brush $[BA_y]_a$ only), resulting in BBPs with narrow molecular weight distributions. With this approach, I created a library of BBPs, which have different characteristics such as length, grafting density, diblock side chains, and modified end groups of the side chains (Figure 2.43). The BBPs have functional groups that later can be attached with passenger molecules such as drugs, radioactive molecules or fluorescence tag. The solubility of BBPs in water can be improved by two ways: first, by replacing the end groups with carboxylic acid-containing radical initiators and, second, by exchanging the end groups of side chains with other CTAs that have carboxylic Z-groups.

For future works, I would like to build a BBPs platform with different monomers. Since I found that the Z-group of C4 in the brush can exchange with the Z-groups of BM in a statistical manner, I would like to investigate my hypothesis about dynamic conjugation (using drugs conjugated to BM). In addition, I also would like to study the statistical interchange using a different type of CTAs.

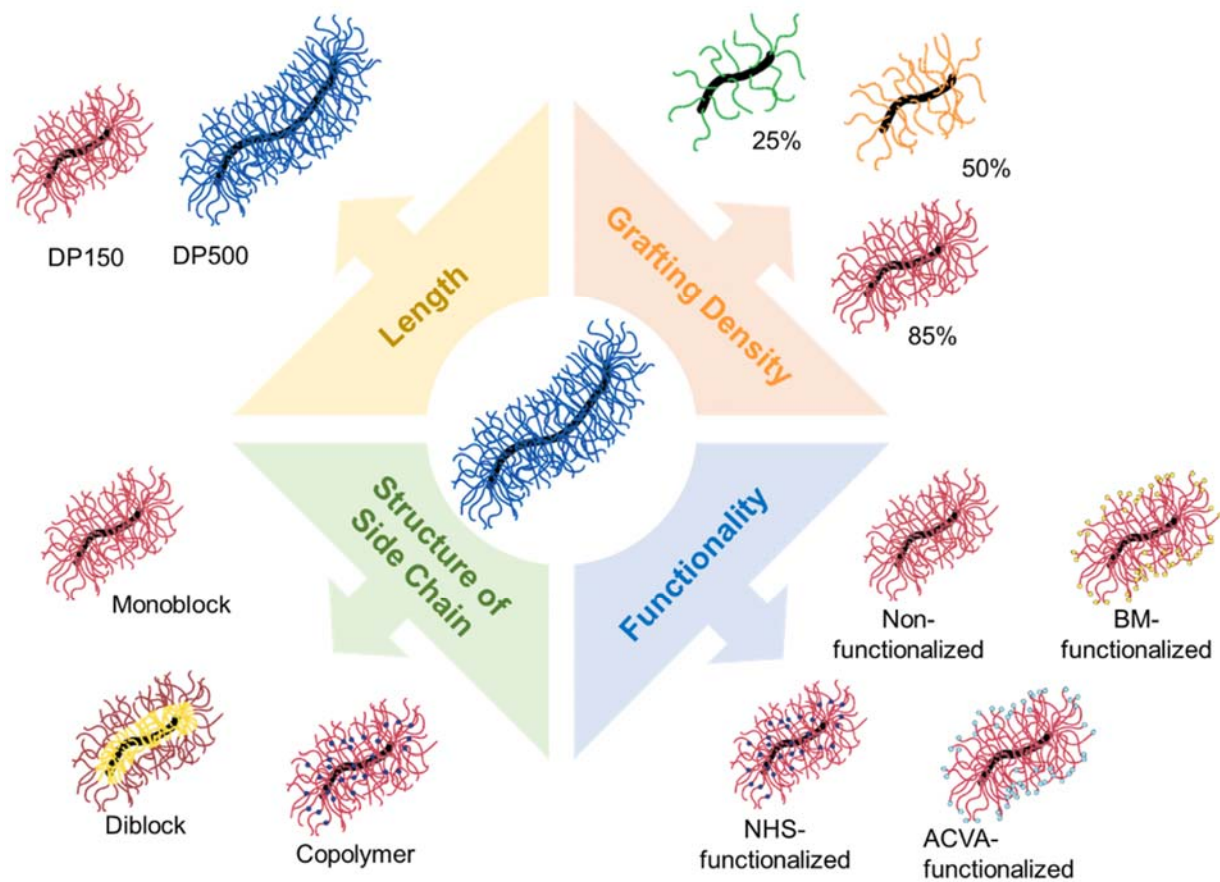


Figure 2.43 Library of NAM-based BBPs that I have produced

CHAPTER 3. *IN VITRO* CELL STUDIES, PHARMACOKINETICS AND BIODISTRIBUTION OF POLY-4-ACRYLOYLMORPHOLINE-BASED BOTTLE BRUSH POLYMER

3.1 INTRODUCTION

Polymer therapeutics has been recognised as one of the most successful clusters of nanomedicines. Since the first polymer-protein conjugates (styrene maleic anhydride neocarzinostatin, SMANCS) was marketed in the early 1990s, research on design and innovation of new polymeric carrier continues to expand. The development of polymeric candidates is not only restricted to the linear chain with new chemical structures but also broaden to more complex architectures.

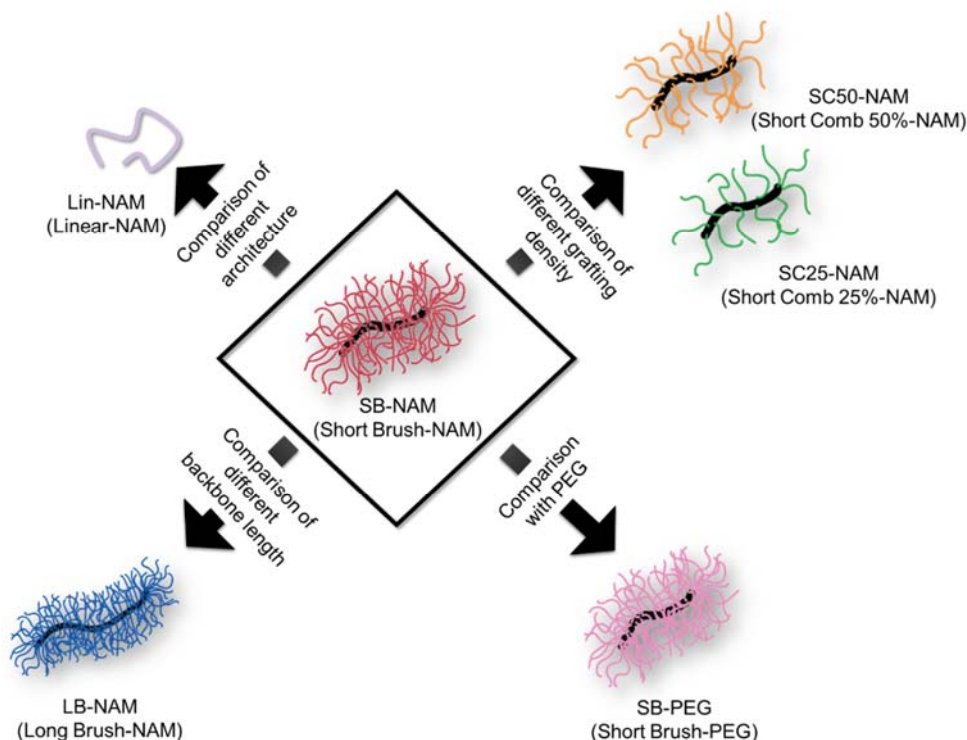
Bottle-brush polymers (BBP) are amongst the polymeric carrier with complex architecture which is still newly explored. As a matter of fact, although research in the synthesis of BBPs has emerged more than 20 years ago, studies on their potential for clinical application have just been started in the last 10 years. Note that most of the studies are limited to *in vitro* evaluation, for example, *in vitro* drug release, cytotoxicity, cell uptake and stability. It is also noteworthy that the majority of the studies employed BBPs with nearly-round structure, due to the similar length between backbone and side chain. This means the information of their behaviours as an anisotropic structure in biological compartments is still little known. In 2015, the *in vivo* performance, which includes pharmacokinetics and biodistribution, of anisotropic PEG-based BBPs was reported by Müllner *et al.*⁶², and then followed by Li *et al.*⁹⁴ in 2018 and Zhang *et al.*⁹¹ in 2019. They demonstrated how different aspect ratio^a of the BBPs demonstrated different pharmacokinetics and biodistribution.

Poly-4-acryloylmorpholine (poly(NAM)) is a polymer with a hydrophilic/hydrophobic ratio of its chemical structure similar to PEG, and therefore, might have similar behaviour in solution. It has potential *in vivo* application, yet has not been extensively studied. Poly(NAM)-coated poly(lactic acid) (PLA) nanoparticles¹³⁵ and poly(NAM)-stealth liposomes¹³⁶ were the

^aAspect ratio is ratio between length and diameter of the BBPs. When the diameter of all BBPs are made similar, the aspect ratio is only determined by the length of the backbone

only two reported studies of poly(NAM). Both poly(NAM)-decorated nanocarriers showed prolonged plasma residence, suggesting the stealth capability of poly(NAM) as in PEG. However, the application of poly(NAM) for biomedicine field as a standalone material has not yet been investigated. In Chapter 2, I have reported synthesis platform of BBPs with (NAM) side chains, resulting in NAM-based BBPs with well-defined structure and sophisticated characteristics (narrow molecular weight distribution, water-soluble, and have functional groups for easy conjugation). The method also enables us to synthesize brushes with tailored structure.

I have gained the knowledge to produce BBPs with desired characteristics, and I now intend to understand the behaviour of the materials in the body. In this chapter, I studied the performance of my NAM-based BBPs in the biological compartment, which includes *in vitro* cytotoxicity, cell uptake, pharmacokinetics and biodistribution in a rat model. The studied polymers are summarized in Scheme 3.1. Also, I have labelled all studied polymers with a simpler name for easier recalling, described in the box.



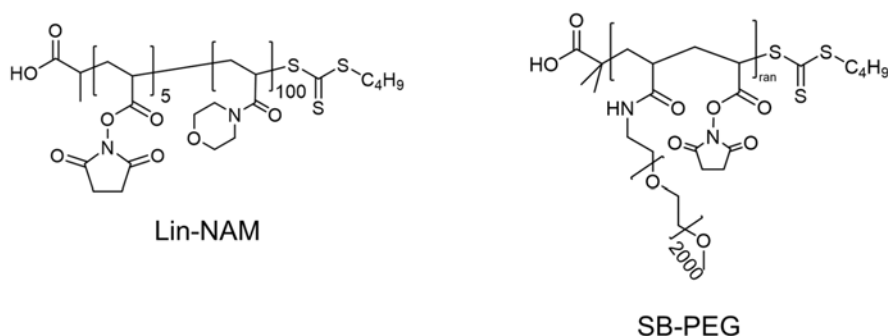
Scheme 3.1 Comparison of the studied polymers.

POLYMER NOMENCLATURE

SB-NAM (Short Brush-NAM)	=	Brush [P(NHSA ₃ -co-NAM ₅₀)] ₁₅₀
LB-NAM (Long Brush-NAM)	=	Brush [P(NHSA ₃ -co-NAM ₅₀)] ₅₀₀
SC50-NAM (Short Comb 50%-NAM)	=	Brush [P(NHSA ₂ -co-NAM ₅₀)] _{50%,150}
SC25-NAM (Short Comb 25%-NAM)	=	Brush [P(NHSA ₂ -co-NAM ₅₀)] _{25%,150}
Lin-NAM (Linear-NAM)	=	Poly(NHSA ₅ -co-NAM ₁₀₀)
SB-PEG (Short Brush-PEG)	=	Brush [P(NHSA ₅ -co-(PEGAm ₄₄) ₄₅)]*

*PEGAm₄₄ = polyethylene glycol acrylamide with 44 units of ethylene glycol (molecular weight 2000 Da)

First, I compared the brushes with linear poly(NAM) (Scheme 3.2) which chain length is similar to twice the length of brushes' side chains (diameter of BBPs). This study aims to investigate whether the *in vitro* and *in vivo* behaviour of the brushes will be different from the linear poly(NAM). Since the diameter of the brushes has a similar length to linear poly(NAM), there is a possibility both types of NAM-based polymers will have similar behaviour. However, I hypothesized that the major axis (length) of the brushes would play a more dominant role and, thus, they would show better performance, including prolonged plasma retention and low clearance.



Scheme 3.2 Chemical structure of Lin-NAM and SB-PEG

Second, I compared my NAM-based BBPs with PEG-based BBPs (Scheme 3.2). The purpose of this study is to examine the performance of poly(NAM) in BBPs relative to the widely used PEG. I hypothesized that my NAM-based BBPs would show similar biological performance to PEG-based BBPs, due to their similarities in the chemical structure. Hence, I also proposed that poly(NAM) could be an alternative to PEG.

Third, I compared the biological performance of brushes with different grafting density (GD). The study involved NAM-based BBPs with backbone DP150 and GD ~85%, ~50% and ~25%. I postulated that their distinctive feature regarding the structure flexibility might impact their pharmacokinetics, biodistribution and interaction with cells.

To resume, the hypotheses being addressed in this chapter are:

1. All NAM-based BBPs are not toxic and thus, biocompatible.
2. Due to the appropriate size, all NAM-based BBPs will be able to be internalized by cells.
3. The BBPs will outperform the linear structure in regards to their biological performance.
4. The backbone length of BBPs will give an impact on their biological behaviour.
5. The density of side chain will influence their biological behaviour.
6. The NAM-based BBPs will exhibit similar behaviour to PEG-based BBPs.

3.2 EXPERIMENTAL METHOD

3.2.1 Materials

For this experiments, I used SB-NAM, LB-NAM, Lin-NAM and SB-PEG synthesized by my collaborator, Dr. Andrew Kerr from University of Warwick, United Kingdom. Triethylamine (TEA), ethanolamine and hydrogen peroxide were purchased from Sigma-Aldrich. Alexa Fluor™ 488 Cadaverine (Alexa-488), LysoTracker™ Deep Red, LysoSensor™ Green DND-189, Hoechst 33342 and Gibco Dulbecco's Modified Eagle Medium (DMEM) were purchased from Thermo Fisher Scientific. Cyanine5.5 amine (Cy5.5) was purchased from Lumiprobe. [14C]-ethanolamine was purchased from American Radiolabeled Chemicals. Ultima Gold™ and Solvable™ were purchased from Perkin Elmer.

Solvents used were N,N-dimethylformamide (DMF) (Sigma-Aldrich), acetone (Sigma-Aldrich), dimethylacetamide (DMAc) and diethyl ether (Sigma-Aldrich). All solvents were analytical grade.

3.2.2 Synthesis Procedure

3.2.2.1 Synthesis of Lin-NAM

NAM (460 mg, 4.00 mmol, 100 eq.), NHSA (34 mg, 0.20 mmol, 5 eq.), PABTC (9.1 mg, 3.80×10^{-2} mmol, 1 eq.) and ACVA (1.3 mg, 4.75×10^{-3} mmol, 0.125 eq.) were dissolved in 0.95 ml anhydrous dioxane in a 3 ml vial fitted with a stirrer bar and rubber septum. The reaction mixture was degassed with nitrogen for 10 minutes, placed in an oil bath set to 70°C for 5 h and then precipitated twice into diethyl ether, dried under vacuum to yield a pale yellow powder.

3.2.2.2 Fluorescence Labelling

a. Labelling with Alexa-488

SB-NAM (10 mg, 3.33×10^{-3} mmol NHSA units), Alexa-488 cadaverine (0.03 mg, 4.68×10^{-5} mmol) and TEA (1 mg, 9.88×10^{-3} mmol) were dissolved in 250 μ L of anhydrous DMF. The mixture was stirred for 2 days at room temperature, protected from light. Ethanolamine (2 μ L, 3.27×10^{-2} mmol) was then added, and the reaction was stirred for a further 4 h. The DMF was evaporated under a stream of nitrogen and then the residue was re-dissolved in 1 mL Milli-Q water. The solution was immediately passed through a PD-10 Desalting Column (Sephadex G-25 Medium, GE Healthcare), collected into 1 mL fractions. Analysis of the obtained fractions by fluorescence spectrophotometer showed nearly 100% conjugation of the dye onto the polymer. The polymer-containing fractions were combined, washed three times through a centrifuge dialysis tube (100k MWCO) and freeze-dried to yield pale orange powder

with mass of ± 6 mg (yield $\sim 60\%$). The purified compound was then analyzed by UHPLC (Shimadzu) using Luna 5 μm C18(2) 100 Å, LC column 250 \times 4.6 mm (Phenomenex) and acetonitrile as mobile phase. The same procedure was used for the other polymers. For Lin-NAM a 10k MWCO dialysis centrifuge tube was used to purify the compound.

b. Labelling with Cy5.5

SB-NAM (20 mg, 6.66×10^{-3} mmol NHSA units), Cy5.5 (0.10 mg, 1.31×10^{-4} mmol) and TEA (0.32 mg, 3.2×10^{-3} mmol) were dissolved in 500 μL of anhydrous DMF. The mixture was stirred for 2 days at room temperature, in a dark condition. Ethanolamine (2.21 mg, 3.61×10^{-2} mmol) was then added and the reaction was stirred for a further 4 h. The crude reaction was then precipitated two times with 45 mL cold diethyl ether and the solvent residues was evaporated under a stream of nitrogen. The solid residue was re-dissolved in 700 μL Milli-Q water and immediately passed through a PD-10 Desalting Column, collected into 700 μL fractions. The obtained fractions were then freeze-dried and the fractions with polymer powder (pale blue colour) were combined, redissolved in milliQ water. The solution was dialyzed using 6k MWCO Floatalyzer® dialysis device for 3 days and then freeze-dried again to yield pale blue powder with mass of ± 12 mg (yield $\sim 60\%$). The purified compound was then analyzed by GPC with UV detector $\lambda = 684$ nm to reveal pure compound without free dye. The same procedure was used for LB-NAM, SC50-NAM and SC25-NAM.

3.2.2.3 Radiolabelling

[^{14}C]-ethanolamine solution (250 μL , 25 μCi) in H_2O /ethanol was dried under nitrogen stream to remove the solvent. The dried [^{14}C]-ethanolamine was then redissolved in 250 μL DMF. SB-NAM (20 mg, 6.66×10^{-3} mmol NHSA units), TEA (0.3 mg, 2.96×10^{-3} mmol) and [^{14}C]-ethanolamine (2×10^{-3} mmol, 0.25 ml solution in DMF) were dissolved in DMF (0.5 ml) in a 3 ml screw-cap vial, and stirred at room temperature for 48 h. An aliquot of non-radioactive ethanolamine (3 mg, 4.9×10^{-2} mmol) was added to the reaction mixture and stirred for a further

4 h to ensure that all –NHS groups were replaced. The reaction mixture was dried under a stream of nitrogen, re-dissolved in 700 µL of Milli-Q water and immediately passed through a PD10 purification column collected into 700 µL fractions. 5 µL of each fractions was pipetted to a 4-mL scintillation vial, mixed with 3 mL of Ultima Gold, and then analyzed on a Packard Tri-Carb 2000CA liquid scintillation analyzer (2 minutes reading time of each sample) to confirm separation of polymer and free [14C]-ethanolamine. Fraction which contains polymer species (fraction 4-8) were mixed and placed in a Floatalyzer® dialysis device with a 10k MWCO and dialyzed against water for 3 days. The solution was transferred to a pre-weighed vial, dried under a stream of nitrogen to yield the radiolabelled conjugate as a white residue. The dry polymer with the vial was weighed to determine the mass of obtained polymer (yield ~70%), and then re-dissolved in 2 mL normal saline. The specific activity of [14C]-labelled compound was determined by liquid scintillation counting (a mixture of 2 µL of polymer solution with 3 mL of Ultima Gold in a 4-mL scintillation vial), resulting in conjugation efficiency ~80%. A similar procedure was applied for the other polymers.

3.2.3 *In vitro* Cell Studies

3.2.3.1 Cells

3T3 (mouse embryonic fibroblast) cells were donated by Dr. Angus Johnston (Monash University). MDA-MB-231-HM (human breast cancer) cells were donated by Dr. Erica Sloan (Monash University). HEK-293 (human embryonic kidney) cells were donated by Dr. Nicholas Veldhuis (Monash University). 4T1 (mouse mammary carcinoma) cells were purchased from American Type Culture Collection (ATCC). 3T3 were grown in Dulbecco's Modified Eagle Medium (DMEM) supplemented with 20% v/v of foetal calf serum. 4T1, MDA-MB-231 and HEK-293 were grown in DMEM supplemented with 10% v/v of foetal calf serum. Cells were grown as adherent monolayers at 37°C in a 5% CO₂ humidified atmosphere and passaged at approximately 70-80% confluence.

3.2.3.2 Growth Inhibition Assay

Cells (5000/well) were seeded in 96-well plates (150 µL) and allowed to grow for 24 h before adding the compounds. Solution of compounds in cell culture medium (75 µL) at concentrations ranging from 0.001 to 1 mg/mL were added to the wells. After that, the cells were further incubated for 72 h. After 72 h, MTT solution (12 mM in PBS, 10 µL) were added to all wells and the cells were incubated for 4 h. After 4 h, the medium was then removed by aspiration and replaced by DMSO (100 µL) to dissolve the MTT crystals. Absorbance measurements of the plate were carried out using a Synergy HTX (Biotek) plate reader. Determination of viable treated cells was done in comparison to untreated controls (Equation 3.1). Two independent sets of experiments in triplicates were carried out and standard deviations were used for error bars.

$$\% \text{ viability} = \frac{(A_{570} - A_{670})_{\text{sample}}}{(A_{570} - A_{670})_{\text{control}}} \times 100$$

Equation 3.1 Determination of viable cells from MTT cytotoxicity assay

3.2.3.3 Confocal Microscopy

3T3 and MDA-MB-231 cells (20,000 cells/well, 200 µL/well, in DMEM) were plated in a 8-well microscopy slide and incubated overnight at 37°C with 5% CO₂. AlexaFluor® 488 or Cy5.5-labelled polymers dissolved in DMEM were added to the wells (final concentration 0.3 mg/mL per well) and incubated for 24 h. After 24 h, the live cells were washed (1x) with DMEM supplemented with 10% FBS. Colocalization studies were carried out with the following procedures:

a. For Alexa-488-labelled polymers

LysoTracker® Deep Red (final concentration 50 nM) for lysosome staining was added 30 minutes prior to imaging and then followed by the addition of Hoechst 33342 for nuclei staining, 10 minutes prior to imaging (1.5 µL at 1 mg/mL, final concentration 1 µg/mL).

b. For Cy5.5-labelled polymers

LysoSensor Green DND (final concentration 2.3 μ M) for lysosome staining was added 30 minutes prior to imaging and then followed by the addition of Hoechst 33342 for nuclei staining, 10 minutes prior to imaging (1.5 μ L at 1 mg/ml, final concentration 1 μ g/mL).

After lysosome and nuclei staining, the cells were washed once with warm phenol-red free DMEM media (with 10% FBS). The cells were left in colourless media and imaged immediately. Images were recorded using a Leica TCS SP8 (Carl Zeiss, Germany) microscope at a temperature of 37°C confocal, with a HCX PL APO 40x (NA 1.30) oil objective. Images were acquired at 1024×1024, capturing Hoechst 33342 (ex. 392; em. 415-467 nm), AlexaFluor® 488 (ex. 493; em. 501-580 nm) and LysoTracker® Deep Red (ex. 647; em. 650-778 nm) or Cy5.5 (ex. 633; em. 650-734 nm) and LysoSensor Green DND 189 (ex. 458; em. 480 – 607 nm). Image acquisition settings were consistent for samples and controls. Images were processed with the FIJI Image J¹⁵⁶.

3.2.3.4 Flow Cytometry

Cells were seeded in 24-well plates at 100,000 cells per well and then incubated in 400 μ L of compound-free media overnight at 37°C with 5% CO₂. Alexa-488 or Cy5.5-labelled polymers were then added to cells in triplicate, achieving a final concentration of 0.3 mg/mL. Three sets of conditions were tested: incubation at 37°C for 24 h, incubation at 37°C for 3 h, and incubation at 4°C for 3 h. For the incubation at 4°C, the cells were placed on ice for 10 min prior to addition of the compound, and subsequently stored on ice. After incubation, the culture medium was removed, and the cells were washed with cold PBS once and then harvested with trypsin. The detached cells in trypsin were then suspended in 1% w/v bovine serum albumin (BSA), transferred to conical bottom 96-well plates and spun at 1500 g for 5 min. The supernatant was discarded and cell pellets were resuspended in 200 μ L of BSA and stocked on ice until measurement. For the Cy5.5-labelled polymers, the cell pellets were redispersed in 200 μ L of cell fixation solution (1.6% formaldehyde). Propidium iodide (PI) was added to some wells to allow for gating of the living cells population. Samples were analyzed

using an S100EXi flow cytometer (Stratedigm), equipped with 405, 488, 552 and 640 nm solid-state lasers. Cells were analyzed using forward and side scatter gates to exclude debris and cell aggregates. Fluorescence intensity corresponding to untreated cells was subtracted, the data were processed using FlowJo v 8.0 and reported values correspond to the average of the means of fluorescence for a population of 10,000 cells.

3.2.4 Pharmacokinetics and biodistribution studies

3.2.4.1 Animals

All animal experimental protocols were approved by the Monash Institute of Pharmaceutical Sciences Animal Ethics Committee, Monash University, Parkville, VIC, Australia (protocol no. 12960). Animal studies were carried out using Male Sprague Dawley rats (250-350 g). Animals underwent seven days acclimatisation prior to studies and were maintained on a 12 h light/dark cycle at all times.

3.2.4.2 Pharmacokinetics Studies

A day prior to polymers administration, each rat was anaesthetised under isoflurane (2.5-5% v/v) and then cannulas (1 m length, polyethylene tubing 0.96 OD×0.58 ID mm or 0.80 OD×0.50 ID mm, Paton Scientific, Victor Harbour, Australia) were surgically inserted into the right jugular vein and carotid artery (to facilitate intravenous (IV) administration and blood collection, respectively) as previously described.¹⁶³ The rats were then placed into individual metabolic cages (to permit separate collection of urine) and allowed to recover overnight prior to dosing. Each animal was not fasted. Prior to injection, blank blood samples (0.15 mL) were obtained from the carotid artery and blank urine were also collected.

The compounds were formulated in phosphate buffered saline (PBS) or normal saline with concentration equivalent to 2 $\mu\text{Ci/mL}$. 0.5 mL of formulation (equivalent to 1 μCi) was

administered intravenously via the jugular cannula with 1 mL/min infusion rate. The cannula was then flushed with 0.5 mL of heparinized saline to ensure complete infusion of the dose. New urine collectors were then assembled. Subsequent blood samples (0.15 mL) were taken at 1, 5, 10, 20, 30, 60, 120, 180, 240, 360, 480, and 1440 min after dose administration. Blood samples were placed immediately into tubes containing 10 IU of heparin and centrifuged for 5 min at 3500 g. Plasma (50 μ L) was collected, transferred to a scintillation vial and mixed with 3 mL of Ultima Gold scintillation cocktail prior to scintillation counting.

3.2.4.3 Biodistribution Studies

At the end of the pharmacokinetics studies (24 h), animals were humanely killed by injecting a lethal dose of sodium pentobarbital (via the jugular vein cannula) and the following organs were collected: liver, spleen, pancreas, kidneys, heart, lungs and brain. The tissues were stored in pre-weighed polypropylene tubes and frozen (-20°C) until processing.

Organ samples were homogenized using a gentleMACS Dissociator (Miltenyi Biotec) with 5 mL of MilliQ water, and triplicate samples from each tissue homogenate (typically 50-100 mg of tissue) were placed into 20-mL scintillation vials, after which 2 mL of Solvable (Perkin Elmer) was added. An identical second set of samples was processed in the same way with the addition of a known quantity of radiolabel (spiked) prior to the addition of Solvable. The spiked samples are for correction of any reduction in radioactivity counting efficiency due to the sample preparation process.

Samples were then heated at 60°C overnight to facilitate tissue digestion. The samples were cooled to room temperature and 200 μ L hydrogen peroxide (30% w/v) were added to each vial. Samples were left open at room temperature until bubbles ceased. Ultima Gold (10 mL) was then added and the mixtures were vortexed. The samples were then stored at 4°C in the dark, without agitation, for at least 3 days prior to scintillation counting. Blank organs (non-spiked only) and Solvable blank (spiked and non-spiked) also were treated as above to provide for background correction. All samples were then scintillation counted at 12°C. Processing efficiency was calculated using Equation 3.2.

$$\text{Efficiency} = \frac{\text{spiked tissue}_{\text{dpm}} - \text{tissue}_{\text{dpm}}}{\text{spiked solution}_{\text{dpm}}}$$

Equation 3.2 Tissue processing efficiency

where $\text{spiked tissue}_{\text{dpm}}$ was the mass-corrected (subtracted by blank tissue) radioactivity measured in the spiked samples, $\text{tissue}_{\text{dpm}}$ was the mass-corrected (subtracted by blank tissue) radioactivity in the non-spiked tissue samples, and $\text{spiked solution}_{\text{dpm}}$ was the known amount of radioactivity added to the spiked Solvable blank. Effectively, the calculation indicates the efficiency of counting, using the known (spiked) amount of radioactivity in each tissue as a reference. This value for efficiency was used to correct the [14C] content in the processed sample using the following equation:

$$\text{Tissue}_{\text{dpm,corr}} = \frac{\text{Tissue}_{\text{dpm}}}{\text{efficiency}}$$

Equation 3.3 Correction of [14C] content

The radioactivity in the whole organ was then calculated knowing the mass fraction of the whole organ present in the processed sample. The results are expressed as either the percentage of injected dose per organ or the percentage of injected dose per gram of tissue.

3.2.4.4 Urine

Urine, pooled from immediately after dose administration until 24 h, was collected at the end of the study. A blank urine sample was also collected prior to compound administration to provide background correction. After accounting for the volume of pooled urine collected, a 50 μL aliquot was taken and mixed with 3 mL of Ultima Gold, vortexed and then scintillation counted. After background subtraction, the radiolabel content of the sample was corrected for

the total volume of urine collected and converted to a percentage of the total administered dose.

3.2.4.5 Calculation of Pharmacokinetic Parameters

The radiolabel concentration in plasma/whole blood samples were converted to microgram equivalent concentrations using the specific activity of the radiolabelled compounds. Non-compartmental pharmacokinetic parameters were calculated with Excel using the PK solver add-in¹⁶⁴, doses were normalized to 5 mg/kg. The non-compartment analysis (NCA) IV bolus model was used, in which the AUC_{0-24} was calculated using the linear trapezoidal method. The elimination half-life ($t_{1/2}$), the terminal volume of distribution ($V_{d,\beta}$) and total clearance (Cl) were also determined from the model. An estimate of initial distribution volume, or volume of central compartment (V_c) was calculated from the dose/ $C_{p,0}$. $C_{p,0}$ is concentration in plasma at the moment of completion of the injection, which value is obtained by extrapolating the plasma concentration curve to time zero. Statistical significance was assessed using either ordinary one-way ANOVA or student t-test, depending on the number of compounds being analyzed.

3.3 RESULTS AND DISCUSSION

3.3.1 Biocompatibility Studies

Toxicity is one important parameter that should be assessed for a material that is intended for biological application. PNAM have been known as biocompatible polymers¹⁶⁵, however the toxicity of PNAM in brush structure has never been reported elsewhere. To investigate this, I selected four of the NHS-functionalized NAM-based BBPs (SB-NAM, LB-NAM, SC25-NAM and SC50-NAM) and evaluated their biocompatibility against cells in an *in vitro* cell growth inhibition assay. Beside NAM-based BBPs, I also tested linear polyNAM (Lin-NAM) and BBPs with PEG side chains. Lin-NAM, a comparison for the grafted structure of BBPs, was designed to be equivalent to the diameter of the BBPs, the smallest dimension of

the BBPs, which might play a role in the clearance of brush molecules via renal filtration. Therefore I produced Lin-NAM with DP of 100, which is twice the length of BBPs' side chains (length of BBPs' side chain = radius of BBPs). NHS-functionalization was also applied to Lin-NAM by copolymerizing NAM and 5% of NHS.

SB-PEG is a standard comparison for NAM-based BBPs due to its extensive use in biological application and its widely known ability to extend blood circulation of drugs and nanoparticles. I aimed to produce SB-PEG with side-chain structure, diameter and backbone length as equal as the short brush, SB-NAM. To achieve these criteria, SB-PEG was synthesized by my colleague, Dr. Andrew Kerr (University of Warwick, United Kingdom) by grafting-through of PEG acrylamide (PEGAm) macromonomers and NHS via RAFT polymerization. The PEG side chain has a molecular weight of 2,000 g/mol, which is equivalent to 44 repeating units of ethylene glycol, and thus, is similar to the DP of the NAM-based BBPs side chains. However, due to the low efficiency of grafting-through method, aiming for SB-PEG with a backbone DP of 150 as in SB-NAM led to substantially high dispersity. Therefore, for this study, I used SB-PEG with a backbone DP of 50, which I considered still comparable with the SB-NAM.

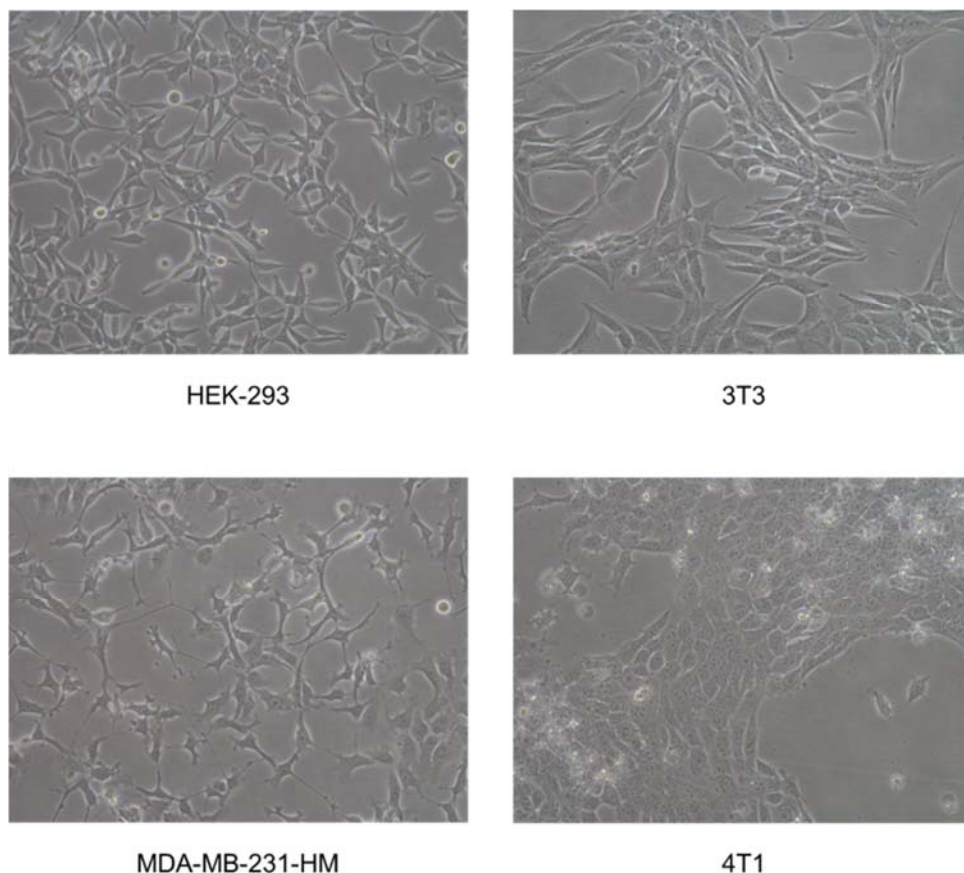


Figure 3.1 Morphology of cell lines used for viability studies in 80% confluence

The biocompatibility assays were performed using four cell lines (HEK-293, 3T3, 4T1 and MDA-MB-231-HM) for 72 h. HEK-293 (human embryonic kidney) and 3T3 (mouse embryonic fibroblast) cells were used as a model of “normal” cells, while MDA-MB-231-HM (triple-negative human breast adenocarcinoma) and 4T1 (mouse mammary carcinoma) were used as a model of breast cancer cells. MDA-MB-231-HM and 4T1 were utilized due to the intended future application of the NAM-based BBPs for delivering anticancer drugs. The microscopic image of all cell lines at 80% confluence is shown in Figure 3.1.

All tested compounds, except SC25-NAM, did not exhibit toxicities against all cells, up to concentration of 0.5 mg/mL, which is represented by more than 50% cell viability (Figure 3.2 and Figure A.19 Appendix). This value is higher than those in inorganic nanoparticles such as silver nanoparticles (0.05 mg/mL)¹⁶⁶, gold nanorods (0.0125 mg/mL) and PEGylated gold nanorods (0.2 mg/mL)¹⁶⁷. Some toxicities were shown by SC25-NAM towards MDA-MB-231-

HM cells from concentration of 0.01 mg/mL or higher. This is probably because SC25-NAM is internalized by MDA-MB-231 cells more than SB-NAM and SC50-NAM. To investigate this, I conducted cell association study using flowcytometer and the results are discussed in the next section.

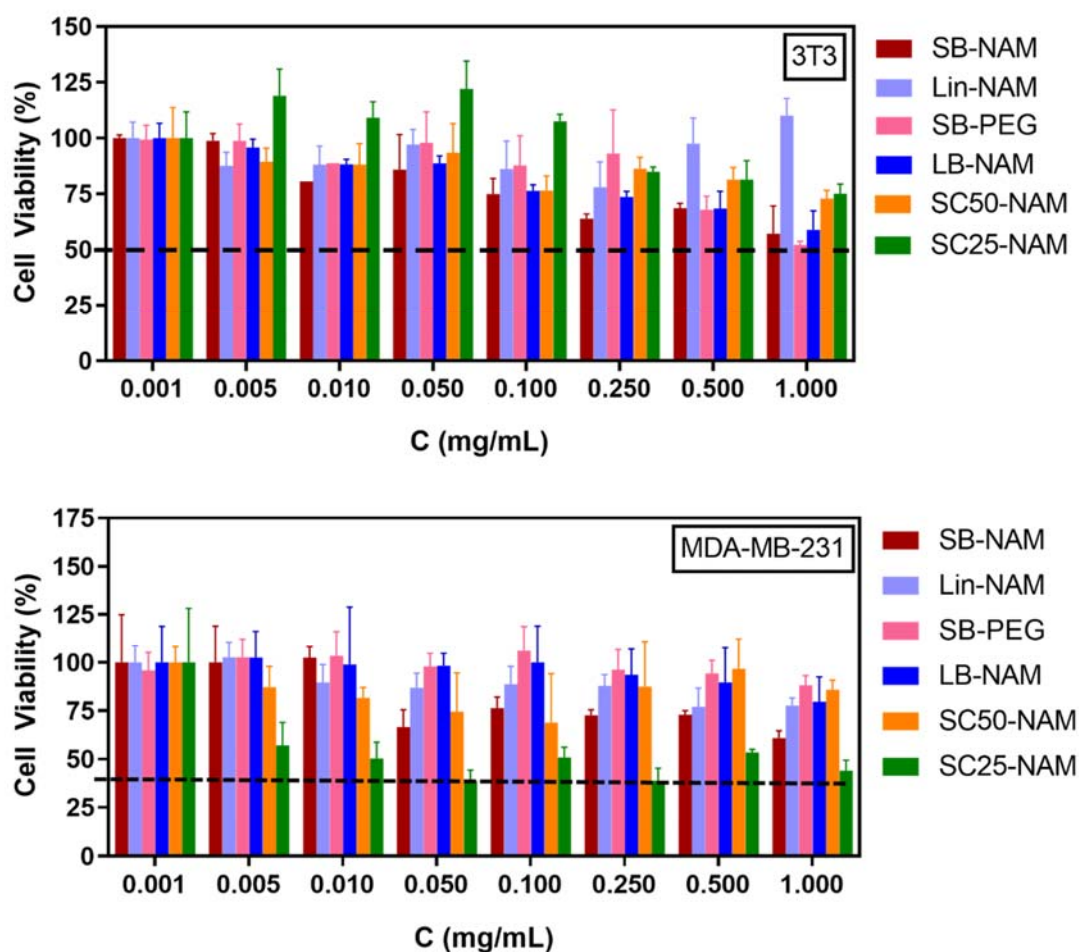


Figure 3.2 Toxicity profile of the compounds in 3T3 and MDA-MB-231-HM cells determined by MTT assay after incubation for 72 h at 37°C (mean \pm SD, $n = 3$).

In general, all NAM-based BBPs are not toxic against “healthy” cell lines, HEK-293 and 3T3, which suggests their biocompatibility to be used in biological application. SB-NAM, LB-NAM and SC50-NAM are also not toxic towards cancerous cells, MDA-MB-231-HM and 4T1, indicating their characteristic as inert polymeric carriers. The toxicity of SC25-NAM towards

MDA-MB-231-HM cells suggested their cell-specific cytotoxicity. However, further investigation is required for the future works to assess this phenomenon.

3.3.2 Cell Association

Cellular association or internalization is an essential parameter for a polymeric carrier that should be evaluated, particularly when it is designed to deliver its cargo to the cells. Aiming to investigate how the NAM-based brush polymers associate with cells, I conducted quantitative cell association experiments in 3T3 and MDA-MB-231-HM cells, using flow cytometry. The cells were incubated with the Alexa488-labelled or Cy5.5-labelled compounds at a concentration up to $0.3 \text{ mg} \cdot \mu\text{L}^{-1}$, to prevent unwanted toxicity, at three different conditions (3 h at 4°C and 37°C and 24 h at 37°C).

The correlation between the fluorescence signal and concentration of polymers in cells was determined by generating a calibration curve from each fluorescence-labelled polymer⁵⁶. The slope of the linear fit from all compounds was then averaged, which value is used to determine the correction factor for each compound. The fluorescence intensity of each material was then normalized using the obtained correction factor. The details of the generated calibration curves and correction factors are shown in Appendix, Figure A.20, Table A.2, Figure A.21 and Table A.3. Generally, all compounds showed very low uptake at 4°C and increased cell internalization at 37°C from 3 h to 24 h in both cells (Figure 3.3 and Figure 3.5), indicating the energy-dependent endocytosis, a typical cell uptake mechanism of nano-sized objects^{168,169}.

a. Influence of Different Architecture

SB-NAM was internalized less than Lin-NAM in both cell lines (Figure 3.3a). This is probably due to the linear structure of Lin-NAM that forms ball-like conformation in solution, resulting in a smaller diameter in comparison with the diameter of SB-NAM. Moreover, it has been found that ball-like shape needs lower membrane bending energy during endocytosis, compared to rod-like structure¹⁷⁰⁻¹⁷², and therefore would be internalized faster. Interestingly,

a discrepancy was found between the cell uptake in 3T3 and MDA-MB-231-HM cells, where in 3T3, the difference between Lin-NAM and SB-NAM is more significant. I speculated that this difference is influenced by which cellular uptake pathway is more preferred by each cell type. This postulation is based on the work by Santos *et al.*¹⁷³, who found that the endocytic pathway of polystyrene nanoparticles in HeLa (human cervix epithelium) cells and 132N1 (human brain astrocytoma) was mainly via clathrin-mediated endocytosis, while their uptake by A549 (human lung epithelium) cells was more preferably via caveolae-mediated pathway. They suggested that the uptake of the same nanoparticles might occur via different pathways in different cells, and thus, exhibit a different pattern of internalization.

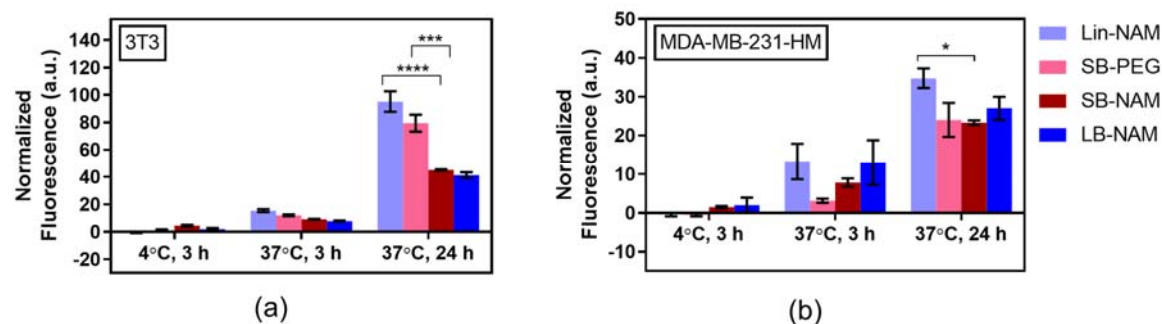


Figure 3.3 Cellular fluorescence intensity associated with AlexaFluor™ 488 as determined by flow cytometry after incubation of the compounds for 3 h at 4°C, 3 h at 37°C and 24 h at 37°C in 3T3 and MDA-MB-231-HM cells. Data represents normalized geometric mean of fluorescence \pm SD for independent experiments done in triplicates: * $p < 0.05$, *** $p < 0.001$, **** $p < 0.0001$.

b. Comparison Between PNAM and PEG

As shown in Figure 3.3, the uptake of SB-NAM by 3T3 cells is lower than SB-PEG (close-to-spherical structure due to its side chain/backbone length ratio), potentially also due to the size and shape of SB-PEG, similar reason as in Lin-NAM. Interestingly, equal uptake is shown by both materials in MDA-MB-231-HM cells, suggesting preferential uptake of both cells, due to the likelihood of different uptake mechanism performed by the cells. Also, the accumulation of nanoparticles inside cells is a net yield between uptake and exocytosis¹⁷⁴. In

accordance with this, the discrepancy in cell association between SB-NAM and SB-PEG in 3T3 cells might also be due to different exocytosis rate demonstrated by this cell type.

With this comparative study, I concluded that SB-NAM and SB-PEG showed a similar property regarding the uptake by MDA-MB-231-HM cancer cell lines, prompting PNAM potency as an alternative for PEG. In addition, compared to SB-PEG, SB-NAM was not internalized by healthy cells (3T3). This feature might be beneficial for a disease-specific drug delivery system. However, a more comprehensive study on the cellular endocytosis and exocytosis of BBPS is required to understand their intracellular trafficking, and then be used to determine the best design of BBPs which can be internalized more by cancer cells, but not by healthy cells.

c. Influence of Backbone Length

SB-NAM and LB-NAM do not show a significant difference in cell uptake, suggesting that increasing the length by three times (40 nm and 130 nm) does not prominently affect the cell uptake (Figure 3.3). This result is not in agreement with the previously reported PEG-based BBPs by Zhang *et al.*⁹¹, which compared BBPs with length of 34, 60 and 119 nm. In that study, the cellular uptake of BBPs in SH-SY5Y and HUVEC cells increased as the length increase. In another study reported by Li *et al.*⁹⁴ using molecular brushes with side chains consisting of block copolymer PAA and PEG, reverse result was shown, where the shorter brushes (20×71 nm) showed higher cellular uptake in MCF-7 cells than the long brush (20×176 nm, 2.5 times longer). However, the loading of the brushes with cargo (IR780, a photothermal therapy agent) might also affect the internalization by the cells. Then in previously reported PEGMA-based brush polymers, it has been demonstrated that BBPs with size 35×1120 exhibited three times higher cellular uptake in RAW264.7 macrophages, compared to the 35×220 nm BBPs (~6× shorter) and 35×35 nm (~30× shorter).⁶² Considering the cells used were macrophages, these results are expected since particles larger than 200 nm tend to be internalized by macrophages due to the macrophage nature as foreign material eliminator. Interestingly, a study reported by

Cui *et al.*¹⁷⁴ showed that the uptake of single-walled carbon nanotubes (195 nm, 390 nm and 630 nm) by RAW264.7 macrophage cells was length independent. They suggested that the intracellular accumulation of the carbon nanotube is independent of the length as long as the length is below 1 μm , which is in agreement with my results on NAM-based BBPs. However, since the information about the effect of BBPs length on the cell uptake of BBPs are still limited and the preceding published results do not imply consistent rules, I suggest a more comprehensive study should be conducted in the future by normalizing all parameters which might interfere with the parameter of interest.

d. Influence of Grafting Density

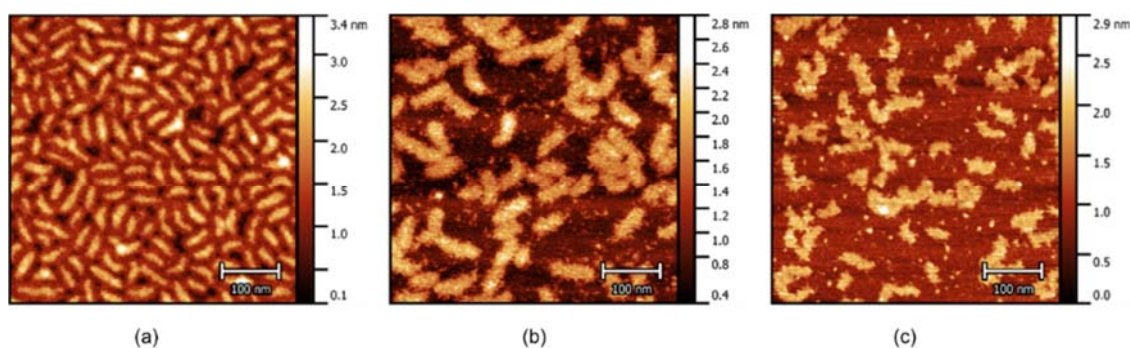


Figure 3.4 Atomic Force Microscopy (AFM) images of (a) SB-NAM, (b) SC50-NAM and (c) SC25-NAM. The scale bar represents 100 nm.

I also investigated the role of grafting density using Cy5.5-labelled SB-NAM, SC50-NAM and SC25-NAM. The uptake trend of the three compounds in both cells, 3T3 and MDA-MB-231-HM is similar, where the internalization of SB-NAM is the lowest (Figure 3.5). In MDA-MB-231 cells, however, the difference is more pronounced. While the internalization of SB-NAM is relatively low, the uptake of SC25-NAM and SC50-NAM was significantly higher, even at 3 h incubation (Figure 3.5b). At 24 h incubation, I observed an increase in cell uptake by decreasing the grafting density of short brushes.

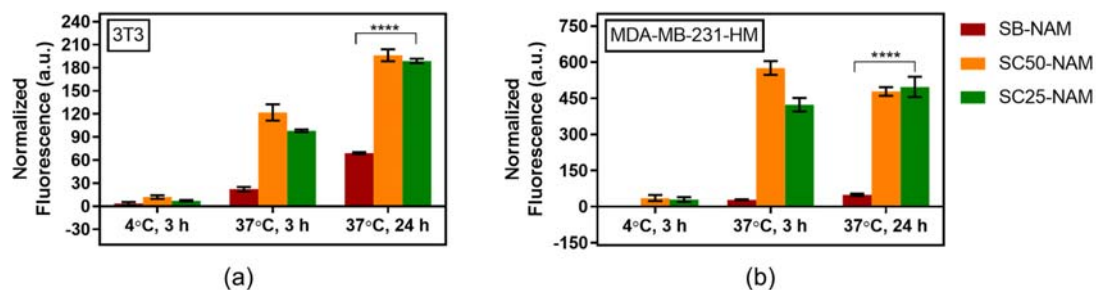


Figure 3.5 Cellular fluorescence intensity associated with Cy5.5 as determined by flow cytometry after incubation of the compounds for 3 h at 4°C, 3 h at 37°C and 24 h at 37°C in 3T3 and MDA-MB-231-HM cells. Data represents normalized geometric mean of fluorescence \pm SD for independent experiments done in triplicates: * $p < 0.05$, ** $p < 0.01$, *** $p < 0.001$, **** $p < 0.0001$.

Lowering the grafting density of the BBPs supposedly reduces the stiffness of the backbone due to lower steric overcrowding of the side chains.¹⁷⁵ In the case of the NAM-based short BBPs, the difference in the stiffness between SB-NAM, SC50-NAM and SC25-NAM is shown qualitatively by the AFM images (Figure 3.4). From the previous works from Sun *et al.*¹⁷⁶ using spherical (polymeric core)–(lipid shell), it has been shown that stiffer particles are internalized to a greater extent than the softer ones. The reason is that the soft nanoparticles experience deformation during internalization, which needs higher wrapping energy by the cell membrane, resulting in slower uptake. Similarly, Zhao *et al.*¹⁷⁷ demonstrated that stiff rod-like micelles are more likely to be taken up by breast cancer cells than the soft rod. However, my results showed the opposite, where the more flexible brushes (SC25-NAM) showed the highest cellular uptake, followed by the semi-rigid SC50-NAM and the rigid SB-NAM. I postulated this is the impact of lowering grafting density to 25%, which causes the structure to bend and/or shrink to smaller sizes and thus encounter more cell uptake.

Beside the stiffness of the brushes, the grafting density itself might influence the cellular uptake. In an *in vitro* study by Walkey *et al.*,¹⁷⁸ it was shown that the grafting density of PEG on the surface of Au nanoparticles can determine the composition of the adsorbed protein layer. As an implication of this, increasing PEG grafting density up to 0.5 PEG/nm² resulted in 20-169 reduction of macrophage uptake (using J774A.1 cells) relative to the non-grafted

AuNP. Although the cells used in that study was macrophage, the difference of uptake shown by SB-NAM, SC50-NAM and SC25-NAM in this study might be caused by the same reason. However, further study using macrophage would be useful to confirm this hypothesis.

3.3.3 Cell Internalization

Since I have demonstrated that the NAM-based BBPs were associated with cells, I then progressed to confirm the intracellular localization of the polymers by confocal microscopy. I hypothesized that the BBPs were internalized by cells and would be found in lysosome since their size is in the range to promote endocytosis.

For the first set of study, I compared SB-NAM, LB-NAM, Lin-NAM, and SB-PEG, using the AlexaFluor™488-labelled polymers (green). After incubation of 3T3 and MDA-MB-231 cells with the polymers for 24 h, the polymer staining was visible inside the cells, confirming polymers internalization by the cells and not only bound to the membrane. LysoTracker® (red) and Hoechst® (blue) were added to assess localization into the lysosome and nucleus, respectively. The merged images of the red, green and blue channels demonstrate colour coincidence of the polymer with the lysosomes of MDA-MB-231 cells (Figure 3.6 and Appendix, Figure A.22), confirming the internalization via endocytosis pathway, which is in line with flow cytometry data.

Interestingly, I observed only small amount of lysosome localization of the polymers in 3T3 cells, yet the polymers were verified inside the cells by considering the proximity of the green colours to the nucleus (Appendix, Figure A.23). Some factors might contributed to this phenomena. First, it can be caused by the size difference between lysosome of 3T3 and MDA-MB-231-HM. It has been acknowledged that lysosomal size can change in several human disease and enlarged lysosomes are known to reduce exocytosis.¹⁷⁹ Since 3T3 is considered “healthier”, which lysosome size is smaller, than MDA-MB-231-HM, I suggest the exocytosis happened to a greater extent. A more detail study is required to investigate this hypothesis.

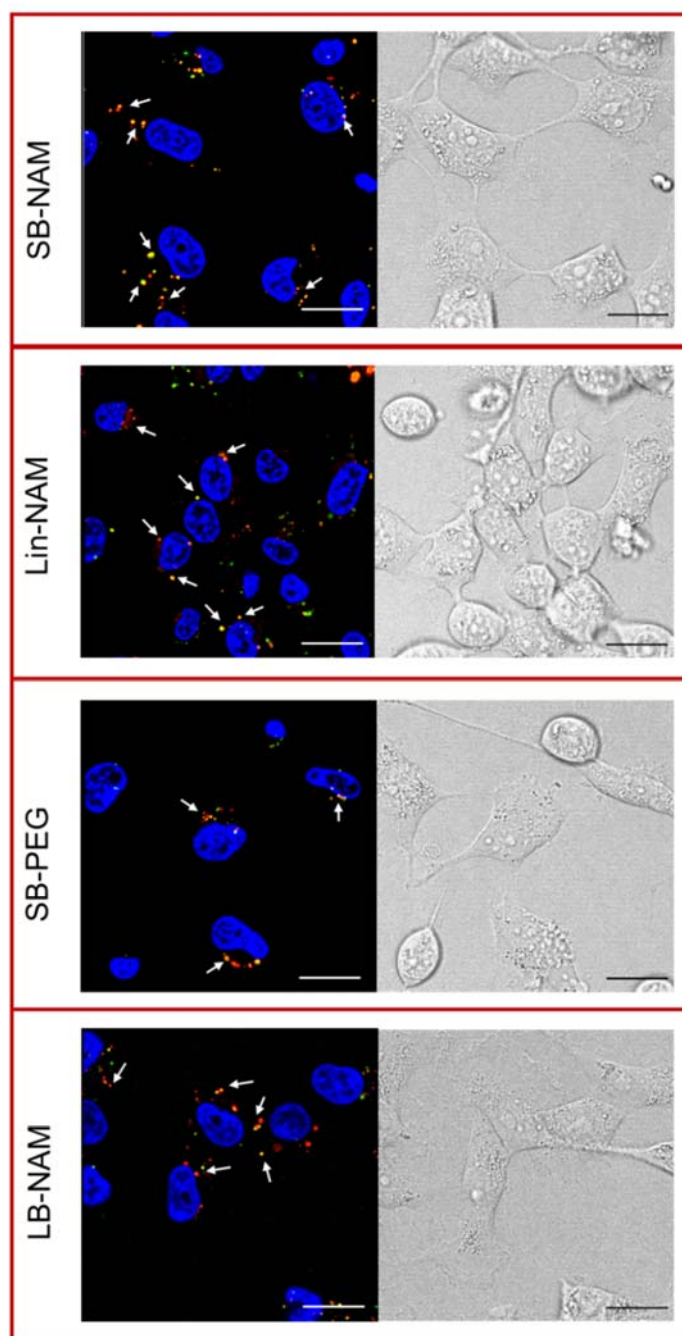


Figure 3.6 Confocal images of MDA-MB-231-HM cells treated with Alexa-488-labelled polymers (green) for 24 h at 37°C at a concentration of 0.3 mg/mL. Lysosomes were stained using Lysotracker® (red), nucleus were stained using Hoechst® (blue). White arrows indicate internalized BBPs. Scale bar 20 μ m.

My second set of study compared the different side-chain density between SB-NAM, SC50-NAM and SC25-NAM, using Cy5.5-labelled polymers. I changed the label to Cy5.5, a

near-infrared (IR) fluorescence-emitting dye, so they can be used for *in vivo* imaging analysis in the next study (Chapter 4). Note that the colour annotation is reversed from Alexa-488-labelled polymer. In this study, Cy5.5-labelled polymer is in the red channel while the lysosome stain (LysoSensor™ green DND 189) is in the green channel. This study also showed that all Cy5.5-labelled polymers were internalized by the cells and colocalized in lysosome (Figure 3.7 and Appendix, Figure A.24 and Figure A.25).

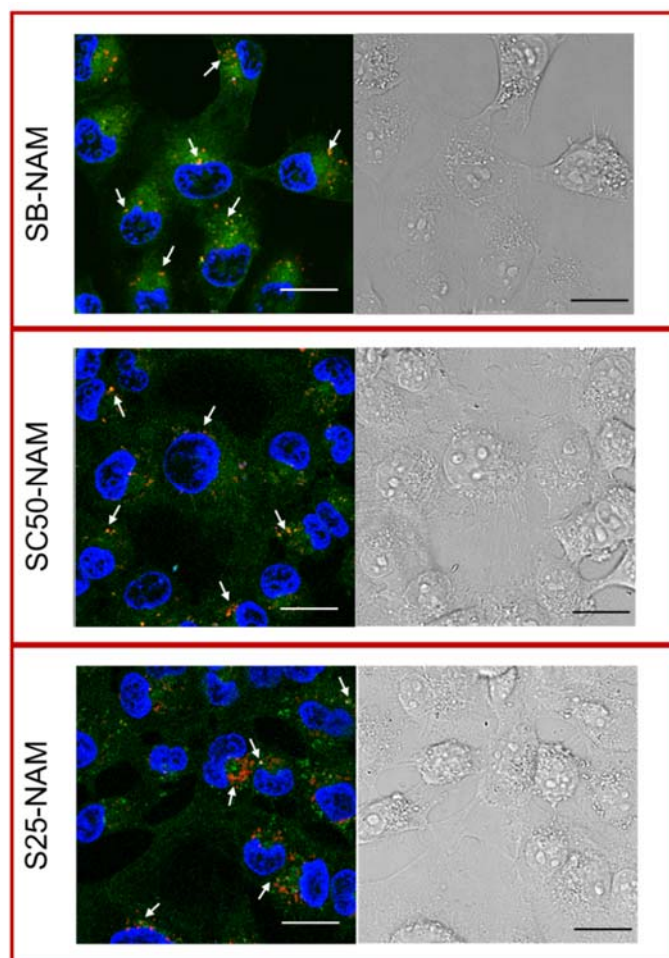


Figure 3.7 Confocal images of MDA-MB-231-HM cells treated with Cy5.5-labelled polymers (red) for 24 h at 37°C at a concentration of 0.3 mg/mL. Lysosomes were stained using LysoSensor® (green), nucleus were stained using Hoechst® (blue). Note that the dot-like structures of lysosome can still be seen, although it seems like the whole cytosol is green. White arrows indicate internalized BBPs. Scale bar 20 μ m.

Results of flow cytometry and microscope imaging indicated that my NAM-based BBPs with the designed size and shape can be internalized by 3T3 and MDA-MB-231-HM cells via endocytosis. Interestingly, the length of the backbone did not significantly affect the cellular uptake. The internalization becomes different when the grafting density is reduced from ~70% to ~50% and ~25%. However, no significant disparity is found between BBPs with grafting density ~50% and ~25%.

3.3.4 *In vitro* Degradation Study

The side chains of the brush polymers are connected to the backbone via an ester bond, while NAM itself is an amide (Figure 3.8). These ester and amide bonds are at risk of unfavourable degradation during their blood journey, which can be caused by some factors such as a change in blood pH as in acidosis condition (blood pH is 7.35 or lower), or the presence of esterase¹⁸⁰ and protease in blood. Therefore, I wanted to investigate if the BBPs would be degraded, especially within a few hours, which will affect their biological performance. To prove this, I carried out an *in vitro* degradation study to challenge the bond against hydrolysis. SB-NAM and SC25-NAM were chosen for this study for their prominent distinctive side chain density.

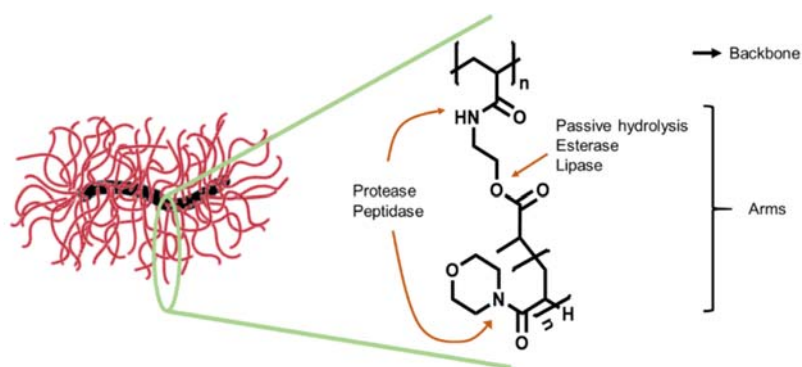


Figure 3.8 Brush illustration and its hydrolyzable groups

First, I would like to examine how degradable the BBPs are in normal blood pH condition, and therefore I incubated the polymers in PBS pH 7.4, in a shaker at 37°C. I hypothesized that decreasing side-chain density would lead to a less stable backbone-arms bond since the BBP core is more accessible for water molecule. In addition to this, I also conducted the study by incubation of polymers in acidic condition, pH 6.5 and pH 5.5, to mimic the acidic tumour microenvironment (for the intended use of BBPs) and lysosome vesicle (for when they are internalized by cells), respectively. I expected more degradation as the pH decrease, since the acid can catalyze the ester hydrolysis.¹⁸¹

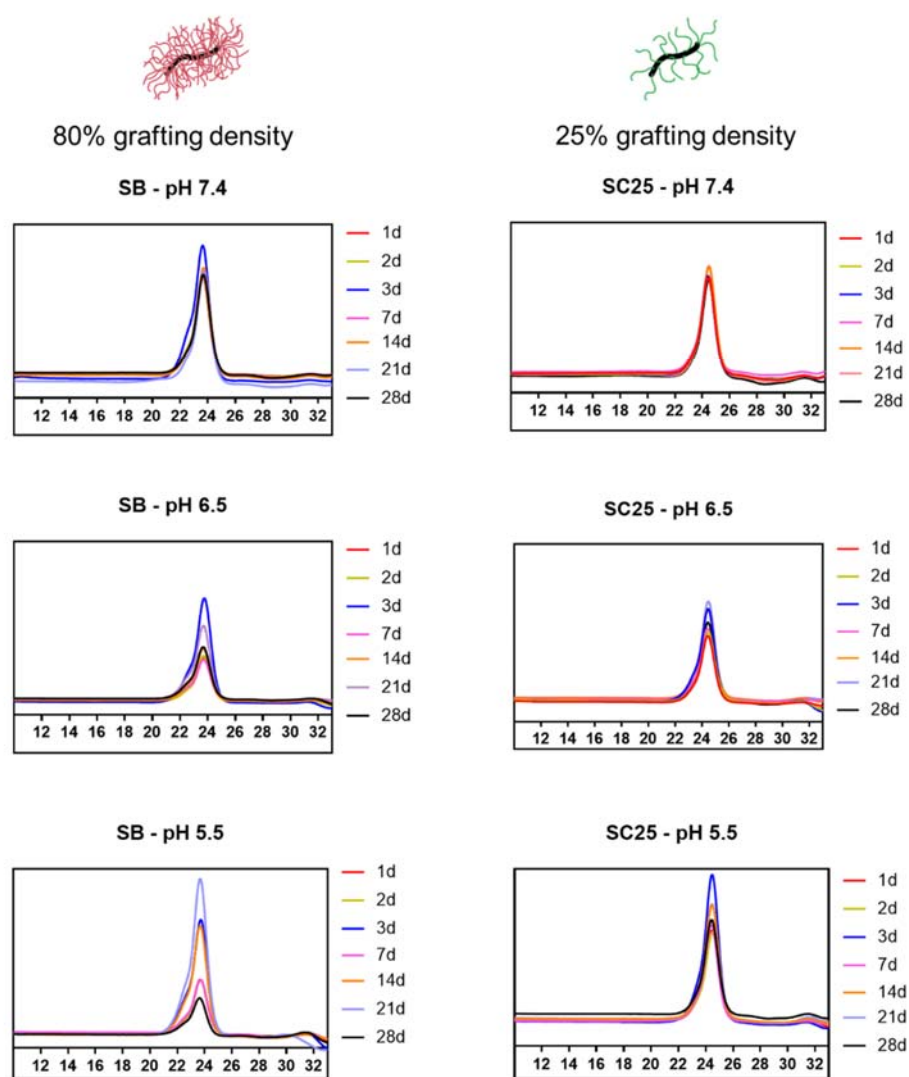


Figure 3.9 GPC chromatograms of SB-NAM and SC25-NAM, after incubation at 37°C in PBS pH 7.4, 6.5 and 5.5 for 28 days. Note, the intensity of the peaks are different due to different sample concentration.

GPC analysis was conducted to inspect any notable shift to longer retention time (lower molecular weight), or any appearance of new peak at 27-32 minutes retention time (molecular weight 6-9 kDa), which corresponds to the peak of released side chains. As a result, I observed no remarkable shift or appearance of new peak in all tested compounds regardless the pH environment, suggesting the stability of the ester bond in above condition (Figure 3.9). I suggest that the stability is caused by the highly packed side chains, which prevent H^+ molecule from entering the central part of the brush molecules, even with only 25% grafting density. Another suggestion might be that ester bonds between two polymer chains (backbone and side chain) are more resistant to hydrolysis than those in small molecules. The pH degradation study suggested that the NAM-based BBPs are relatively stable despite the fact that an ester bond is used to connect the side chain to the backbone. This stability ensures that the BBPs would maintain their overall molecular weight, size and shape when they are circulating in the blood.

3.3.5 Pharmacokinetics and Biodistribution

I have demonstrated that my NAM-based BBPs are water-soluble, not toxic at a concentration below 0.5 mg/mL, internalized by cells and stable to pH-induced hydrolysis. The next essential characteristics that should be assessed are the *in vivo* performance, which stipulates their proficiency as a potential candidate for drug delivery. Some main questions that I need to address are “Will the NAM-based BBPs be able to circulate in the body for long time period?”, “Will they be able to evade glomerular filtration?” and “Will they be vigorously apprehended by the reticuloendothelial system (RES) and therefore disposed in liver and spleen as the dominant RES organs?”. To answer these questions, I then conducted pharmacokinetics and biodistribution studies in healthy rats. I dosed rats since they carry ~20 mL of blood, allowing enough blood sample for all predetermined time points from the same individual rat. This will give a more reliable value compared to using smaller rodents with much

smaller blood volume, such as mice (~1.5 mL), where blood sample from each time point must be taken from a different mouse.

In order to aid detection for quantitative analysis, the polymers were labelled with radioisotope $[^{14}\text{C}]$ -ethanolamine. Labelling with a radioisotope is more preferable to the fluorescence tag since it offers a relatively easier, simpler and faster sample preparation and analysis since extraction of a sample from the biological matrix is not required. Unlike fluorescence signal that can be quenched by the presence of water¹⁸², the radioisotope signal is not affected by water molecules and thus, the reading is more reliable.

As that in fluorescence-labelling, the radioisotopes were also attached to the polymers by taking advantage of the presence of the NHS-acrylate unit in the polymer structure. This created a stable amide bond between acrylate and $[^{14}\text{C}]$ -ethanolamine, which ensure the radioisotope stays within the brushes during their journey in the blood circulation. The obtained ^{14}C -labelled Lin-NAM, SB-NAM and LB-NAM were purified by PD-10 desalting column and then dialyzed to ensure the removal of any excess radiolabels. This purification method is able to produce pure compound as proven by scintillation counting of size exclusion chromatography (SEC) fractions using a Sephadex size exclusion column (LH20, eluent: water) (Figure 3.10).

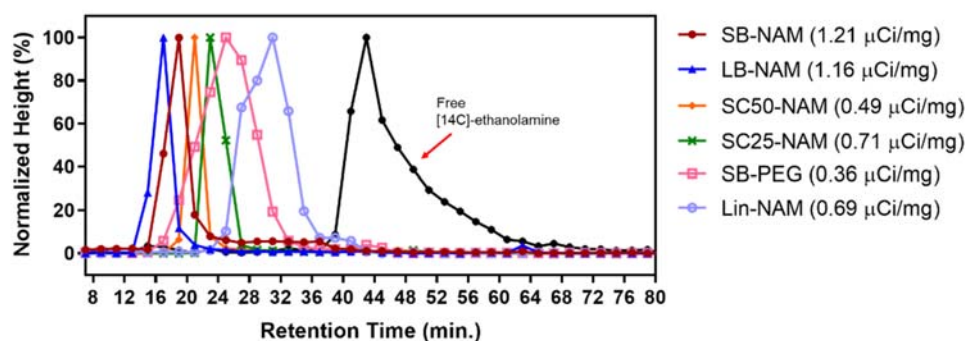


Figure 3.10 SEC Chromatogram of pure $[^{14}\text{C}]$ -labelled polymers obtained by liquid scintillation counting of collected fractions (1 mL per fraction).

The polymers were administered intravenously to male Sprague Dawley rats at a dose of equivalent to 1 μCi (2.5-10 mg/kg, depending on the radioactivity of each polymer). Plasma samples were taken at predetermined time points for 24 h and analyzed with scintillation counting to establish the plasma concentration versus time profiles. The non-compartmental (NC) pharmacokinetic parameters were calculated using PKSolver (Ms. Excel add-in).¹⁶⁴ Urine samples during 24-hour dosing were pooled to obtain the data of residual compounds found in urine.

a. Influence of Different Architecture on Pharmacokinetics and Biodistribution

As shown in Figure 3.11a, Lin-NAM was cleared immediately from the plasma with a clearance rate of approximately 25 mL/h, and a half-life around 2 h (Table 3.1). In contrast, the plasma concentration of SB-NAM was reduced by only less than 50% after 24 hours injection, indicating prolonged plasma retention with a half-life of more than 40 h. The extended circulation of SB-NAM was also reflected by the slow total clearance, which is around 0.4 mL/h (~50 fold slower than Lin-NAM). This clearance value is nearly identical to previously reported poly-PEG star polymers (0.28-0.61 mL/h)¹⁸³, long chain-PEGylated poly-L-Lysine dendrimers (0.4-0.9 mL/h)¹⁸⁴ and PEGMA-based brush polymer (0.42-2.67 mL/h)⁶².

In accordance with clearance, the 24-h plasma exposure (AUC_{0-t}) of SB-NAM was high, which indicates high bioavailability. The initial volume of the central compartment (V_c) of SB-NAM was similar to the blood volume, a typical characteristic for high molecular weight materials that do not readily distribute out of the central compartment. The terminal volume of distribution ($V_{d,\beta}$) of SB-NAM (23 mL), however, was slightly higher than blood volume (approximately 18-20 mL¹⁸⁵), indicating their distribution out of vasculature. The very high $V_{d,\beta}$ of Lin-NAM (~77 mL) is most likely due to very low plasma concentration as a result of rapid excretion, and not due to their distribution to organs. This was confirmed by analyzing the [^{14}C] residual in urine after 24 h, where as much as 50% of the injected dose of Lin-NAM was found in urine, more than 50-fold higher than SB-NAM (Figure 3.11b). These results suggest that the length of brush polymers play a more dominant role than the diameter in terms of evading renal

clearance. This is probably because the short dimension of BBP particles should align with endothelial pores to be able to pass through the glomerulus filter⁴⁶ which has a small probability to occur.

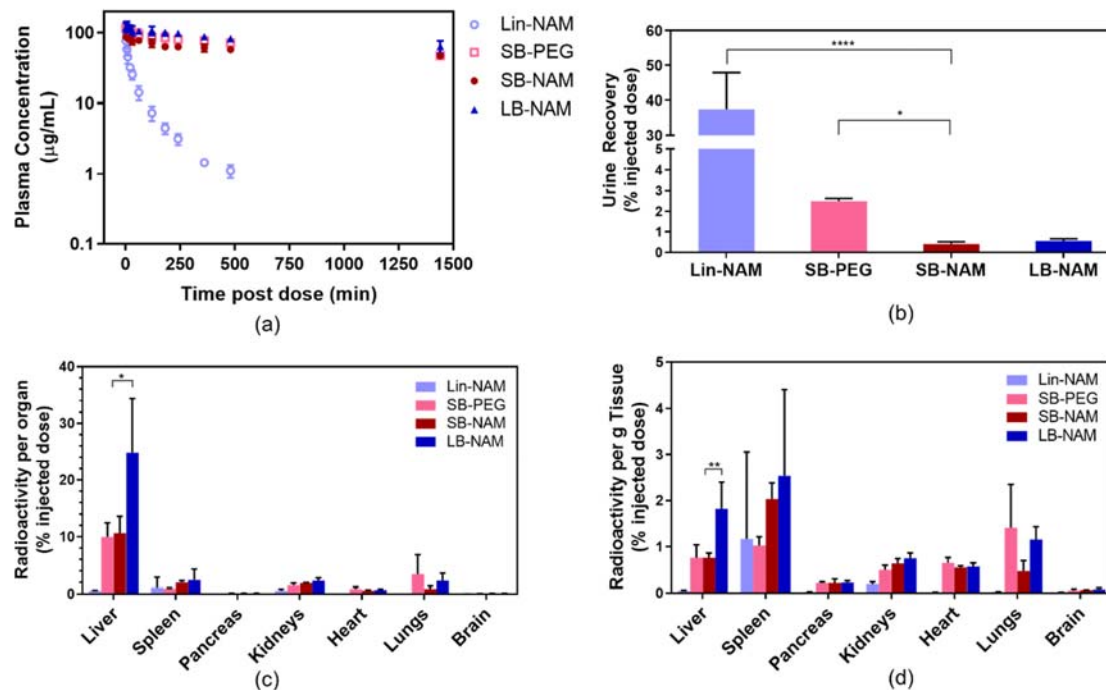


Figure 3.11 (a) Plasma concentration versus time profiles (normalized dose to 5 mg/kg), (b) percent of dose recovery in urine, (c) biodistribution (% injected dose per organ) and (d) biodistribution (% injected dose per g tissue), 24 h after intravenous administration of Lin-NAM, SB-PEG, SB-NAM and LB-NAM at 2.5-10 mg/kg (mean \pm SD, $n=3-4$ rats, * $p<0.05$, ** $p<0.01$, **** $p<0.0001$).

Table 3.1 Calculated pharmacokinetic parameters and urine recovery after intravenous administration of polymers to rats at normalized dose 5 mg/kg (mean \pm SD, $n=3-4$ rats).

Parameter		SB-NAM	LB-NAM	SC50-NAM	SC25-NAM	Lin-NAM	SB-PEG
$t_{1/2}$	(h)	42 \pm 4	34 \pm 3	40 \pm 14	36 \pm 5	2 \pm 0.3	28 \pm 8
C_0	($\mu\text{g/mL}$)	86.5 \pm 5.0	117.2 \pm 20.7	74.0 \pm 1.56	85.3 \pm 13.1	82.3 \pm 18.9	115.1 \pm 17.6
AUC_{0-4}	($\mu\text{g/mL.h}$)	1350 \pm 93	1925 \pm 238	1242 \pm 33	1363 \pm 197	59 \pm 10	1600 \pm 178
$AUC_{0-\infty}$	($\mu\text{g/mL.h}$)	4074 \pm 43	5086 \pm 1136	3634 \pm 1013	3680 \pm 806	62 \pm 10	3460 \pm 522
$V_{d\beta}$	(mL)	22.4 \pm 2.4	14.9 \pm 2.9	23.7 \pm 1.7	21.7 \pm 3.3	76.8 \pm 19.8	17.1 \pm 2.6
CI	(mL/h)	0.368 \pm 0.004	0.305 \pm 0.063	0.433 \pm 0.110	0.422 \pm 0.096	24.707 \pm 4.176	0.441 \pm 0.065
V_{ss}	(mL)	22.2 \pm 2.2	14.9 \pm 1.8	23.5 \pm 1.7	21.5 \pm 3.2	51.9 \pm 14.0	16.8 \pm 2.7
V_c	(mL)	17.4 \pm 1.0	13.1 \pm 2.2	20.3 \pm 0.4	17.9 \pm 2.9	19.2 \pm 5.7	13.3 \pm 1.9

Following plasma circulation, another crucial parameter that should be identified is the dispositions of the polymers in organs, particularly the organs in charge of clearing foreign materials: kidney, liver and spleen. While the kidney has significant role in the clearance of particles below 15 nm, larger particles are most likely cleared by reticuloendothelial system (RES) in the liver and spleen via phagocytosis pathway.¹⁸⁶ To assess this parameter, following intravenous (IV) administration, seven major organs (liver, spleen, pancreas, kidneys, heart, lungs, brain) were collected after 24 h, and the residual [14C] in each organ was quantified. The harvested organs were not perfused, and thus the [14C] counts could be resulted from the entrapped blood, suggesting even lower actual percentages than are obtained in the more vascularized organs.

The data in Figure 3.11c reveal that 24 h after administration, the majority of the [14C] from SB-NAM were recovered in the liver, confirming the clearance of the polymers by the reticuloendothelial system (RES).⁹³ The percentage of accumulations were found only ~10% of injected dose (%ID) per organ for SB-NAM. This value is similar to 220 nm PEGMA-based BBPs⁶² and 64 kDa PolyPEG star polymer¹⁸⁷, and lower than previously reported PEGylated lipid-calcium-phosphate nanoparticles (20-40%)¹⁸⁸ and citric-Au nanoparticles (58%)¹⁸⁹. Lin-NAM was found at a very low amount across all studied organs, apparently due to their extensive excretion by the kidney, as expressed by the high concentration found in urine. The fast renal clearance reduced the exposure time of Lin-NAM to organs, particularly RES organs, and therefore resulted in low total organ accumulation.

b. Comparison between PNAM and PEG

Inevitably, PEG is widely used in nanomedicine, and even most FDA-approved drugs employed PEG in their nanoparticles system.¹⁹⁰ Since PEG has already been a gold standard due to their ability to extend the circulation half-life of nanoparticles, I also compared my SB-NAM with SB-PEG in this study. From the pharmacokinetics study, I found that SB-NAM showed a similar plasma concentration profile to SB-PEG (Figure 3.11a). However, the

clearance of SB-PEG is slightly higher than SB-NAM (0.441 vs 0.368 mL/h, respectively). In addition, the radioactivity found in urine for SB-PEG was also slightly higher than SB-NAM (2.5% vs 0.5% ID) (Figure 3.11b).

As mentioned at the beginning of the Result and Discussion, I produced SB-PEG with a shorter backbone due to limitations of the synthesis by grafting-through method, resulting in PEG brush with high dispersity ($\bar{D} = 1.30$) and nearly spherical structure. The high dispersity means the size of SB-PEG species are distributed broadly, and there could be SB-PEG species with a size below the glomerulus filtration cut off. In addition, PEG possesses a less bulky structure than PNAM, which probably causes the side chain of SB-PEG to squeeze and pass through glomerulus filter. This might be the rationale for higher clearance and urine disposition of SB-PEG compared to SB-NAM.

Comparing SB-NAM and SB-PEG, the accumulation of both polymers in the liver is similar, as shown in Figure 3.11c (~10% ID per organ). Although the accumulation of SB-NAM in the spleen is slightly higher than SB-PEG, particularly when expressed as %ID per g tissue (2% and 1%, respectively), the difference is negligible (Figure 3.11d). The most possible reason is that the difference in polymer size (SB-NAM is slightly longer than SB-PEG). These results provide supportive information to use PNAM as an alternative for PEG, an addition to the previous work on PNAM as outer decoration for liposome¹³⁶ and coating for poly(lactic acid) (PLA) nanoparticles¹³⁵.

c. Influence of Backbone Length on Pharmacokinetics and Biodistribution

Comparing the plasma concentration and PK parameters, LB-NAM showed negligible differences to SB-NAM (Figure 3.11a), indicating no effect given by increasing the backbone length to three times, as long as the elongated structure is still maintained. The radioactivity found in urine also represented similar results. In previously studied PEGMA-based brush polymers, increasing aspect ratio up to ~19-fold resulted in only small increases (3-fold) in clearance⁶². Therefore, no length-dependent plasma retention and clearance between SB-

NAM and LB-NAM is not surprising. The only difference is on the low $V_{d,\beta}$ of LB-NAM which is apparently due to their very high molecular weight that limit their extravasation.

Interestingly, I found quite higher liver accumulation from LB-NAM (~25% ID per organ) compared to SB-NAM (~10%), which is most probably due to its size (Figure 3.11c). Particles with a size of 150-200 nm can be effectively recognized by RES and trapped in the liver and/or spleen¹⁹¹, which is an explanation for higher liver and spleen uptake of the long brush (length ~130 nm) compared to the short one (length ~40 nm). When normalized by organ size, as presented in %ID per g tissue (Figure 3.11d), LB-NAM was disposed to the spleen in slightly greater extent than to liver, indicating that the clearance of LB-NAM by splenic filtration is more preferred.

All these results on SB-NAM vs LB-NAM demonstrated that creating the BBPs with a significant length to diameter ratio might not be necessary as it would cost more dispositions in RES organs. However, a longer backbone provides more side chains, which can offer more functionalization sites to allow higher payload of passenger molecules. Also, since the uptake of LB-NAM to liver and spleen is the most prevalent, its clinical application might be directed to target disease on those organs.

d. Influence of Grafting Density on Pharmacokinetics and Biodistribution

When comparing between different grafting densities, SC50-NAM and SC25-NAM did not exhibit remarkable distinction with SB-NAM in terms of pharmacokinetic profile, indicating no impact on plasma retention given by reducing grafting density up to 25% (Figure 3.12a). This finding is the opposite of PEGylated nanoparticles¹⁹², liposomes¹⁹³ and dendrimers¹⁹⁴, where decreasing the surface PEG density led to reduced circulation time. This surface density-dependency on plasma retention is apparently only applied to spherical materials, and it is more related to the decrease in stealth capacity. In the case of elongated polymers, the overall molecular weight, length and final conformation in solution appeared to dictate their plasma circulation time. However, despite their similar pharmacokinetic profiles, the trend in the percentage of dose recovered in urine was increasing from SB-NAM (0.4%), SC50-NAM

(1.5%) and then SC25-NAM (2.4%) (Figure 3.12b). This is probably because the brush with the lowest grafting density, SC25-NAM, has a more flexible structure that increases the likelihood to pass glomerulus filtration. The similarities in plasma concentration and pharmacokinetics for the three short brushes are also demonstrated in their organ distribution (Figure 3.12c and d). Despite the different grafting density and thus structure rigidity, their dispositions in RES organs, liver and spleen are not distinctive (~10% ID per organ in liver and ~1.7% ID per organ in spleen).

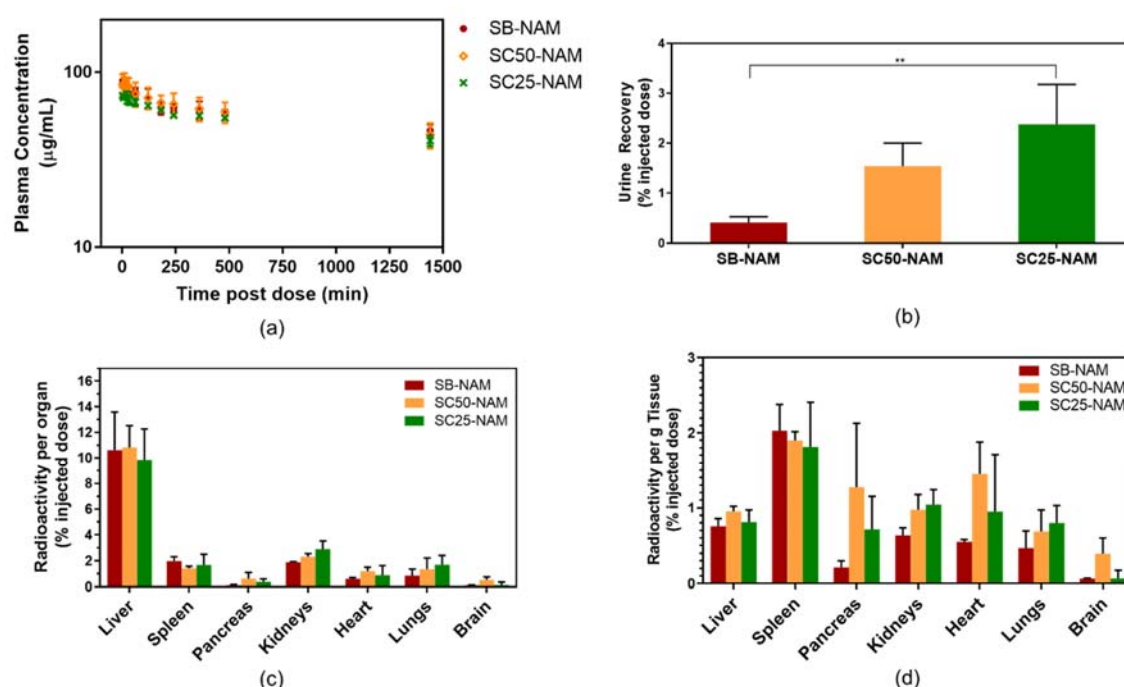


Figure 3.12 (a) Plasma concentration versus time profiles (normalized dose to 5 mg/kg), (b) percent of dose recovery in urine, (c) biodistribution (% injected dose per organ) and (d) biodistribution (% injected dose per g tissue), 24 h after intravenous administration of SB-NAM, SC50-NAM and SC25-NAM at 2.5-10 mg/kg (mean \pm SD, n=3-4 rats, **p<0.01).

So far, there is no published work about the effect of grafting density on the pharmacokinetics and biodistribution of BBPs, and therefore I do not have comparable data. If I correlate the grafting density with the rigidity of BBPs, I could probably compare my data with

other kinds of nanoparticles. However, almost all studies about the effect of nanoparticles rigidity were only done *in vitro*. Müllner *et al.*⁶², studied the effect of BBPs rigidity on pharmacokinetics by comparing BBPs with and without crystalline core, which represent rigid and flexible BBPs, respectively. They found that the long rigid BBPs (aspect ratio 19) exhibited more rapid plasma clearance than the long flexible BBPs, while the short rigid and flexible BBPs (aspect ratio 4) were cleared to a similar extent. Their distribution in the spleen was similar (~10%) when expressed as %ID per g tissue, regardless of the length and rigidity. Based on that results and ours, I postulated that the rigidity does not greatly impact the plasma circulation and biodistribution of short BBPs, as long as the side chains can still prevent the structure from coiling. BBPs with less grafting density (i.e. 25%) will be accounted for less steric hindrance, and therefore provides more space for drug attachment/entrapment.

It is interesting to note that the cellular uptake in non-phagocytic cells of the SB-NAM is different from SC50-NAM and SC25-NAM (Figure 3.5). As mentioned earlier, the grafting density might contribute to the difference on the cell uptake. If this behaviour can be extrapolated to the phagocytic cells, their distribution in RES organs should be different too. However, some studies showed different uptake behaviour between phagocytic and non-phagocytic cells^{195,196}. For example, the uptake of negatively charged gold nanoparticles (AuNP) in RAW264.7 (macrophage) is higher than in HepG2 cells¹⁹⁶. When the charge of AuNP was changed into more positive, there was no difference between the uptakes of both cells. Since I have not studied their internalization in the phagocytic cells, it might be useful to investigate this in the future study.

To summarize, all NAM-based BBPs showed remarkable PK profile, with a circulation half-life ranging from 34-40 hours, indicating their potential to be used as drug delivery carriers. The accumulation of all BBPs with a short backbone (DP150) in RES organs after circulating for 24 h were low (~10%). Their total accumulation in other organs was significantly low (<5%), similar to the previously reported Poly-PEG star polymers¹⁸³, PEGMA-based brush polymer⁶² and PLA-PEG nanoparticles¹⁹⁷. Such low levels of organ uptake indicate that the compounds are still circulating systemically. The very low clearance, together with a low level of unspecific

organ accumulation, suggest that brush/comb NAM polymers could be potential candidates for drug delivery.

3.4 CONCLUSION AND FUTURE DIRECTION

NAM-based polymers are not toxic up to a concentration of 0.5 mg/mL. They demonstrated time and temperature-dependent internalization in cells, confirming the typical energy-dependent cell uptake of nano-sized materials via endosomotropic mechanism, although some of them showed a different rate of uptake. Their internalization into the cells was also confirmed by confocal imaging studies, which showed the presence of the compounds inside the lysosome of the cells. After intravenous injection to rats, all elongated NAM-based BBPs exhibited prolonged circulation compared to linear PNAM, with low clearance and long elimination half-life (more than 30 h), regardless of their aspect ratio and side-chain density. Moreover, their *in vivo* behaviours are comparable to PEG-based BBPs suggesting their potential as alternative to PEG, with the advantage of the synthesis. NAM-based BBPs with a short backbone (DP of 150) exhibited low organ accumulation within 24 h. Collectively, the results suggest that NAM-based BBPs are suitable for drug delivery carriers, from the synthesis standpoint as well as its performance in cell association, pharmacokinetics and biodistribution.

Further study would be necessary to investigate the organ uptake of the polymer over a longer period time. Since the brush/comb polymers were accumulated in normal tissues in relatively low concentration, I am interested in studying their accumulation in the tumour, and determining their ability to undergo enhanced permeability and retention (EPR) effect. I will address this question in Chapter 4.

CHAPTER 4. BIODISTRIBUTION OF 4-ACRYLOYLMORPHOLINE-BASED BOTTLE BRUSH POLYMERS IN 4T1 TUMOUR MICE MODEL

4.1 INTRODUCTION

Cancer is one of the most frequent causes of death globally, and the use of chemotherapeutics for cancer treatment remains problematic, mainly due to the lack of treatment specificity. Since the index therapy of chemotherapy regimens are extremely slim, this unspecified therapy can cause severe and detrimental side effects. Therefore, to reduce the toxicity of the drugs, the necessity of targeted therapy becomes crucial, and this is where nanoparticles play their roles.

Nanoparticles have been broadly investigated for the delivery of cytotoxic drugs. They demonstrate the ability to improve the performance of therapeutics by increasing their solubility and stability as well as extending the blood circulation of the therapeutics. Furthermore, since Maeda's discovery of enhanced permeability and retention (EPR) effect in the mid 1980s¹⁹⁸, numerous different nanoparticle designs have been engineered to employ passive targeting. Based on the principle of EPR effect, macromolecules larger than 40 kDa can extravasate and accumulate in tumour tissues due to increased permeability of tumour vasculature and then be retained there due to improper lymphatic function that reduce the disposal of such materials to lymphatic system.¹⁹⁹

Although the EPR effect seems promising, in most of reported studies, the majority of the investigated nanoparticles failed to accumulate in tumour tissues at high concentration. In fact, only approximately 0.7% of injected dose were distributed to solid tumour²⁰⁰, which disputes the principle of passive targeting by EPR effect. Those injected nanoparticles mostly ended up in the reticuloendothelial system (RES) organs, mainly in the liver and spleen. Therefore, nanoparticle is still an interesting topic of research which goal is to achieve high tumour accumulation.

Particle shape has been recognised as an important parameter that determines the *in vivo* fate of drug carrier systems.^{36,201} Some literature suggested that rod-like particles offer improvement in tumour accumulation compared to their spherical counterpart.²⁰²⁻²⁰⁴ Interestingly, in a study using PEGylated ¹⁹⁸Au-doped nanoparticles, despite the lower tumour accumulation of rod-shaped compared to spheres, the rod-shaped nanoparticles could reach the core of the tumour, while the spheres were only observed on the surface of the tumour.⁴⁸ It has also been shown that rod-shaped nanocrystals with a shorter aspect ratio exhibited higher tumour accumulation than nanocrystals with a higher aspect ratio.²⁰⁵

Among many types of nanoparticles, polymeric nanoparticles have gained tremendous interest in biomedical application due to their flexibility in synthesis and ease of tailoring to various architecture, especially to produce non-spherical structures such as rod-like and worm-like particles. Furthermore, various specific functionalities can be incorporated into the polymer structure for easy attachment of cargo molecules, including drugs, targeting ligand, labelling molecules and other molecules of interest. Some studies have highlighted that rod-shaped and worm-shaped nanoparticles made from polymer also outperform their spherical analogues in term of efficacy in tumour.^{49,94,202}

In Chapter 3, I have demonstrated that my NAM-based bottle brush polymers (BBPs), which include short brush NAM (SB-NAM), long brush NAM (LB-NAM), short comb NAM 50% (SC50-NAM) and short comb NAM 25% (SC25-NAM), exhibited extended blood circulation in healthy animals with half-life varied between 30 to 40 hours. Their distribution in organs, including RES organs, are relatively low. However, the information whether these BBPs will perform passive distribution to tumour still needs to be investigated. In this study, I investigated passive tumour targeting of my NAM-based BBPs. I also evaluated the influence of increasing the backbone length to three times (SB-NAM vs LB-NAM) and reducing grafting density to 25% (SB-NAM vs SC25-NAM).

4.2 EXPERIMENTAL METHOD

4.2.1 Materials

For this experiments, I used Cy5.5-labelled and [14C]-labelled SB-NAM, LB-NAM, and SC25-NAM that I have synthesized with methods described in Chapter 3.

4.2.2 Cells

4T1 (mouse mammary carcinoma) cells were obtained from the European Collection of Cell Cultures (ECACC). The cells were revived from frozen stock 2-3 weeks before experiments and grown in DMEM supplemented with 10% v/v of foetal calf serum. Cells were grown as adherent monolayers at 37°C in a 5% CO₂ humidified atmosphere and passaged at approximately 70-80% confluence.

4.2.3 Animals

Immunocompetent mice (BALB/c) (female, 5-6 weeks of age) were purchased from Monash Animals Research Platform (Victoria, Australia) and underwent acclimatization for 7 days prior to the experiments. Animals were housed on a 12 h light/dark cycle and were provided food and water at all times. The experiments protocol (protocol number 18473) was approved by the Monash Animal Ethics Committee, Monash University (Melbourne, Victoria).

4.2.4 Tumour Induction

4T1 cells were used between passage 8-13. One hour before injection, cells were harvested using TrypLE Reagents (Thermofisher), washed once in dPBS and resuspended to 2.5×10^6 cells/mL in dPBS. 50,000 cells (in a final volume of 20 μ L) were injected into the fourth mammary fat pad of each mouse using a 25G needle, under isoflurane. Tumour size was measured with vernier callipers every 2 days, by measuring the longest (a) and the shortest (b) dimensions of the tumour. To calculate the volume (V), the following equation is used²⁰⁶:

$$V = \frac{4\pi}{3} \times (a \times b^2)$$

Equation 4.1 Calculation of tumour volume based on measurement using manual vernier calliper

4.2.5 Qualitative Biodistribution Studies

When the tumour volume reached 40 mm³, mice were injected with Cy5.5-labelled polymers via tail vein under isoflurane and then put back to the cage. After 24 h, mice were imaged using IVIS imaging system (PerkinElmer, MA, USA) using the included filter settings for Cy5.5 (ex = 640 nm), with an exposure time of 1s, f = 4, pixel = 1x1, and binning factor = 4. After imaging, the mice were euthanized by cervical dislocation or a lethal dose of Pentobarbitone Sodium and then the organs were harvested. All harvested organs were then imaged again using the same IVIS imaging system and setting.

4.2.6 Calculation of Fluorescence Intensity

The fluorescence intensity of each organ from the IVIS image was measured using Fiji ImageJ. Measurement was set to obtain area, integrated density and mean grey value. Using the freehand tool, a region of interest (ROI) from each organ was selected and then measured to gain the three parameter values. ROI from background (five spots) was also selected and measured to obtain the average mean grey value of the background. The obtained integrated density value was then corrected using the following equation:

$$CTF = ID - (A_{ROI} \times \text{average mean of background})$$

Equation 4.2 Calculation of corrected total fluorescence

where CTF is the corrected total fluorescence, ID is integrated density generated from the software, A_{ROI} is the area of selected region from each organs, and the average mean of background is the average of mean grey value of background. The same calculation was also

carried out for blank organs. The resulting CTF values of blank organs were used to subtract the CTF values of compounds-treated organs.

4.2.7 Quantitative Biodistribution Studies

When the tumour volume reached approximately 100 mm³, mice were injected with [14C]-labelled polymers (dose 47-58 mg/kg) via the tail vein under isoflurane. After 24 h, the mice were anesthetized, and the whole blood was withdrawn via cardiac puncture, after which the mice were euthanized either by an overdose of pentobarbitone sodium or cervical dislocation. The organs/tissues, including liver, spleen, pancreas, kidneys, heart, lungs, and tumour, were then collected.

Organ samples were homogenized using a gentleMACS Dissociator (Miltenyi Biotech) with 2 mL of MilliQ water and duplicate samples from each tissue homogenate (containing 20 mg of tissue) were placed into 4-mL scintillation vials, after which 500 µL of Solvable (Perkin Elmer) was added. From two samples of each organ, one was processed with the addition of a known quantity of radiolabel (spiked) prior to the addition of Solvable. The spiked samples are for correction of any reduction in radioactivity counting efficiency due to the sample preparation process.

Samples were then heated at 60°C overnight to facilitate tissue digestion. The samples were cooled to room temperature and 50 µL hydrogen peroxide (30% w/v) were added to each vial. Samples were left open at room temperature until bubbles ceased. Ultima Gold (3 mL) was then added and the mixtures were vortexed. The samples were then stored at 4°C in the dark, without agitation, for at least 3 days prior to scintillation counting. Blank organs (non-spiked only) and Solvable blank (spiked and non-spiked) also were treated as above to provide background correction. All samples were then scintillation counted on a Packard Tri-Carb 2000CA liquid scintillation analyzer (Meriden, CT) at 12°C.

Processing efficiency was calculated, using the same Equation 3.2:

$$\text{Efficiency} = \frac{\text{spiked tissue}_{\text{dpm}} - \text{tissue}_{\text{dpm}}}{\text{spiked solution}_{\text{dpm}}}$$

where $\text{spiked tissue}_{\text{dpm}}$ was the mass-corrected (subtracted by blank tissue) radioactivity measured in the spiked samples, $\text{tissue}_{\text{dpm}}$ was the mass-corrected (subtracted by blank tissue) radioactivity in the non-spiked tissue samples, and $\text{spiked solution}_{\text{dpm}}$ was the known amount of radioactivity added to the spiked Solvable blank. Effectively, the calculation indicates the efficiency of counting, using the known (spiked) amount of radioactivity in each tissue as a reference. This value for efficiency was used to correct the [14C] content in the processed sample using the same Equation 3.3:

$$\text{Tissue}_{\text{dpm,corr}} = \frac{\text{Tissue}_{\text{dpm}}}{\text{efficiency}}$$

The activity in the whole organ was then calculated knowing the mass fraction of the entire organ present in the processed sample. The results are expressed as either the percentage of injected dose present in the organ or the percentage of injected dose per gram of tissue.

4.3 RESULTS AND DISCUSSION

4.3.1 Tumour Induction

Although using a combination of nanoparticles and EPR effect sounds promising, with an increasing number of research and publications citing nanoparticles and EPR, failure on most of their clinical translation remains a big issue.^{198,199} The reasons for this problem are still indecisive, but it is well-known that cancer biology is very complex. As such, providing a tumour model for assessing a novel drug delivery system, which can resemble the real tumour condition as close as possible to that in human, is required.

Ectopic xenograft models are widely used for studies of nanoparticles^{61,94,207} due to their ease of growth and reproducibility. With this model, the human-derived cancer cells are subcutaneously injected into the body part of immunocompromised mice. “Ectopic” means that the transplanted site is usually different from the origin of the cultured cells. For example, transplantation of breast cancer cells, which are originated from mammary tissues, to hind leg of mice.

It is widely known that the immune system and inflammation play a crucial role in cancer progression. In human, the successfully growing tumour has conquered the opposition from the immune system after years, and thus, they have developed to a high level of genetic diversity. On the other hand, the immune system of the animals in xenograft models is knocked down to allow the tumour, which derived from human, grow freely with minimum defense from natural immune system. Hence, xenograft models will produce a localized and relatively homogenous tumour that represents a different microenvironment than that of human cancer.²⁰⁶

Another type of murine tumour model, named syngeneic model, offer two benefits.²⁰⁸ First, this model involves implantation of mouse-derived cancer cells, and therefore utilizes immune-competent mice. Although cancer in mice is different than that in human, by using this model, the role of immune response in cancer progression and metastasis can be included. Second, the interaction between cancer cells and host tissue will not be disrupted by inter-species interactions, because the genetic background of the implanted cancer cells are the same as the host. This model can mimic a more real neoplastic situation in a human patient because the immune system is still maintained. Therefore, I chose a syngeneic model to study the distribution of my BBPs to tumour. In addition, I injected the cancer cell line into the site of origin of the cancer cells (orthotopic) and therefore allowed the tumours to grow according to their natural environment.

The 4T1 mouse-derived triple-negative mammary tumour is chosen for the syngeneic model of breast cancer in this study due to its similarity to advanced human breast cancer, especially when the primary tumours reach >3 to 4 mm in diameter.²⁰⁹ The 4T1 cells are known

for their easy inoculation into the mammary gland, allowing the primary tumour to grow in its genuine site. In this study, the cells were injected into the fourth mammary fat pad (Figure 4.1a and b).

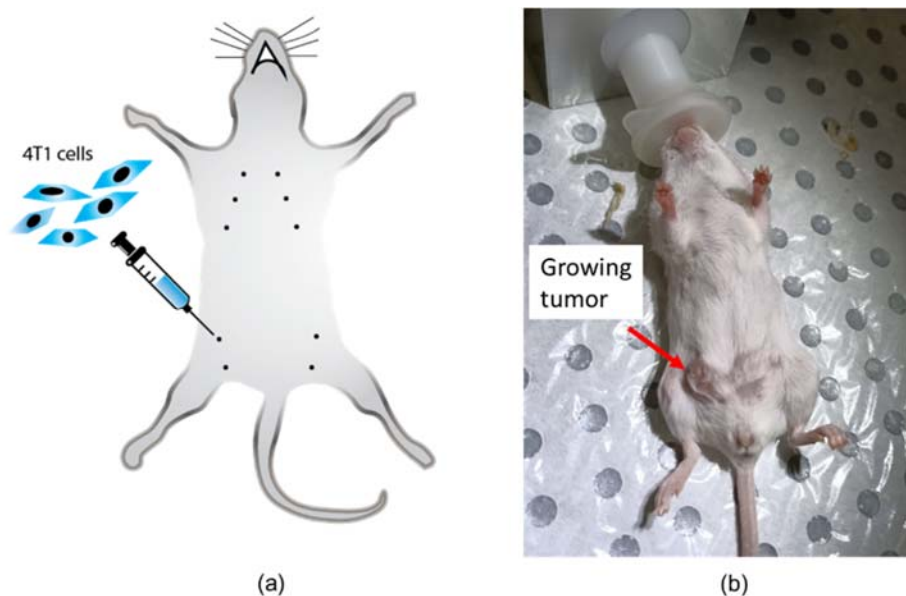


Figure 4.1 (a) Schematic illustration of 4T1 cells inoculation to mouse and (b) tumour bearing female BALB/c mice

In the previously reported study, the onset of tumour after inoculation of 10,000 and 100,000 4T1 cells were 8-10 days and 6-8 days, respectively.²¹⁰ Since I transplanted 50,000 4T1 cells, I suggested that the tumour would be palpable within 6-10 days. Indeed, I observed that 25 of 30 mice showed a measurable tumour on day-10 post-inoculation (Table 4.1). However, the other five mice started to grow palpable tumour later within 11-13 days post-inoculation.

Interestingly, despite the same onset of the palpable tumour, not all mice grew tumour at the same rate, resulting in a high deviation in tumour size on each measurement day (Figure 4.2a). Figure 4.2b showed the inter-mouse variability on the tumour growth rate, where some mice showed rapid growth of tumour and reached $\sim 100 \text{ mm}^3$ tumour 4-5 days after the onset

of palpable tumours (green and orange curve), while some mice exhibited slow tumour growth and only reached ~60 mm³ 10 days after the onset (purple curve).

Table 4.1 Tumour growth analysis of 4T1 cells in syngeneic female BALB/c mice

Parameters	Number of mice (%)
Onset of palpable tumour ^a	10 days
	25 of 30 (83%)
	>10 days
	5 of 30 (17%)
Tumour size reached within 20 days ^b	90-150 mm ³
	18 of 30 (60%)
	40-80 mm ³
	10 of 30 (33%)
	<20 mm ³
	2 of 30 (7%)

^atime when the tumour can be felt

^bmeasured using manual vernier calliper

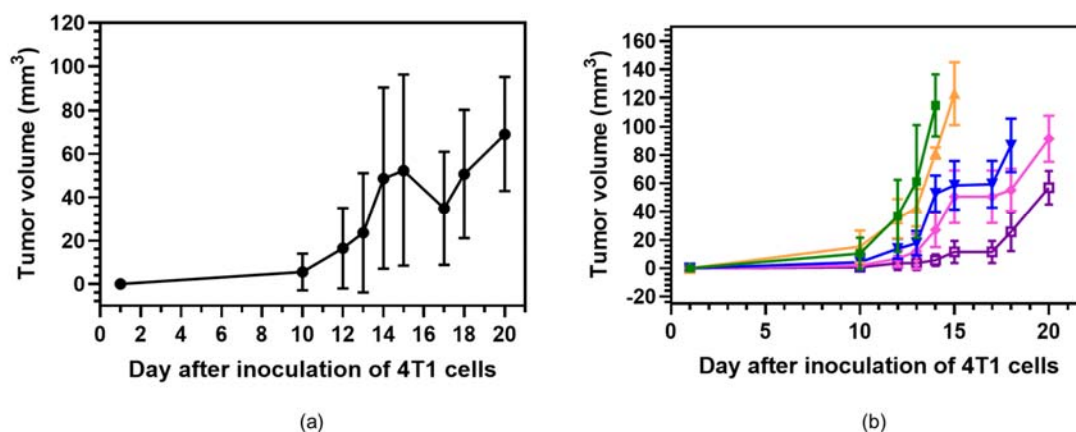


Figure 4.2 Profile of 4T1 tumour growth (a) from all female BALB/c mice (n=28, mean±SD) (b) grouped by similar tumour growth rate (each curve shows n=5-7, mean±SD)

Since immune system plays a vital role in cancer development, it is understandable that a high degree of inter-mouse variability exists in syngeneic models with respect to tumour growth rate.²¹¹ This fact provides an advantage of using syngeneic models, where the variability in cancer progression is similar to the real neoplastic condition. However, to minimize the influence of tumour size in the distribution of the BBPs, I grouped the mice based on the similar tumour growth rate, and used one group for one compound when the group already

developed $\sim 100 \text{ mm}^3$ tumour. Additionally, since 4T1 is highly metastatic,^{209,212} I set the experimental endpoint for a maximum of 20 days post-inoculation (or 10 days after tumours were palpable) to minimize the risk of metastasis, and thus, diminish the influence of metastatic condition in animals.

4.3.2 Qualitative Biodistribution Studies

In this study, I visualized the ability of the BBPs to perform passive distribution by *in vivo* imaging, 24 hours after compound injection. I employed SB-NAM, LB-NAM and SC25-NAM to investigate the effect of backbone length (SB-NAM vs LB-NAM) and grafting density (SB-NAM vs SC25-NAM). SB-NAM and LB-NAM have a more rigid structure with different length, while SB-NAM and SC25-NAM have similar length but have different structure conformation due to different grafting density. From the pharmacokinetic study in rats (non-tumour), the three compounds exhibited a similar pharmacokinetic profile. However, LB-NAM was accumulated in the liver $\sim 2\times$ higher than SB-NAM and SC25-NAM.

Cy5.5-labelled polymers were injected intravenously via the tail vein. After 24h, the accumulation of the BBPs at 4T1 tumour site was imaged *in vivo* using IVIS Lumina II (Perkin Elmer) imaging system. Remarkably, all BBPs travelled to the tumour site, which are shown by bright luminescent in the tumour area of mice IVIS image (Figure 4.3). However, I postulated that it might be affected by their peripheral position relative to other organs. Besides, the hair that covers the skin above the tumour was shaved due to inoculation procedure, which probably makes the image become more visible than other parts of the body.

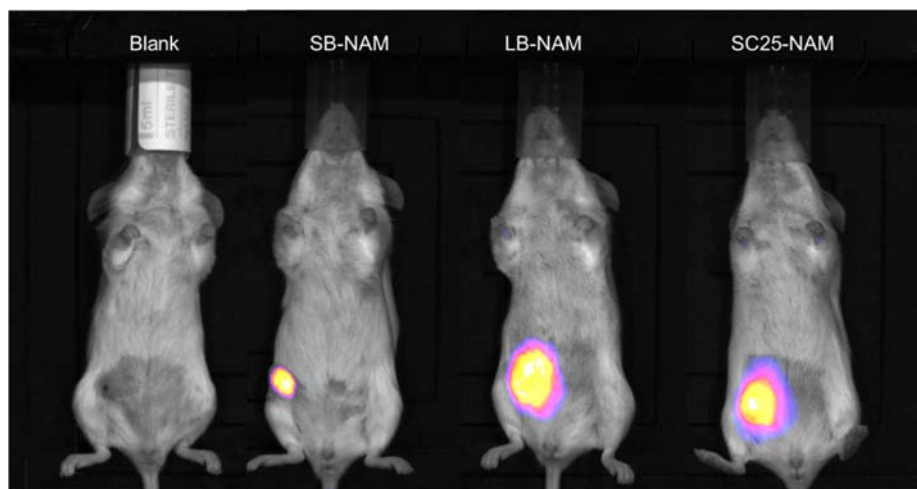


Figure 4.3 IVIS images of BBPs accumulation in tumours 4T1 tumour-bearing mice, treated with Cy5.5-labelled polymers.

To prove that the live images were not false positive due to tissue location and hair interference, I then harvested the tumour tissues and other organs (liver, spleen, pancreas, kidneys, heart and lungs) and then imaged them again. In the untreated mice (Figure 4.4, blank), only the liver showed bright luminescence visually. This is due to the autofluorescence characteristic of liver as a place for multiple metabolic and detoxification processes, involving various endogenous fluorophores.^{213,214} Interestingly, in mice treated with the three Cy5.5-labelled BBPs, beside the liver, the tumour tissues also emitted intense luminescence, confirming the substantial distribution of BBPs to this organ (Figure 4.4).

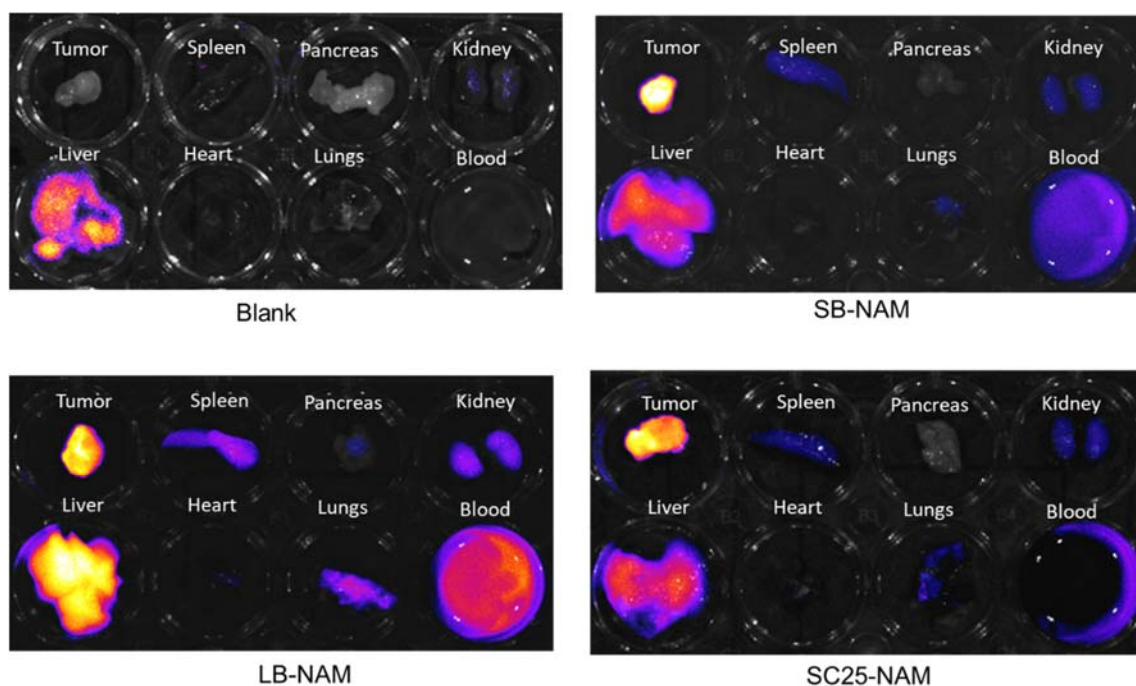


Figure 4.4 IVIS images obtained from an individual scan of ex-vivo organs of each mouse on a well-plate 24 hours after administration of Cy5.5-labelled polymers.

In mice treated with SB-NAM and SC25-NAM, the fluorescence intensities in tumour tissue are more pungent than in the liver. By qualitatively comparing with control and taking into account the autofluorescence of the liver, it can be suggested that SB-NAM and SC25-NAM were distributed to tumour tissue with higher distribution density than liver. In mice treated with LB-NAM, the tumour and liver emitted a similar luminescence intensity, indicating an equal distribution of LB-NAM to both tissues. Similar to other studied BBPs, other organs (spleen, pancreas, kidney, heart and lungs) demonstrated significantly weaker fluorescence relative to tumour and liver.

To compare the fluorescence intensities of organs derived from different mice, I carried out simultaneous imaging of all organs from all mice (Figure 4.5). By imaging all organs together at the same time, organs from blank mouse, including the liver, do not emit fluorescence signal since the fluorescence intensity is now relative to other fluorescent-containing organs (autoscaling). Across all observed organs, those harvested from LB-NAM-

treated mouse showed brighter fluorescence signal, with tumour and liver are the most prominent.

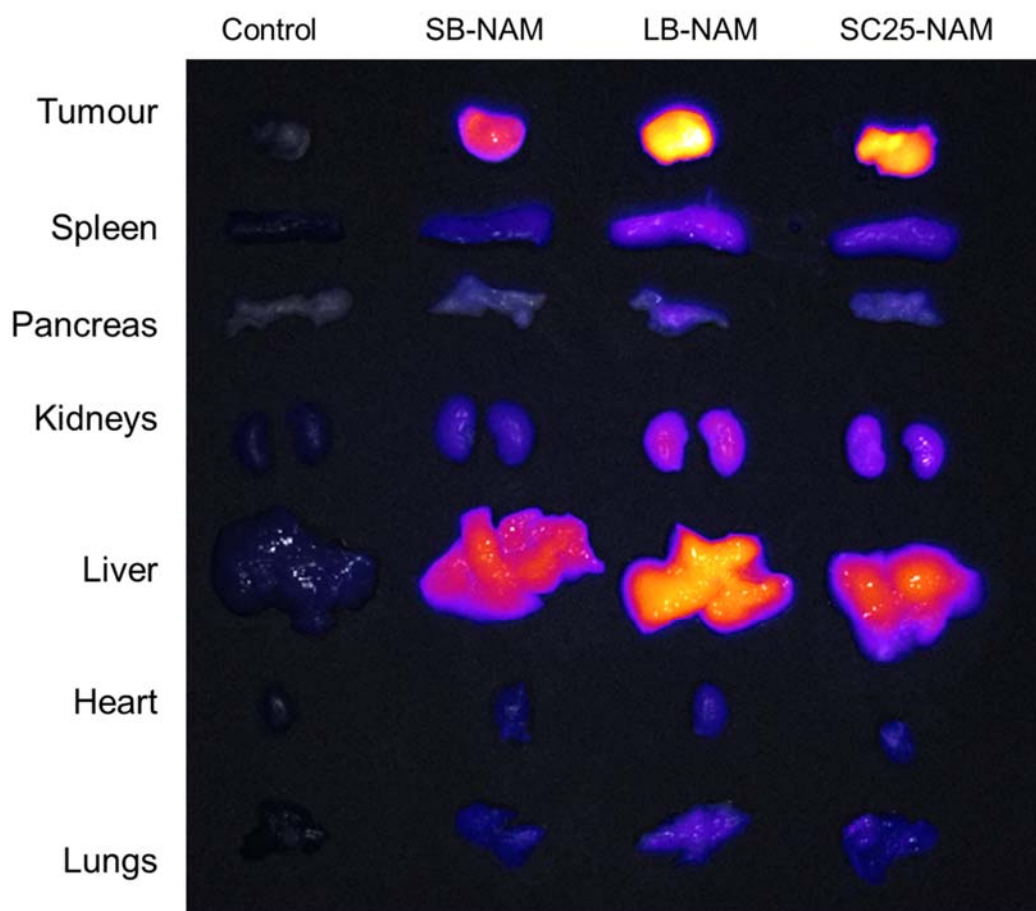


Figure 4.5 IVIS images obtained from a simultaneous scan of ex-vivo organs on a black mat 24 hours after administration of Cy5.5-labelled polymers.

Aiming to obtain a more objective comparison of fluorescent intensity between organs, I quantified the fluorescence value using Fiji ImageJ. The results are summarized in Figure 4.6. Comparing the total corrected fluorescence among organs, all BBPs showed the highest fluorescent in liver, followed by tumour and then spleen. Accumulation of LB-NAM in the liver is the highest among the three studied BBPs, which is in agreement with biodistribution study in rats. Surprisingly, the level of fluorescence in the tumour is higher than in the spleen,

suggesting the ability of the BBPs to pass through splenic filtration as well as passive retention in tumour tissues.

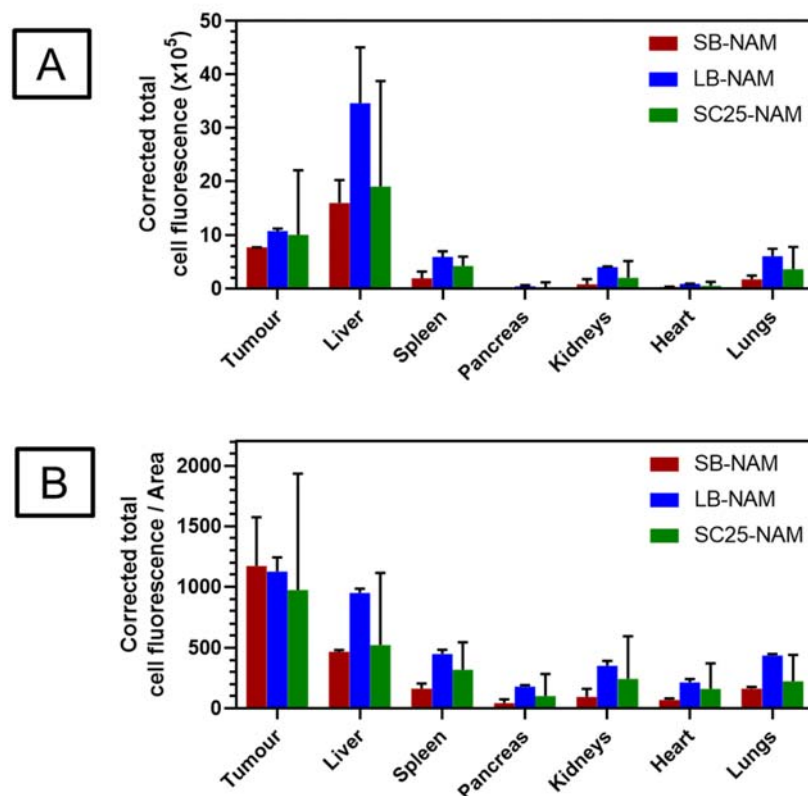


Figure 4.6 Biodistribution of Cy5.5-labelled BBPs after sacrificed at 24 h: (A) fluorescence per organ and (B) normalized fluorescence by area. Fluorescence values were obtained from IVIS images analysis using Fiji ImageJ. All BD data represent the mean \pm SD ($n = 2$).

When I divided the total fluorescence by the area of ROI to normalize the size of the tissues, I found a discrepancy in regards to the trend of accumulation. The deposition of SB-NAM and SC25-NAM in tumour tissue is higher than in the liver, while LB-NAM showed equal distribution in both tissues. Among the three compounds, SB-NAM showed the highest tumour/liver ratio (2.50), followed by SC25-NAM (1.86) and then LB-NAM (1.18). This suggests the capability of brushes with a short backbone to accumulate in tumour tissues while

minimizing deposition in the liver. In addition, BBP with a more rigid structure due to dense side chains tends to accumulate more in tumour, in comparison with BBP with less side chains.

Labelling a polymer with a fluorophore tag is a popular way of research for biomedical application. It offers some advantages such as high sensitivity, enhanced spatial and temporal resolutions and rapid image acquisition.^{215,216} It also enables multimodality imaging to track the real-time biodistribution of nanoparticles across various time points in an individual animal by a non-invasive visualization and measurement. However, some issues must be taken into consideration when using fluorescence label. The aforementioned autofluorescence of the tissue can impact the analysis of measurement. Since different tissues have a diverse range of autofluorescence, comparing the biodistribution of a nanoparticle across various organs (e.g. liver and spleen from an individual animal) might suffer from inaccuracy. In addition, since the fluorescence emission can be quenched by the presence of water²¹⁷ and blood component²¹⁶, the water content and amount of blood residue in each organ will also affect the signal reading. For example, from the ex-vivo organ imaging in Figure 4.4, I expected strong luminescence of the blood since I am acknowledged by results from pharmacokinetics in rats (Chapter 3) that the BBPs retained in the blood for more than 24 hours. However, from this study, the blood did not show fluorescence glowing in mice treated with SB-NAM and SC25-NAM and weak fluorescence glowing in mouse treated with LB-NAM. I also expected luminescence of the spleen as one of RES organs that contributes to nanoparticles elimination, however, the image showed the opposite result where only weak fluorescence glowing is visible in the spleen. Overall, since I am aware of the limitations of using a fluorescence label, I did not rely on these results to quantify the biodistribution of the BBPs. Therefore, for a more quantitative result and minimize artifacts from tissue heterogenities, another labelling technique was employed using radioisotope [14C]-ethanolamine as labelling agent.

4.3.3 Quantitative Biodistribution Studies

To confirm the real biodistribution of the BBPs quantitatively, I conducted quantitative biodistribution studies by injecting [14C]-labelled BBPs. The data are expressed as % injected

dose (%ID) per gram tissue (Figure 4.7) to justify different organ size. However, I also presented the data as % injected dose per organ (Figure A.29) for a bigger view of the distribution of the whole injected dose. In general, the biodistribution study of the BBPs showed relatively low accumulation in two main reticuloendothelial system (RES) organs, liver and spleen, with a value between 7-22 %ID per gram of each tissue after 24 hours circulation. This value is lower than previously reported ^{198}Au -Doped PEGylated nanorod (~58% in liver and ~50% in spleen)⁴⁸ with the same 24 hours circulation time.

a. Influence of Backbone Lengths on Biodistribution

The distribution of LB-NAM in the liver and spleen is higher than SB-NAM, clearly most significant in spleen disposition (Figure 4.7). This can be explained due to the longer backbone, which increases the propensity to interact with phagocytic cells. While the deposition of SB-NAM in liver is higher than in spleen, the deposition of LB-NAM in both organs were equal. The longer backbone of LB-NAM might contribute to their high splenic entrapment. The trend of fractions found in the liver and spleen are inversely reflected by the fraction of compounds left in blood circulation, where the fraction of LB-NAM left in the blood was lower than SB-NAM (19% vs 30% ID per gram tissue, respectively).

Interestingly, despite the discrepancies in liver and spleen distribution, the accumulation of SB-NAM and LB-NAM in the tumour is not significantly different, with LB-NAM is slightly higher (mean values are 15.37% vs 13.90% ID per g tissue for LB-NAM and SB-NAM, respectively). This suggests little dependency of backbone length to tumour uptake, as long as the shape is still elongated, which is in accordance with the previously reported PEGMA-based BBPs with longer backbone and diameter.⁶¹

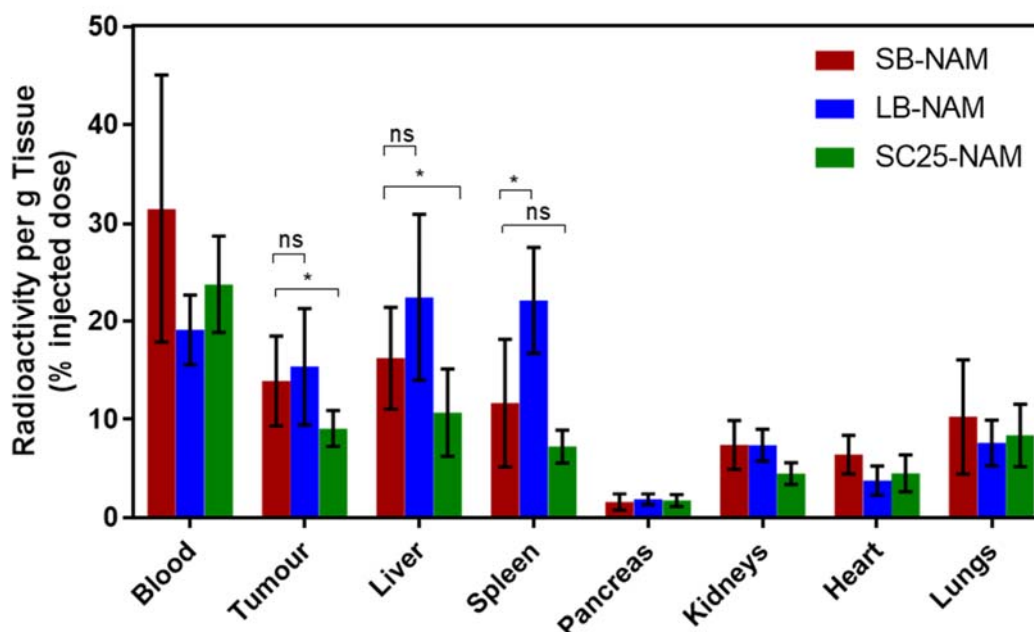


Figure 4.7 Biodistribution of ^{14}C -labelled BBPs after sacrifice at 24 h. All BD data represent the mean \pm SD ($n = 6-7$ mice); (* = p -value < 0.05).

b. Influence of Grafting Density on Biodistribution

SB-NAM and SC25-NAM showed a similar trend of biodistribution proportion across all studied organs (Figure 4.7). However, the organ uptake of SC25-NAM is generally lower than SB-NAM. This is particularly shown in tumour uptake, where the difference is statistically significant (% dose per gram, 13.90% vs 9.06% for SB-NAM and SC25-NAM, respectively). This result suggests that the grafting density of BBPs, which also attributes to their flexibility, might play a role in their biodistribution. Interestingly, when I calculated the total percentage of %ID per g tissue from blood, liver, spleen, pancreas, kidneys, heart, lungs and tumour, the percent recovery for SC25-NAM is relatively low (~70% vs ~99% for SC25-NAM and SB-NAM, respectively), as shown in Table A.4, Appendix. This indicated that SC25-NAM was also distributed to other places. My hypothesis is that SC25-NAM might be excreted in urine to a greater extent than SB-NAM. I did not generate the urine recovery data since the experiment did not focus on pharmacokinetics. However, the urine recovery from PK study in rats demonstrated a higher value of SC25-NAM, which I assume to be similar to mice.

Generally, although the pharmacokinetics of the compounds were not evaluated, these findings suggested that the backbone length and structure flexibility influence the clearance of the NAM-based BBPs in tumour-bearing mice. The tumour accumulation of the NAM-based BBPs is quite remarkable, with a mean value approximately 14%, 15% and 9% ID per g tissue for SB-NAM, LB-NAM and SC25-NAM, respectively. These values are similar to the previously reported PEGMA-based BBPs studied by Müllner *et al.*⁶¹ (9-14%, 48 h) and higher than PEGMA-based rod-like and worm-like micelles (~3%, 48 h)²⁰⁷, PAMAM-OH dendrimers (~5%, 24 h)²¹⁸, PEGylated polylysine dendrimers (~3%, 72 h)²¹⁹, PEGylated Au nanorods (2%, 24 h)²⁰⁴, PEGylated ¹⁹⁸Au-Doped nanorods (~1%, 24 h)⁴⁸ and RGD-decorated Au nanorods (~5%, 6 h)²²⁰. In the study done by Perry *et al.*²²¹, it has been demonstrated that nanoparticle accumulation in tumour is dependence on the tumour model and location, and correlate with tumour microvessel density. For example, the accumulation of PRINT nanoparticles in 344SQ tumour (high microvessel density), was higher than in A549 tumour (low microvessel density). Hence, it is hard to make comparison between the NAM-based BBPs and other nanoparticles reported elsewhere due to variation in the tumour model used in each study. However, my findings showed the potential application of my NAM-based BBPs as a drug delivery carrier in triple-negative breast cancer due to their ability to accumulate in this type of tumour tissues. A longer biodistribution study, e.g. 48 hours, might be necessary to investigate the trend of tissue deposition after the compounds are completely cleared from the blood.

It is interesting to observe a discrepancy on the trend of organ biodistribution of the brushes between fluorescence and radioactive data. Generally, the highest distribution of all compounds (normalized by area) using the fluorescence data was in the tumour, followed by the liver, spleen and then lungs. However, when using radioactive data, the trends change. The liver showed the highest distribution, with only small difference with tumour and spleen. Also, in LB-NAM, the distribution in the liver is higher than in spleen when using the fluorescence data, but is similar when using radioactive data. As mentioned earlier, there are

several factors that can affect the accuracy of fluorescence data, especially when the data is generated from imaging and not analysis of the fluorescence species. However, fluorescence imaging can be used as a practical, convenient and straightforward way for initial experiment to assess and visualize the biodistribution of nanoparticles. Analysis of the polymer species using radiolabel might give better accuracy.

4.4 CONCLUSION AND FUTURE DIRECTION

This study demonstrated that the NAM-based BBPs could be potential candidates for delivery carrier of anticancer drugs. LB-NAM showed relatively high accumulation in RES organs, liver and spleen, which is unfavourable. SB-NAM and SC25-NAM exhibited lower liver and spleen accumulation than LB-NAM. In the case of tumour accumulation, all three BBPs showed remarkable tumour uptake (9-14%). Overall, these findings suggested that the backbone length and structure flexibility influence the biodistribution of the NAM-based BBPs in a syngeneic orthotopic tumour model. A study in different tumour model might be necessary to explore the potency of the NAM-based BBPs to be used in various type of tumour.

CHAPTER 5. SUMMARY AND FUTURE PERSPECTIVE

I have established a new method of synthesis of NAM-based BBP using Reversible Addition-Fragmentation Chain Transfer (RAFT) polymerization, grafting from CTA-shuttled R-group approach. RAFT polymerization was used to synthesize the backbone as well as the side chains. This method offers simple, easy, and versatile reaction preparation and purification, making it possible for large-scale production. By modifying the ratio of $CTA_{shuttle}/CTA_{backbone}$ and end group of side chains, I could create and characterize a library of NAM-based BBP with control of length, side-chain structure, grafting density and end group functionalities, resulting in BBPs with a well-defined structure, remarkable dispersity ($\bar{D} < 1.35$) and are suitable for biological application.

I also found that the Z-groups tethered to the tips of the side chains might be exchanged statistically with Z-groups from other RAFT agents. Although still at early stage, my preliminary study using polyCTAs has verified this hypothesis. A more comprehensive study focusing on the Z-group interchange behaviour is necessary, for example using different RAFT agent. The Z-groups interchange provides the opportunity for a new technique of drug attachment in a simple and fast manner, especially to attach a combination of drugs.

All NAM-based BBPs were relatively non-toxic to four cell lines (3T3, HEK-293, MDA-MB-231-HM and 4T1) and could be internalized by the cells (3T3 and MDA-MB-231-HM). The pharmacokinetics study in healthy rats revealed that all NAM-based BBPs exhibited remarkably prolonged plasma circulation (half-life > 30 hours) compared to their associated linear polymers. Their deposition in major RES organs, liver and spleen, were relatively low ($< 15\%$), except for BBPs with backbone DP500 ($\sim 25\%$), indicating their ability to evade phagocytosis by macrophages. My NAM-based BBPs also demonstrated comparable excellence towards PEG-based BBPs, indicating their potencies to be used as an alternative for PEG.

Studies in 4T1 syngeneic orthotopic tumour models demonstrated their relatively high distribution to tumour tissues (9-14% ID per g tissue) after 24 hours of administration, indicating their ability to perform passive targeting to tumour tissue. The very low clearance, together with a low level of unspecific organ accumulation and relatively high accumulation in tumour tissues, suggest that my BBPs could be excellent candidates for drug delivery applications.

Since my NAM-based BBPs have shown pronounced potential as polymeric drug delivery carriers, I suggested studying the *in vitro* and *in vivo* performance by conjugating with drug molecules for a more relevant clinical application. Pharmacokinetics and biodistribution study for a more extended period time might also be necessary to examine the possibility of unfavourable long-term organ accumulation of the polymers. Pharmacokinetics study after repeat injection of NAM-based BBPs might be beneficial to investigate the chance of the ABC phenomenon. In addition to biodistribution study in the 4T1 tumour model, study in other types of tumour can be worthwhile for a more diverse knowledge of BBPs behaviour towards different tumour diseases, including metastatic condition. Lastly, I also suggested the study of the NAM-based BBPs for a broader biological application, for example as a nanocarrier for diagnostic agent and diseases other than cancer.

REFERENCES

- 1 Foundation, E. S. 2004. ESF Forward Look on Nanomedicine 2005. (Strasbourg cedex, France).
- 2 Duncan, R. & Gaspar, R. 2011. Nanomedicine(s) under the Microscope. *Mol. Pharm.* **8**, 2101.
- 3 Blanco, E., Shen, H. & Ferrari, M. 2015. Principles of nanoparticle design for overcoming biological barriers to drug delivery. *Nat. Biotechnol.* **33**, 941.
- 4 Cho, K., Wang, X., Nie, S., Chen, Z. & Shin, D. M. 2008. Therapeutic Nanoparticles for Drug Delivery in Cancer. *Clin. Cancer Res.* **14**, 1310.
- 5 Astruc, D. 2015. Introduction to Nanomedicine. *Molecules* **21**, E4.
- 6 Estanqueiro, M., Amaral, M. H., Conceição, J. & Sousa Lobo, J. M. 2015. Nanotechnological carriers for cancer chemotherapy: The state of the art. *Colloids Surf., B* **126**, 631.
- 7 Barenholz, Y. 2012. Doxil® — The first FDA-approved nano-drug: Lessons learned. *J. Control. Release* **160**, 117.
- 8 Chatelut, E., Delord, J.-P. & Canal, P. 2003. Toxicity Patterns of Cytotoxic Drugs. *Invest. New Drugs* **21**, 141.
- 9 Maeda, H., Ueda, M., Morinaga, T. & Matsumoto, T. 1985. Conjugation of poly(styrene-co-maleic acid) derivatives to the antitumor protein neocarzinostatin: pronounced improvements in pharmacological properties. *J. Med. Chem.* **28**, 455.
- 10 Matsumura, Y. & Maeda, H. 1986. A New Concept for Macromolecular Therapeutics in Cancer Chemotherapy: Mechanism of Tumoritropic Accumulation of Proteins and the Antitumor Agent Smancs. *Cancer Res.* **46**, 6387.
- 11 Boisselier, E. & Astruc, D. 2009. Gold nanoparticles in nanomedicine: preparations, imaging, diagnostics, therapies and toxicity. *Chem Soc Rev* **38**, 1759.
- 12 Lee, S. H. & Jun, B.-H. 2019. Silver Nanoparticles: Synthesis and Application for Nanomedicine. *Int. J. Mol. Sci.* **20**, 865.
- 13 Nedyalkova, M. *et al.* 2017. Iron oxide nanoparticles – In vivo/in vitro biomedical applications and in silico studies. *Adv Colloid Interface Sci* **249**, 192.
- 14 Tan, W. B. & Zhang, Y. 2005. Surface modification of gold and quantum dot nanoparticles with chitosan for bioapplications. *J Biomed Mater Res A* **75A**, 56.
- 15 Zhang, Z. *et al.* 2019. Holo-Lactoferrin Modified Liposome for Relieving Tumor Hypoxia and Enhancing Radiochemotherapy of Cancer. *Small* **15**, 1803703.
- 16 Adler-Moore, J. *et al.* 2019. Preclinical Safety, Tolerability, Pharmacokinetics, Pharmacodynamics, and Antifungal Activity of Liposomal Amphotericin B. *Clin. Infect. Dis.* **68**, S244.
- 17 Vera-González, N. *et al.* 2020. Anidulafungin liposome nanoparticles exhibit antifungal activity against planktonic and biofilm *Candida albicans*. *J. Biomed. Mater. Res.* **108**, 2263.
- 18 Narang, A. S., Chang, R. K. & Hussain, M. A. 2013. Pharmaceutical Development and Regulatory Considerations for Nanoparticles and Nanoparticulate Drug Delivery Systems. *J. Pharm. Sci.* **102**.
- 19 Park, J. H. *et al.* 2008. Polymeric nanomedicine for cancer therapy. *Prog. Polym. Sci.* **33**, 113.
- 20 Verhoef, J. J. F. & Anchordoquy, T. J. 2013. Questioning the use of PEGylation for drug delivery. *Drug Deliv. Transl. Res.* **3**, 499.
- 21 Stolnik, S. *et al.* 1994. Surface Modification of Poly(lactide-co-glycolide) Nanospheres by Biodegradable Poly(lactide)-Poly(ethylene glycol) Copolymers. *AAPS J.* **11**, 1800.
- 22 Davis, F. F. 2002. The origin of peganology. *Adv. Drug Deliv. Rev.* **54**, 457.

- 23 Abuchowski, A., van Es, T., Palczuk, N. C. & Davis, F. F. 1977. Alteration of immunological properties of bovine serum albumin by covalent attachment of polyethylene glycol. *J. Biol. Chem.* **252**, 3578.
- 24 Abuchowski, A., McCoy, J. R., Palczuk, N. C., van Es, T. & Davis, F. F. 1977. Effect of covalent attachment of polyethylene glycol on immunogenicity and circulating life of bovine liver catalase. *J. Biol. Chem.* **252**, 3582.
- 25 Ryan, S. M., Mantovani, G., Wang, X., Haddleton, D. M. & Brayden, D. J. 2008. Advances in PEGylation of important biotech molecules: delivery aspects. *Expert Opin. Drug Deliv.* **5**, 371.
- 26 Beltrán-Gracia, E., López-Camacho, A., Higuera-Ciapara, I., Velázquez-Fernández, J. B. & Vallejo-Cardona, A. A. 2019. Nanomedicine review: clinical developments in liposomal applications. *Cancer Nanotechnol.* **10**, 11.
- 27 Pasut, G. & Veronese, F. M. 2009. PEG conjugates in clinical development or use as anticancer agents: an overview. *Adv. Drug Deliv. Rev.* **61**, 1177.
- 28 Duncan, R. 2003. The dawning era of polymer therapeutics. *Nat. Rev. Drug Discov.* **2**, 347.
- 29 Canal, F., Sanchis, J. & Vicent, M. J. 2011. Polymer-drug conjugates as nano-sized medicines. *Curr Opin Biotechnol* **22**, 894.
- 30 Duncan, R. 2017. Polymer therapeutics at a crossroads? Finding the path for improved translation in the twenty-first century. *J. Drug Target.* **25**, 759.
- 31 Duncan, R. 2014. Polymer therapeutics: Top 10 selling pharmaceuticals - What next? *J. Control. Release* **190**, 371.
- 32 Ekladios, I., Colson, Y. L. & Grinstaff, M. W. 2018. Polymer–drug conjugate therapeutics: advances, insights and prospects. *Nat. Rev. Drug Discov.* **18**, 273.
- 33 Longmire, M. & Kobayashi, H. 2008. Clearance properties of nano-sized particles and molecules as imaging agents: considerations and caveats. *Nanomed J.* **3**, 703.
- 34 Haraldsson, B., Nyström, J. & Deen, W. M. 2008. Properties of the Glomerular Barrier and Mechanisms of Proteinuria. *Physiol. Rev.* **88**, 451.
- 35 Ringsdorf, H. 1975. Structure and properties of pharmacologically active polymers. *J. Polym. Sci., Polym. Symp.* **51**, 135.
- 36 Fish, M. B., Thompson, A. J., Fromen, C. A. & Eniola-Adefeso, O. 2015. Emergence and Utility of Nonspherical Particles in Biomedicine. *Ind. Eng. Chem. Res.* **54**, 4043.
- 37 Toy, R., Peiris, P. M., Ghaghada, K. B. & Karathanasis, E. 2014. Shaping cancer nanomedicine: The effect of particle shape on the in vivo journey of nanoparticles. *Nanomed J.* **9**, 121.
- 38 Doshi, N. & Mitragotri, S. 2010. Macrophages recognize size and shape of their targets. *PLoS ONE* **5**, 1.
- 39 Champion, J., Walker, A. & Mitragotri, S. 2008. Role of Particle Size in Phagocytosis of Polymeric Microspheres. *AAPS J.* **25**, 1815.
- 40 Champion, J. A. & Mitragotri, S. 2006. Role of target geometry in phagocytosis. *Proc. Natl. Acad. Sci. U. S. A.* **103**, 4930.
- 41 Champion, J. A. & Mitragotri, S. 2009. Shaped induced inhibition of phagocytosis of polymer particles. *Pharm. Res.* **26**.
- 42 Sharma, G. *et al.* 2010. Polymer particle shape independently influences binding and internalization by macrophages. *J. Control. Release* **147**, 408.
- 43 Moghimi, S. M., Porter, C. J. H., Muir, I. S., Llum, L. & Davis, S. S. 1991. Non-phagocytic uptake of intravenously injected microspheres in rat spleen : Influence of particle size and hydrophilic coating. *Biochem. Biophys. Res. Commun.* **177**.
- 44 Cesta, M. F. 2006. Normal Structure, Function, and Histology of the Spleen. *Toxicol. Pathol.* **34**, 455.

- 45 Moghimi, S. M. 1995. Mechanisms of splenic clearance of blood cells and particles: towards development of new splenotropic agents. *Adv. Drug Deliv. Rev.* **17**, 103.
- 46 Geng, Y. *et al.* 2007. Shape effects of filaments versus spherical particles in flow and drug delivery. *Nature Nanotechnology* **2**.
- 47 Park, J.-H. *et al.* 2008. Magnetic Iron Oxide Nanoworms for Tumor Targeting and Imaging. *Adv. Mater.* **20**, 1630.
- 48 Black, K. C. L. *et al.* 2014. Radioactive ¹⁹⁸Au-Doped Nanostructures with Different Shapes for In Vivo Analyses of Their Biodistribution, Tumor Uptake, and Intratumoral Distribution. *ACS Nano* **8**, 4385.
- 49 Christian, D. A. *et al.* 2009. Flexible Filaments for in Vivo Imaging and Delivery: Persistent Circulation of Filomicelles Opens the Dosage Window for Sustained Tumor Shrinkage. *Mol. Pharm.* **6**, 1343.
- 50 Peiris, P. M. *et al.* 2012. Enhanced Delivery of Chemotherapy to Tumors Using a Multicomponent Nanochain with Radio-Frequency-Tunable Drug Release. *ACS Nano* **6**, 4157.
- 51 Huang, X., Teng, X., Chen, D., Tang, F. & He, J. 2010. The effect of the shape of mesoporous silica nanoparticles on cellular uptake and cell function. *Biomaterials* **31**, 438.
- 52 Meng, H. *et al.* 2011. Aspect Ratio Determines the Quantity of Mesoporous Silica Nanoparticle Uptake by a Small GTPase-Dependent Macropinocytosis Mechanism. *ACS Nano* **5**, 4434.
- 53 Gabizon, A. & Papahadjopoulos, D. 1988. Liposome formulations with prolonged circulation time in blood and enhanced uptake by tumors. *Proc. Natl. Acad. Sci. U. S. A.* **85**, 6949.
- 54 Nair, P. R. *et al.* 2018. Filomicelles Deliver a Chemo-Differentiation Combination of Paclitaxel and Retinoic Acid That Durably Represses Carcinomas in Liver to Prolong Survival. *Bioconj. Chem.* **29**, 914.
- 55 Cai, S., Vijayan, K., Cheng, D., Lima, E. M. & Discher, D. E. 2007. Micelles of Different Morphologies-Advantages of Worm-like Filomicelles of PEO-PCL in Paclitaxel Delivery. *Pharm. Res.* **24**, 2099.
- 56 Larnaudie, S. C. *et al.* 2018. Cyclic peptide-poly(HPMA) nanotubes as drug delivery vectors: In vitro assessment, pharmacokinetics and biodistribution. *Biomaterials* **178**, 570.
- 57 Larnaudie, S. C. *et al.* 2017. Cyclic Peptide-Polymer Nanotubes as Efficient and Highly Potent Drug Delivery Systems for Organometallic Anticancer Complexes. *Biomacromolecules* **19**.
- 58 Larnaudie, S. C., Brendel, J. C., Jolliffe, K. A. & Perrier, S. b. S. b. 2017. pH-Responsive, Amphiphilic Core-Shell Supramolecular Polymer Brushes from Cyclic Peptide-Polymer Conjugates.
- 59 Pelras, T., Duong, H. T. T., Kim, B. J., Hawket, B. S. & Müllner, M. 2017. A 'grafting from' approach to polymer nanorods for pH-triggered intracellular drug delivery. *Polymer* **112**, 244.
- 60 Müllner, M., Yang, K., Kaur, A. & New, E. J. 2018. Aspect-ratio-dependent interaction of molecular polymer brushes and multicellular tumour spheroids. *Polym. Chem.* **9**, 3461.
- 61 Müllner, M., Mehta, D., Nowell, C. J. & Porter, C. J. H. 2016. Passive tumour targeting and extravasation of cylindrical polymer brushes in mouse xenografts. *Chem. Comm.* **52**, 9121.
- 62 Müllner, M. *et al.* 2015. Size and Rigidity of Cylindrical Polymer Brushes Dictate Long Circulating Properties In Vivo. *ACS Nano* **9**, 1294.
- 63 Shen, D., Yu, H. & Huang, Y. 2005. Densely grafting copolymers of ethyl cellulose through atom transfer radical polymerization. *Journal of Polymer Science Part A: Polymer Chemistry* **43**, 4099.
- 64 Beers, K. L., Gaynor, S. G., Matyjaszewski, K., Sheiko, S. S. & Mo, M. 1998. The synthesis of densely grafted copolymers by Atom Transfer Radical Polymerization. *Macromolecules* **31**, 9413.

- 65 Krivorotova, T., Jonikaite-Svegziene, J., Radzevicius, P. & Makuska, R. 2014. Synthesis by RAFT polymerization and properties of anionic cylindrical molecular brushes bearing poly(acrylic acid) side chains. *Reactive and Functional Polymers* **76**, 32.
- 66 Gao, H. & Matyjaszewski, K. 2007. Synthesis of molecular brushes by "grafting onto" method: combination of ATRP and click reactions. *J. Am. Chem. Soc* **129**, 6633.
- 67 Yu-Su, S. Y. *et al.* 2009. Crystallization of Molecular Brushes with Block Copolymer Side Chains. *Macromolecules* **42**, 9008.
- 68 Lee, H.-I., Pietrasik, J. & Matyjaszewski, K. 2006. Phototunable temperature-responsive molecular brushes prepared by ATRP. *Macromolecules* **39**, 3914.
- 69 Lin, T.-P. *et al.* 2017. Effects of Grafting Density on Block Polymer Self-Assembly: From Linear to Bottlebrush. *ACS Nano* **11**, 11632.
- 70 Wang, Y., Ren, R., Ling, J., Sun, W. & Shen, Z. 2018. One-pot "grafting-from" synthesis of amphiphilic bottlebrush block copolymers containing PLA and PVP side chains via tandem ROP and RAFT polymerization. *Polymer* **138**, 378.
- 71 Radzinski, S. C. *et al.* 2016. Preparation of Bottlebrush Polymers via a One-Pot Ring-Opening Polymerization (ROP) and Ring-Opening Metathesis Polymerization (ROMP) Grafting-Through Strategy. *Macromol. Rapid Commun.* **37**, 616.
- 72 Lai, H. *et al.* 2014. A new strategy to synthesize bottlebrushes with a helical polyglutamate backbone via N-carboxyanhydride polymerization and RAFT. *Chem. Comm.* **50**, 14183.
- 73 Müllner, M., Mehta, D. C., Nowell, C. J. & Porter, C. J. H. 2016. Passive tumour targeting and extravasation of cylindrical polymer brushes in mouse xenografts. *Chemical Communications* **52**, 9121.
- 74 Hiorns, R. C. *et al.* 2012. A brief guide to polymer nomenclature (IUPAC Technical Report). *Pure Appl. Chem.* **84**, 2167.
- 75 Kahovec, J. *et al.* 1997. Source-based nomenclature for non-linear macromolecules and macromolecular assemblies (IUPAC Recommendations 1997). *Pure Appl. Chem.* **69**, 2511.
- 76 Barbey, R. *et al.* 2009. Polymer Brushes via Surface-Initiated Controlled Radical Polymerization: Synthesis, Characterization, Properties, and Applications. *Chem. Rev* **109**, 5437.
- 77 Du, J.-Z., Tang, L.-Y., Song, W.-J., Shi, Y. & Wang, J. 2009. Evaluation of Polymeric Micelles from Brush Polymer with Poly(ϵ -caprolactone)-b-Poly(ethylene glycol) Side Chains as Drug Carrier. *Biomacromolecules* **10**, 2169.
- 78 Guo, Y. *et al.* 2017. Well-defined podophyllotoxin polyprodrug brushes: preparation via RAFT polymerization and evaluation as drug carriers. *Polym. Chem.* **8**, 901.
- 79 Yu, Y. *et al.* 2013. Well-Defined Degradable Brush Polymer – Drug Conjugates for Sustained Delivery of Paclitaxel. *Mol. Pharm.* **10**, 867.
- 80 Yu, Y. *et al.* 2015. A degradable brush polymer-drug conjugate for pH-responsive release of doxorubicin. *Polym. Chem.* **6**, 953.
- 81 Zou, J. *et al.* 2015. Well-defined diblock brush polymer - drug conjugates for sustained delivery of paclitaxel. *Biomater. Sci.* **3**, 1078.
- 82 Johnson, J. A. *et al.* 2010. Drug-Loaded, Bivalent-Bottle-Brush Polymers by Graft-through ROMP. *Macromolecules* **43**, 10326.
- 83 Johnson, J. A. *et al.* 2010. Core-Clickable PEG-Branch-Azide Bivalent-Bottle-Brush Polymers by ROMP: Grafting-Through and Clicking-To. *J. Am. Chem. Soc.* **133**, 559.
- 84 Sowers, M. A. *et al.* 2014. Redox-responsive branched-bottlebrush polymers for in vivo MRI and fluorescence imaging. *Nat. Commun.* **5**.
- 85 Blum, A. P., Kammeyer, J. K. & Gianneschi, N. C. 2016. Activating peptides for cellular uptake via polymerization into high density brushes. *Chem. Sci.* **7**, 989.

- 86 Qi, Y. *et al.* 2016. A brush-polymer/exendin-4 conjugate reduces blood glucose levels for up to five days and eliminates poly(ethylene glycol) antigenicity. *Nat. Biomed. Eng.* **1**.
- 87 Wang, C. *et al.* 2018. Conjugated Polymer Brush Based on Poly(L-lysine) with Efficient Ovalbumin Delivery for Dendritic Cell Vaccine. *ACS Appl. Bio. Mat.* **1**, 1972.
- 88 Wang, D. *et al.* 2019. Bottlebrush-architected poly(ethylene glycol) as an efficient vector for RNA interference in vivo. *Sci. Adv.* **5**, eaav9322.
- 89 Lu, X. *et al.* 2016. Effective Antisense Gene Regulation via Noncationic, Polyethylene Glycol Brushes. *J. Am. Chem. Soc.* **138**, 9097.
- 90 Jia, F. *et al.* 2017. Depth-Profiling the Nuclease Stability and the Gene Silencing Efficacy of Brush-Architected Poly(ethylene glycol)-DNA Conjugates. *J. Am. Chem. Soc.* **139**, 10605.
- 91 Zhang, Z. *et al.* 2019. Length effects of cylindrical polymer brushes on their in vitro and in vivo properties. *Biomater. Sci.* **7**, 5124.
- 92 Zhao, J. & Stenzel, M. H. 2018. Entry of nanoparticles into cells: the importance of nanoparticle properties. *Polym. Chem.* **9**, 259.
- 93 Ernsting, M. J., Murakami, M., Roy, A. & Li, S. D. 2013. Factors controlling the pharmacokinetics, biodistribution and intratumoral penetration of nanoparticles. *J. Control. Release* **172**, 782.
- 94 Li, H. *et al.* 2018. Molecular bottlebrush as a unimolecular vehicle with tunable shape for photothermal cancer therapy. *Biomaterials* **178**, 620.
- 95 Shilyagina, N. Y. *et al.* 2017. Effective delivery of porphyrazine photosensitizers to cancer cells by polymer brush nanocontainers. *J. Biophotonics* **10**, 1189.
- 96 Zolotarskaya, O. Y., Yuan, Q., Wynne, K. J. & Yang, H. 2013. Synthesis and Characterization of Clickable Cytocompatible Poly(ethylene glycol)-Grafted Polyoxetane Brush Polymers. *Macromolecules* **46**, 63.
- 97 Bühler, J. *et al.* 2014. Selective Uptake of Cylindrical Poly(2-Oxazoline) Brush-AntiDEC205 Antibody-OVA Antigen Conjugates into DEC-Positive Dendritic Cells and Subsequent T-Cell Activation. *Chem. Eur. J.* **20**, 12405.
- 98 Lu, X. *et al.* 2015. Providing Oligonucleotides with Steric Selectivity by Brush-Polymer-Assisted Compaction. *Journal of the American Chemical Society* **137**, 12466.
- 99 Hörtz, C. *et al.* 2015. Cylindrical brush polymers with polysarcosine side chains: A novel biocompatible carrier for biomedical applications. *Macromolecules* **48**, 2074.
- 100 Sheiko, S. S., Sumerlin, B. S. & Matyjaszewski, K. 2008. Cylindrical molecular brushes: Synthesis, characterization, and properties. *Prog. Polym. Sci.* **33**, 759.
- 101 Müllner, M. & Müller, A. H. E. 2016. Cylindrical polymer brushes – Anisotropic building blocks, unimolecular templates and particulate nanocarriers. *Polymer* **98**, 389.
- 102 Müllner, M. 2016. Molecular Polymer Brushes in Nanomedicine. *Macromol. Chem. Phys.* **217**, 2209.
- 103 Helms, B., Mynar, J. L., Hawker, C. J. & Fréchet, J. M. J. 2004. Dendronized Linear Polymers via “Click Chemistry”. *Journal of the American Chemical Society* **126**, 15020.
- 104 Schappacher, M., Billaud, C., Paulo, C. & Deffieux, A. 1999. Synthesis, dimensions and solution properties of linear and macrocyclic poly(chloroethyl vinyl ether)-g-polystyrene comblike polymers. *Macromol. Chem. Phys.* **200**, 2377.
- 105 Sperling, L. H. 2006. *Introduction to physical polymer science*. 4th ed. edn, (Hoboken, N.J. : Wiley, 2006).
- 106 Szabo, T. L. 2005. in *Plastics (Third Edition)* (ed Thomas L. Szabo) 21 (Butterworth-Heinemann).
- 107 Matyjaszewski, K. 2002. *Handbook of Radical Polymerization*. 1st ed. edn, (2002).
- 108 Matyjaszewski, K. & Spanswick, J. 2005. Controlled/living radical polymerization. *Mater. Today* **8**, 26.

- 109 Grubbs, R. B. & Grubbs, R. H. 2017. 50th Anniversary Perspective: Living Polymerization-Emphasizing the Molecule in Macromolecules. *Macromolecules* **50**, 6979.
- 110 Jenkins, A. D., Jones, R. G. & Moad, G. 2009. Terminology for reversible-deactivation radical polymerization previously called "controlled" radical or "living" radical polymerization (IUPAC Recommendations 2010). *Pure Appl. Chem.* **82**, 483.
- 111 Nicolas, J. *et al.* 2013. Nitroxide-mediated polymerization. *Prog. Polym. Sci.* **38**, 63.
- 112 Grubbs, R. B. 2011. Nitroxide-Mediated Radical Polymerization: Limitations and Versatility. *Polym. Rev.* **51**, 104.
- 113 Matyjaszewski, K. 2012. Atom Transfer Radical Polymerization (ATRP): Current Status and Future Perspectives. *Macromolecules* **45**, 4015.
- 114 Tang, W. & Matyjaszewski, K. 2007. Effects of Initiator Structure on Activation Rate Constants in ATRP. *Macromolecules* **40**, 1858.
- 115 Tang, W. & Matyjaszewski, K. 2006. Effect of Ligand Structure on Activation Rate Constants in ATRP. *Macromolecules* **39**, 4953.
- 116 Discekici, E. H., Anastasaki, A., Read de Alaniz, J. & Hawker, C. J. 2018. Evolution and Future Directions of Metal-Free Atom Transfer Radical Polymerization. *Macromolecules* **51**, 7421.
- 117 Boyer, C. *et al.* 2009. Bioapplications of RAFT Polymerization. *Chem. Rev.* **109**, 5402.
- 118 Perrier, S. 2017. 50th Anniversary Perspective: RAFT Polymerization - A User Guide. *Macromolecules* **50**, 7433.
- 119 Boyer, C. *et al.* 2009. Bioapplications of RAFT polymerization. *Chem. Rev.* **109**, 5402.
- 120 Martin, L., Gody, G. & Perrier, S. 2015. Preparation of complex multiblock copolymers via aqueous RAFT polymerization at room temperature. *Polym. Chem.* **6**, 4875.
- 121 Bray, C., Peltier, R., Kim, H., Mastrangelo, A. & Perrier, S. 2017. Anionic multiblock core cross-linked star copolymers via RAFT polymerization. *Polym. Chem.* **8**, 5513.
- 122 Liu, B., Kazlauciusas, A., Guthrie, J. T. & Perrier, S. 2005. One-pot hyperbranched polymer synthesis mediated by reversible addition fragmentation chain transfer (RAFT) polymerization. *Macromolecules* **38**, 2131.
- 123 Quinn, J. F., Chaplin, R. P. & Davis, T. P. 2002. Facile synthesis of comb, star, and graft polymers via reversible addition-fragmentation chain transfer (RAFT) polymerization. *J. Polym. Sci. A Polym. Chem* **40**, 2956.
- 124 Zheng, Z., Ling, J. & Muller, A. H. E. 2014. Revival of the R-group approach: A "CTA-shuttled" grafting from approach for Well-defined cylindrical polymer brushes via RAFT polymerization. *Macromol. Rapid Commun.* **35**, 234.
- 125 Kerr, A., Hartlieb, M., Sanchis, J., Smith, T. & Perrier, S. 2017. Complex multiblock bottle-brush architectures by RAFT polymerization. *Chem. Comm.*
- 126 Armstrong, J. K. *et al.* 2007. Antibody against poly(ethylene glycol) adversely affects PEG-asparaginase therapy in acute lymphoblastic leukemia patients. *Cancer* **110**, 103.
- 127 Hershfield, M. S. *et al.* 2014. Induced and pre-existing anti-polyethylene glycol antibody in a trial of every 3-week dosing of pegloticase for refractory gout, including in organ transplant recipients. *Arthritis Res. Ther.* **16**, R63.
- 128 Rau, R. E. *et al.* 2018. Outcome of pediatric patients with acute lymphoblastic leukemia/lymphoblastic lymphoma with hypersensitivity to pegaspargase treated with PEGylated Erwinia asparaginase, pegcrisantaspase: A report from the Children's Oncology Group. *Pediatr Blood Cancer* **65**, e26873.
- 129 Garay, R. P., El-Gewely, R., Armstrong, J. K., Garratty, G. & Richette, P. 2012. Antibodies against polyethylene glycol in healthy subjects and in patients treated with PEG-conjugated agents. *Expert Opin. Drug Deliv.* **9**, 1319.

- 130 Hong, L., Wang, Z., Wei, X., Shi, J. & Li, C. 2020. Antibodies against polyethylene glycol in human blood: A literature review. *J. Pharmacol. Toxicol. Methods* **102**, 106678.
- 131 Bauer, M. *et al.* 2012. Poly(2-ethyl-2-oxazoline) as Alternative for the Stealth Polymer Poly(ethylene glycol): Comparison of in vitro Cytotoxicity and Hemocompatibility. *Macromol. Biosci.* **12**, 986.
- 132 Hu, Y., Hou, Y., Wang, H. & Lu, H. 2018. Polysarcosine as an Alternative to PEG for Therapeutic Protein Conjugation. *Bioconjug. Chem.* **29**, 2232.
- 133 Xu, F., Li, H., Luo, Y.-L. & Tang, W. 2017. Redox-Responsive Self-Assembly Micelles from Poly(N-acryloylmorpholine-block-2-acryloyloxyethyl ferrocenecarboxylate) Amphiphilic Block Copolymers as Drug Release Carriers. *ACS Appl. Mater. Interfaces*.
- 134 Schiavon, O., Caliceti, P., Ferruti, P. & Veronese, F. M. 2000. Therapeutic proteins: a comparison of chemical and biological properties of uricase conjugated to linear or branched poly(ethylene glycol) and poly(N-acryloylmorpholine). *Farmaco* **55**, 264.
- 135 Ishihara, T. *et al.* 2010. Evasion of the Accelerated Blood Clearance Phenomenon by Coating of Nanoparticles with Various Hydrophilic Polymers. *Biomacromolecules* **11**, 2700.
- 136 Kierstead, P. H. *et al.* 2015. The effect of polymer backbone chemistry on the induction of the accelerated blood clearance in polymer modified liposomes. *J. Control. Release* **213**, 1.
- 137 Gody, G., Barbey, R., Danial, M. & Perrier, S. 2015. Ultrafast RAFT polymerization: multiblock copolymers within minutes. *Polym. Chem.* **6**, 1502.
- 138 Gregory, A. & Stenzel, M. H. 2012. Complex polymer architectures via RAFT polymerization: From fundamental process to extending the scope using click chemistry and nature's building blocks. *Prog. Polym. Sci.* **37**, 38.
- 139 Wang, Y., Zheng, Z., Huang, Z. & Ling, J. 2017. A CTA-shuttled R-group approach: A versatile synthetic tool towards well-defined functional cylindrical polymer brushes via RAFT polymerization. *Polym. Chem.* **8**, 2659.
- 140 Ferguson, C. J. *et al.* 2005. Ab Initio Emulsion Polymerization by RAFT-Controlled Self-Assembly. *Macromolecules* **38**, 2191.
- 141 Favier, A., Charreyre, M. T. r. s. & Pichot, C. 2004. A detailed kinetic study of the RAFT polymerization of a bi-substituted acrylamide derivative: Influence of experimental parameters. *Polymer* **45**, 8661.
- 142 Larnaudie, S. C., Brendel, J. C., Jolliffe, K. A. & Perrier, S. 2016. Cyclic peptide-polymer conjugates: Grafting-to vs grafting-from. *J. Polym. Sci. A: Polym. Chem.* **54**, 1003.
- 143 Gody, G., Maschmeyer, T., Zetterlund, P. B. & Perrier, S. 2014. Exploitation of the degenerative transfer mechanism in RAFT polymerization for synthesis of polymer of high livingness at full monomer conversion. *Macromolecules* **47**, 639.
- 144 Steinhauer, W., Hoogenboom, R., Keul, H. & Moeller, M. 2010. Copolymerization of 2-Hydroxyethyl Acrylate and 2-Methoxyethyl Acrylate via RAFT: Kinetics and Thermoresponsive Properties. *Macromolecules* **43**, 7041.
- 145 Favier, A., Charreyre, M. T. r. s. & Pichot, C. 2004. A detailed kinetic study of the RAFT polymerization of a bi-substituted acrylamide derivative: Influence of experimental parameters. *Polymer* **45**, 8661.
- 146 Williams, A. & Ibrahim, I. T. 1981. A new mechanism involving cyclic tautomers for the reaction with nucleophiles of the water-soluble peptide coupling reagent 1-ethyl-3-(3'-(dimethylamino)propyl)carbodiimide (EDC). *J. Am. Chem. Soc.* **103**, 7090.
- 147 Wróblewska, A. *et al.* 2017. Approach toward the Understanding of Coupling Mechanism for EDC Reagent in Solvent-Free Mechanosynthesis. *Org. Lett.* **19**, 5360.
- 148 Alam, M. M., Jack, K. S., Hill, D. J. T., Whittaker, A. K. & Peng, H. 2019. Gradient copolymers – Preparation, properties and practice. *Eur. Polym. J.* **116**, 394.
- 149 Soto-Cantu, E. *et al.* 2011. Versatility of Alkyne-Modified Poly(Glycidyl Methacrylate) Layers for Click Reactions. *Langmuir* **27**, 5986.

- 150 Benaglia, M., Alberti, A., Giorgini, L., Magnoni, F. & Tozzi, S. 2013. Poly(glycidyl methacrylate): A highly versatile polymeric building block for post-polymerization modifications. *Polym. Chem.* **4**, 124.
- 151 Liu, E. Y., Jung, S. & Yi, H. 2016. Improved Protein Conjugation with Uniform, Macroporous Poly(acrylamide-co-acrylic acid) Hydrogel Microspheres via EDC/NHS Chemistry. *Langmuir* **32**, 11043.
- 152 Way, D. V., Braido, R. S., dos Reis, S. A., Lara, F. A. & Pinto, J. C. 2019. Miniemulsion RAFT Copolymerization of MMA with Acrylic Acid and Methacrylic Acid and Bioconjugation with BSA. *Nanomaterials* **9**, 828.
- 153 Nicolas, J., Mantovani, G. & Haddleton, D. M. 2007. Living Radical Polymerization as a Tool for the Synthesis of Polymer-Protein/Peptide Bioconjugates. *Macromol. Rapid Commun.* **28**, 1083.
- 154 Hermanson, G. T. 2013. *Bioconjugate Techniques*. (Elsevier Science & Technology, 2013).
- 155 Nečas, D. & Klapetek, P. 2012. Gwyddion: an open-source software for SPM data analysis. *Cent. Eur. J. Phys.* **10**, 181.
- 156 Schindelin, J. *et al.* 2012. Fiji: An open-source platform for biological-image analysis. *Nat. Methods* **9**, 676.
- 157 Willcock, H. & O'Reilly, R. K. 2010. End group removal and modification of RAFT polymers. *Polym. Chem.* **1**, 149.
- 158 Perrier, S., Takolpuckdee, P. & Mars, C. A. 2005. Reversible Addition-Fragmentation Chain Transfer Polymerization: End Group Modification for Functionalized Polymers and Chain Transfer Agent Recovery. *Macromolecules* **38**, 2033.
- 159 Chen, M., Moad, G. & Rizzardo, E. 2009. Thiocarbonylthio End Group Removal from RAFT-Synthesized Polymers by a Radical-Induced Process. *J. Polym. Sci. A: Polym. Chem.* **47**, 6704.
- 160 Lin, R. Y. *et al.* 2000. Histamine and tryptase levels in patients with acute allergic reactions: An emergency department-based study. *J. Allergy Clin. Immunol.* **106**, 65.
- 161 Peaston, R. T. & Weinkove, C. 2004. Measurement of catecholamines and their metabolites. *Ann. Clin. Biochem.* **41**, 17.
- 162 Badcock, N. R., Spence, J. G. & Stern, L. M. 1987. Blood Serotonin Levels in Adults, Autistic and Non-Autistic Children—With a Comparison of Different Methodologies. *Ann. Clin. Biochem.* **24**, 625.
- 163 Boyd, B. J. *et al.* 2006. Cationic Poly-L-lysine Dendrimers: Pharmacokinetics, Biodistribution, and Evidence for Metabolism and Bioresorption after Intravenous Administration to Rats. *Mol. Pharm.* **3**, 614.
- 164 Zhang, Y., Huo, M., Zhou, J. & Xie, S. 2010. PKSolver: An add-in program for pharmacokinetic and pharmacodynamic data analysis in Microsoft Excel. *Computer Methods and Programs in Biomedicine* **99**, 306.
- 165 Gorman, M., Chim, Y. H., Hart, A., Riehle, M. O. & Urquhart, A. J. 2014. Poly(N-acryloylmorpholine): A simple hydrogel system for temporal and spatial control over cell adhesion. *J. Biomed. Mater. Res.* **102**, 1809.
- 166 Hussain, S. M., Hess, K. L., Gearhart, J. M., Geiss, K. T. & Schlager, J. J. 2005. In vitro toxicity of nanoparticles in BRL 3A rat liver cells. *Toxicol In Vitro* **19**, 975.
- 167 Wang, Y. *et al.* 2013. Comparison Study of Gold Nanohexapods, Nanorods, and Nanocages for Photothermal Cancer Treatment. *ACS Nano* **7**, 2068.
- 168 Salvati, A. *et al.* 2011. Experimental and theoretical comparison of intracellular import of polymeric nanoparticles and small molecules: toward models of uptake kinetics. *Nanomed-Nanotechnol.* **7**, 818.
- 169 Iversen, T.-G., Skotland, T. & Sandvig, K. 2011. Endocytosis and intracellular transport of nanoparticles: Present knowledge and need for future studies. *Nano Today* **6**, 176.

- 170 Li, Y., Krger, M. & Liu, W. K. 2015. Shape effect in cellular uptake of PEGylated nanoparticles: comparison between sphere, rod, cube and disk. *Nanoscale* **7**, 16631.
- 171 Chithrani, D. B. & Chan, W. C. W. 2007. Elucidating the Mechanism of Cellular Uptake and Removal of Protein-Coated Gold Nanoparticles of Different Sizes and Shapes. *Nano Lett.* **7**, 1542.
- 172 Chithrani, D. B., Ghazani, A. A. & Chan, W. C. W. 2006. Determining the size and shape dependence of gold nanoparticle uptake into mammalian cells. *Nano Lett.* **6**, 662.
- 173 dos Santos, T., Varela, J., Lynch, I., Salvati, A. & Dawson, K. A. 2011. Effects of transport inhibitors on the cellular uptake of carboxylated polystyrene nanoparticles in different cell lines. *PLoS ONE* **6**, e24438.
- 174 Cui, X., Wan, B., Yang, Y., Ren, X. & Guo, L.-H. 2017. Length effects on the dynamic process of cellular uptake and exocytosis of single-walled carbon nanotubes in murine macrophage cells. *Sci. Rep.* **7**, 1518.
- 175 Rathgeber, S., Pakula, T., Wilk, A., Matyjaszewski, K. & Beers, K. L. 2005. On the shape of bottle-brush macromolecules: Systematic variation of architectural parameters. *J. Chem. Phys.* **122**.
- 176 Sun, J. *et al.* 2015. Tunable Rigidity of (Polymeric Core)–(Lipid Shell) Nanoparticles for Regulated Cellular Uptake. *Adv. Mater.* **27**, 1402.
- 177 Zhao, J., Lu, H., Yao, Y., Ganda, S. & Stenzel, M. H. 2018. Length vs. stiffness: which plays a dominant role in the cellular uptake of fructose-based rod-like micelles by breast cancer cells in 2D and 3D cell culture models? *J. Mater. Chem. B* **6**, 4223.
- 178 Walkey, C. D., Olsen, J. B., Guo, H., Emili, A. & Chan, W. C. W. 2012. Nanoparticle Size and Surface Chemistry Determine Serum Protein Adsorption and Macrophage Uptake. *J. Am. Chem. Soc.* **134**, 2139.
- 179 Araujo, M. E. G., Liebscher, G., Hess, M. W. & Huber, L. A. 2020. Lysosomal size matters. *Traffic* **21**, 60.
- 180 Fukami, T. & Yokoi, T. 2012. The Emerging Role of Human Esterases. *Drug Metab. Pharmacokinet.* **27**, 466.
- 181 Cordes, E. H. & Bull, H. G. 1974. Mechanism and catalysis for hydrolysis of acetals, ketals, and ortho esters. *Chem. Rev.* **74**, 581.
- 182 Dobretsov, G. E., Syrejschikova, T. I. & Smolina, N. V. 2014. On mechanisms of fluorescence quenching by water. *Biophysics* **59**, 183.
- 183 Yang Khor, S. *et al.* 2015. Molecular weight (hydrodynamic volume) dictates the systemic pharmacokinetics and tumour disposition of PolyPEG star polymers. *Nanomed-Nanotechnol.* **11**, 2099.
- 184 Kaminskas, L. M. *et al.* 2008. The Impact of Molecular Weight and PEG Chain Length on the Systemic Pharmacokinetics of PEGylated Poly L-Lysine Dendrimers. *Mol. Pharmaceutics* **5**, 449.
- 185 Lee, H. B. & Blafox, M. D. 1985. Blood Volume in the Rat The estimation of blood volume is important in studies. *J. Nucl. Med.* **25**, 72.
- 186 Cataldi, M., Vigliotti, C., Mosca, T., Cammarota, M. & Capone, D. 2017. Emerging Role of the Spleen in the Pharmacokinetics of Monoclonal Antibodies, Nanoparticles and Exosomes. *Int. J. Mol. Sci.* **18**.
- 187 Khor, S. Y. *et al.* 2016. The Pharmacokinetics and Biodistribution of a 64 kDa PolyPEG Star Polymer After Subcutaneous and Pulmonary Administration to Rats. *J. Pharm. Sci.* **105**, 293.
- 188 Liu, Y., Hu, Y. & Huang, L. 2014. Influence of polyethylene glycol density and surface lipid on pharmacokinetics and biodistribution of lipid-calcium-phosphate nanoparticles. *Biomaterials* **35**, 3027.
- 189 Morais, T. *et al.* 2012. Effect of surface coating on the biodistribution profile of gold nanoparticles in the rat. *Eur. J. Pharm. Biopharm.* **80**, 185.

- 190 Anselmo, A. C. & Mitragotri, S. 2019. Nanoparticles in the clinic: An update. *Bioeng. Transl. Med.* **4**, e10143.
- 191 Johnston, A. P. R., Such, G. K., Ng, S. L. & Caruso, F. 2011. Challenges facing colloidal delivery systems: From synthesis to the clinic. *Curr. Opin. Colloid Interface Sci.* **16**, 171.
- 192 Mosqueira, V. C. F. M. *et al.* 2001. Biodistribution of Long-Circulating PEG-Grafted Nanocapsules in Mice: Effects of PEG Chain Length and Density. *Pharm. Res.* **18**, 1411.
- 193 Ishida, T. *et al.* 2005. Accelerated blood clearance of PEGylated liposomes following preceding liposome injection: Effects of lipid dose and PEG surface-density and chain length of the first-dose liposomes. *J. Control. Release* **105**, 305.
- 194 Kaminskas, L. M. *et al.* 2009. Partly-PEGylated Poly-L-lysine Dendrimers Have Reduced Plasma Stability and Circulation Times Compared With Fully PEGylated Dendrimers. *J. Pharm. Sci.* **98**, 3871.
- 195 Claudia, M., Kristin, Ö., Jennifer, O., Eva, R. & Eleonore, F. 2017. Comparison of fluorescence-based methods to determine nanoparticle uptake by phagocytes and non-phagocytic cells in vitro. *Toxicology* **378**, 25.
- 196 Liu, X., Huang, N., Li, H., Jin, Q. & Ji, J. 2013. Surface and Size Effects on Cell Interaction of Gold Nanoparticles with Both Phagocytic and Nonphagocytic Cells. *Langmuir* **29**, 9138.
- 197 Sheng, Y. *et al.* 2009. In vitro macrophage uptake and in vivo biodistribution of PLA-PEG nanoparticles loaded with hemoglobin as blood substitutes: effect of PEG content. *J. Mater. Sci. Mater. Med.* **20**, 1881.
- 198 Nichols, J. W. & Bae, Y. H. 2014. EPR: Evidence and fallacy. *J. Control. Release* **190**, 451.
- 199 Danhier, F. 2016. To exploit the tumor microenvironment: Since the EPR effect fails in the clinic, what is the future of nanomedicine? *J. Control. Release* **244**, 108.
- 200 Stefan, W. *et al.* 2016. Analysis of nanoparticle delivery to tumours. *Nat. Rev. Mater.* **1**, 1.
- 201 Truong, N. P., Whittaker, M. R., Mak, C. W. & Davis, T. P. 2015. The importance of nanoparticle shape in cancer drug delivery. *Expert Opin. Drug Deliv.* **12**, 129.
- 202 Chu, K. S. *et al.* 2013. Plasma, tumor and tissue pharmacokinetics of Docetaxel delivered via nanoparticles of different sizes and shapes in mice bearing SKOV-3 human ovarian carcinoma xenograft. *Nanomed-Nanotechnol.* **9**, 686.
- 203 Chauhan, V. P. *et al.* 2011. Fluorescent Nanorods and Nanospheres for Real-Time In Vivo Probing of Nanoparticle Shape-Dependent Tumor Penetration. *Angew. Chem.* **50**, 11417.
- 204 Arnida, Janát-Amsbury, M. M., Ray, A., Peterson, C. M. & Ghandehari, H. 2011. Geometry and surface characteristics of gold nanoparticles influence their biodistribution and uptake by macrophages. *Eur. J. Pharm. Biopharm.* **77**, 417.
- 205 Tian, B., Zhang, X., Yu, C., Zhou, M. & Zhang, X. 2015. The aspect ratio effect of drug nanocrystals on cellular internalization efficiency, uptake mechanisms, and in vitro and in vivo anticancer efficiencies. *Nanoscale* **7**, 3588.
- 206 Jung, J. 2014. Human tumor xenograft models for preclinical assessment of anticancer drug development. *Toxicol. Res.* **30**, 1.
- 207 Kaga, S. *et al.* 2017. Influence of Size and Shape on the Biodistribution of Nanoparticles Prepared by Polymerization-Induced Self-Assembly. *Biomacromolecules* **18**, 3963.
- 208 Rashid, O. M. & Takabe, K. 2015. Animal models for exploring the pharmacokinetics of breast cancer therapies. *Expert Opin. Drug Metab. Toxicol.* **11**, 221.
- 209 Pulaski, B. A. & Ostrand-Rosenberg, S. 2000. Mouse 4T1 Breast Tumor Model. *Curr. Protoc. Immunol.* **39**, 20.2.1.
- 210 Pulaski, B. A. & Ostrand-Rosenberg, S. 1998. Reduction of Established Spontaneous Mammary Carcinoma Metastases following Immunotherapy with Major Histocompatibility Complex Class II and B7.1 Cell-based Tumor Vaccines. *Cancer Res.* **58**, 1486.

- 211 Loizides, C. *et al.* 2015. Model-Based Tumor Growth Dynamics and Therapy Response in a Mouse Model of De Novo Carcinogenesis. *PLoS ONE* **10**, e0143840.
- 212 Baklaushev, V. P. *et al.* 2017. Luciferase Expression Allows Bioluminescence Imaging But Imposes Limitations on the Orthotopic Mouse (4T1) Model of Breast Cancer. *Sci. Rep.* **7**, 7715.
- 213 Croce, A. C. *et al.* 2008. Liver autofluorescence properties in animal model under altered nutritional conditions. *Photochem. Photobiol. Sci.* **7**, 1046.
- 214 Saitou, T. *et al.* 2018. Tissue Intrinsic Fluorescence Spectra-Based Digital Pathology of Liver Fibrosis by Marker-Controlled Segmentation. *Front Med (Lausanne)* **5**, 350.
- 215 Arms, L. *et al.* 2018. Advantages and Limitations of Current Techniques for Analyzing the Biodistribution of Nanoparticles. *Frontiers in Pharmacology* **9**, 802.
- 216 Liu, Y., Tseng, Y.-c. & Huang, L. 2012. Biodistribution Studies of Nanoparticles Using Fluorescence Imaging: A Qualitative or Quantitative Method? *Pharm. Res.* **29**, 3273.
- 217 Dobretsov, G., Syrejschikova, T. & Smolina, N. 2014. On mechanisms of fluorescence quenching by water. *Biophysics* **59**, 183.
- 218 Sadekar, S., Ray, A., Janàt-Amsbury, M., Peterson, C. M. & Ghandehari, H. 2011. Comparative Biodistribution of PAMAM Dendrimers and HPMA Copolymers in Ovarian-Tumor-Bearing Mice. *Biomacromolecules* **12**, 88.
- 219 Kaminskas, L. M. *et al.* 2011. Characterisation and tumour targeting of PEGylated polylysine dendrimers bearing doxorubicin via a pH labile linker. *J. Control. Release* **152**, 241.
- 220 Zhang, L. *et al.* 2019. Tumor Chemo-Radiotherapy with Rod-Shaped and Spherical Gold Nano Probes: Shape and Active Targeting Both Matter. *Theranostics* **9**, 1893.
- 221 Perry, J. L. *et al.* 2017. Mediating Passive Tumor Accumulation through Particle Size, Tumor Type, and Location. *Nano Lett.* **17**, 2879.

APPENDIX

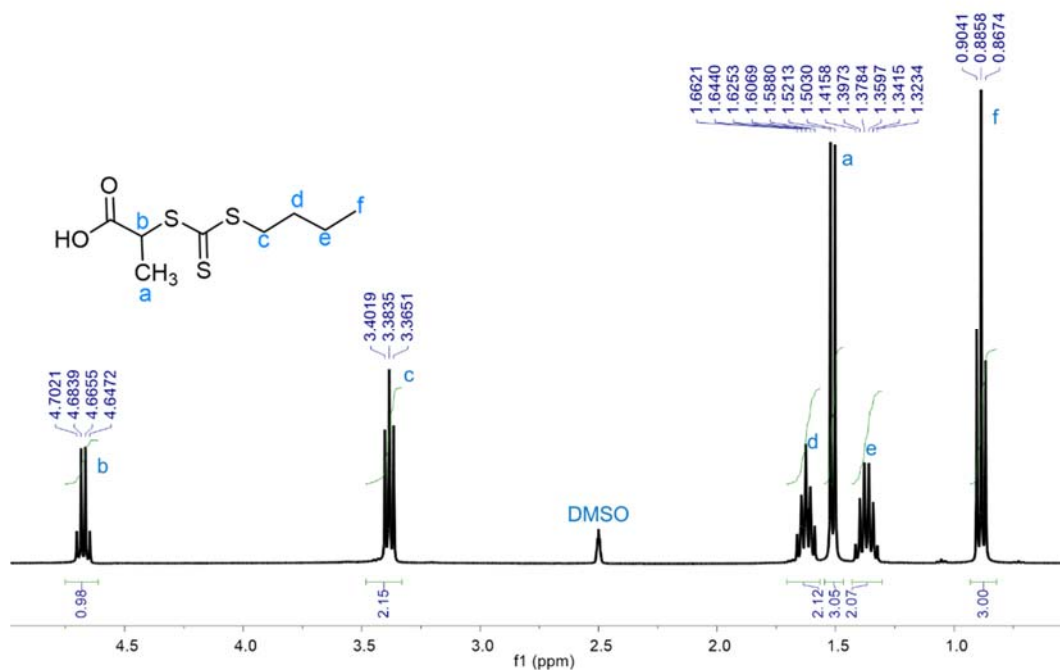


Figure A.1 ¹H NMR spectrum of C4 performed in d₆-DMSO

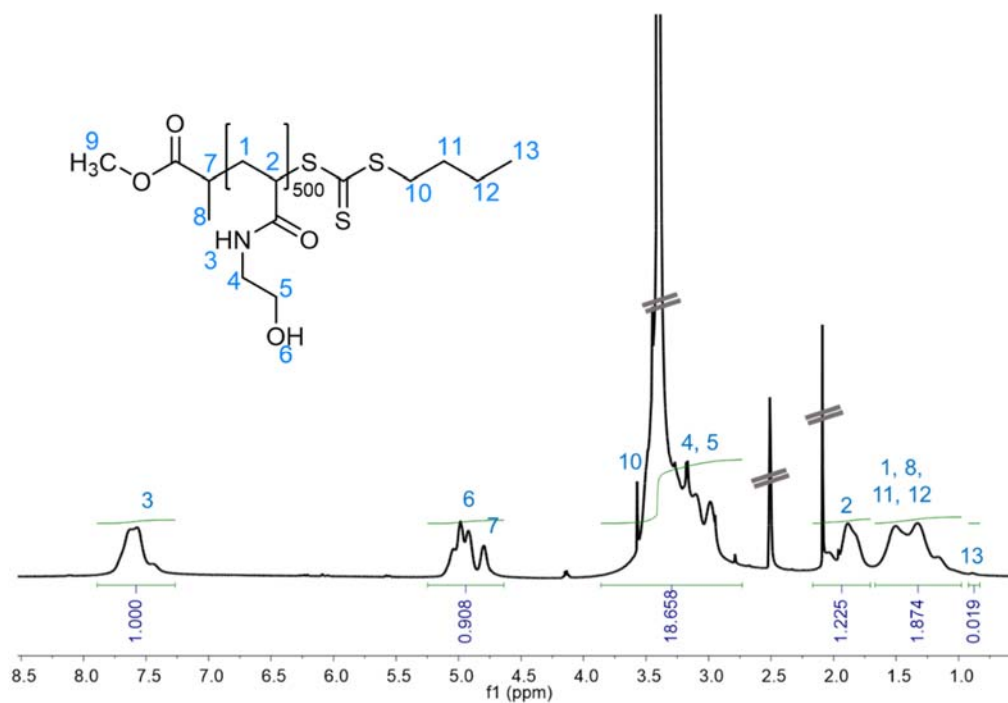


Figure A.2 Representative ¹H NMR spectrum of PHEAm₅₀₀ performed in d₆-DMSO

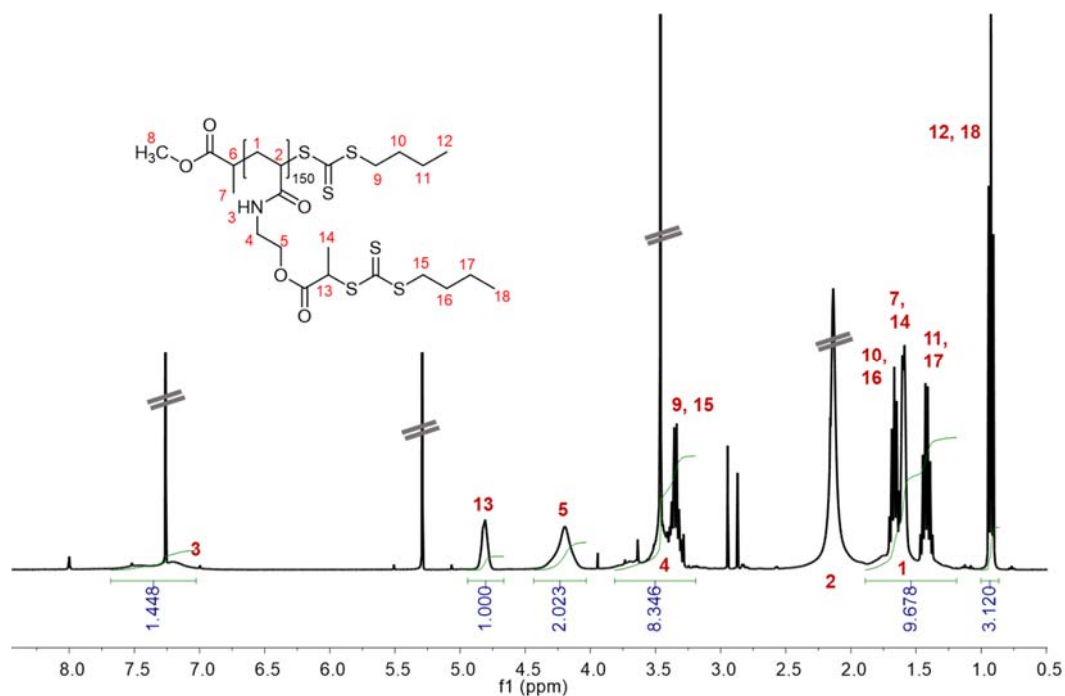


Figure A.3 Representative ^1H NMR spectrum of isolated PCTA-PHEAm₁₅₀ performed in CDCl_3

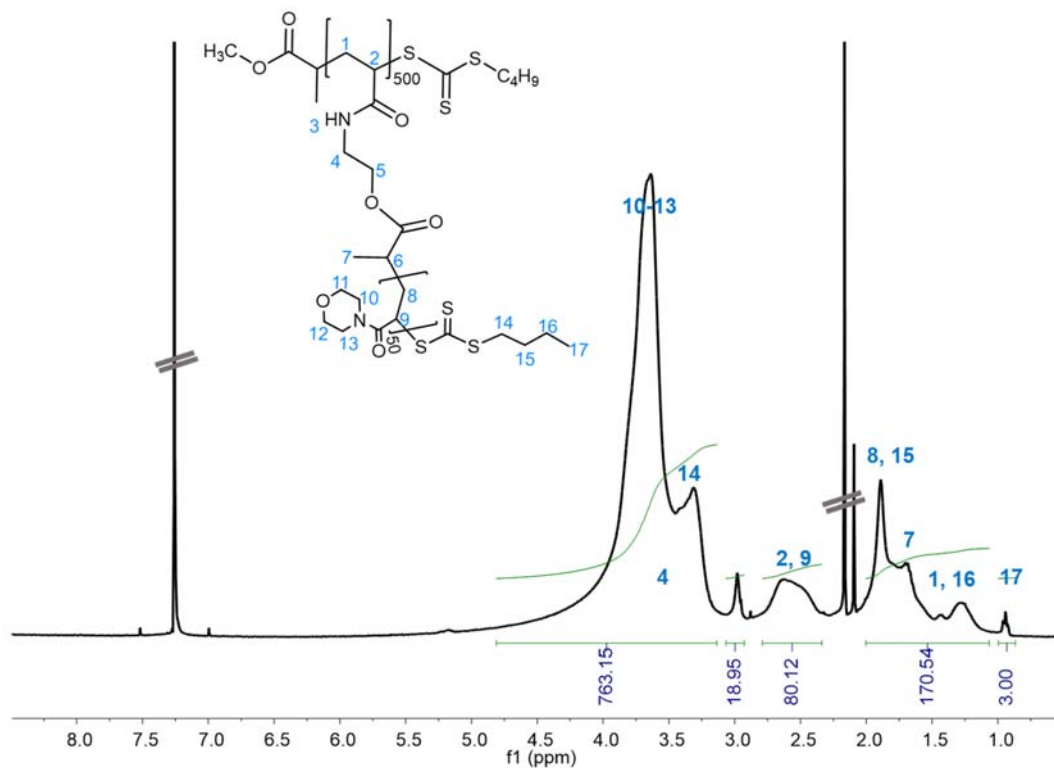


Figure A.4 Representative ^1H NMR spectrum of isolated brush [PNAM₅₀]₅₀₀ performed in CDCl_3

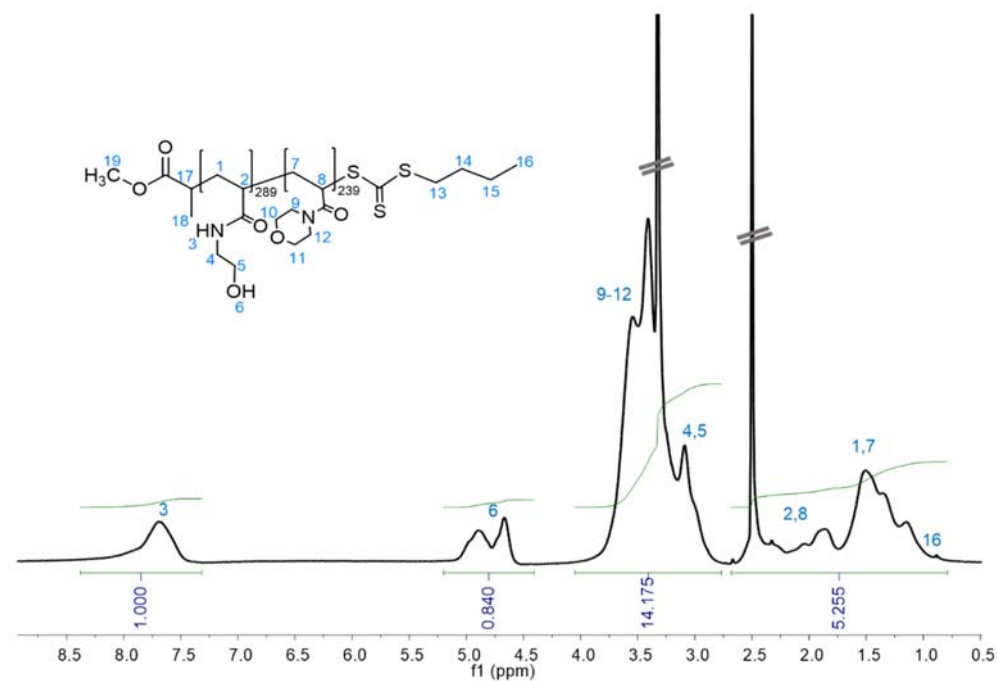


Figure A.5 Representative ^1H NMR spectrum of $P(\text{HEAm-co-NAM})_{50\%,500}$ performed in $d_6\text{-DMSO}$

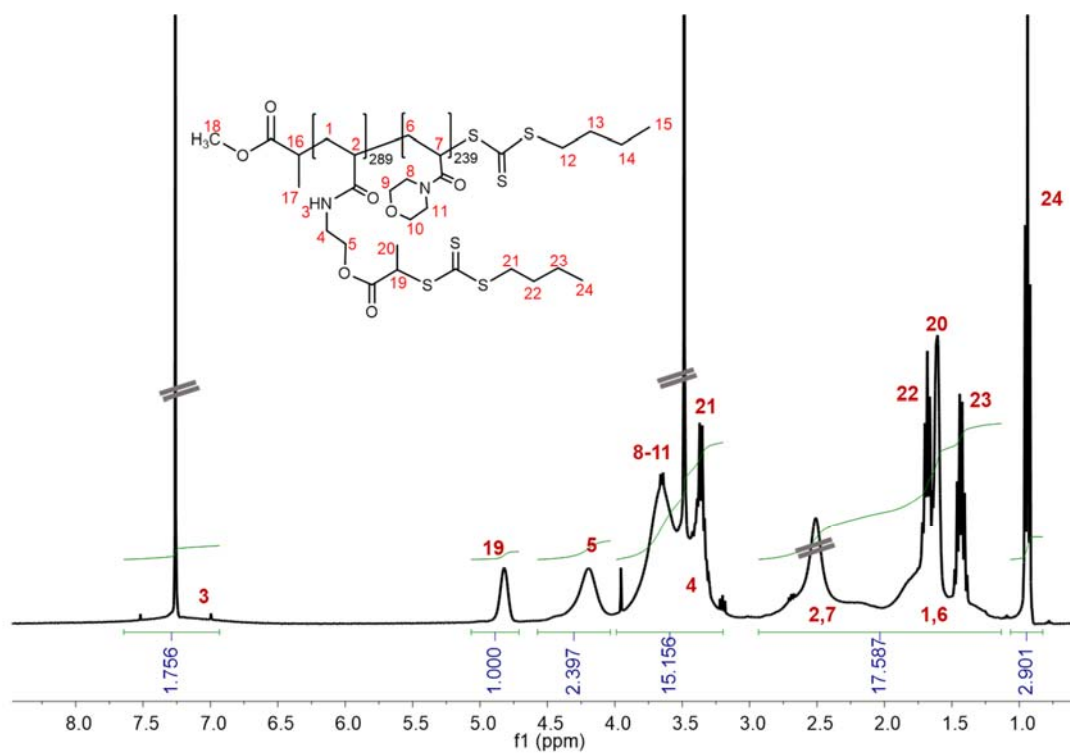


Figure A.6 Representative ^1H NMR spectra of isolated $P\text{CTA-}P(\text{HEAm-co-NAM})_{50\%,500}$ performed in CDCl_3

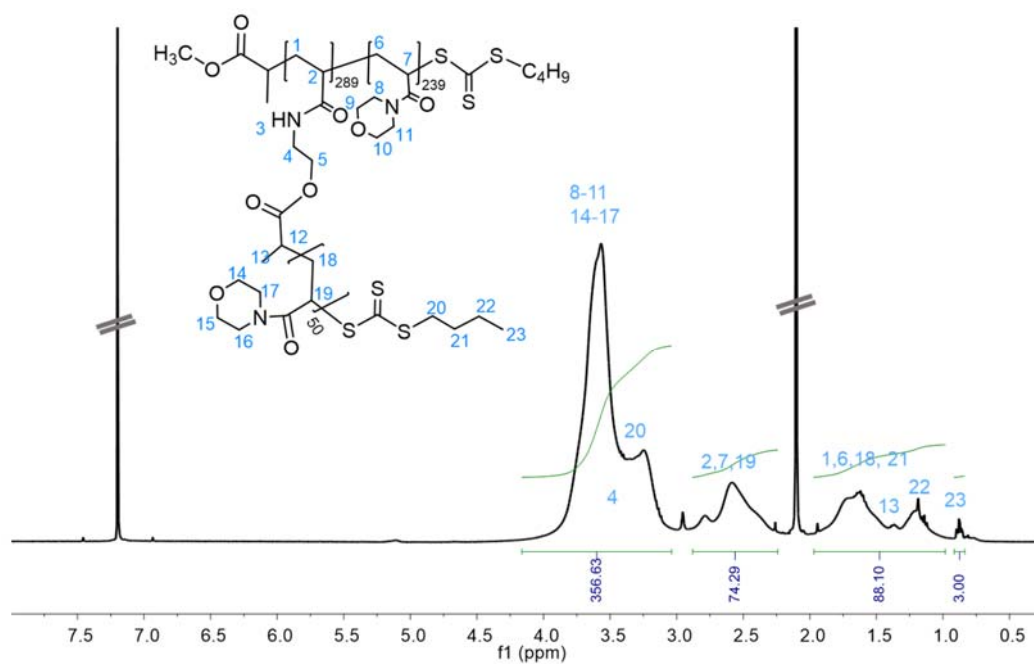


Figure A.7 Representative ¹H NMR spectra of isolated brush [PNAM₅₀]_{50%,500} performed in CDCl₃

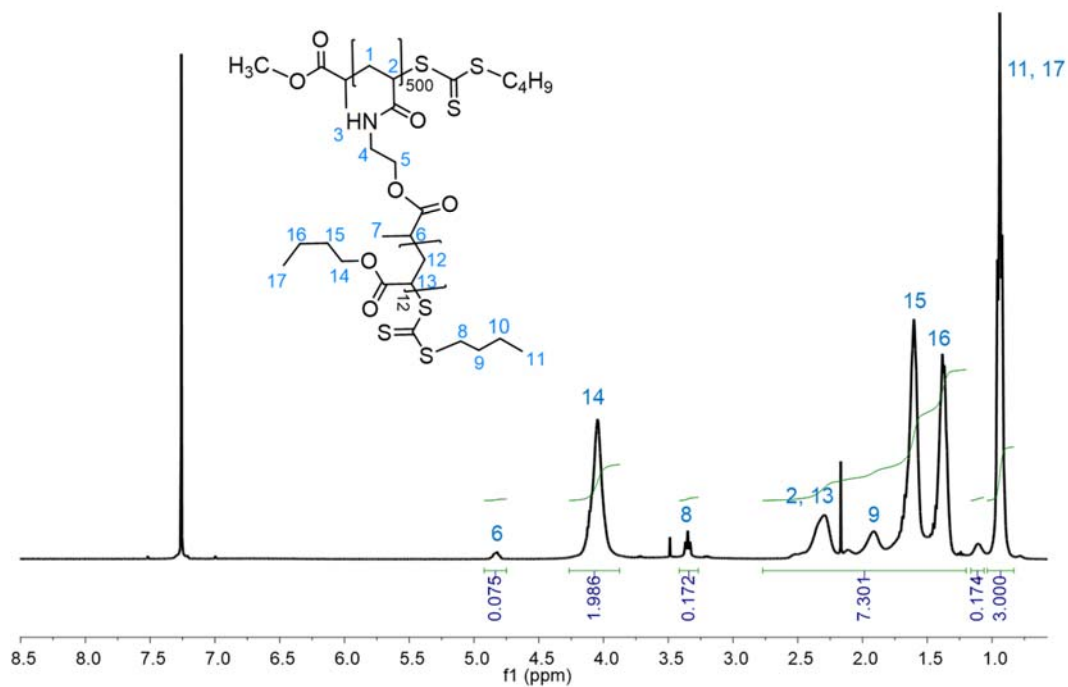


Figure A.8 Representative ¹H NMR spectrum of isolated brush [PnBA₁₂]₅₀₀ performed in CDCl₃

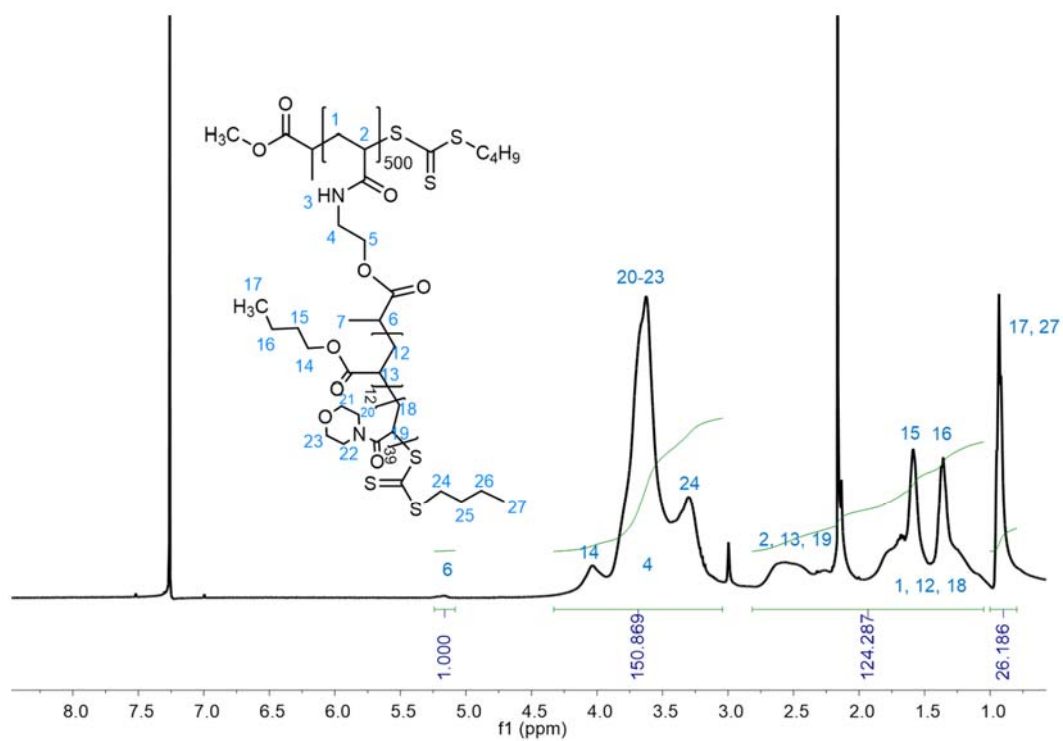


Figure A.9 Representative 1H NMR spectra of isolated brush $[PnBA_{12}-b-PNAM_{39}]_{500}$ performed in CDCl₃

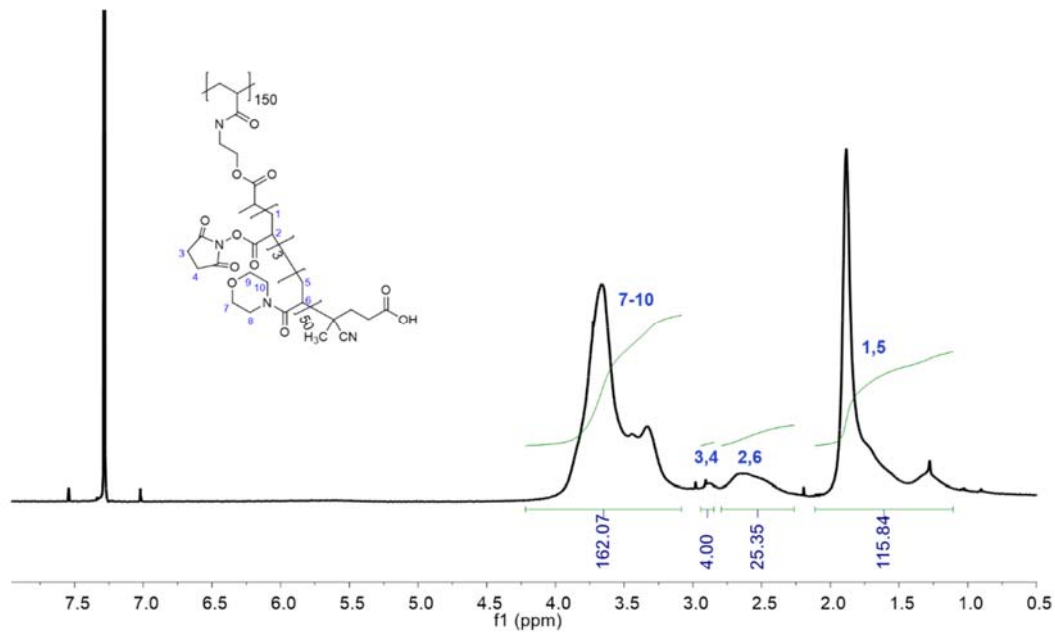


Figure A.10 Representative 1H NMR spectra of isolated brush $[P(NHSA_3-co-NAM_{50})]_{150}$ performed in CDCl₃

BM:PABTC = 1:1

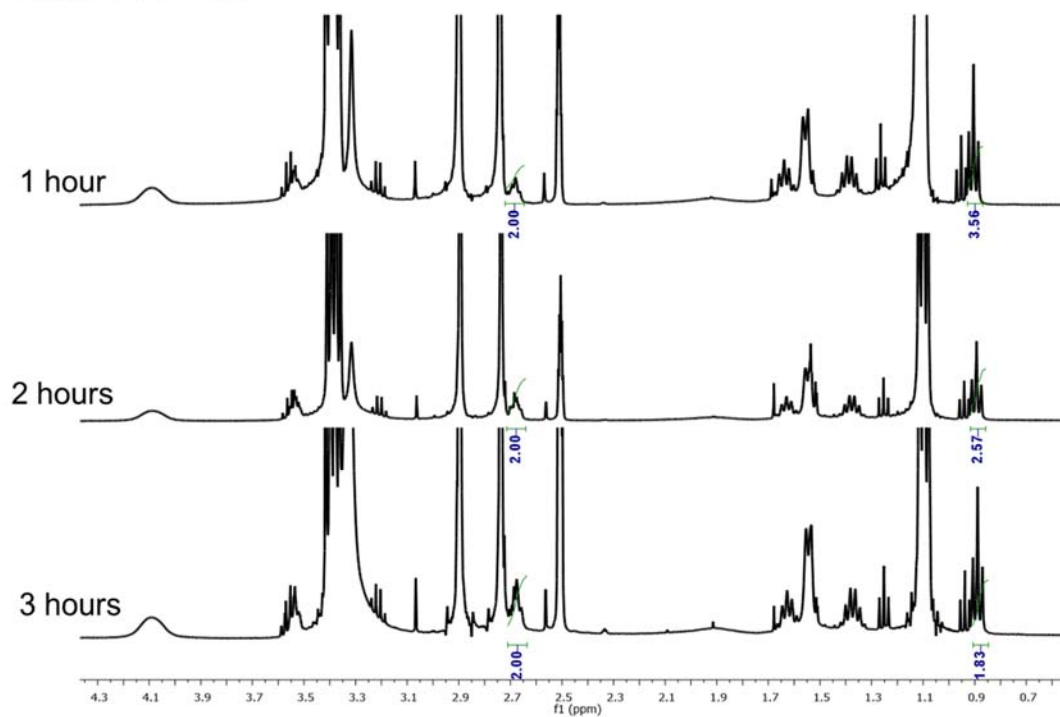


Figure A.11 Interchange analysis of BM/PABTC 1:1

BM:PABTC = 5:1

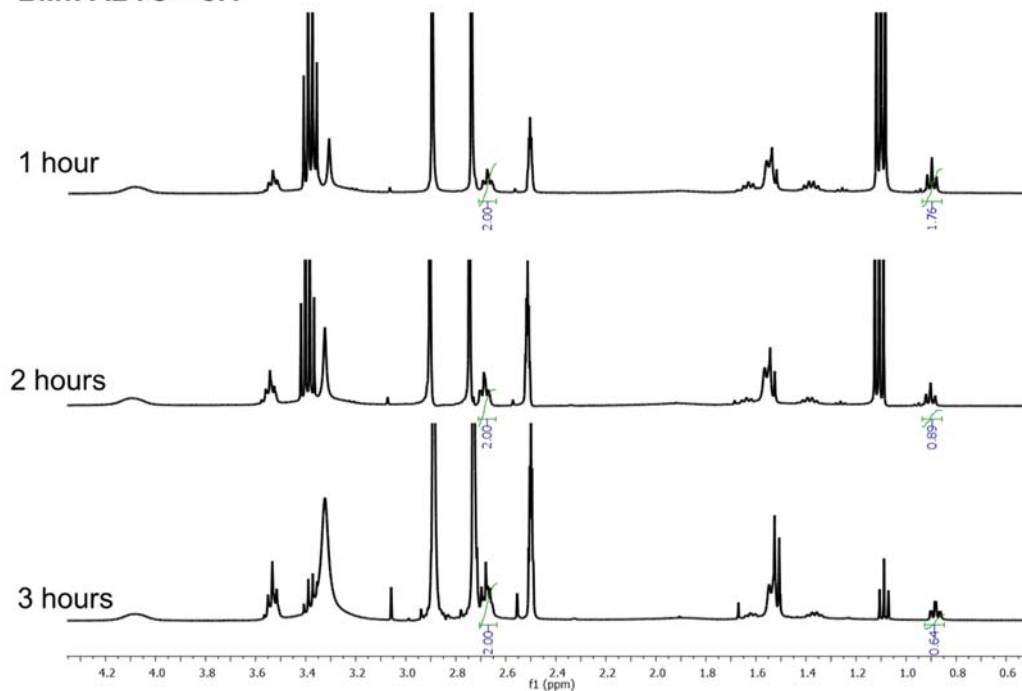


Figure A.12 Interchange analysis of BM/PABTC 5:1

BM:PABTC = 10:1

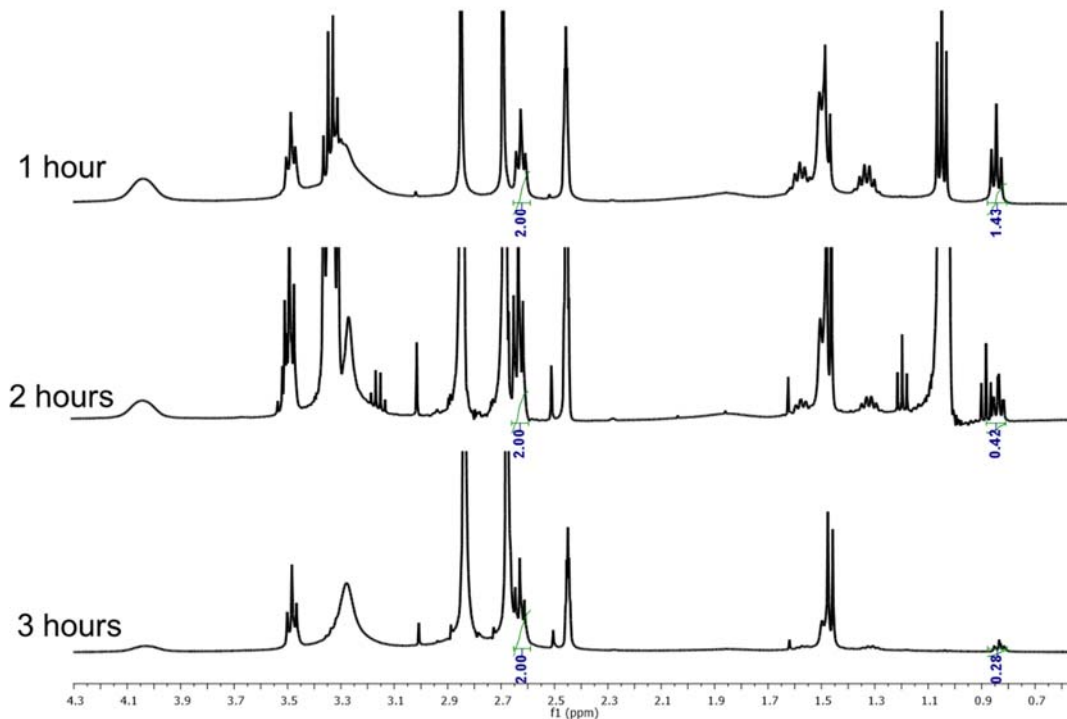


Figure A.13 Interchange analysis of BM/PABTC 10:1

Table A.1 Calculation of BM proportion compared to PABTC in polyCTA after interchange

BM/PABTC	Time	BM*	PABTC**	%BM	%PABTC
1:1	1 h	2.00	3.56	36	64
	2 h	2.00	2.57	44	56
	3 h	2.00	1.83	52	48
5:1	1 h	2.00	1.76	53	47
	2 h	2.00	0.89	69	31
	3 h	2.00	0.64	76	24
10:1	1 h	2.00	1.43	58	42
	2 h	2.00	0.42	82	18
	3 h	2.00	0.28	88	12

* δ (ppm) 2.68, 2H, quint

** δ (ppm) 0.88, 3H, t

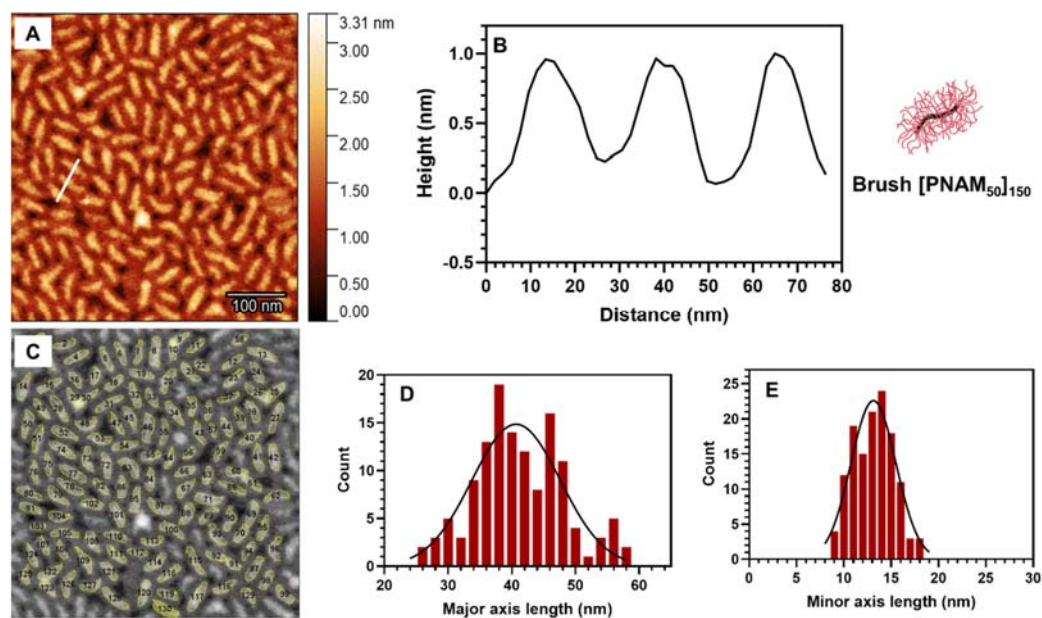


Figure A.14 (A) The AFM image of brush $[PNAM_{50}]_{150}$, the white line shows the representative particles for the cross sectional heights analysis, (B) the cross sectional height curve of brush $[PNAM_{50}]_{150}$ (C) selected region of interest for particle size analysis, (D) size distribution and Gaussian fit of major axis and (E) size distribution and Gaussian fit of minor axis

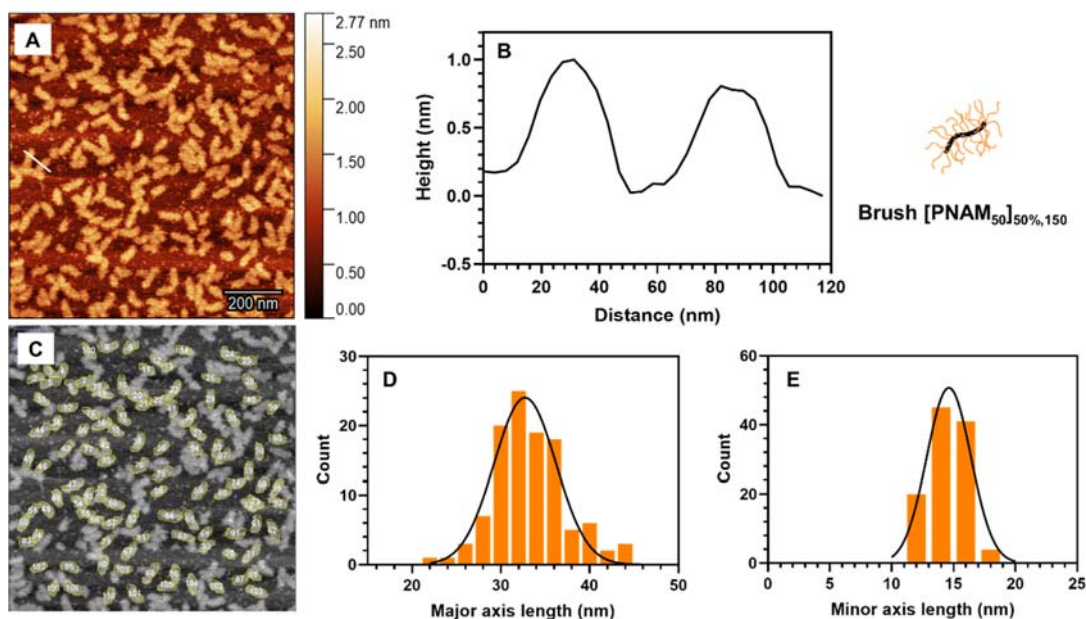


Figure A.15 (A) The AFM image of brush $[PNAM_{50}]_{50\%,150}$, the white line shows the representative particles for the cross sectional heights analysis, (B) the cross sectional height curve of brush $[PNAM_{50}]_{50\%,150}$ (C) selected region of interest for particle size analysis, (D) size distribution and Gaussian fit of major axis and (E) size distribution and Gaussian fit of minor axis

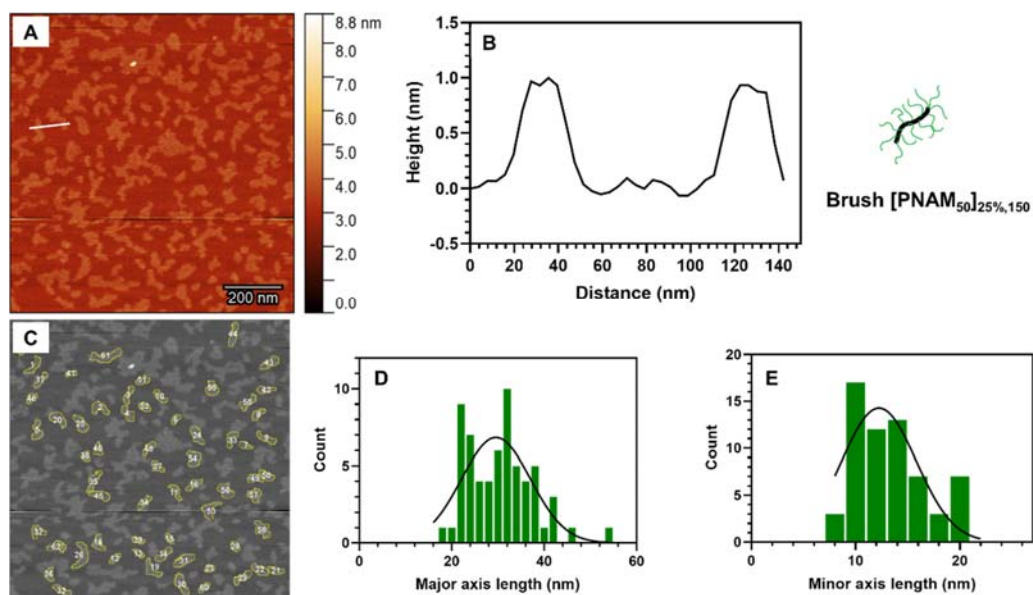


Figure A.16 (A) The AFM image of brush $[PNAM_{50}]_{25\%,150}$, the white line shows the representative particles for the cross sectional heights analysis, (B) the cross sectional height curve of brush $[PNAM_{50}]_{25\%,150}$ (C) selected region of interest for particle size analysis, (D) size distribution and Gaussian fit of major axis and (E) size distribution and Gaussian fit of minor axis

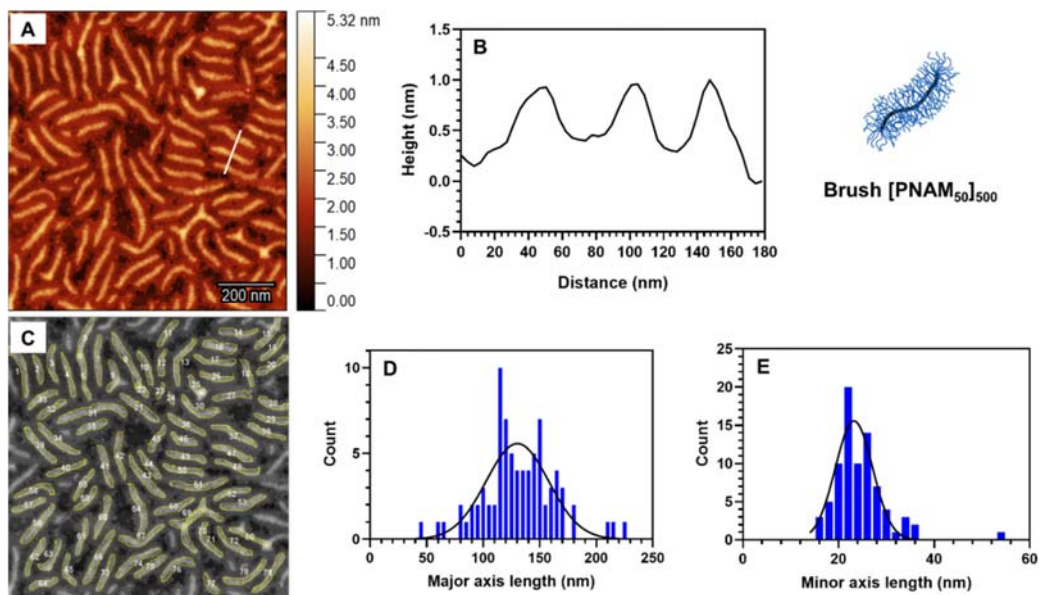


Figure A.17 (A) The AFM image of brush $[PNAM_{50}]_{500}$, the white line shows the representative particles for the cross sectional heights analysis, (B) the cross sectional height curve of brush $[PNAM_{50}]_{500}$ (C) selected region of interest for particle size analysis, (D) size distribution and Gaussian fit of major axis and (E) size distribution and Gaussian fit of minor axis

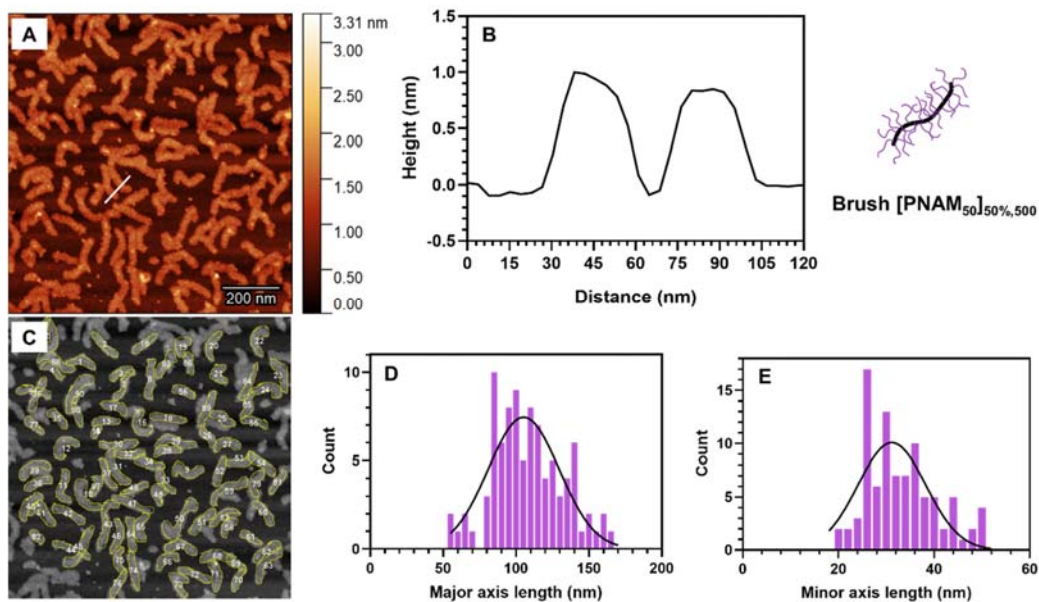


Figure A.18 (A) The AFM image of brush $[PNAM_{50}]_{50\%,500}$, the white line shows the representative particles for the cross sectional heights analysis, (B) the cross sectional height curve of brush $[PNAM_{50}]_{50\%,500}$ (C) selected region of interest for particle size analysis, (D) size distribution and Gaussian fit of major axis and (E) size distribution and Gaussian fit of minor axis

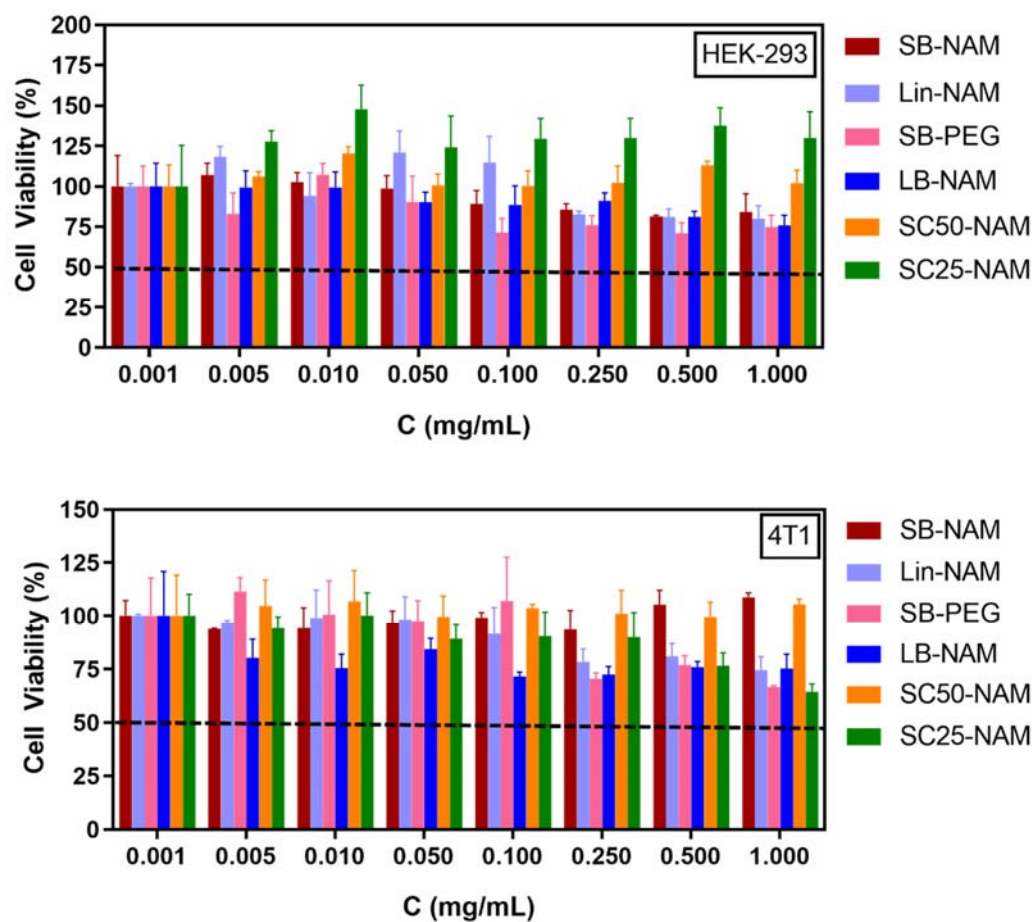
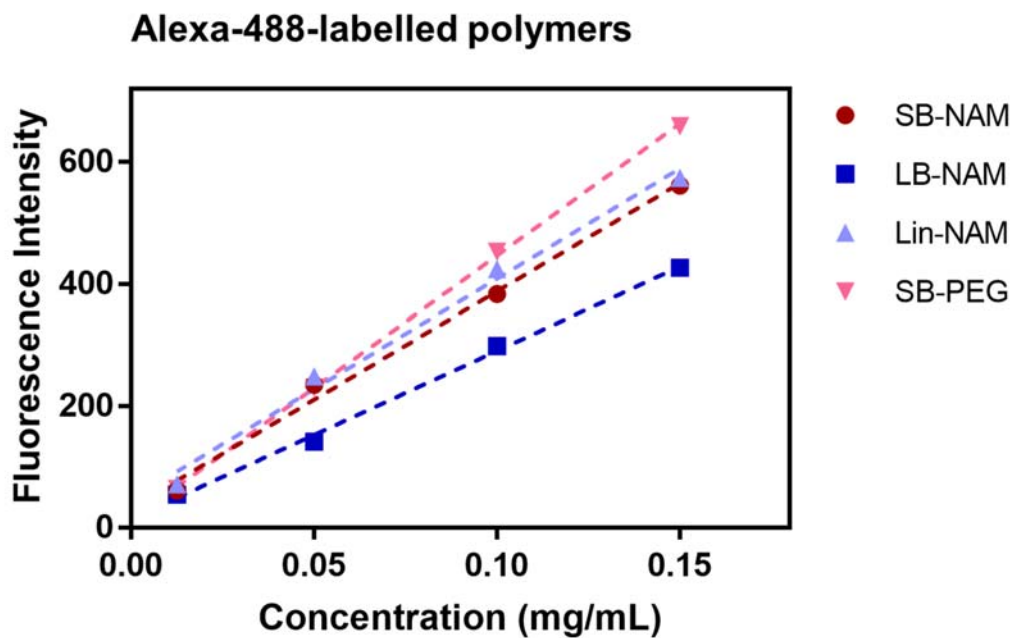


Figure A.19 Toxicity profile of the compounds in HEK-293 and 4T1 cells determined by MTT assay after incubation for 72 h at 37°C (mean \pm SD, $n = 3$)



--- Linear fit SB-NAM $Y = 3547 \cdot X + 32.97$ $r^2 = 0.9933$

--- Linear fit LB-NAM $Y = 2758 \cdot X + 14.47$ $r^2 = 0.9974$

--- Linear fit Lin-NAM $Y = 3615 \cdot X + 46.9$ $r^2 = 0.9904$

--- Linear fit SB-PEG $Y = 4336 \cdot X + 12.67$ $r^2 = 0.9997$

Figure A.20 Calibration curve of Alexa-488-labelled polymers

Table A.2 Calculation of fluorescence correction factors for Alexa-488-labelled polymers

	SB-NAM	LB-NAM	Lin-NAM	SB-PEG	Average
Slope	3547	2758	3615	4336	3564
Correction factor	1.0048	1.2922	0.9859	0.8220	1.010

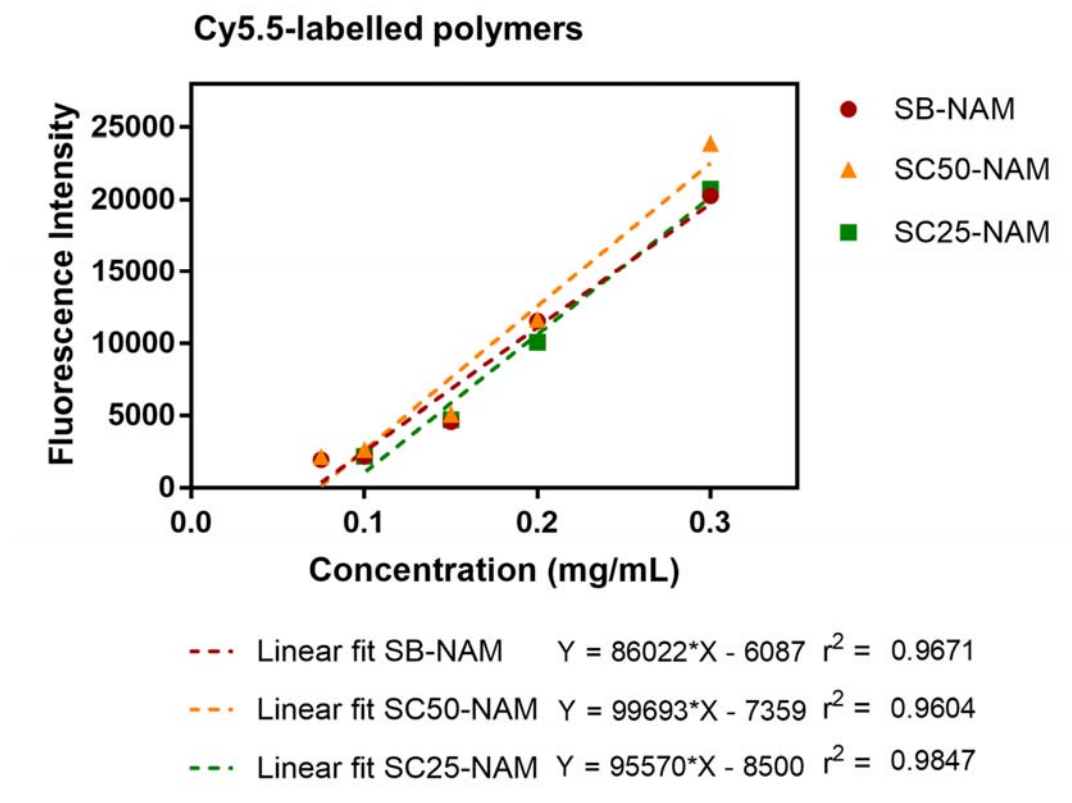


Figure A.21 Calibration curve of Cy5.5-labelled polymers

Table A.3 Calculation of fluorescence correction factors for Cy5.5-labelled polymers

	SB-NAM	SC50-NAM	SC25-NAM	Average
Slope	86022	99693	95570	93762
Correction factor	1.0900	0.9405	0.9811	1.0039

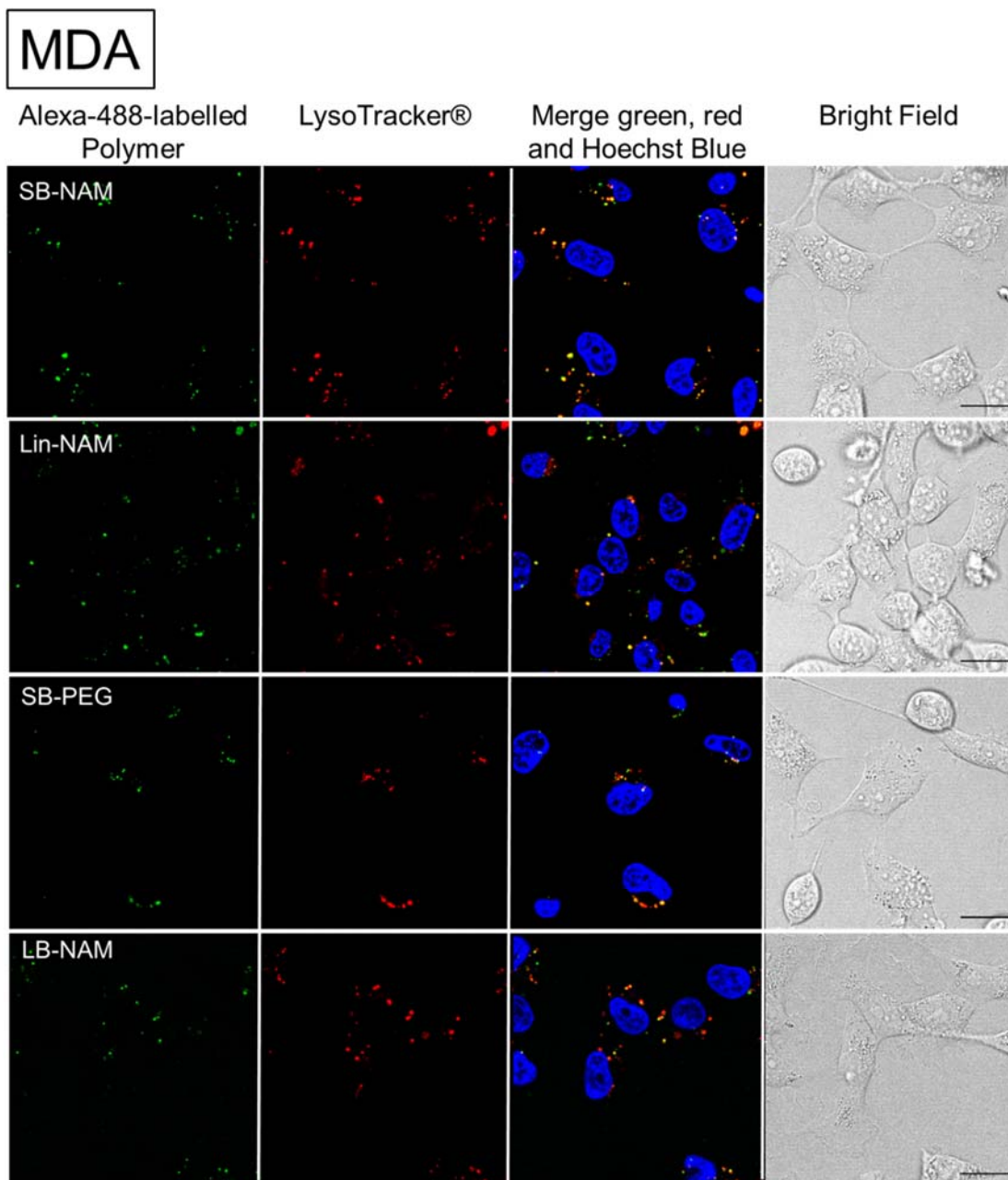


Figure A.22 Confocal images of MDA-MB-231 breast cancer cells treated with AlexaFluor™ 488-labelled polymers (green) for 24 h at 37°C at a concentration of 0.3 mg/mL. Lysosomes were stained using LysoTracker® (red), nucleus were stained using Hoechst® (blue). Scale bar 20 µm.

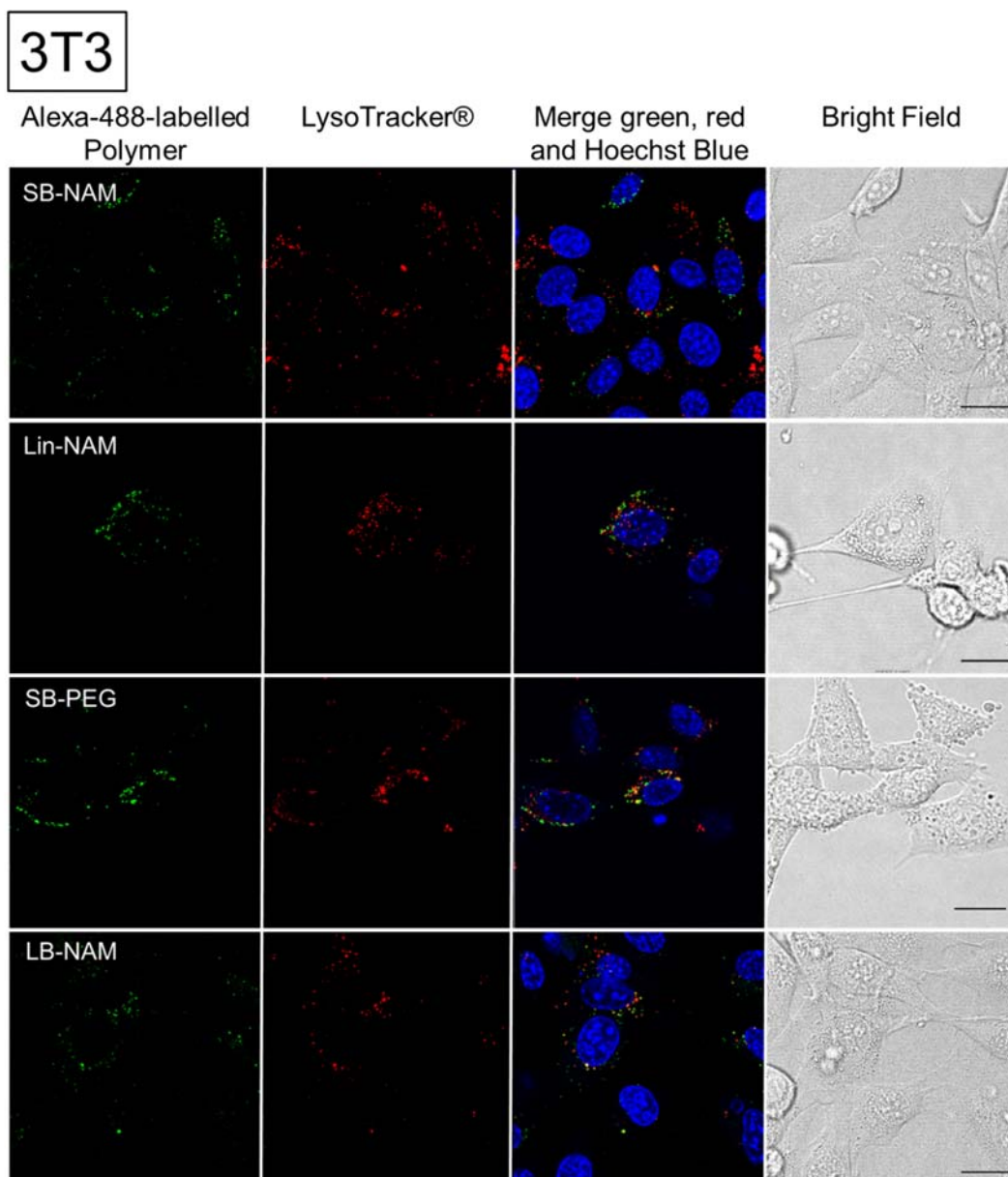


Figure A.23 Confocal images of 3T3 cells treated with AlexaFluor™ 488-labelled polymers (green) for 24 h at 37°C at a concentration of 0.3 mg/mL. Lysosomes were stained using LysoTracker® (red), nucleus were stained using Hoechst® (blue). Scale bar 20 µm.

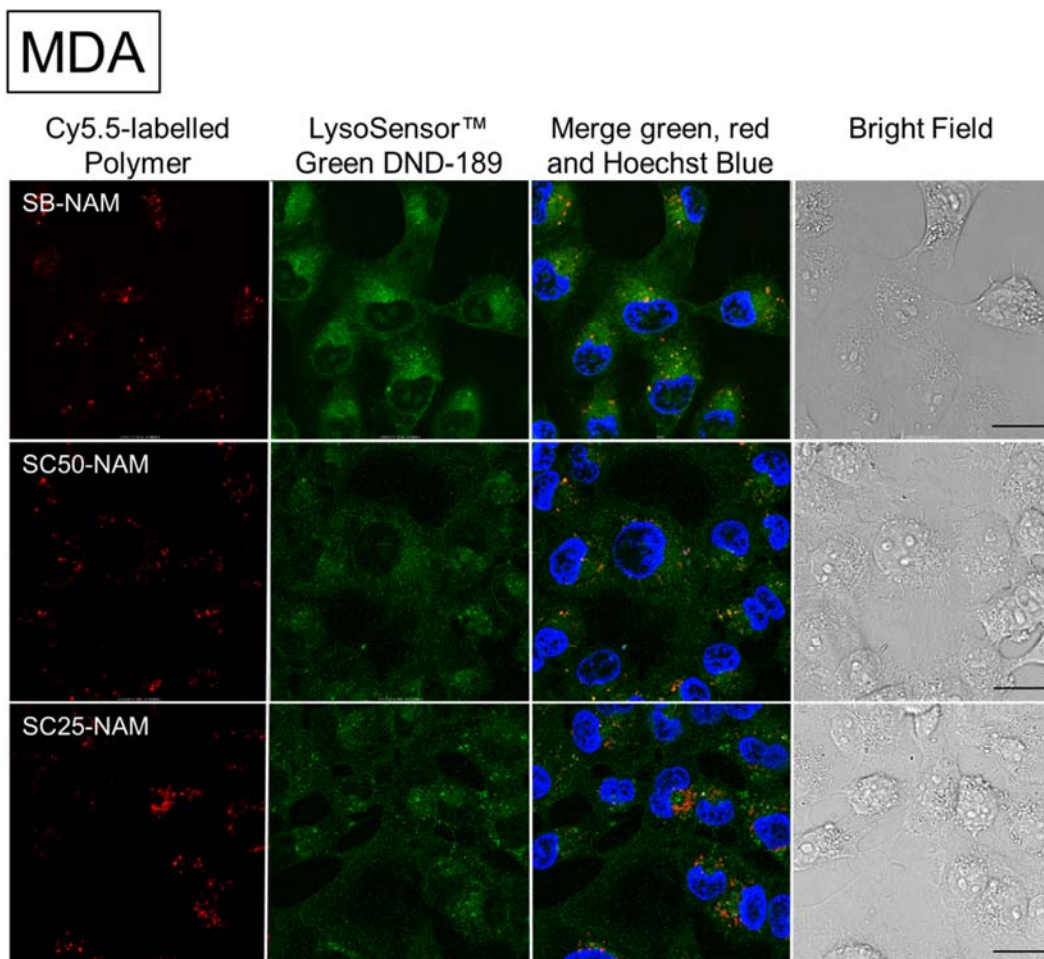


Figure A.24 Confocal images of MDA-MB-231-HM cells treated with Cy5.5-labelled polymer for 24 h at 37°C at a concentration of 0.3 mg/mL. LysoSensor™ green DND 189 (green), nucleus were stained using Hoechst® (blue).
Scale bar 20 µm.

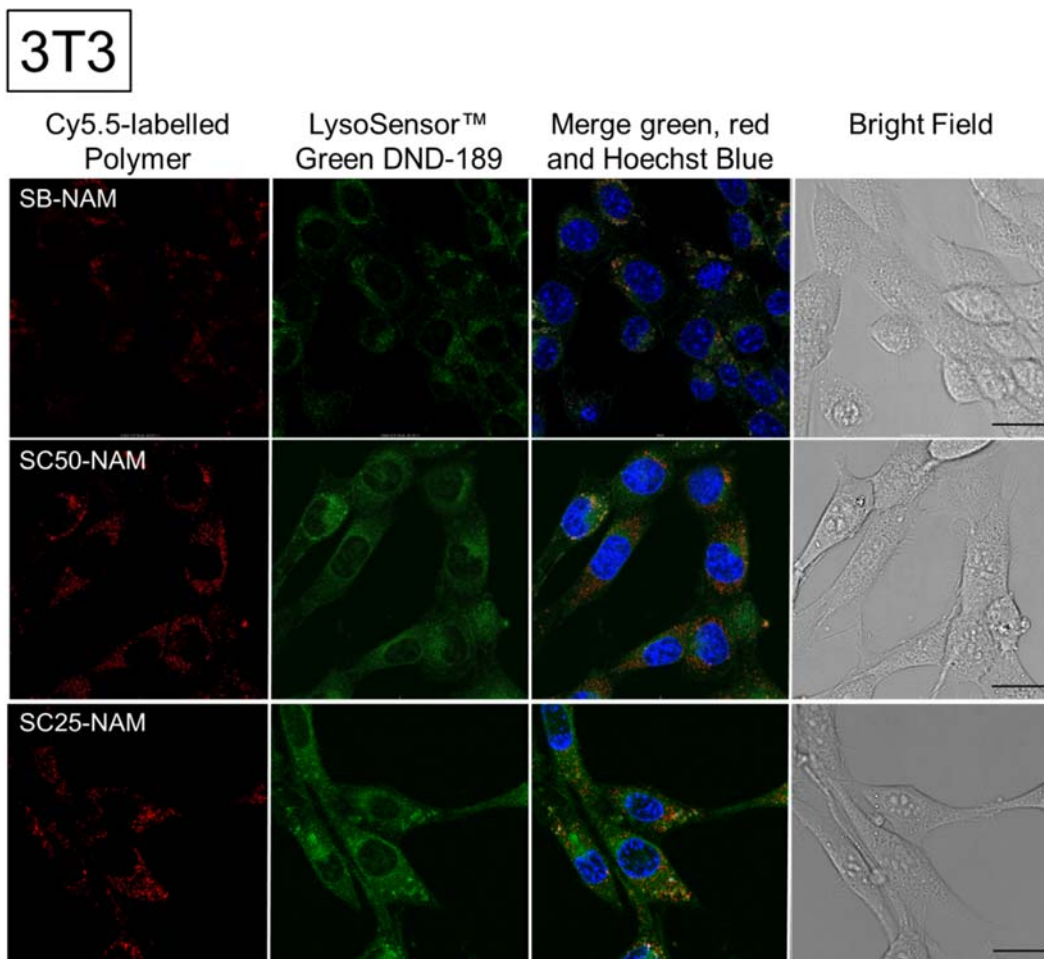


Figure A.25 Confocal images of 3T3 cells treated with Cy5.5-labelled polymer for 24 h at 37°C at a concentration of 0.3 mg/mL. Lysosomes were stained using LysoSensor™ green DND 189 (green), nucleus were stained using Hoechst® (blue). Scale bar 20 μ m.

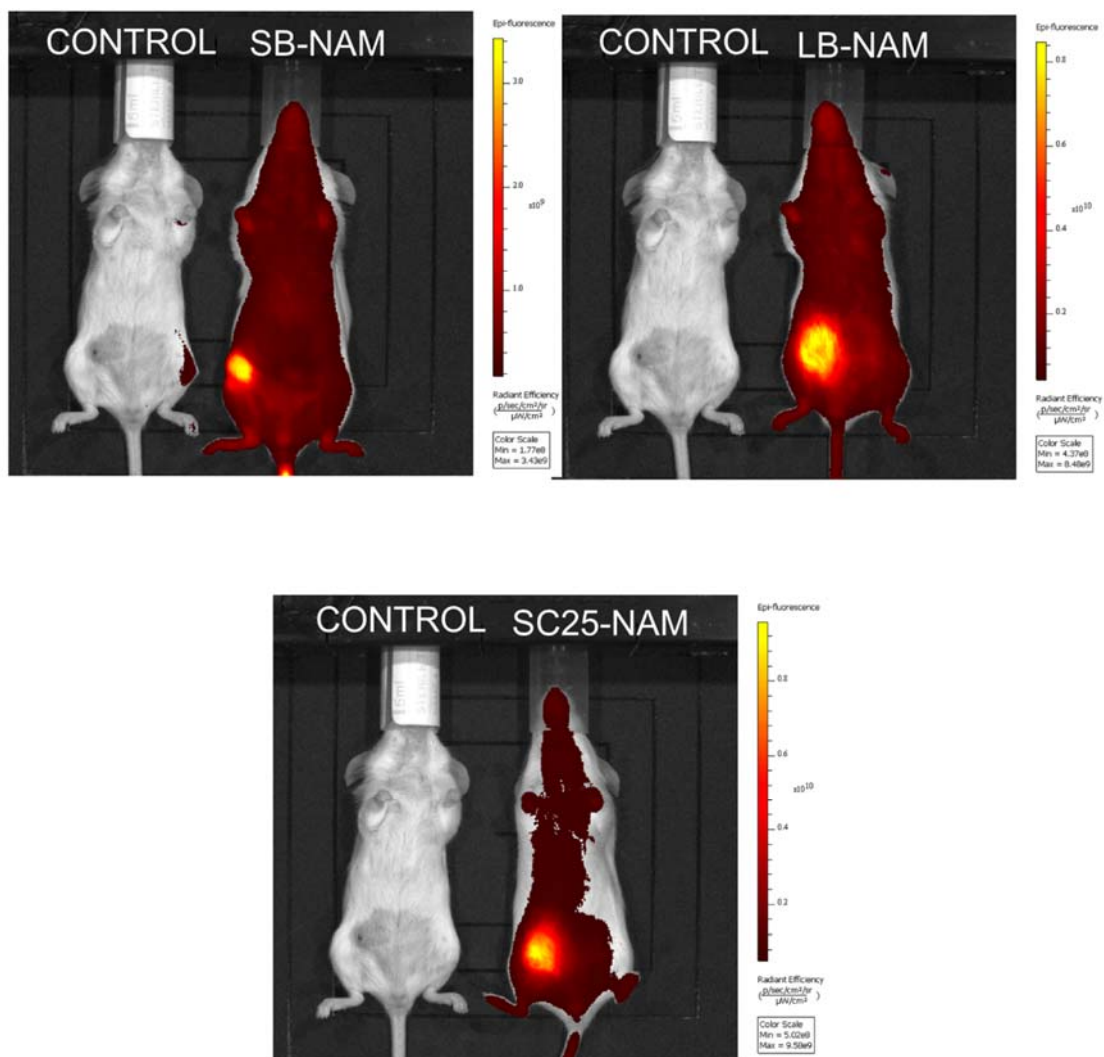


Figure A.26 Raw Image of mice from IVIS system 24 hours after injection of Cy5.5-labelled polymers

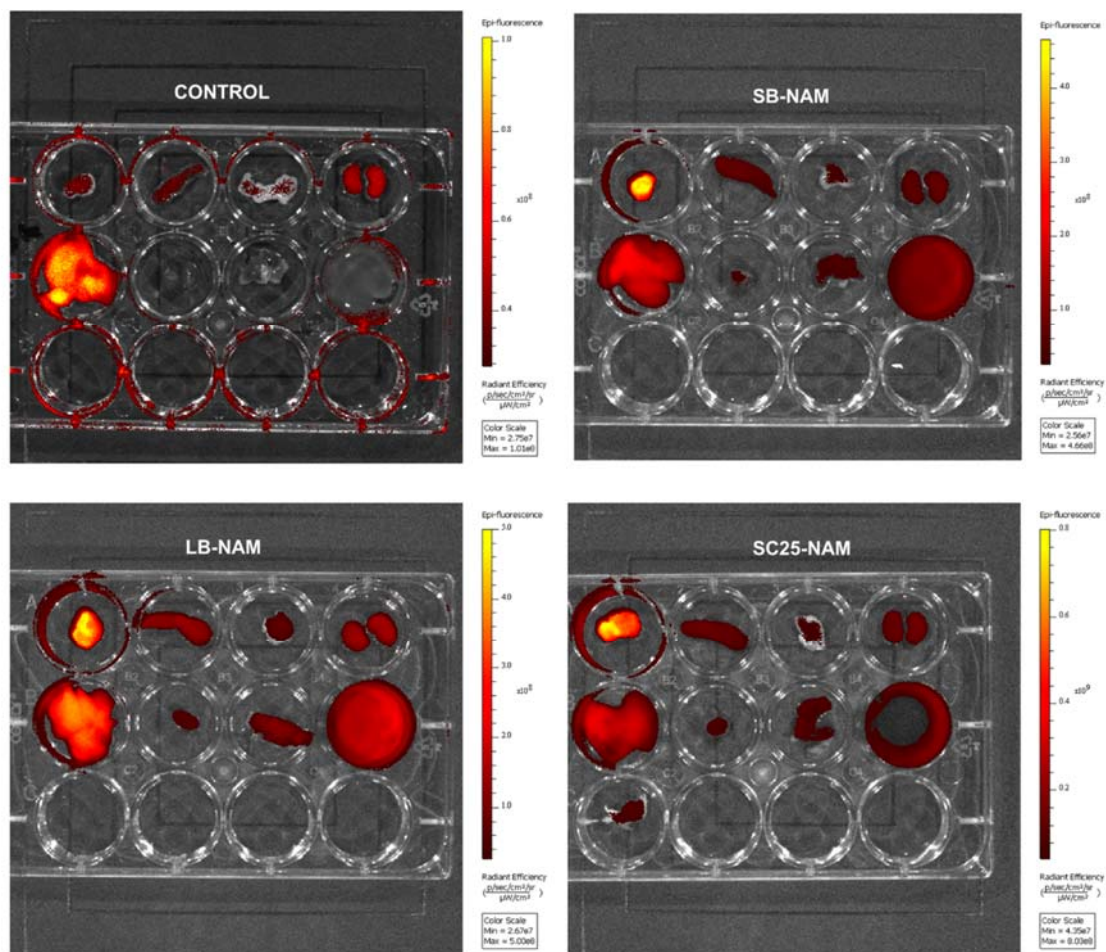


Figure A.27 Raw images of organs from individual scan from IVIS system 24 hours after injection of Cy5.5-labelled polymers

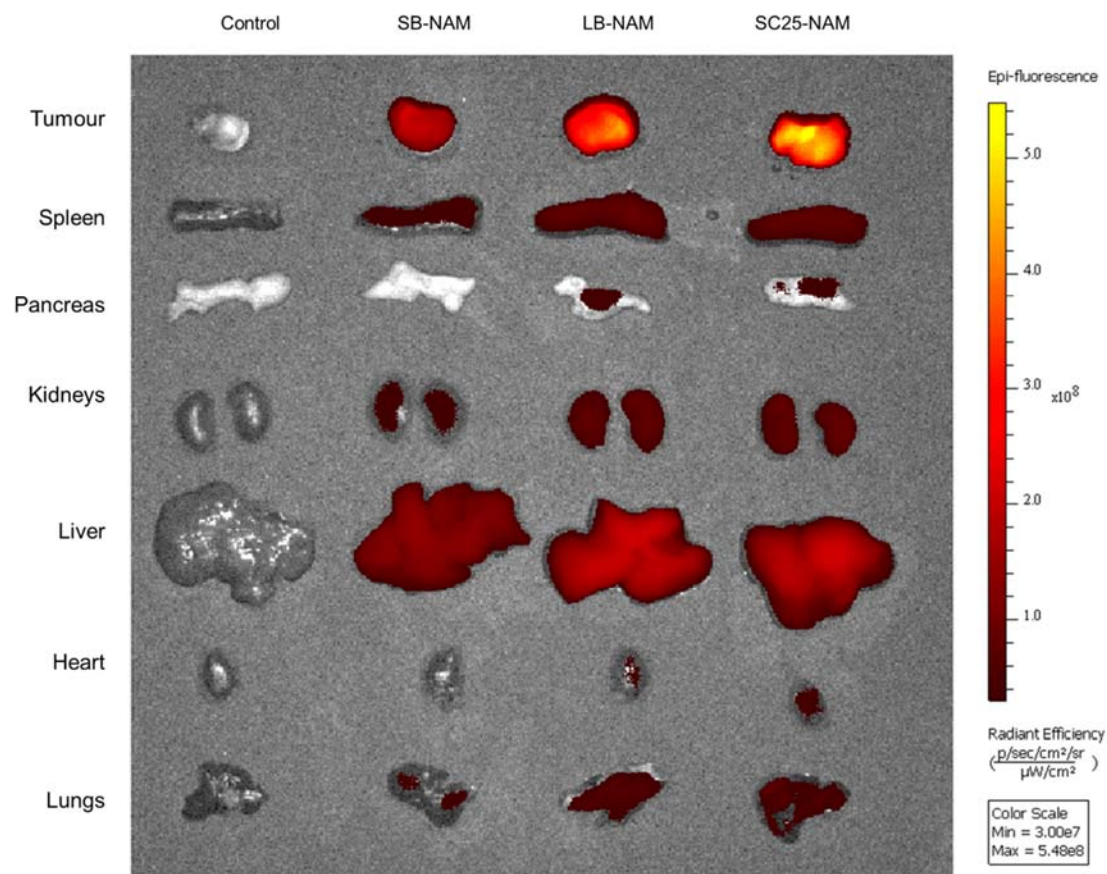


Figure A.28 Raw image of organs from simultaneous scan from IVIS system 24 hours after injection of Cy5.5-labelled polymers

Table A.4 Biodistribution of NAM-based BBPs in 4T1 tumour-bearing mice (%ID per g tissue)

	SB-NAM		LB-NAM		SC25-NAM	
Blood	31.46	± 13.58	19.12	± 3.57	23.78	± 4.92
Liver	16.25	± 5.2	22.47	± 8.48	10.67	± 4.44
Spleen	11.65	± 6.48	22.14	± 5.41	7.23	± 1.66
Pancreas	1.58	± 0.82	1.86	± 0.55	1.73	± 0.61
Kidneys	7.38	± 2.48	7.36	± 1.62	4.49	± 1.11
Heart	6.41	± 1.96	3.77	± 1.48	4.51	± 1.86
Lungs	10.26	± 5.81	7.60	± 2.32	8.37	± 3.17
Tumor	13.90	± 4.58	15.37	± 5.97	9.06	± 1.81
%Recovery	98.89		99.69		69.84	

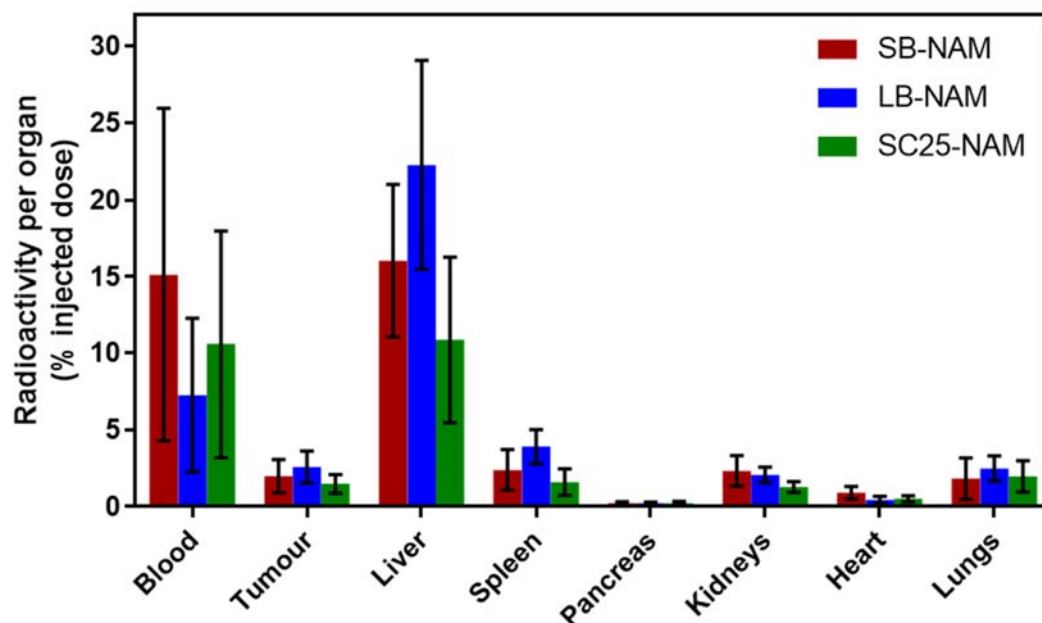


Figure A.29 Biodistribution of ¹⁴C-labelled BBPs after sacrifice at 24 h, expressed by %ID per organ. All BD data represent the mean ± SD (n = 6–7 mice).